JOHANNES KEPLER
UNIVERSITÄT LINZ | JKU

TNF
Technisch-Naturwissenschaftliche
Fakultät

The Hydraulic Buck Converter - Conceptual Study and Experiments

DISSERTATION

zur Erlangung des akademischen Grades

Doktor

im Doktoratsstudium der

Technischen Wissenschaften

Eingereicht von:

Dipl.–Ing. Helmut Kogler

Angefertigt am:

Institut für Maschinenelemente und hydraulische Antriebstechnik

Beurteilung:

o.Univ.–Prof. Dipl.–Ing. Dr.techn. Rudolf Scheidl (Betreuung)

Prof. Dr.–Ing. habil. Joachim Rudolph

Linz, Februar 2012

To my grandmother Maria.

Preface

The main advantage of hydraulic drive technology is its unrivalled force and power density. Small size hydraulic actuators can drive huge forces, but, hydraulics has the blemish of bad efficiency if proportional control is applied. This is a major reason why hydraulics loses ground to other drive technologies in terms of competitiveness. Furthermore, proportional- or servo valves are often highly sophisticated, fairly expensive and sensitive components. The importance of energy efficiency increases steadily due to rising energy costs and the demand for environmental friendly technology.

„Digital Hydraulics“ is an attempt to give an answer to this demand on simpler, more efficient, cheaper and more reliable hydraulic actuators. Two research groups, the Department of Intelligent Hydraulics and Automation (IHA) at the Tampere University of Technology in Finland and the Institute of Machine Design and Hydraulic Drives (IMH) at the Johannes Kepler University in close cooperation with the Austrian Center of Competence in Mechatronics (ACCM) in Linz started 10 years ago to intensively work on such types of hydraulic systems. While the IHA is concentrating on hydraulic digital-analogue converters, the IMH deals with fast switching hydraulic systems like, for instance, the hydraulic buck converter. Both research groups transfer concepts from digital electronics to hydraulics. This has not been possible for long, because of missing qualified components. For some years now, fast enough valves are available as prototypes to realise switching converter concepts in hydraulics.

This work focuses on the hydraulic buck converter. Basically, many other converter principles from electrical engineering like, for instance, the boost-, boost buck- or the resonance converter can be realised in hydraulics as well. Hydraulic switching converters represent dynamic systems, which require adequate mathematical models, control, fast valves and sensors. Hence, the proper design of such devices requires a mechatronic approach.

Summary

This thesis concerns the Hydraulic Buck Converter (HBC), which is a concept transferred from electric drive technology to hydraulics. In contrast to resistance control the HBC enables an energy efficient operation of hydraulic drives. This type of power control belongs to the class of fast switching hydraulic systems. Conventional resistance control uses proportional valves, which are responsible for the bad efficiency, since the surplus of pressure is dissipated by the metering of the valve. Moreover, proportional valves are expensive and sensitive against oil contamination. Fast switching hydraulic drives employ digital switching valves with a response time in the range of $1\,ms$. Because of their simple design such valves can be produced at low costs and, furthermore, they are robust against oil contamination. HBCs according to the current stage of switching valve technology operate at a switching frequency in the range of $100\,Hz$ in pulse-width-mode. The fluid in a pipe inductance is accelerated by the switching of a valve for a certain pulse time of the corresponding duty ratio, which is the control input of the converter. The occurring spill-over of kinetic energy of the fluid is used to draw oil from a lower to a higher pressure level, which results in a higher efficiency of the configuration. Furthermore, the HBC is even able to recuperate energy.

In this work the concept of the hydraulic buck converter is investigated. The potential of this drive technology is discussed by a number of simulations and experiments. The fast switching of the valves provokes high pressure pulsations in the hydraulic pipe system, which are often unwanted at the load. Thus, for a sound understanding of the dynamic behaviour of an HBC wave propagation in the fluid must be taken into account. To smoothen the excited pressure fluctuation due to the switching process a pulsation damper, e.g. a hydraulic accumulator, is applied. Also the dynamic behaviour of such accumulators plays a crucial role in hydraulic switching control. Due to the application of gas loaded hydraulic dampers for pressure attenuation a loss of stiffness in the load system occurs. The resulting softness of the system can be compensated by certain control strategies at least partially. A corresponding analysis is carried out and a flatness based controller design for a fast switching hydraulic drive is proposed in this work. The resulting non-linear controller designs are evaluated by simulations and by a number of experiments. Finally, an outlook of further developing steps of the HBC is presented.

Kurzfassung

Diese Dissertation beschäftigt sich mit dem hydraulischen Tiefsetzsteller (engl. Hydraulic Buck Converter), welcher in Analogie aus der elektrischen Antriebstechnik abgeleitet ist. Der HBC zählt zu den schnell schaltenden hydraulischen Systemen und erlaubt im Gegensatz zur Proportionalhydraulik einen energieeffizienten Betrieb von hydraulischen Antrieben. Die Druckstellung bei konventionellen hydraulischen Antrieben erfolgt über das Prinzip der Widerstandssteuerung durch Proportionalventile. Schnell schaltende hydraulische Antriebe verzichten für die Druckreduzierung gänzlich auf den Einsatz von Stetigventilen, welche für den schlechten Wirkungsgrad verantwortlich sind. Weiters können schaltende Ventile deutlich kostengünstiger produziert werden und sind unempfindlich gegenüber Ölverschmutzung. Die verwendeten Ventile besitzen eine Schaltzeit im Bereich von $1\,ms$. Der Konverter wird bei einer konstanten Schaltfrequenz in der Größenordnung von $100\,Hz$ in Pulsweitenmodulation betrieben. Dabei wird das Fluid in einer Rohrleitung, der Induktivität, durch das Schalten eines Ventils für die Zeit der angelegten Pulsdauer maximal beschleunigt. Durch den dabei anfallenden Überschuss an kinetischer Energie wird Öl von einem niedrigen auf ein höheres Druckniveau gebracht, was die wesentliche Wirkungsgradsteigerung mit sich bringt. Weiters ist es mit dem beschriebenen Konzept auch möglich Energie zu rekuperieren.

Das Konzept des hydraulischen Tiefsetzstellers wird in dieser Arbeit theoretisch untersucht, sowie anhand von Simulationen und Experimenten erörtert. Bei schnell schaltenden hydraulischen Antrieben werden Druckpulsationen im System angeregt. Daher muss für die Auslegung eines HBC auch Wellenausbreitung im Fluid berücksichtigt werden. Um die Druckpulsationen zu reduzieren kommen bei derartigen Antrieben Pulsationsdämpfer zum Einsatz. Dabei spielt das dynamische Verhalten dieser Energiespeicher eine entscheidende Rolle. Durch die Verwendung von gasgefüllten hydraulischen Speichern zum Glätten der Druckpulsationen verliert das Gesamtsystem seine Steifigkeit. Die damit entstandene Weichheit des hydraulischen Antriebes kann jedoch teilweise durch regelungstechnische Maßnahmen kompensiert werden, was für eine Vielzahl von Anwendungen mit ausreichender Genauigkeit möglich ist. Eine dementsprechende Analyse und ein flachheitsbasierter Reglerentwurf für einen schnell schalten hydraulischen Antrieb werden in dieser Arbeit ebenfalls durchgeführt und mit Experimenten überprüft. Zum Schluss wird noch ein Ausblick auf weitere Entwicklungsschritte präsentiert.

Acknowledgement

First, I want to express my deepest gratitude to Prof. Rudolf Scheidl, who gave me the possibility to enrich my knowledge in technical science, in particular, hydraulic drive technology. He always found the time to give me necessary support and, moreover, with his inspiring suggestions he contributed significantly to the success of this work.

I gratefully acknowledge the attendance of Prof. Joachim Rudolph for the second examination of this thesis. Furthermore, I appreciate his worthy suggestions concerning flatness, observers and state transformations, which were very helpful for me.

In many scientific concerns I appreciate the courtesy of Prof. Bernhard Manhartsgruber. Every time, when I reached my scientific limits he gave me the necessary hint to proceed.

Many thanks to my colleagues Andreas Tairych, Rainer Haas, Eugenio Leati and Markus Resch for their fellowship, to Siegfried Grammer for his prudent technical support and, to Silvia Hackl for her straightforward maintenance in non-scientific concerns.

Significant parts of this work were done in research projects of the Austrian Center of Competence in Mechatronics (ACCM), in particular in a project with Bosch Rexroth as an industrial partner. ACCM - which is a COMET K2 center - is funded by the Austrian Federal Government, the Federal State Upper Austria, and by ACCM's scientific partners.

A major partner of the ACCM is the Linz Center of Mechatronics (LCM). I enjoyed and still appreciate the teamwork with the researchers of the LCM business unit for Hydraulic Drives and Actuation Systems, in particular, Bernd Winkler, Andreas Plöckinger, Karl Ladner, Peter Ladner, Paul Foschum and Bernhard Hofmann.

Furthermore, I would like to mention the worthy assistance of Markus Mairhofer, Thomas Richter, Hannes Falkner, Michael Ehrentraut and Josef Schäffler, who accompanied my research in the frameworks of their student's projects and diploma theses, respectively.

Finally, I want to thank my parents, who granted me a well protected childhood and, who encouraged me to do those things which finally turned out to be beneficial and meaningful. My sincere thanks for your support, your confidence and your never ending love. *Liebe Eltern, ich danke Euch!*

Helmut Kogler

Linz, the 27^{th}February 2012

Contents

1 Hydraulic Switching Control **1**
1.1 A Historic Hydraulic Switching Converter 2
1.2 Basic Hydraulic Switching Control 4
1.3 The Wave Converter 5
1.4 The Resonance Converter 7
1.5 Digital Hydraulic Valve System 8
1.6 Fast Switching Hydraulic Concepts 10
1.6.1 The Hydraulic Buck Converter 11
1.6.2 The Hydraulic Boost Converter 13
1.6.3 The Hydraulic Boost Buck Converter 13

2 Theory of the Hydraulic Buck Converter **15**
2.1 Modes of Operation 15
2.1.1 Flow Control Mode 16
2.1.2 Pressure Control Mode 18
2.1.3 Characteristics 20
2.1.4 Efficiency 21
2.2 Limiting Effects and Nonidealities 24
2.2.1 Digital Valves 24
2.2.2 Wave Propagation 27
2.2.3 Hydraulic Parasitic Effects 29
2.2.3.1 Parasitic Inductance 29
2.2.3.2 Parasitic Capacity 32
2.2.3.3 Long Pipes and Hoses 33
2.2.4 Switching Frequency 34
2.2.5 Noise 34
2.3 Design Aspects 35
2.3.1 Load Specifications 36
2.3.2 Switching Frequency 36
2.3.3 Digital Valves 37
2.3.4 Inductance 40
2.3.5 Accumulator 41
2.3.5.1 Pressure Attenuation 42
2.3.5.2 Decoupling from Supply Lines 43
2.3.5.3 Accumulators for Fast Switching Hydraulics 44
2.3.6 Basic Design Procedure of an HBC 48
2.3.7 Block Design 49
2.3.8 Auxiliary Equipment 50
2.4 Pressure Attenuators 52

2.4.1 Helmholtz Resonator . . . 52
2.4.2 Vibration Compensator . . . 53
2.4.3 $\lambda/4$ - Compensator . . . 53

3 Basic Experiments 55
3.1 First Prototype . . . 55
3.2 Improved Test Rig . . . 60
3.2.1 Design of an HBC with Check Valves . . . 60
3.2.2 Analysis of Different Inductance Geometries . . . 64
3.2.3 Compact Design of the Inductance . . . 70
3.2.3.1 Threaded Spindle Inductance . . . 70
3.2.3.2 Coil Inductance . . . 71
3.3 Re-Design for Low Power Applications . . . 72
3.4 Theory versus Measurements . . . 77

4 Advanced Dynamic Modelling and Simulation 78
4.1 Time Domain Models . . . 79
4.1.1 The Orifice Equation . . . 79
4.1.2 Accumulator . . . 82
4.2 Time-Frequency-Domain-Iteration . . . 85
4.2.1 Formulation of the Problem . . . 87
4.2.2 Discretisation and Restriction to the Switching Interval . . . 88
4.2.3 Improvement of the Calculation Performance . . . 91
4.3 Simulation . . . 92
4.3.1 Model Verification . . . 92
4.3.2 Analysis of a certain working point . . . 93
4.3.3 Converter Characteristics . . . 95

5 Controller Design 102
5.1 Model for Synthesis . . . 103
5.2 Models for Simulation . . . 104
5.2.1 Simulation Model of the HBC . . . 104
5.2.2 Model for Comparison . . . 106
5.3 Linear Controller Design . . . 107
5.3.1 P-Controller . . . 107
5.3.2 Compensation Controller . . . 109
5.4 Flatness Based Control . . . 113
5.4.1 Flat Output and Feedforward Control . . . 114
5.4.2 Controller Design . . . 116
5.4.3 Observer Design . . . 118
5.4.3.1 Complete Observer . . . 121
5.4.3.2 Load Observer . . . 127
5.4.3.3 Reduced Observer . . . 134
5.4.4 Trajectory Planning . . . 139
5.4.4.1 Pre-Processing Method . . . 140
5.4.4.2 Pre-Filter . . . 141

6 Advanced Experiments 144
6.1 Energy Comparison . . . 144

6.2 Linear Drive Control Experiments . . . 149
6.2.1 Converter Characteristics . . . 150
6.2.2 Position Control . . . 152

7 Future Prospects 156
7.1 Efficient System Configuration . . . 156
7.2 Components . . . 159
7.2.1 Digital Valves . . . 159
7.2.2 Inductance . . . 160
7.3 Exploiting the Load Capacitance . . . 160
7.4 Fast Switching Converters . . . 161

A Appendix 164
A.1 Theoretic Characteristics in Recuperation Mode . . . 164
A.1.1 Flow Control Mode . . . 164
A.1.2 Pressure Control Mode . . . 165
A.1.3 Characteristics . . . 166
A.1.4 Efficiency . . . 167
A.2 Analytic Solution of Pressure Build Up Eq. (4.2) . . . 168
A.3 A Linear Model for the Pressure Build Up in a Hydraulic Accumulator . . . 169
A.4 TFDI-Simulations . . . 170
A.4.1 Identification . . . 170
A.4.2 Simulation Analysis . . . 171
A.5 Control Simulations . . . 172
A.5.1 Simulation Parameters . . . 172
A.5.2 Implementation of the Cylinder Model . . . 172

B Bibliographical Notes 176

C Curriculum Vitae 178

List of Figures 179

List of Tables 183

Bibliography 184

Nomenclature 188

Index 195

1. Hydraulic Switching Control

A great advantage of hydraulic systems is the ability to achieve high forces with a relatively small overall size. This high power density is confronted with a bad efficiency if proportional control is applied, which is nowadays the standard method to reduce the supplied pressure to that required by the load. Proportional control is a type of resistance control, where the surplus of pressure is dissipated by a metering orifice, like depicted in Fig. 1.1. In the case of lifting the load at a constant velocity, where the orifice R_T is

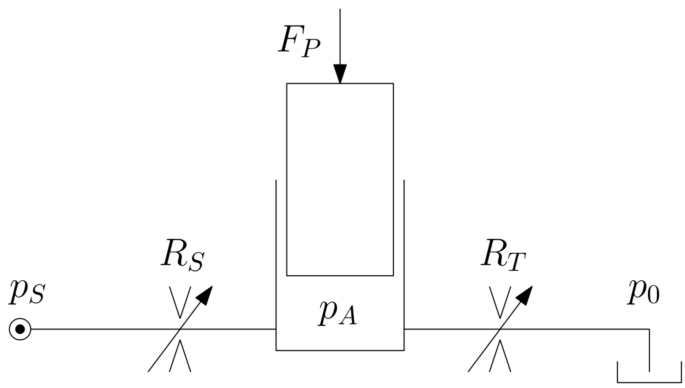

Figure 1.1.: Resistance control

assumed to be shut, the efficiency can be determined by

$$\eta_{up} = \frac{p_A}{p_S}. \tag{1.1}$$

Considering, that the hydraulic power supply is designed to the maximum occurring load, which is only rarely demanded at a large number of applications, a huge amount of energy is wasted. However, considering again the configuration of Fig. 1.1 now in case of lowering the load, when the orifice R_S is shut, the efficiency reads

$$\eta_{down} = \frac{p_0}{p_A} \approx 0, \tag{1.2}$$

with the ambient pressure p_0. If a large process force is applied to the plunger substantial amounts of energy are wasted.

For many years now the fluid power community attempts to raise the efficiency of hydraulic drives in order to stay competitive with other drive technologies and to cope with the challenge of limited energy resources. A few centuries ago, one of the serious competitors, the electrical drive technology, was also confronted with a bad efficiency in almost the same manner, since only resistance control was available with the need for better control. Resistance control were problematic due to the losses and the heat problems and were only applied for low power applications. The machine converter technologies, such as the Ward-Leonard converter, yet remarkably efficient, were large and heavy devices with great inertia, hence with only slow dynamic response. But the rapid development of high-power diodes, field-effect transistors and thyristors opened a wide range of new drive concepts based on switching technology. Such drives achieve high efficiencies even at low load voltages. Other concepts are able to recuperate energy at certain load cycles or they are even able to boost the load voltage to higher levels than the supply voltage. However, most of all switching concepts are harnessing the spill-over of the kinetic energy stored in inductances, which is excited by the switching process. So, in contrast to pure resistance control, the switching drives represent dynamic systems. This circumstance requires a sound understanding of the dynamic behavior of such systems to achieve the intended drive properties. The large number of energy efficient switching drives in electrical engineering might be enough motivation to ask for the realisation of switching techniques in hydraulics.

But the high efficiency is not the only benefit of switching hydraulic systems. Another interesting aspect is the possibility of a low cost manufacturing of the essential components. Basically, switching valves can be produced very cheaply because of their simple design. Their extreme robustness against oil contamination is a further major advantage of this technology. These advantages are contrasted by high pressure pulsations, that bring additional stress to the components and possibly terrible noise. However, in times of rising energy costs and the evident climate change due to the exploitation of fossil resources it should be worth to think about new energy saving methods. Switching hydraulics has a high potential to contribute to this.

In contrast to other efficient hydraulic concepts, like for instance, displacement drives or load sensing systems, in this work a constant pressure supply is considered, which is common in many industrial applications but can be realised in mobile hydraulics as well. In the following sections an overview of established and novel switching concepts in hydraulics are presented.

1.1. A Historic Hydraulic Switching Converter

The first application of switching hydraulics was invented in 1796 by Joseph Michel Montgolfier as an improvement of John Whitehurst's pulsation engine of the year 1772. The device is called the hydraulic ram, which is a mechanism to pump water from a reservoir to a basin at a higher level, like depicted in Fig. 1.2. For this purpose the potential energy

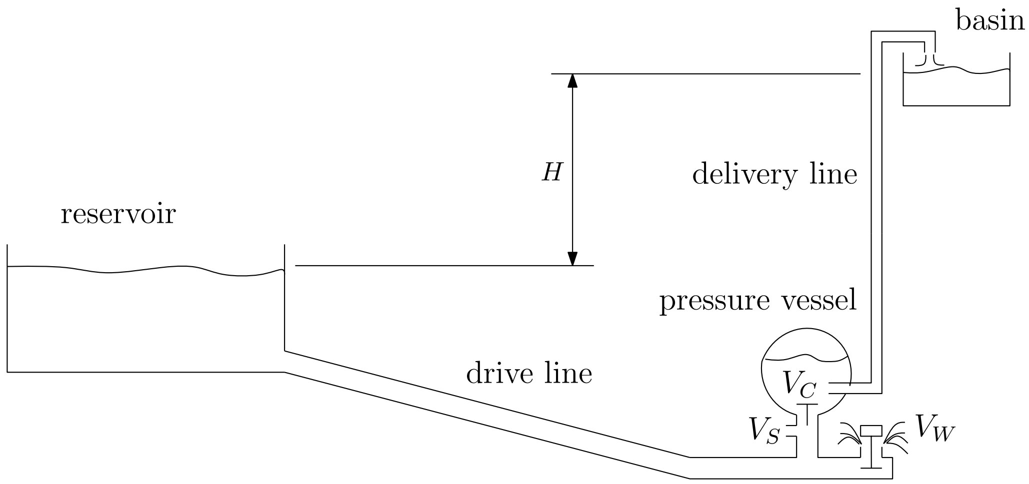

Figure 1.2.: Working principle of the hydraulic ram

of water from a reservoir or a small river is converted into kinetic energy in the slopy drive line by opening the waste valve V_W. When the water flow is high enough the pressure at the end of the drive line exceeds the closing force of the waste valve, which will be shut rapidly. The spill-over of the kinetic energy in the drive line causes a high pressure at the end of the drive line that opens the high pressure sided check valve V_C. Thus, the water flows into the pressure vessel and further via the delivery line to the target tank, which is situated much higher than the reservoir. The high pressure in the vessel decelerates the flow in the drive line until the check valve closes. When the pressure is low enough, the waste valve opens and the cycle starts again. For a correct working behaviour and to avoid too large pressure peaks, the pressure vessel is designed as an air vessel. The necessary amount of air is guaranteed by the snifting valve V_S that allows to inject air into the configuration at every working cycle.

The hydraulic ram was the first hydraulic system that used the kinetic energy of flowing water in combination with some different check valves to keep the engine running without any external propulsion system. The main reason for mentioning the hydraulic ram is, that its basic working principle corresponds to the hydraulic boost converter and, moreover, to the hydraulic buck converter in recuperation mode. There the fluid is also accelerated by opening a tank sided switching valve and the spill-over of the kinetic energy in the pipe allows to boost pressure or to feed some fluid back into the high pressure supply line, respectively.

It is remarkable, that nowadays the principle of the hydraulic ram is still in use in some high valleys in the mountains to ensure the water supply for the cattle on the alp. In Fig. 1.3 the realisation of the hydraulic ram by Easton & Amos is illustrated, which was introduced at the world exhibition in Crystal Palace in the year 1851.

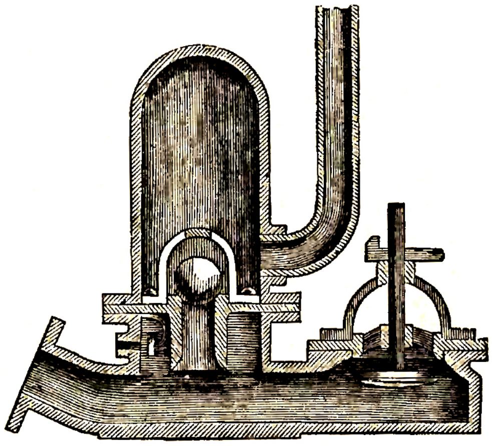

Figure 1.3.: Hydraulic ram by Easton & Amos in 1851

1.2. Basic Hydraulic Switching Control

In the middle of the 1990's Gall and Senn presented in [8] an energy efficient linear hydraulic drive, illustrated in Fig. 1.4. The main intention of this concept is to raise the efficiency by exploiting the inertia of the load in combination with so called free-wheeling valves for saving energy. For lifting the load the supply sided valve V_S is opened for a

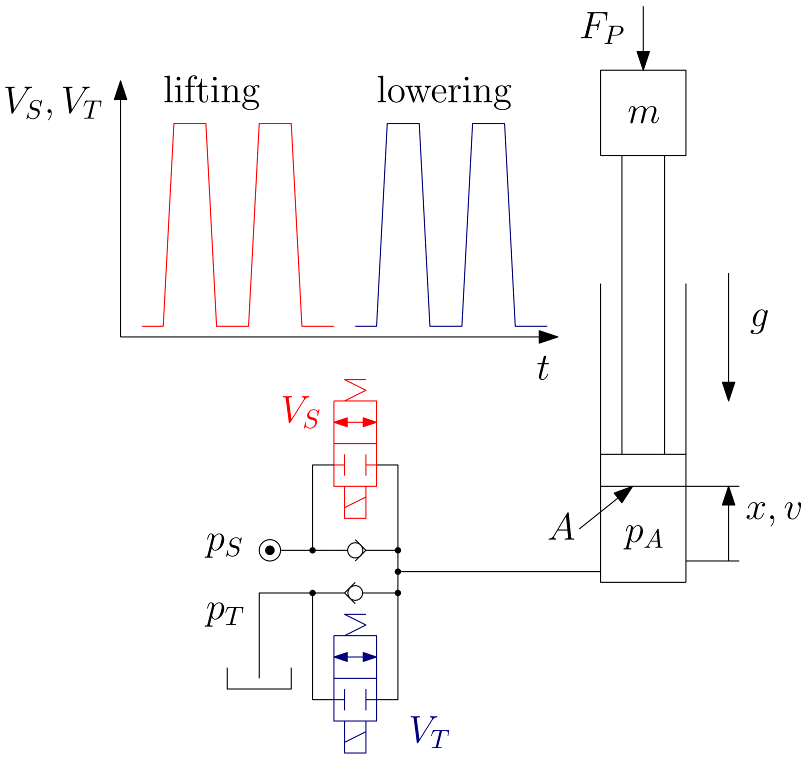

Figure 1.4.: Energy efficient positioning via free-wheeling valves

certain amount of time and when the valve is closed again, the kinetic energy of the load initiates a flow via the tank sided check valve until the load stops. For the opposite motion the potential energy of the dead mass and further the potential of the load force F_P can be used to feed oil back to the supply line and, thus, to recuperate energy by switching the tank sided valve V_T. The free-wheeling check valves caused the higher efficiency and reduced the noise due to switching. The investigations [8] were carried out in a single pulse mode, but this does not contradict a periodic switching. Because of the dynamics and the nominal pressure drop of the free-wheeling check valves the tank has to be pre-pressurised to avoid cavitation. The simulation results at that time promised a potential of saving energy up to 70% and experiments showed that this configuration is basically working. Gall and Senn already pointed out, that the technical effort for realisation is very low.

By exploiting the inertia of a dead load nearly arbitrary high inductances can be realised, which is important to reduce the ripples in the flow rate due to the switching process and, thus, to reduce the losses of the drive. The equivalent inductance of the configuration depicted in Fig. 1.4 compared to the fluid inertia in a simple pipe can be assessed by

$$\frac{m}{A^2}\dot{q} = p_A - \frac{d}{A^2}q - \frac{mg}{A} \text{ with } q = Av, \tag{1.3}$$

which represents a transformation of the kinetics of the cylinder drive into the characteristic quantities of a hydraulic inductance. Gall and Senn carried out the experiment with a dead mass of $m \approx 300\,kg$ and a cross-section of about $A \approx 3\,cm^2$, which leads according to Eq. (1.3) to an equivalent inductance of $L_h = \frac{m}{A^2} \approx 3 \cdot 10^9 \frac{kg}{m^4}$. A simple pipe line, as used in an HBC, with the length of $1.5\,m$ and an hydraulic diameter of $8\,mm$ delivers only an inductance $L \approx 3 \cdot 10^7 \frac{kg}{m^4}$ and, thus, the fluid inertia is about $\frac{1}{100}$ of the system illustrated in Fig. 1.4. The main deficiency of the Gall and Senn concept is the low force capacity of the drive due to the small cross-section of the cylinder, which restricts this approach to a lower number of applications. Furthermore, for an optimal operation also very large and very fast valves are required, which were not available at that time. However, a configuration with fast and high flow rate valves and a high load inertia provides an energy efficient, robust and low cost hydraulic drive.

1.3. The Wave Converter

Due to the compressibility and inertia of hydraulic oil, the phenomenon of wave propagation in pipe lines occurs. Numerous theoretic and experimental work has been devoted to wave propagation in hydraulic transmission lines and various mathematical models have been worked out. In [3, 44, 53] the frequency behavior of pipe lines including the adequate modelling of the dynamic friction in the linear case is treated and powerful models for simulation are presented. The results show that a pipe line has multiple eigen resonances with corresponding eigen modes. These modes appear as standing waves in the transmission line if they are excited, for instance, by periodic switching of a valve. In a wave converter, a switching valve operates in pulse width mode at a constant switching frequency exactly at the first resonance frequency of the pipe. This broadband periodic rectangular switching excites also the higher order modes of the pipe. At the pipes mid-point all uneven modes have a pressure node. A side-branch connected at the mentioned location has no pressure pulsation of odd orders. If the first side-branch has half the length of the first pipe, a further pipe attached at its mid-point has no pressure pulsations of orders $2, 6, 10, \ldots$. Further side-branches following that design strategy can filter even higher pressure modes. This is the basic principle of the so called wave converter, which was presented in [40] and is depicted in Fig. 1.5.

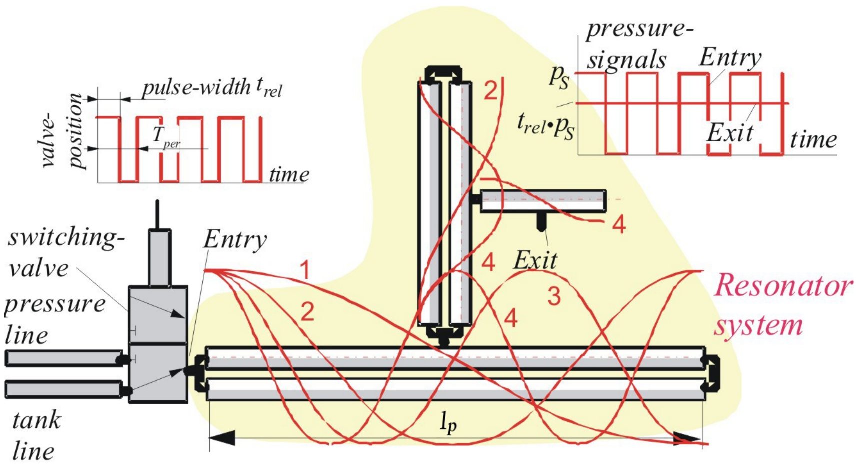

Figure 1.5.: The wave converter from [39]

As mentioned, the switching valve operates in pulse width mode and connects the pipe alternately to supply pressure and tank pressure, respectively. The average pressure value is set by the on-time of the valve, which is called pulse width t_{rel}. Since the whole system is resonating at its eigen frequencies its energy consumption is determined only by the fluid friction due to wave propagation. The average flow rate to a consumer situated at the exit of the last pipe causes the main pressure drop at the switching valve. So this switching concept allows to control the pressure at the load at high efficiency. Of course, this property was the main motivation to develop a drive that rises the energy efficiency of a controllable hydraulic system by utilising the eigen resonances of a pipe system. A major problem is that the dimension of the wave converter depends on the switching frequency or vice versa. The main design constraints are determined by

$$l_p = \frac{c_0}{2f_S}, \tag{1.4}$$

where l_p is the length of the first pipe line, c_0 the speed of sound in the fluid and f_S the switching frequency. For instance a switching frequency of 100 Hz requires a length of approximately $6\,m$ of the first pipe line. A reasonably compact wave converter for industrial applications would require a switching frequency in the range of $1\,kHz$, which is far beyond what can be realised in an economic way today.

1.4. The Resonance Converter

A well established converter concept in electrical engineering is the resonance converter. The basic circuit is depicted in Fig. 1.6. A resonance converter of this type operates at switching frequencies just above the resonance point of the oscillating system. In this frequency range the decay of the output voltage strongly depends on the frequency. This property allows to control the output voltage of the drive. In [38, 9, 31, 32] the successful

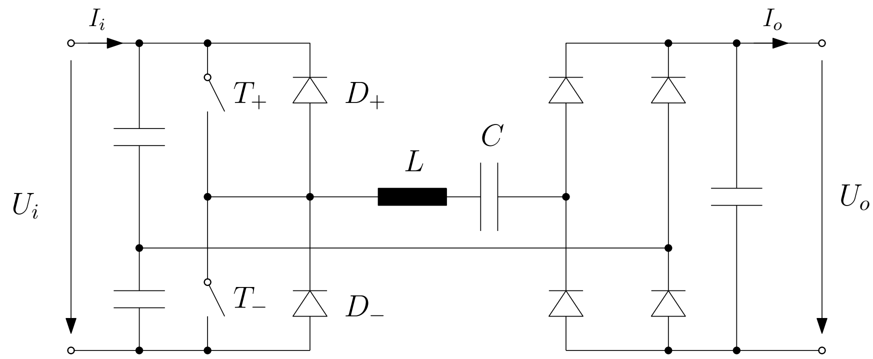

Figure 1.6.: Electrical resonance converter

transfer of this electrical drive concept to hydraulics is presented. The hydraulic resonance converter (HRC) is shown in Fig. 1.7, where the oscillating part is realised by a spring mass oscillator. The displacement of this oscillator corresponds to the flow rate at the output, hence it is a dual working principle to the wave converter. Also this converter uses the sensitive dependence of the output flow rate on frequency above the resonant point of the spring mass oscillator. The simple version of the hydraulic resonance converter uses 3 valves for operation which is called single chamber converter (SCC). The control of the 3 valves can be examined in the upper right diagram in Fig. 1.7. The symmetric double chamber converter (DSC) uses 6 valves and has some performance advantages compared to the single chamber converter, but both types are rather costly. The design of the hydraulic resonance converter depends again strongly on the achievable switching frequency. To obtain handy proportions of the converter a switching frequency of at least $100\,Hz$ is necessary.

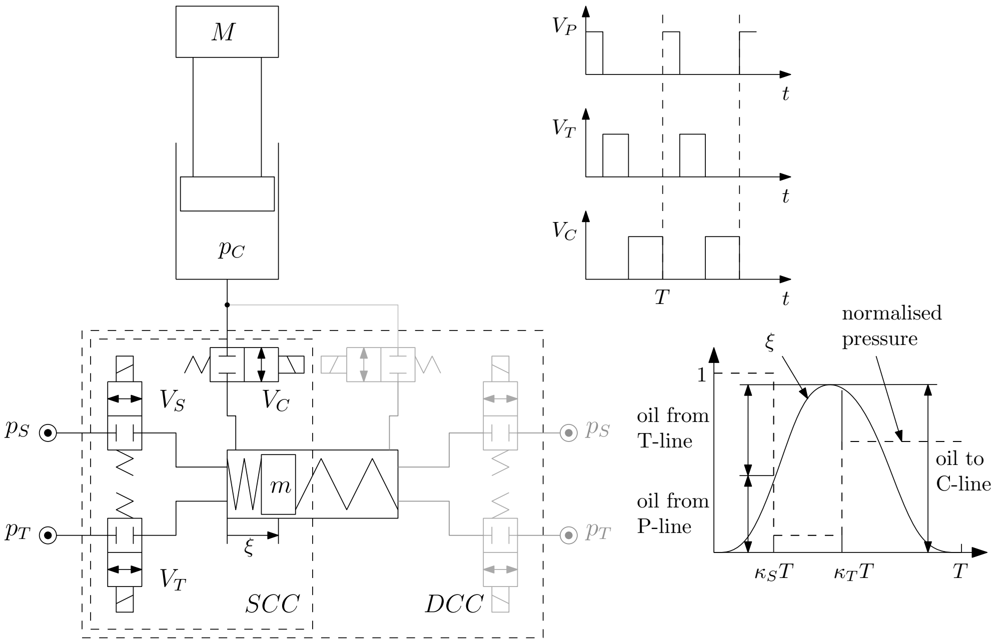

Figure 1.7.: Hydraulic resonance converter from [32]

1.5. Digital Hydraulic Valve System

Another technique transferring electronic principles to hydraulics is the method of digital hydraulic valve systems. The main intention is to replace expensive and sensitive servo valves by a number of low cost on/off valves. Considering $n = 4$ parallel arranged valves with different nominal flow ratios, as e.g. $1 : 2 : 4 : 8$, the summed flow rate of all valves can be quantised into 2^n discrete flow rates. Thus, a 4 bit hydraulic D/A-converter can be realised. Figure 1.8 shows the basic principle and the corresponding drawing symbol. In the digital approach the valves have to be arranged in parallel for best flow conditions.

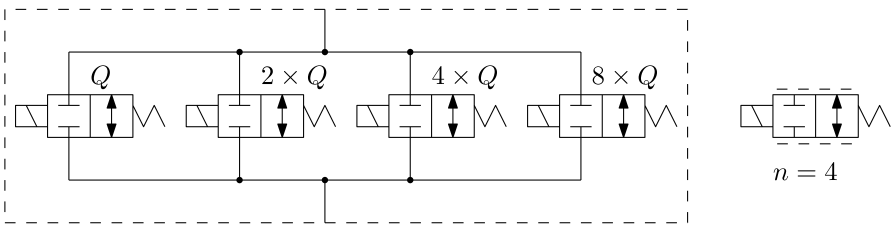

Figure 1.8.: Digital hydraulic valve

For this reason the different on/off valves have to be located on a compact valve block, for instance, as depicted in Fig. 1.9. The corresponding characteristic properties are listed in Tab. 1.1. In this case the controllability of the flow rate differs from conventional proportional control. In theory a common servo valve can deliver any flow rate within its working range, but in practice non-linearities as, e.g., hysteresis, valve overlap or even flow forces, cause quantitative uncertainty in the flow rate. This uncertainty depends

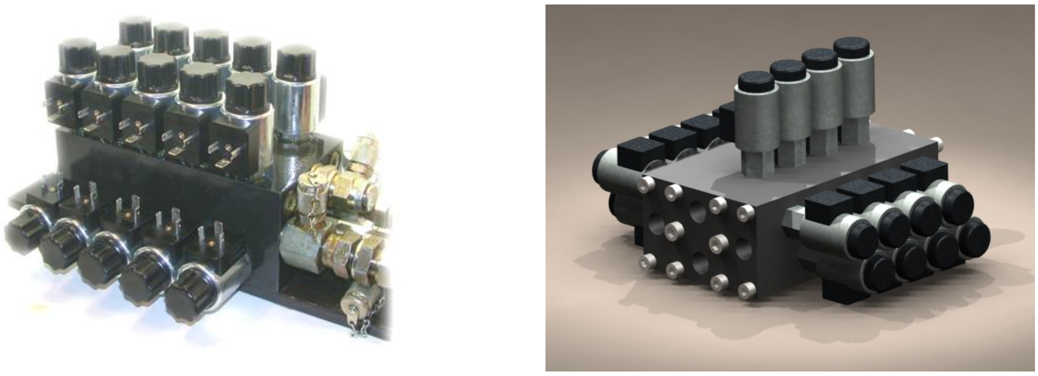

(a) (b)

Figure 1.9.: Different digital valve blocks from [20]

	Fig. 1.9a	Fig. 1.9b
Valves:	Hydac WS08W-01	Rexroth KSDE
Dimensions ($h \times w \times d$):	$150 \times 200 \times 240\,mm$	$170 \times 200 \times 310\,mm$
Weight:	$\approx 18\,kg$	$\approx 26\,kg$
nominal flow rate Q_N:	$70\frac{l}{min}@35bar$	$80\frac{l}{min}@35bar$
maximum pressure p_{max}:	$250\,bar$	$500\,bar$
maximum pressure drop Δp_{max}:	$100\,bar$	$> 220\,bar$

Table 1.1.: Data of digital valve blocks from Fig. 1.9

on the quality and in turn on the price of the valve. In the opposite, the flow rate through a certain digital valve is strictly quantised, but this flow characteristics is realised without any uncertainty. This is another benefit of the digital approach. The degree of controllability depends on the number of the used on/off valves as shown in Fig. 1.10. Another major advantage of the digital hydraulic valve concept is the robustness in terms of oil contamination and malfunction of a valve. If one valve is breaking down, the application is still controllable, even though at reduced controllability and higher energy consumption. To provide this benefit with conventional hydraulics a complete and thus expensive back up system would have to be invested.

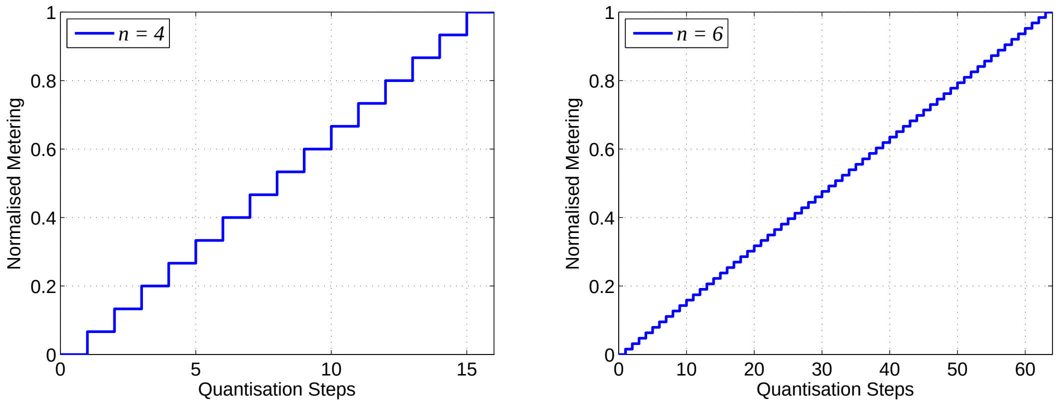

Figure 1.10.: Different quantisation levels of digital hydraulic valve systems

The main advantages of digital hydraulic valve systems can be concluded by:

- Simple and low-cost valves
- Simple control electronics
- High reliability
- Small power losses due to meter-in meter-out control
- Non-sensitive against oil contamination
- No need for spool position feedback
- No leakage if seat type valves are used

The interested reader will find more basic information about digital hydraulic valve systems in [20, 21].

1.6. Fast Switching Hydraulic Concepts

In contrast to conventional switching hydraulic systems, fast switching hydraulics is characterised by continuous periodic switching of the valves. The fastest switching times of the valves are nowadays in the range of 1 ms, the required value depends strongly on the necessary switching frequency. Actually, the previously mentioned wave converter and resonance converter introduced in Sections 1.3 and 1.4 also belong to the family of fast switching hydraulics. These converters also represent highly efficient hydraulic concepts, but they either suffer from very large size or are rather costly. Therefore, this section focuses on simpler yet efficient switching concepts, which can be transferred from electronics to hydraulics conveniently and which promise a compact and cost effective realisation.

1.6.1. The Hydraulic Buck Converter

The most simple converter which can be transferred from electronics to hydraulics is the so called buck converter. The electrical circuitry of this traditional step down converter is depicted in Fig. 1.11. It consists basically of a switch S, a diode D, an inductance L, a capacitor C, and the load R_L. The switch, which is commonly realised by a field-

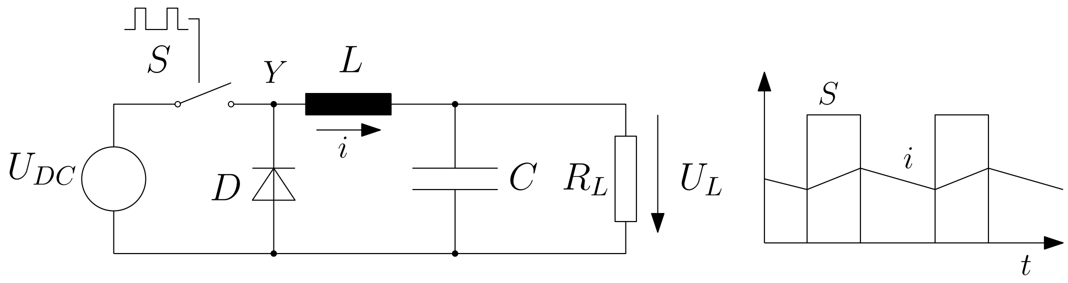

Figure 1.11.: Electrical buck converter

effect transistor, connects the circuit to supply voltage for a certain duration of time. During that time the current in the inductance increases. When the switch interrupts the connection, the inductance is further driving a certain current, because of its stored energy. Thus, the current flows through the diode and the energy in the inductance will decrease because of the inverse polarity. Due to this phase of operation energy is saved and, thus, the efficiency increased over a resistance voltage controller. After the switch is closed again, the current in the inductance increases again. The circuit operates at a certain frequency in pulse-width-mode (PWM). The ratio between the on- and off-time is called duty cycle κ. The switching frequency has to be chosen sufficiently above the natural frequencies of the whole system to obtain the desired behavior. For attenuation of the voltage ripples due to switching a sufficiently large capacitor is situated at the load.

The hydraulic pendant of the electric buck converter is depicted in Fig. 1.12. Its corresponding elements are a switching valve, a check valve, the inductance - realised simply by a pipe - and an accumulator to smoothen the pressure ripples at the load, which is represented by an ordinary orifice in this simple case. The hydraulic buck converter (HBC)

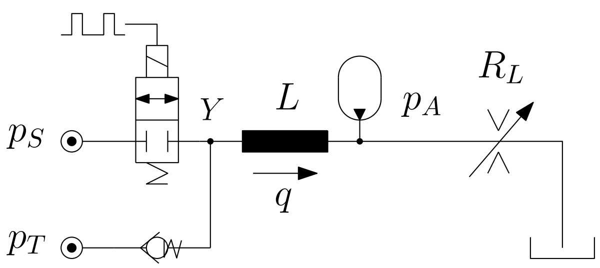

Figure 1.12.: Simple hydraulic buck converter

also uses the spill-over of kinetic energy stored in the inductance to raise the efficiency of the system. After closing the active switching valve, the inertia of the fluid enforces a flow through the tank sided check valve. Since this check valve has a finite size and dynamics, a certain pressure drop will occur during the suction phase. Thus, the tank has to be pre-pressurised to a certain level to avoid cavitation.

The converter operates like its electrical pendant in PWM-mode at a constant frequency sufficiently high above the natural frequencies of the drive. In contrast to electronics, where the switching frequencies are in the *kHz*-range, switching in hydraulics will take place in the range of fifty up to a few hundred Hertz depending on the application. This limit does not only depend on the dynamic performance of the available valve, but also on hydraulic parasitic capacity effects of the fluid, which make switching at much higher frequencies unfeasible. In Fig. 1.12 a simple HBC for only one flow direction is depicted. A more relevant design is the both-way HBC which can be seen in Fig. 1.13. By spending

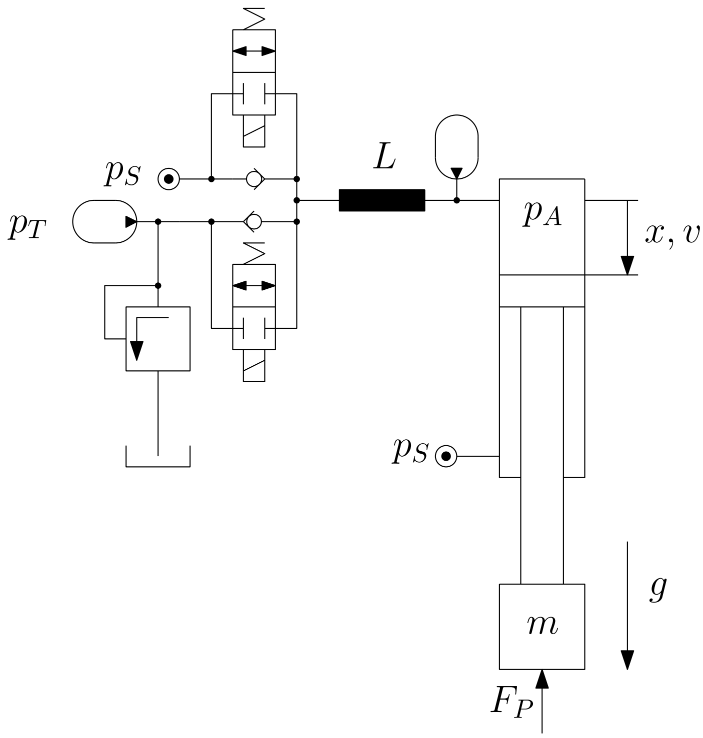

Figure 1.13.: Both-way hydraulic buck converter

another valve stage the flow through the converter can be controlled in both directions. With this type of the HBC it is possible to control, e.g., a differential cylinder. To this end the cylinder has to be operated in plunger mode, i.e., the annulus chamber has to be connected to supply pressure permanently. In the mentioned figure also the pre-pressured tank system is illustrated, which is realised by a pressure relief valve at least in this exemplary case. The accumulator in the tank line is acting as a reservoir to provide the needed fluid in the suction phase when the piston extends.

Prior theoretical investigations and experimental results of the author are published in [13, 15].

1.6.2. The Hydraulic Boost Converter

Another simple switching concept constitutes the hydraulic boost converter, shown in Fig. 1.14. As the name promises, this is a step up converter which allows to boost the

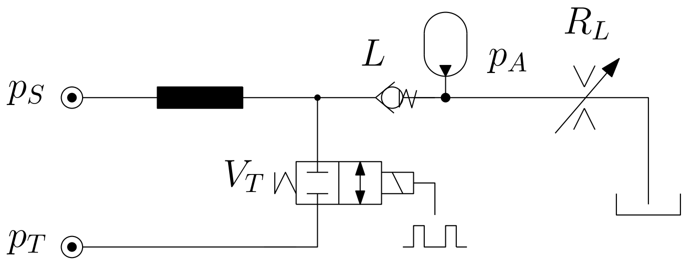

Figure 1.14.: Hydraulic boost converter

pressure at the load to higher levels than the supply pressure. The converter also operates in PWM-mode and its working cycle starts with accelerating the oil in the inductance by opening the valve V_T. After closing the valve the pressure at the check valve rises above the load pressure due to the spill-over of the kinetic energy in the pipe and, thus, the flow via the check valve is forced. At this point is has to be remarked, that the load pressure cannot be lower than the supply pressure, at least in steady state. Of course, this boost converter equals the historically first hydraulic switching converter, the hydraulic ram. A further interesting detail is the analogy of the working principle between the boost converter and the both-way HBC in the reverse flow direction. Using the ability to boost the pressure in this flow direction, energy can be recuperated into the supply system.

In comparison to the simple hydraulic buck converter from Fig. 1.12 the hydraulic boost converter actually consists of the same basic components, which are arranged in a way to achieve a totally different behavior of the system. This structural flexibility shows the high potential of switching hydraulics.

1.6.3. The Hydraulic Boost Buck Converter

An advanced switching principle is the hydraulic boost buck converter, which is depicted in Fig. 1.15. The converter unifies the benefits of the boost and the buck converter, which consequently consists of two converter stages, the boost and the buck stage, respectively. Hence, the considered configuration is able to operate in one flow direction either as a step down or as a step up converter, depending on the power need at the load, which

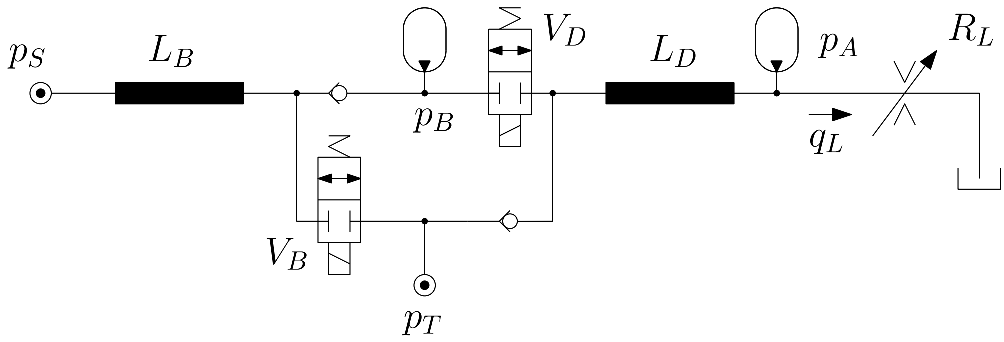

Figure 1.15.: The hydraulic boost-buck converter

shows a broad variability. In buck mode simply the switching valve V_D has to be pulsed at a certain switching frequency in PWM-mode. On the other hand, the boost mode is characterised by pulsing the valve V_B, while the valve V_D has to be kept open constantly. Thus, the load pressure p_A equals the boost pressure p_B, at least assuming that the resistance of the valve can be neglected. In Fig. 1.15 one can also discover the preloaded tank system to avoid cavitation due to the limited size and dynamics of the check valves. In the mentioned figure, the tank system is not determined in detail. But, if the tank pressure is realised simply by a pressure relief valve, then both valves V_B and V_D have to be pulsed simultaneously in buck mode to prevent a depletion of the pre-pressured tank system. In this case, the boost pressure p_B will be higher than the load pressure p_A, which is another limitation for the achieveable pressure boost.

In electrical engineering the boost buck converter is also called split-pi converter, due to its characteristic arrangement of inductances and capacities. However, the boost buck converter must not be mistaken with the buck boost or Ćuk converter, respectively, because of their different principles of operation. Of course, both mentioned configurations allow either to reduce or to boost the supply voltage efficiently, but both principles are inverting the polarity of the supply voltage, which does not make any sense in hydraulics.

2. Theory of the Hydraulic Buck Converter

The major motivation for the development of fast switching hydraulic systems, in particular, hydraulic switching converters, is the high potential to improve the efficiency of a large number of hydraulic drives and actuators. Also the possible low cost manufacturing of the essential components and their robustness against oil contamination make the concept of switching hydraulics promising. In contrast to common resistance control, which is a static principle, switching converters represent dynamic systems. Hence, for a convenient design of such converters, a sound understanding of the behaviour of such systems is necessary. The hydraulic buck converter (HBC) is one of the most simple switching converters. This was the main reason to select it out of the many converter principles which are thinkable. It also serves as a representative example to investigate the basic principles of operation and main characteristics of power flow and efficiency. Furthermore, the major inevitable non-idealities will be presented and how they influence the system behaviour. The third major part in this chapter concerns some basic design rules. This chapter presents just theoretical work, experimental results are discussed in later chapters.

2.1. Modes of Operation

The electric buck converter depicted in Fig. 1.11 operates at two different modes, called the discontinuous and the continuous mode, as explained for instance in [45]. In the discontinuous mode, the current through the inductance vanishes during the off-time of the switch before the next switching cycle starts. Thus, in discontinuous mode the duty ratio κ corresponds to a certain average current, depending on the load voltage. The continuous mode is characterised by the proper balance between the rise and decay of the current during the on- and off-time of the switch, which means, that the duty ratio corresponds to a mean voltage at the node Y of the converter from Fig. 1.11. The transition from one to the other mode of operation is determined by the duty ratio κ and the load resistance or load pressure, respectively. Because the HBC is analog to the electric buck converter, there exist also two different modes of operation in hydraulics, which are named flow control mode and pressure control mode, respectively. In this section the considerations are focused on the simple hydraulic buck converter as shown in Fig. 1.12. As already mentioned before, the inductance of the converter is simply realised by a pipe. At first the modes of operation will be derived for a lumped parameter pipe model, i.e., an inductance L and a static resistance R. Of course, the flow through a pipe is a more complicated process, because of wave propagation in the fluid. Later, it will be shown that the lumped parameter pipe model reflects the converter behaviour reasonably, if the converter is properly designed. For simplicity purpose the investigations will be carried out under the following further assumptions:

- The sizes of the switching valve and the check valve are infinitely large, thus they do not cause any pressure drop.
- The switching valve and the check valve are infinitely fast, i.e., their switching time is zero.
- The required dynamic response of the overall system is much slower than the switching process. Thus, the load pressure and the load flow rate are assumed to be constant during one switching period. This means that the accumulator for pressure attenuation has infinite capacitance.
- The supply pressure and the tank pressure are assumed to be constant, i.e., the converter is completely decoupled from the peripheral hydraulics.

These assumptions lead to the most simple system for analysis, which is depicted in Fig. 2.1. Since all valves are assumed to be infinitely large, the switching valve is represented by a simple switch. Also the depiction of the check valve indicates an ideal characteristics. Thus, the only dissipative element is the pipe's Hagen-Poiseuille resistance, which determines the efficiency of this converter model.

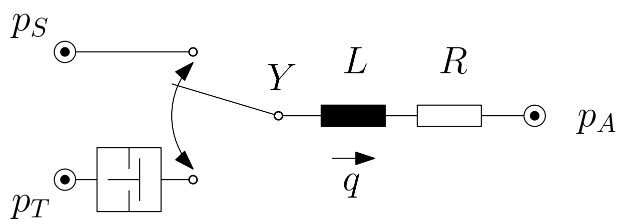

Figure 2.1.: Basic principle of the Hydraulic Buck Converter

2.1.1. Flow Control Mode

The main characteristic of the flow control mode is that the actual flow rate through the pipe decays to zero at each cycle. Hence as mentioned before, this mode of operation is also called discontinuous mode like in power electronics. The corresponding pressures and flow rates are depicted in Fig. 2.2. During the on-time of the switching valve, which

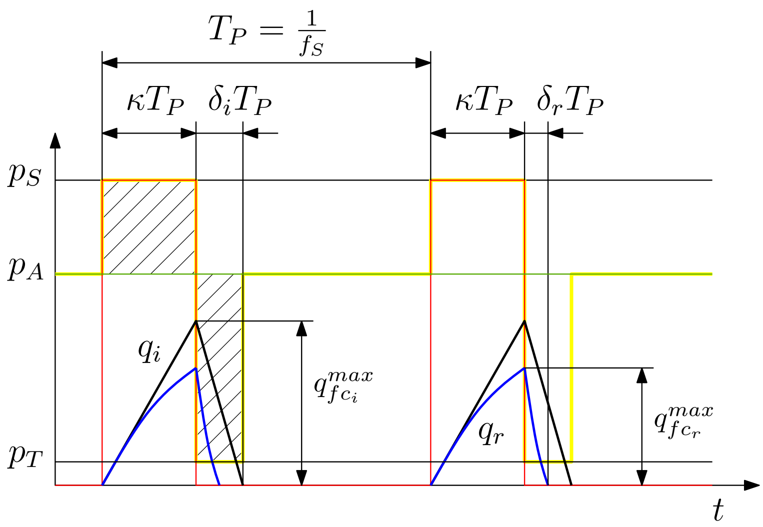

Figure 2.2.: Flow control mode

is determined by the duty ratio κ and the switching frequency $f_S = \frac{1}{T_P}$, the flow rate through the pipe increases. After closing the valve, the pressure at the node point Y (see. Fig. 2.1) falls to tank pressure due to the impulse of the oil in the pipe. Thus, the kinetic energy of the fluid decreases due to the negative pressure difference over the inductance pipe. In this phase fluid enters through the tank sided check valve. The relative time, which is needed for the vanishing of the flow rate in the suction phase, is called free-wheeling ratio δ. This free-wheeling is characteristic for the flow control mode and a formula for δ in case of a pure inductance (ideal situation - therefore index i) reads

$$\delta_i = \frac{p_S - p_A}{p_A - p_T}\kappa, \tag{2.1}$$

where p_S, p_T and p_A are the supply-, the tank-, and the consumer pressure. In this relation the free-wheeling ratio is independent of the inductance of the pipe. Taking a static resistance of the pipe into account the relation modifies to

$$\delta_r = \frac{f_S L}{R} \ln\left(\frac{p_A - p_T}{p_S - p_T + (p_A - p_S)e^{\left(-\frac{R\kappa}{L f_S}\right)}}\right), \tag{2.2}$$

which is derived from the solution of the differential equation of the flow rate through a lumped inductance and resistance (index r stands for real situation). Using this free-wheeling ratio δ_r result, the average flow rate in flow control mode can be derived easily. Using the maximum flow rate of one switching cycle

$$q_{fc_r}^{max} = \frac{p_S - p_A}{R}\left(1 - e^{-\frac{R}{L}\kappa T_P}\right), \tag{2.3}$$

the mean flow rate in flow control mode reads

$$\begin{aligned}\overline{q}_{fc}(\kappa) &= \frac{1}{T}\left\{\frac{p_S-p_A}{R}\int_0^{\kappa T_P}(1-e^{-\frac{R}{L}t})\mathrm{d}t+\right.\\ &\left.+\int_0^{\delta_r T_P}\left[\left(q_{fc_r}^{max}-\frac{p_T-p_A}{R}\right)e^{-\frac{R}{L}t}+\frac{p_T-p_A}{R}\right]\mathrm{d}t\right\}\\ &= \left(\frac{f_S L(p_A-p_T)}{R^2}\right)\ln\left(\frac{p_A-p_T}{p_S-p_T+(p_A-p_S)e^{-\frac{R\kappa}{Lf_S}}}\right)+\frac{p_S-p_A}{R}\kappa. \end{aligned} \tag{2.4}$$

The limiting process of R tending to zero delivers

$$\overline{q}_{fc}(\kappa)\Big|_{R\to 0} = \frac{1}{2}\frac{(p_S^2+p_Ap_T-p_Sp_A-p_Sp_T)}{(p_A-p_T)Lf_S}\kappa^2. \tag{2.5}$$

Thus, the flow rate in flow control mode correlates quadratically to the duty ratio κ, at least in case of no static resistance. From Eq. (2.5) it becomes clear, that the average flow rate through the converter depends on the load pressure p_A. This fact is important for the application of certain control strategies to achieve a desired motion of the load. Also the switching frequency and the inductance appear as major design parameters of the converter.

2.1.2. Pressure Control Mode

If the duty ratio κ and the free-wheeling ratio δ fulfill the equation

$$\kappa+\delta=1 \tag{2.6}$$

a transition from flow- to pressure control mode occurs. At higher duty cycles the flow rate does not vanish before the next switching cycle starts. Substituting Eq. (2.2) into Eq. (2.6) delivers the transition ratio

$$\kappa^{\#} = \frac{1}{R}\left(\ln\left(\frac{(p_S-p_A)e^{-\frac{R}{Lf_S}}+p_A-p_T}{p_S-p_T}\right)Lf_S+R\right). \tag{2.7}$$

The limiting process of R tending to zero yields

$$\kappa^{\#}\Big|_{R\to 0} = \frac{p_A-p_T}{p_S-p_T}, \tag{2.8}$$

which indicates, that the transition ratio depends on the load pressure p_A. The pressure control mode ($\kappa > \kappa^{\#}$) is illustrated in Fig. 2.3. In contrast to the flow control mode the duty cycle κ does not enforce an average flow rate, but an average pressure at the node

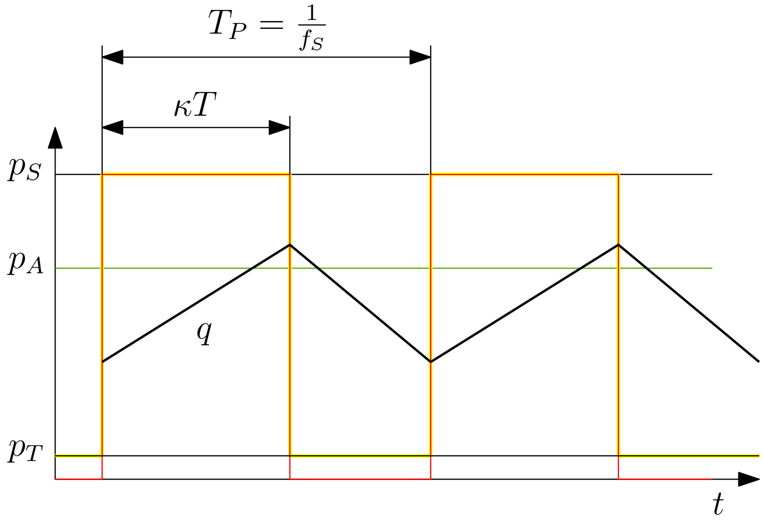

Figure 2.3.: Pressure control mode

point Y of the converter, which reads

$$p_Y = p_T + (p_S - p_T)\,\kappa. \tag{2.9}$$

This mode of operation can also be forced by a converter configuration as depicted in Fig. 2.4, which has no check valves. In this case both valves have to be pulsed alternately,

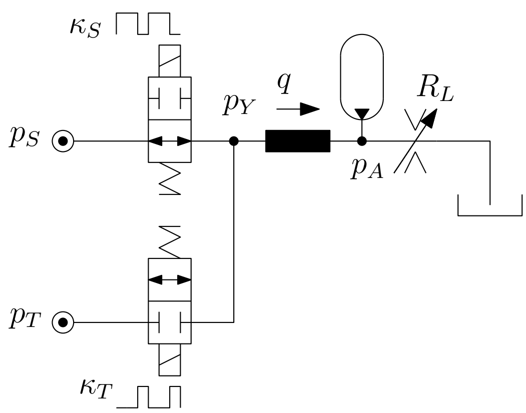

Figure 2.4.: HBC without check valves

their pulse width fulfill the relation

$$\kappa_S = 1 - \kappa_T \tag{2.10}$$

and, thus, the converter always acts in pressure control mode. The electric power consumption for switching the valves is approximately twice that of the HBC using passive check valves. Further difficulties of this mode of operating an HBC, as for instance the synchronisation of the valves, will be discussed later.

2.1.3. Characteristics

The characteristic diagram of the HBC resulting from the Eqs. (2.4), (2.7) and (2.9) is illustrated in Fig. 2.5 in a normalised form. The corresponding numerical data of the considered HBC are listed in Tab. A.1. In the diagram each line represents a characteristic

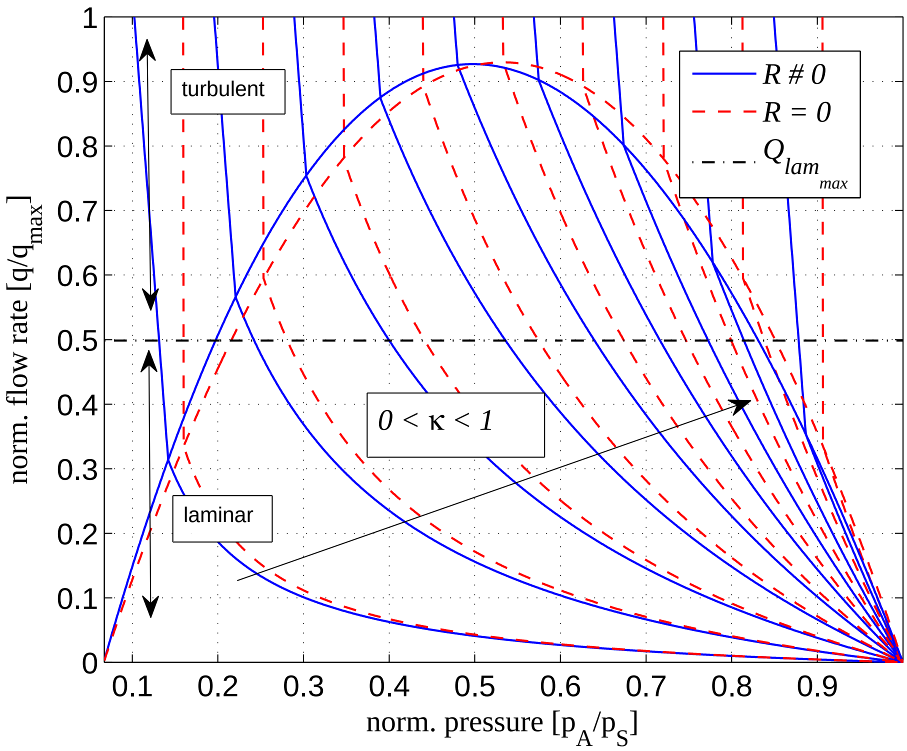

Figure 2.5.: Characteristic diagram of the HBC

for a constant duty ratio κ. The two different fields of characteristics show the behaviour with a resistance R (solid line) and without (dashed line) of the inductance pipe. The parabolic lines stand for the working points, where the operating mode changes from flow control mode into pressure control mode and vice versa. The dash-dotted line shows the border, where the average flow rate through the inductance is changing from laminar to turbulent, if a simple usual stationary transition criterion ($Re \approx 2300$) of a pipe flow is employed. Hence, the characteristics beyond this line are in fact hardly meaningful; due to the strongly rising flow resistance it is not a relevant operating area. So, the converter obviously mainly operates in flow control mode.

If the HBC is designed to operate in both flow directions, as depicted in Fig. 1.13, it is also possible to recuperate energy by switching of the tank sided valve. The overspill of kinetic energy of the oil in the inductance initiates an energy feed back into the supply line. The very basic principle of the recuperation mode is again illustrated in Fig. 2.6 under the assumptions, that had been declared at the beginning of the section. It can be seen, that in this mode of operation the converter behaves like a boost converter as depicted in Fig.

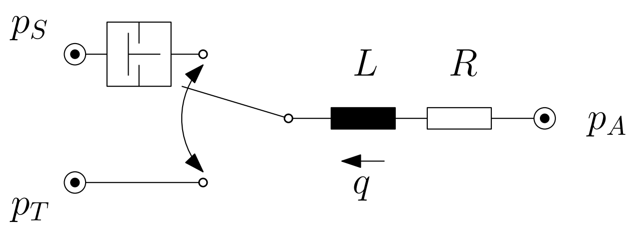

Figure 2.6.: Basic principle in recuperation mode

1.14. The characteristics of the recuperation mode can be calculated in the same manner as done for the forward flow direction in Subsections 2.1.1 and 2.1.2, respectively. The results are depicted in Fig. 2.7, in form of a diagram. The corresponding formulae are given in the Appendix in Section A.1.

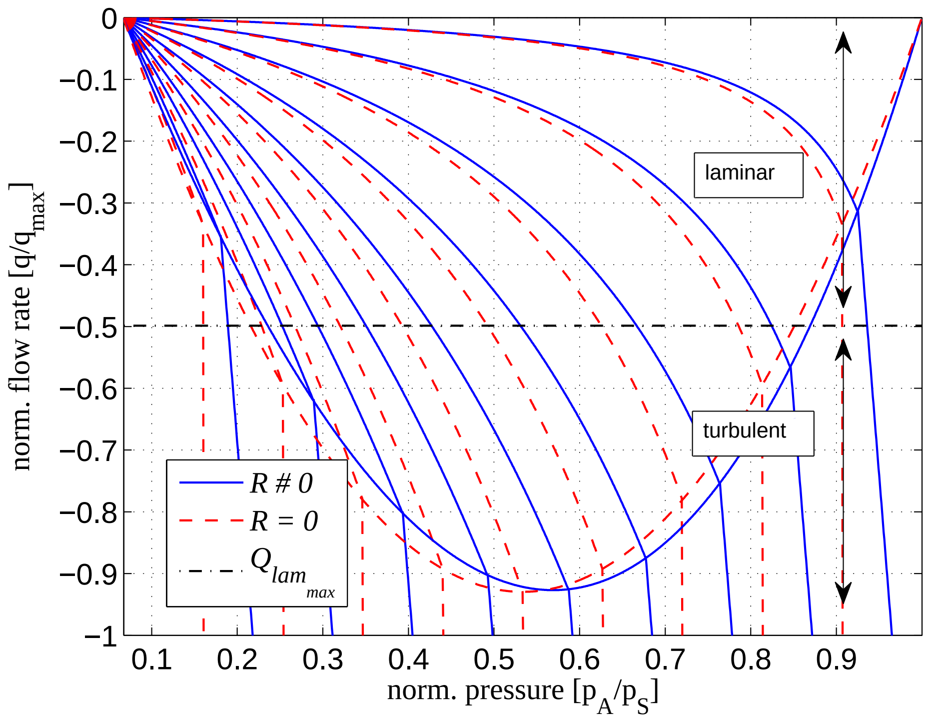

Figure 2.7.: Theoretical recuperation characteristics

2.1.4. Efficiency

The HBC is a three-port system with the pressure ports p_S, p_T and p_A as supply-, tank- and load pressure. Thus, the behaviour of the HBC will be compared with a 3/3-proportional valve as depicted in Fig. 2.8 with $p_T \leq p_A \leq p_S$. The comparison focuses on the efficiency characteristics in steady state, i.e., at a constant load pressure p_A in each working point. Hence, no valve dynamics of the proportional valve needs to be

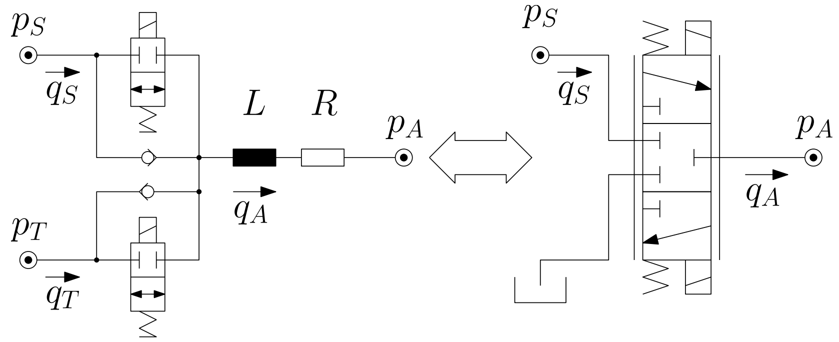

Figure 2.8.: Full HBC and 3/3-valve

considered. As before, the switching valves of the converter are assumed to be sufficiently large, such that their pressure drop can be neglected. Also the size of the proportional valve is irrelevant, since the needed pressure at the load is metered by one edge of the valve. With these assumptions it becomes clear, that in case of the HBC only the static resistance R is responsible for dissipation, while the proportional valve dissipates the pressure surplus according to the actual load. The actual efficiency of the converter in a certain operating point (κ, p_A) in the forward flow direction is defined by

$$\eta^{\rightarrow}_{HBC} = \frac{\int_0^{T_P} p_A q_A \mathrm{d}t}{\int_0^{T_P} \left(p_S q_S + p_T q_T\right) \mathrm{d}t} \tag{2.11}$$

regardless of the mode of operation. In flow control mode the theoretic efficiency reads

$$\eta^{\rightarrow}_{fc} = \frac{\left(\frac{f_S L}{R} \ln\left(\frac{p_A - p_T}{p_S - p_T - (p_S - p_A) e^{-\frac{R\kappa}{L f_S}}}\right) + \frac{(p_S - p_A)\kappa}{(p_A - p_T)}\right) p_A}{\frac{p_T f_S L}{R} \ln\left(\frac{p_A - p_T}{p_S - p_T - (p_S - p_A) e^{-\frac{R\kappa}{L f_S}}}\right) + \frac{p_S (p_S - p_A)\kappa}{(p_A - p_T)} + \frac{f_S L}{R}\left(1 - e^{-\frac{R\kappa}{L f_S}}\right) \frac{\left(p_S p_A + p_S p_T - p_A p_T - p_S^2\right)}{(p_A - p_T)}} \tag{2.12}$$

and in pressure control mode

$$\eta^{\rightarrow}_{pc} = \frac{R\left(\kappa p_S + (1-\kappa) p_T - p_A\right) p_A}{L\left(\frac{e^{\frac{R(1-\kappa)}{L f_S}} + e^{\frac{R\kappa}{L f_S}} - 2 e^{\frac{R}{L f_S}}}{e^{\frac{R}{L f_S}} - 1} f_S \left(p_S - p_T\right)^2 + \frac{R}{L}\left(\kappa\left(p_S - p_A\right) p_S - (1-\kappa)\left(p_A - p_T\right) p_T\right)\right)}. \tag{2.13}$$

The transition between the two different efficiency characteristics takes place at the transition ratio $\kappa^{\#}$ according to Eq. (2.7). The proportional counterpart is simply a metering orifice. The efficiency reads

$$\eta^{\rightarrow}_{HPD} = \frac{p_A q_A}{p_S q_S} \underset{q_A = q_S}{\overset{}{\underset{\uparrow}{=}}} \frac{p_A}{p_S}, \tag{2.14}$$

which only depends on the load pressure p_A. The resulting efficiency characteristics for a number of working points are depicted in Fig. 2.9. In the left diagram the characteristics depending on κ and p_A is illustrated, again in a normalised way. The coloured surface

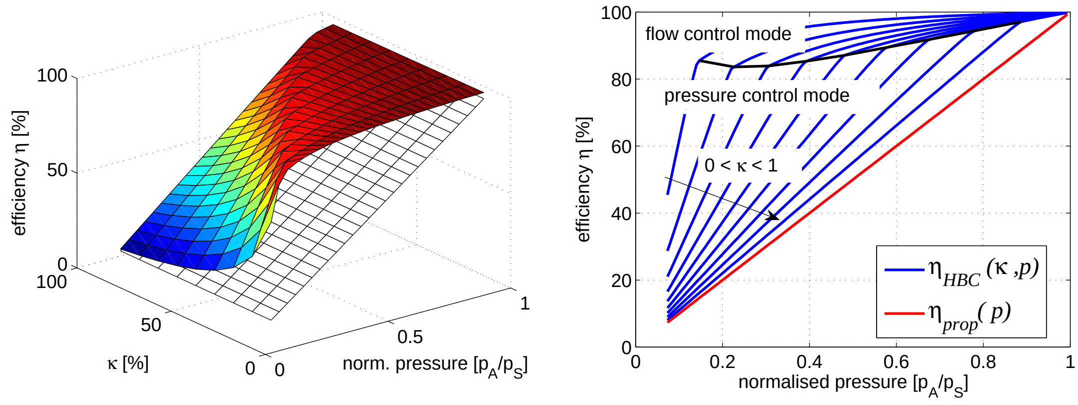

Figure 2.9.: Theoretic efficiency in the forward flow direction

represents the efficiency of the HBC in the forward flow direction, the white surface shows the efficiency of resistance control. In the right diagram a projection of the left diagram is depicted. The transition from flow control to pressure control mode takes place, where the different curves of the flow control mode change into nearly straight lines with different slopes in pressure control mode, which is indicated by the black line. In fact, according to Eq. (2.13), the efficiency characteristics in pressure control mode is nonlinear. But due to the fact, that $\frac{p_T}{p_S}$ is small, i.e., the tank pressure is very low compared to the supply pressure, the characteristics in pressure control mode have a nearly linear shape. In this case, the losses and thus the mean pressure drop $\Delta p = p_S - p_A = Rq_A$ of the HBC are almost proportional to the flow rate q_A. In contrast to this, in flow control mode the relations are nonlinear, even though the tank pressure is also negligible compared to the supply pressure.

In the opposite flow direction, i.e., in recuperation mode, the inserted hydraulic power is defined by the pair (p_A, q_A) from the consumer side. In this case, the main efficiency improvement is based on feeding fluid back to the pressure supply port. But also the flow directed to the tank system represents a usable power in the general case, since the tank is pre-pressurised and, thus, also this potential is basically usable. But, since the pressure ratio $\frac{p_T}{p_S}$ should be very low, the expected amount of energy fed to tank line is practically negligible. The relation concerning the HBC in reverse flow direction reads

$$\eta_{HBC}^{\leftarrow} = \frac{\int_0^{T_P} (p_S q_S + p_T q_T)\,\mathrm{d}t}{\int_0^{T_P} p_A q_A \mathrm{d}t}. \tag{2.15}$$

The detailed analytical results are similar to those of the forward flow direction. Hence, only the defining equations will be presented at this point. As before with the power characteristics in recuperation mode the corresponding results of the theoretical efficiency in recuperation mode are presented in Subsection A.1.4 in the Appendix. The efficiency of the resistance inverse flow mode is almost zero due to

$$\eta_{HPD}^{\leftarrow} = \frac{p_0}{p_A} \approx 0, \tag{2.16}$$

where p_0 is the ambient pressure. The resulting characteristics are depicted in Fig. 2.10 in the same manner as in forward flow direction. The transition between pressure- and flow control mode corresponds to the bend in the surface and at the black line on the right hand side, respectively. In contrast to the forward flow direction the characteristics in pressure control mode of the recuperating direction have nearly the form $\eta\left(\frac{1}{p_A}\right)$ at a constant duty ratio κ. This can be explained by the fact, that the efficiency in recuperation mode is the reciprocal of the forward flow direction (compare Eq. (2.11) and Eq. (2.15)), where the characteristics are nearly straight lines.

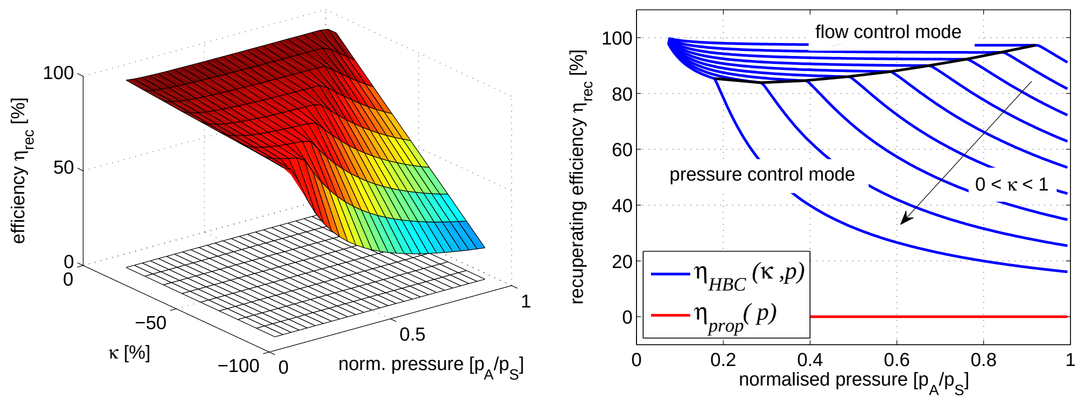

Figure 2.10.: Theoretic recuperation efficiency

2.2. Limiting Effects and Nonidealities

In the previous section the characteristics were derived from quite ideal conditions. In reality this simple point of view is disturbed by a number of effects. The non-idealities of an HBC are much stronger than of the electric buck converter and need to be modelled properly to obtain a good estimate of reality. This section discusses the major limits of the simple model and the respective technical problems.

2.2.1. Digital Valves

The task of the switching valves is to connect different hydraulic ports and to enable power flow for a well defined time κT_P. In case of PWM controlled systems it is essential that the switching time of the valves is much shorter than the switching frequency $f_S = \frac{1}{T_P}$ to realise an adequate hydraulic pulse width κT_P. The previous theoretical investigations assumed infinitely large valves with a negligible switching time. Much more than in electronic switching systems this assumption is difficult to realise in hydraulics. The main problem is not the size and thus the resistance of a hydraulic valve, but the short switching time. In Fig. 2.11 a typical opening curve of a magnetically actuated fast switching hydraulic spool valve is depicted, where h denotes the stroke of the valve spool with respect to time. The dashed line describes the intended ideal valve operation, the

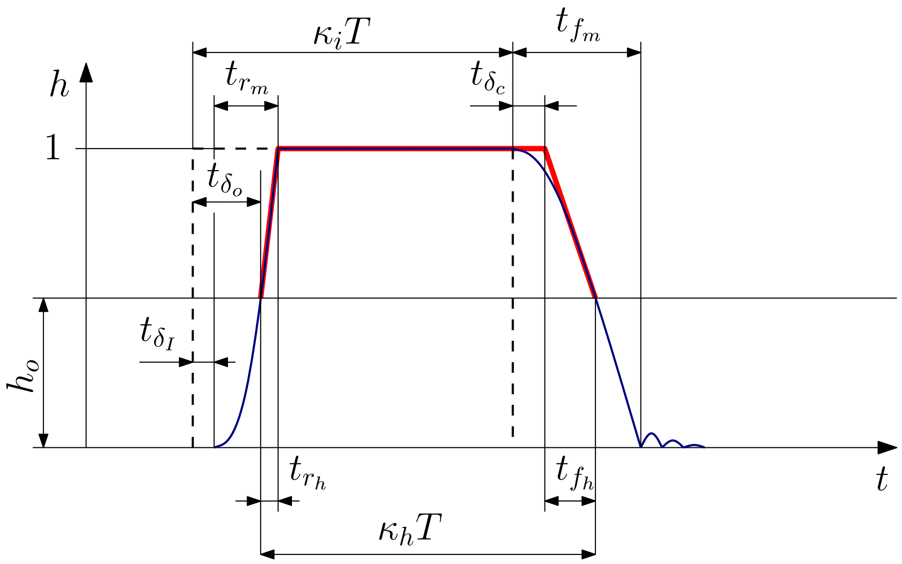

Figure 2.11.: Spool movement of a digital hydraulic valve

dark solid line illustrates the actual position of the spool, and the bold red line shows the real hydraulic pulse. The valve overlap h_o of spool valves may go up to 50% of the full stroke at least for fast switching spool valves. Of course, poppet valves do not have any valve overlap in most cases. The main delay time in the opening process is the sum of t_{δ_I}, the valve current lag, and t_{r_m} the mechanical rise time of the spool. The hydraulic rise time can be approximated by

$$t_{r_h} = t_{\delta_I} + t_{r_m} - t_{\delta_o} \tag{2.17}$$

with t_{δ_o} being the delay time from signal occurrence until the spool edge leaves the valve covering. Depending on the valve construction, in particular on the design of the solenoid armature, the beginning of the closing movement of the spool may be delayed by oil stiction. This phenomenon is accounted by the parameter t_{δ_c}. The hydraulic closing can be further approximated by a straight line with the fall time t_{f_h}, where the valve is not in an overlap state. At the end of the spool movement small ripples in the position may occur, when the spool is bouncing at its end position. This depends on the damping of the valve and, hence, on the construction of the valve. In the case depicted in Fig. 2.11

the relation between the ideal and real switching can be approximated by

$$\kappa_h = \kappa_i + \frac{1}{T_P}\left(t_{\delta_c} + t_{f_h} - t_{\delta_o}\right) \tag{2.18}$$

with κ_i as the intended and κ_h as the hydraulic duty ratio and under the assumption, that the hydraulic switching times are sufficiently low. To quantify the mentioned relations it is necessary to measure the position of the spool which is mostly not feasible at common valves. Furthermore, in the transition areas, where the valve is actuated for a very short time and does not completely open or close, the relations are more complicated. Such valve responses are called ballistic modes and are depicted in Fig. 2.12. A description of

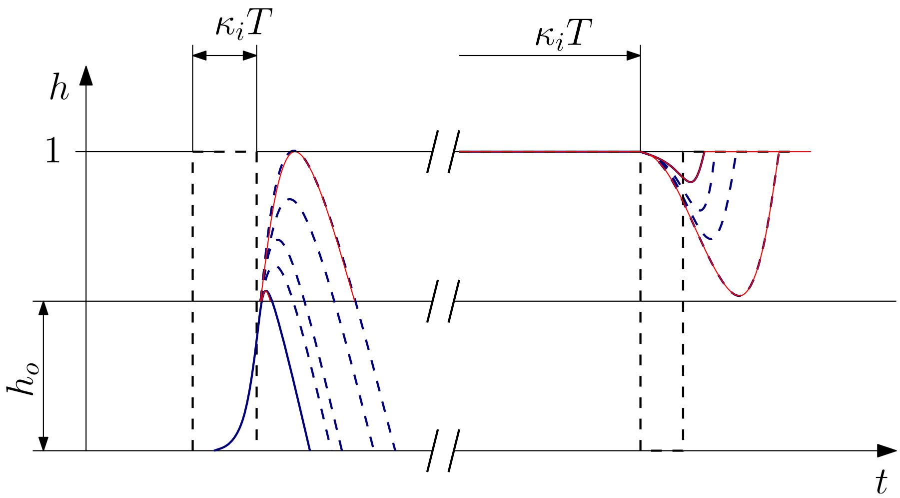

Figure 2.12.: Ballistic switching modes

these transitions needs a comprehensive model which accounts for the dynamic behaviour of the electro-magnetic system, of the power electronics, and of the spool mechanics. Furthermore, the occurring flow forces play a certain role in this operating area of the valve. This very challenging modelling task would blow up this work excessively and, since elaborate valve models are not in the focus, it is not done in this work. Some facts concerning the design and optimisation of fast switching hydraulic valves can be found for example in [50]. Qualitatively, the full relation between the ideal duty ratio κ_i and the hydraulic κ_h would have the shape as depicted in Fig. 2.13. The difference between both exemplary lines depends mainly on the the construction of the valve and may be strongly affected by oil stiction. However, since the spool position is not measured in a common switching valve, the valve response has to be identified in pulse-width-mode in combination with the whole HBC. This method will be discussed later in detail.

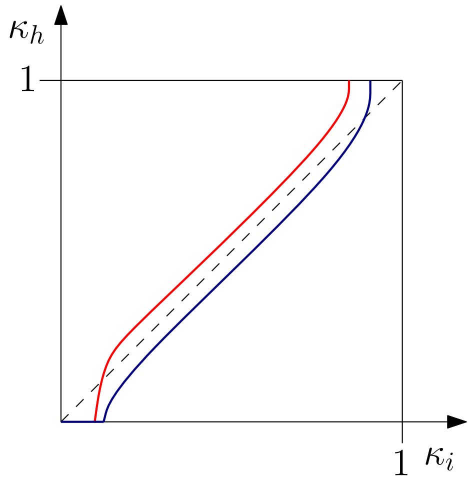

Figure 2.13.: Different relations between intended (κ_i) and the hydraulic (κ_h) duty ratios

2.2.2. Wave Propagation

Since oil is a compressible and inertial fluid, pressure waves may be excited, particularly in transmission lines. In fast switching hydraulic systems a periodic broad band excitation due to the sharp switching edges of the valves occurs. For this reason waves are travelling forth and back in the pipe lines. Resonance effects can arise, if the natural frequencies of the transmission lines are met. In case of the HBC, where the main inductance is realised by such a transmission line, wave propagation has a certain influence on the performance of the converter and, thus, has to be taken into account for a good (or optimal) design. Appropriate models of this physical effect are necessary for simulation in the design process. The occurring pressure levels in an HBC allow a linear dynamic modelling of the laminar flow in pipe lines as pointed out in [3] or [44]. There, the effect of wave propagation and the frequency dependent friction in a straight pipe with a circular cross-section as depicted in Fig 2.14 are described by transfer functions in the frequency domain depending on the axial coordinate x as follows:

$$\begin{bmatrix} \hat{p}_1(s,x) \\ \hat{Q}_1(s,x) \end{bmatrix} = \begin{bmatrix} \cosh\left(\gamma(s)x\right) & -Z(s)\sinh\left(\gamma(s)x\right) \\ -\frac{1}{Z(s)}\sinh\left(\gamma(s)x\right) & \cosh\left(\gamma(s)x\right) \end{bmatrix} \begin{bmatrix} \hat{p}_0(s,x) \\ \hat{Q}_0(s,x) \end{bmatrix} \tag{2.19}$$

with

$$Z(s) = Z_0\sqrt{-\frac{J_0\left(R^*\right)}{J_2\left(R^*\right)}} \tag{2.20}$$

$$Z_0 = \frac{\sqrt{E'\rho}}{r_p^2\pi} \tag{2.21}$$

$$\gamma(s) = \frac{s}{c_0}\sqrt{-\frac{J_0\left(R^*\right)}{J_2\left(R^*\right)}} \tag{2.22}$$

$$c_0 = \sqrt{\frac{E'}{\rho}} \tag{2.23}$$

$$R^* = j\sqrt{\frac{s}{\nu}} r_p \tag{2.24}$$

and j as the imaginary unit. The transcendental nature of the transfer function of Eq.

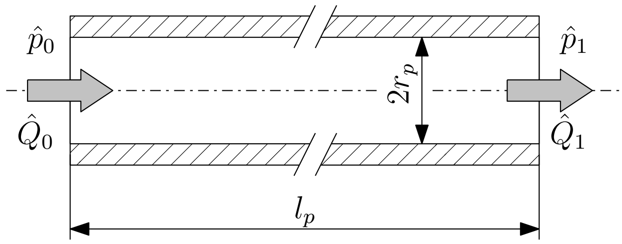

Figure 2.14.: Straight pipe

(2.19) impedes an analytic calculation of the system response in time domain, hence, numerical methods have to be applied. An efficient calculation can be achieved by the method of the Fast-Fourier-Transformation, which is valid for periodic processes. Assuming, that the HBC is operating in a steady state at a constant switching frequency, a strictly periodic process is represented. Thus, the system response in time domain can be efficiently calculated by the Inverse-Fast-Fourier-Transformation. Therefore, most of the used models in this work are reshaped to the form

$$\begin{bmatrix} \hat{Q}_0 \\ \hat{Q}_1 \end{bmatrix} = \begin{bmatrix} \frac{1}{Z\tanh(\gamma l_p)} & -\frac{1}{Z\sinh(\gamma l_p)} \\ -\frac{1}{Z\sinh(\gamma l_p)} & -\frac{1}{Z\tanh(\gamma l_p)} \end{bmatrix} \begin{bmatrix} \hat{p}_0 \\ \hat{p}_1 \end{bmatrix}, \tag{2.25}$$

with the pipe length l_p. The argument s is omitted at least where no confusion is possible. The considerations are only valid, if all the assumptions of adequate pressure levels and laminar pipe flow are fulfilled. An application of this modelling method requires a proper design of the pipe network to obtain meaningful results.

In addition to stationary periodic system responses, the closed loop performance of different control concepts in combination with an HBC will be investigated. There, transient effects are of major interest. Thus, the simulations have to be carried out in time domain. For the simulation of wave propagation in hydraulic transmission lines in time domain the toolbox *HydroLib* is used, which was developed at the Johannes Kepler University. The *HydroLib* toolbox provides transmission line simulation models based on a linear method of characteristics (MOC) with frequency dependent boundary friction as pointed out in [43, 53]. Detailed information about the *HydroLib* toolbox can be obtained from [24].

2.2.3. Hydraulic Parasitic Effects

The switching of an HBC occurs at very low time constants compared to the dynamics of the load motion. Within these small time spans a certain amount of fluid has to pass the valves, which are connected to the other components of the HBC. The faster a switching process, the higher is the effect of inertia of the fluid in the corresponding bores of the valve block. Therefore, this effect has to be considered in the design of a hydraulic switching converter. Such parasitic inductances ($L_{p_1}, \ldots, L_{p_8}$) are shown in the schematic of Fig. 2.15. At certain switching states some bores represent dead end pipes. The resulting dead volume C_Y has to be charged and discharged, respectively, at each switching cycle, which contributes a noteworthy part to the overall power losses. Furthermore, long supply- (L_S) or tank lines (L_T) also influence the behaviour of the whole configuration. To realise high dynamics at the load it is important to eliminate the inertia of such long peripheral pipe lines. However, those mentioned effects may influence the performance of a switching converter in a negative way. This makes is worth to get a sound understanding of this effects for the purpose of elimination or at least reduction of their negative influence.

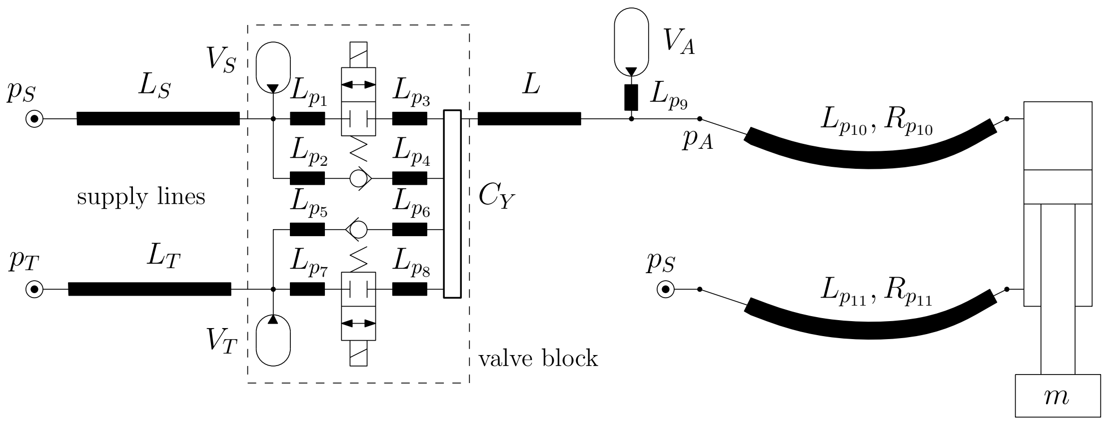

Figure 2.15.: Parasitic effects in an HBC

2.2.3.1. Parasitic Inductance

In fast switching hydraulic systems the valves are designed for switching times of lower than one millisecond. That fast opening or closing of a valve is not followed directly by the flow rate. Due to parasitic inductances, which represent additional fluid inertia, the flow through the valve is delayed at each switching cycle, which results in two different problems: (i) The fluid in such an inductance has to be accelerated quickly to enable the flow through a fast switched valve; (ii) if a valve shuts quickly, either cavitation or pressure peaks - the so called water hammer phenomenon - may occur. The following considerations give a rough estimation to assess these effects, where the parasitic pipe inductances are treated as lumped parameter systems.

Avoidance of Cavitation The following calculations are referred to the inductances L_{p_3} and L_{p_7} of Fig. 2.15, where cavitation may occur if the switching valve is closed quickly. To keep the relations simple only an estimate is given. An infinitely fast valve switching is assumed as depicted in Fig. 2.16. At first, the valve is considered to be open in

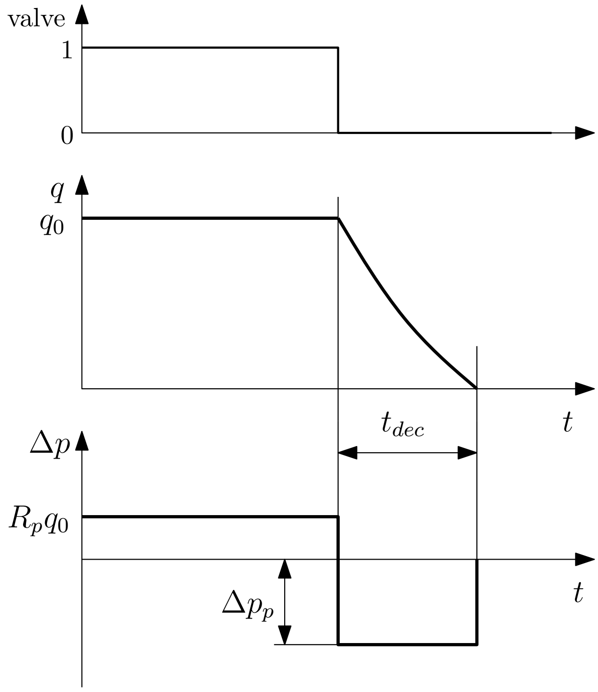

Figure 2.16.: Parasitic effect of an inductance

steady position and the initial flow rate q_0 and the corresponding pressure drop at the parasitic inductance reads $R_p q_0$. If the valve is closed immediately the flow rate through the parasitic inductance calculates to

$$\begin{aligned} q(t_{dec}) &= \frac{\Delta p_p}{R_p} + e^{\left(-\frac{R_p}{L_p} t_{dec}\right)} \left(q_0 - \frac{\Delta p_p}{R_p}\right) \\ &= 0. \end{aligned} \tag{2.26}$$

with the time t_{dec}, where the flow stops. For simplicity, a constant pressure drop for the complete deceleration process is assumed. Hence, the necessary pressure drop for decelerating the flow rate through a parasitic pipe reads

$$\Delta p_p = -\frac{R_p e^{\left(-\frac{R_p}{L_p} t_{dec}\right)} q_0}{1 - e^{\left(-\frac{R_p}{L_p} t_{dec}\right)}} \tag{2.27}$$

and by neglecting the static resistance it follows

$$\Delta p_p|_{R_p \to 0} = -L_p \frac{q_0}{t_{dec}}. \tag{2.28}$$

In this case the resulting pressure drop $\varDelta p_p$ can be interpreted as the minimum tank pressure in order to avoid cavitation at the spool edge. Now it becomes clear, that the lower the value of the parasitic inductance the lower the necessary tank pressure to avoid cavitation. For a rough numerical estimation the time t_{dec} needs to be defined. In fact, the calculations were carried out with a vanishing switching time, but in practice the flow rate through the parasitic inductance must be stopped until the valve is shut. For this reason, the switching time t_{f_h} from Fig. 2.11 can be substituted for t_{dec}. In case of L_{p3} the initial flow rate q_0 can be estimated from the worst case of the maximum steady flow rate through the valve, which is determined by the following relation:

$$q_0 = \frac{Q_N}{\sqrt{p_N}} \sqrt{p_S - p_A + R_h q_0}. \tag{2.29}$$

R_h is the static resistance of the main inductance of the HBC. The only physically reasonable solution of Eq. (2.29) for q_0 reads:

$$q_0 = \frac{1}{2p_N} Q_N \left(\sqrt{Q_N^2 R_h^2 + 4p_N p_S - 4p_N p_A} - Q_N R_h \right), \tag{2.30}$$

which is the initial flow rate of the decelerating process. For L_{p_7} the initial flow rate has to be calculated with the tank pressure p_T instead of the supply pressure p_S, respectively.

Pressure Attenuation Considering the accumulator V_A and the parasitic inductance L_{p_9} of Fig. 2.15 for pressure attenuation at the load, the Helmholtz resonator formed by these two elements should not impede the filtering of the pressure pulsations by V_A. The approximate natural frequency of the Helmholtz resonator reads

$$\begin{aligned} \omega_H &= \sqrt{\frac{1}{L_{p_9} C_A}} \\ &= \sqrt{\frac{d_p^2 \pi n \bar{p}_A}{4\rho l_{p_9} V_A \left(\frac{p_0}{\bar{p}_A}\right)^{\left(\frac{1}{\varkappa}\right)}}}. \end{aligned} \tag{2.31}$$

The parameters of the resonator have to be configured in a way, that its natural frequency is higher than the pulsation frequencies that must be dampened. Obviously, this can be assured with a small enough parasitic inductance L_{p_9}. Simultaneously, for the purpose of pressure attenuation the accumulator must have a sufficiently large capacitance C_A. The procedure to configure the pulsation damper will be introduced later in Subsection 2.3.5.

Avoidance of the Water Hammer Phenomenon If a valve is closed quickly, a wave is excited in the connected pipe line travelling to the pipe's end, where it will be reflected towards the valve again. If the closing time of the valve t_c is lower than the travelling time of the wave to the end of the pipe and back again, then the water hammer phenomenon occurs. Thus, the critical length of an parasitic inductance like L_{p_1} can be estimated by

$$l_{p_1} = t_c \frac{c_0}{2} \tag{2.32}$$

with $c_0 = \sqrt{\frac{E_{oil}}{\rho_{oil}}}$ as the speed of sound in the fluid. With regard to Fig. 2.11 certainly the closing time t_{f_h} is relevant. This estimation and further details can be found in [28].

2.2.3.2. Parasitic Capacity

In Fig. 2.15 the capacity C_Y has to be charged and discharged at each switching cycle. This cavity is determined by the block design and consists, e.g., of intersections or simply dead end bores in the valve block. Two problems are caused by the cavity C_Y. The volume V_Y must be pressurised up to supply pressure p_S at the beginning of the duty cycle. The surplus of pressure with respect to the load pressure p_A is consequently lost by means of throttling. On the other hand, the time which is needed for discharging V_Y delays and shortens the suction phase form tank. Similar is valid in the recuperating direction. In Fig. 2.17 the resulting capacity effect is illustrated. The red line in the

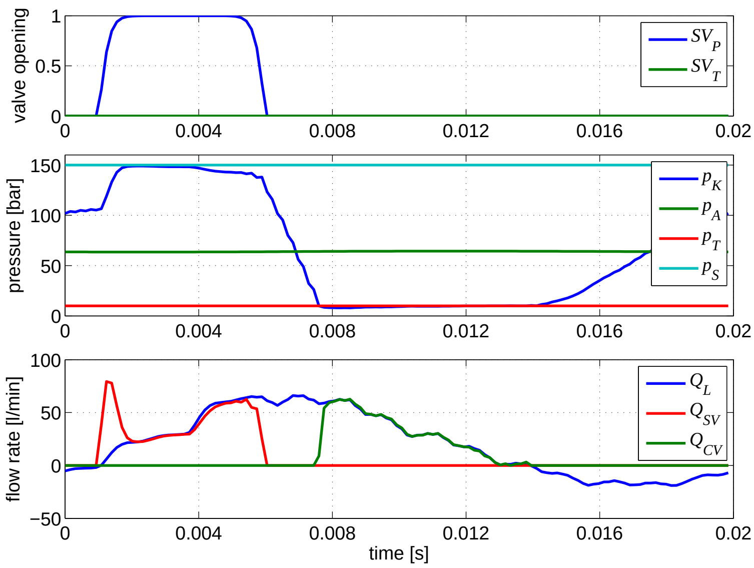

Figure 2.17.: Parasitic capacity effect; numeric values for this configuration listed in Tab. A.4

lower diagram represents the flow rate through the supply sided switching valve. When the valve is closed (upper diagram) the flow through the main inductance of the converter discharges the so called node volume V_Y and the node pressure (blue line in the middle diagram) descends to tank pressure. The suction phase from tank does not start before

p_Y falls below tank pressure. The flow rate through the tank sided check valve is indicated by the green line in the lower diagram. That suction is key for the energy saving of the HBC in forward mode. Thus, in order to gain a high efficiency it is important to keep this parasitic capacity as low as possible. Due to different operating points of the HBC and different pressure conditions in the node volume because of some internal resonance effects, two different estimations of the charging power losses can be given. The worst case reads

$$\hat{P}_{C_Y} = \frac{(p_S - p_T)\, p_S}{E_{oil}} f_S V_Y \left(1 - \frac{p_A}{p_S}\right), \tag{2.33}$$

which occurs in pressure control mode, where the node volume V_Y has to be charged from tank pressure to supply pressure when the switching cycle starts. The factor $\left(1 - \frac{p_A}{p_S}\right)$ indicates that not all of the charging power is lost. However, in most operating points the converter acts in flow control mode, where the average power losses due to capacity effects can be estimated by

$$\bar{P}_{C_Y} \approx \frac{(p_S - p_A)\, p_S}{E_{oil}} f_S V_Y \left(1 - \frac{p_A}{p_S}\right), \tag{2.34}$$

because the node volume only has to be charged from p_A to p_S. Another important parasitic effect of the mentioned capacity is a resulting Helmholtz resonator in combination with the main inductance of the converter. In case of a proper block design and, thus, a very small node volume, the natural frequency of this resonator will be sufficiently beyond the switching frequency. However, the natural frequency of this resonator has to be checked in each HBC design.

2.2.3.3. Long Pipes and Hoses

Basically, in a constant pressure system pipes or hoses connect a hydraulic consumer to its control unit and this unit with the supply system. In many cases the hydraulic supply system is situated far away from the consumer. Thus, the pipe lines (L_S, L_T in Fig. 2.15) are often rather long. Hence, the drive has to cope with an additional inertia at the load, which lowers the dynamics of the drive. Whether it is a proportional or a fast switching drive, both types are confronted with this problem. In view of fast switching systems, the accumulators for pressure attenuation on the supply- (V_S) and on the tank side (V_T) from Fig. 2.15 can be used for decoupling functions. Under the assumption that the inertia of the supply line is much higher than the inertia of the load, the decoupling accumulator must provide the amount of fluid needed immediately at the load until the supply line flow is accelerated. On tank side, the respective accumulator must be able to allocate the fluid from the load until the tank line flow is accelerated. Then, the fastest load dynamics possible with a given HBC can actually be achieved. The pressure variations in the accumulators (V_S and V_T) have to be considered as well. Details of configuring an accumulator can be found in Subsection 2.3.5.

In case of a converter, which is connected to the cylinder via long hoses ($L_{p_{10}}$, $L_{p_{11}}$), it is important to mention, that the dynamic calculations have to account for an additional load inertia. Therefore, the inductance of the pipe lines between the HBC and the cylinder have to be added to the mass of the dead load. Similar is valid for viscous damping. The corresponding equation of motion of the load reads

$$\left(m + L_{p_{10}} A_1^2 + L_{p_{11}} A_2^2\right) \dot{v} = p_A A_1 - p_S A_2 - \left(d_v + R_{p_{10}} A_1^2 + R_{p_{11}} A_2^2\right) v \tag{2.35}$$

with the dead load m and the cross-sections of the cylinder chambers A_1 and A_2, respectively.

2.2.4. Switching Frequency

For the sake of a smooth motion of the load, a very high switching frequency would be desirable. Then, the flow rate pulses and thus the pressure pulsations would become very small and no attenuation devices would be necessary. Furthermore, the stiffness of the drive would be maximum. However, both electronic and hydraulic switching converters have to cope with limited switching frequencies and both have to use attenuation devices that likely soften the system's dynamics. The influence of the switching frequency on the behaviour of a system is derived, e.g., in [16, 17]. There the author points out, that if the switching frequency is much higher than the natural frequencies of the system a continuous modelling for control issues is possible. In contrast to power electronics, where switching frequencies of several *kHz* are common, the maximum achievable switching frequencies in hydraulics are in the range of $100\,Hz$, at least at the time being. The hydraulic application controlled with those switching frequencies should have its natural frequencies below $10\,Hz$, to make the assumption of a continuous system approximately valid. This circumstance requires a sophisticated control strategy to compensate the softness of the resulting hydraulic drive.

Another limiting factor is that hydraulic systems suffer from relatively high capacitance effects. For too high switching frequencies only a charging and discharging of these capacitances via the valve dominates and no more energy saving takes place.

2.2.5. Noise

Due to the switching process sharp pressure edges, which are necessary for the energy saving effects, occur especially in the node capacity C_Y. This switching process also generates corresponding cycling stresses to the surrounding block material. The nearly rectangular pressure signal features a very broad band frequency spectrum as depicted in Fig. 2.18, which is audibly emitted. Unfortunately, there are many spectral components of the pressure signal in the hearable range of human beings. Thus, the engineering of fast switching hydraulics will have to cope also with the noise problems to achieve a broad customer acceptance. However, in this work no further investigations on noise problems were carried out.

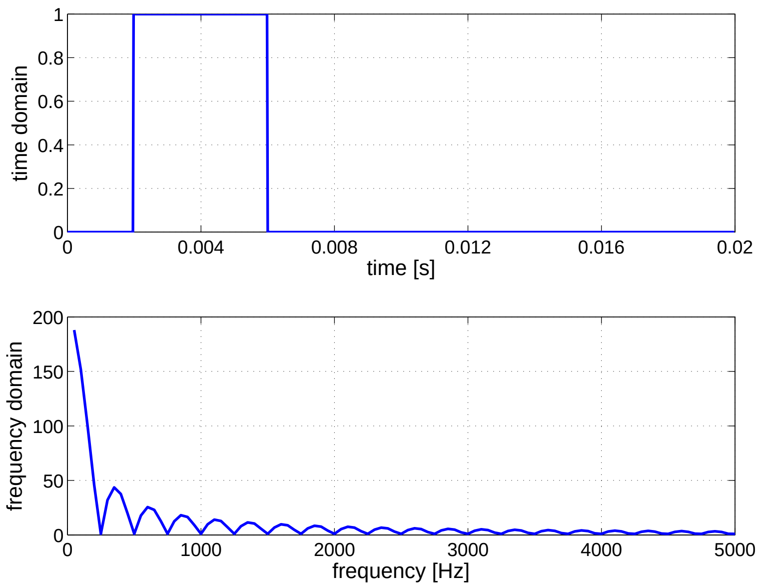

Figure 2.18.: Noise generation due to a broad band frequency excitation by switching ($f_S = 50\,Hz$; $\kappa = 20\%$)

2.3. Design Aspects

The essential components of efficient switching hydraulic systems are switching valves, check valves, accumulators and, of course, the pipe system. All these components have to fulfill certain requirements to obtain the intended behaviour of the drive. Also the switching frequency has to be determined properly. The pressure pulsation due to the switching process has to be attenuated by an accumulator which is situated at the output of the HBC. Thus, the hydraulic drive loses its stiffness and the converter interacts with the load at certain operating points. For this reason it is also important to define the load requirements precisely. A differential cylinder is the most frequently used actuator for most linear hydraulic drives. Hence, in the following a design procedure of a fast switching hydraulic drive consisting of a differential cylinder with a dead load controlled by an HBC as illustrated in Fig. 1.13 is proposed. In the following sub-sections simple design rules for the HBC and for its components, respectively, are presented. These rules are based on the simple models of Sections 2.1 and 2.2.

2.3.1. Load Specifications

The first step in configuring a hydraulic drive is to get information about the hydraulic actuator as depicted, for instance, in Fig. 1.13. In this circuitry, the annulus chamber of the cylinder is connected to supply pressure, hence the corresponding cross-sections of the cylinder has to be defined to achieve the desired forces at the load. For an efficient operation of the system, the ratio of both cross-sections should be determined such, that the mean pressure of the piston sided chamber lies exactly in the middle between supply pressure and tank pressure, assuming that no process force is applied yet. Thus, an equal force can be provided in both directions of movement. If the drive has mainly to lift and to lower a dead load, the gravity force must be taken in to account in the design of the cross-section ratio. Also the desired dynamic load behaviour has to be determined. The maximum frequency of the load movement f_A is an important specification parameter, which has a strong influence on the maximum size of the accumulator for pressure attenuation. A further interesting parameter is the absolute value of the maximum desired piston velocity $|v_{max}|$, which defines the maximum flow rate through the converter. This value has big influence on the design of the main component of the HBC, the inductance. The essential specifications for the design of a fast switching hydraulic drive for this exemplary case are listed in Tab. 2.1.

Parameter	Variable
supply pressure	p_S
load mass	m
process force	F_P
cross-section of piston	A_1
annulus cross-section	A_2
maximum piston velocity	v_{max}
maximum load frequency	$2\pi f_A = \omega_A$

Table 2.1.: Load specifications

2.3.2. Switching Frequency

The minimum switching frequency is basically determined by the maximum dynamics desired at the load. Therefore, the load system in combination with the accumulator at the output of the HBC must be analysed. As mentioned before, the switching frequency should be in the range

$$f_S \gtrsim 10\frac{\omega_A}{2\pi}, \tag{2.36}$$

i.e., approximately ten times higher than the natural frequency of the oscillator formed by the dead load and the gas spring of the accumulator

$$\omega_A \approx \sqrt{\frac{\bar{p}_A A_1^2 \varkappa}{m V_A \left(\frac{p_{0G}}{\bar{p}_A}\right)^{\frac{1}{\varkappa}}}}. \tag{2.37}$$

Of course, this maximum load frequency ω_A depends strongly on the mean operating pressure $\bar{p}_A$. Therefore the relevant operating points have to be determined properly.

But the switching frequency resulting from Eq. (2.36) in combination with Eq. (2.37) may be higher than what is technically feasible with today's switching valves.

2.3.3. Digital Valves

In an HBC basically two different types of on/off valves are in use; on the one hand the active switching valves and on the other hand the passive check valves for energy saving and recuperation. Independent of the valve type, the basic requirement trends are, that the valves are very large[1] and fast. Assuming, that in PWM control the switching time is very short compared to the duration in opened position, the size of the valves would determine the main resistance, which has to be kept to a minimum to keep losses low. But, for any valve concept, the larger the size of a switching valve, the larger is the size of the spool or the poppet and the required stroke of the switching motion. This limits the valve band width due to its higher spool mass and stroke, respectively. Thus, a natural trade-off between size of a valve and fast response capabilities exists.

It is essential to keep the switching time of the valve as low as possible, because during the rise and fall time flow metering occurs and, thus, throttle losses increase. Especially check valves have to switch very fast. They are passive components and are switching due to the surrounding pressure conditions. Check valves are mainly used for energy saving prospects in the suction phase and in the recuperation phase, respectively. Depending on the different operating points of the HBC, the time spans where energy saving or recuperation takes place are often very short. The better their dynamic performance the higher the energy saving effects will be. Furthermore, at the tank sided check valve only a low pressure drop is available for opening the valve due to the low tank pressure. This imposes particular requirements of response dynamics and size to prevent cavitation.

Further, too long opening and closing times of the active valves limit the achievable duty ratios in the view of a proper pulse width modulation. Of course, the speed of the

[1] in the sense of a large nominal flow rate

spool and thus the sharpness of the switching edge depends on the applied force, which is mostly generated by a solenoid. Thus, the maximum switching frequency, band width and, further the effective valve size depend on the power of the solenoid at least at directly controlled switching valves. Of course, it is possible to design piloted switching valves to achieve higher flow ratios at high band width, but these types of valves are currently under development and are not ready for use yet. Today, just a few different directly solenoid actuated switching valves are available, which were developed, for instance, at the Linz Center of Mechatronics ([29, 30, 48, 49, 50, 51]) and which are available for field tests of hydraulic switching technology. A selection of the available switching valves and their basic characteristics are listed in Tab. 2.2.

Switching Valve Type	$Q_N[\frac{l}{min}@5bar]$	$t_{SW}[s]$	Figure	Literature
comb valve	45	0.001	2.19	[50]
pilot valve	10	0.001	2.20	[30]
piloted multi poppet valve	85	< 0.001	2.21	[49]
check valve	30	< 0.001	2.22	[29]

Table 2.2.: Switching valves developed at the Linz Center of Mechatronics

In Fig. 2.19 a prototype of a directly controlled, so called, comb valve is depicted. In con-

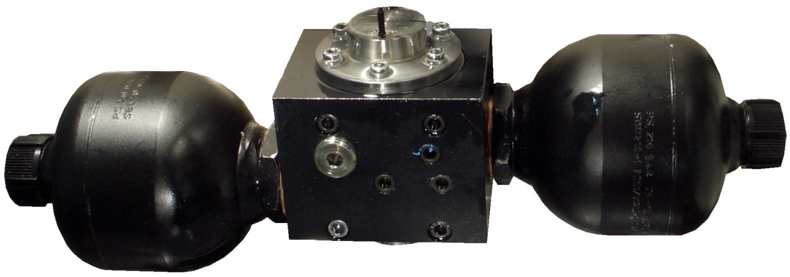

Figure 2.19.: Comb valve

trast to its forerunners the valve has already a compact design with a standard mounting dimension. Unfortunately, the conventional accumulators for pressure attenuation and decoupling make the whole converter configuration quite unhandy, and have insufficient dynamical response for switching control.

In Fig. 2.20 a compact switching valve of a small nominal flow rate is illustrated. Its distinctive property is its on-board power electronics. This valve only needs one cable for the power supply and one cable for communication with the controller for the digital switching signal. It is a very compact and effective switching unit, which is already tested for a fatigue endurance limit at a switching frequency of 200 Hz. This valve was originally developed as a pilot valve stage, but it is also in use as a main valve of low power fast switching hydraulic applications today. Depending on the needs, the valve can be realised as a 2/2 normally off, normally on or even as a 3/2-version.

Figure 2.20.: Pilot valve

A multi poppet valve using the previously mentioned pilot valve is illustrated in Fig. 2.21. This valve consists of 14 separate valve pistons arranged around the pilot stage. The valve

Figure 2.21.: Piloted multi poppet valve

is so fast, that its main stage opens earlier than the pilot stage. Remarkable is further the fact that the single poppets are needles of needle bearings, which are extremely cheap and allow the realisation of a fast switching valves with a huge nominal flow rates at very low manufacturing costs.

Fig. 2.22 shows a fast plate type check valve of very small overall size. The spring,

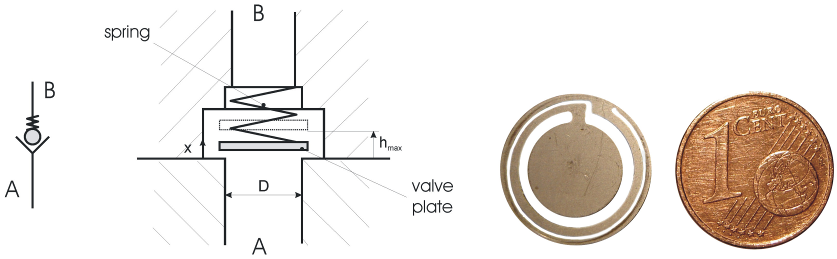

Figure 2.22.: Fast plate check valve

which holds the valve plate in a well defined position has the form of a circular beam situated around the plate. Since the valve plate and the spring are made of the same material, the complete valve can be produced very cheaply by laser cutting or etching. The natural frequency of this spring-plate combination is about $400\,Hz$, which makes the valve interesting for switching converters. The valve can be easily scaled for large flow rates.

2.3.4. Inductance

In power electronics the inductance of a buck converter is mostly determined by current ripple requirements, often in term of a certain percentage of the average current. To keep the ripples as low as possible the inductance has to be maximised. In hydraulics a large inductance is also helpful to avoid the transition from laminar to turbulent flow in the pipe line. For energy saving prospects it is also advantageous to have a large inductance. However, in hydraulics the inability to realise arbitrary high inductance values makes the design of the inductance more delicate[2]. If the switching frequency is in the range of the natural frequencies of the inductance pipe, wave propagation in the pipe has to be taken into account. Therefore, a certain criterion is needed, if a transmission line can be treated as a compact inductance with lumped parameters. In hydraulics and also in high frequency electronics a common criterion is to limit the length of transmission lines to $\frac{1}{20}, \ldots, \frac{1}{10}$ of the wave length of the main operating frequency spectrum. In accordance with this length-frequency ratio the maximum pipe length can be determined by

$$l_{p_{max}} \lesssim \frac{c_0}{10 f_S}, \tag{2.38}$$

with the speed of sound in the fluid c_0 and $l_{p_{max}}$ the maximum length of the pipe. This approximation provides the necessary gap between the switching frequency f_S and the first natural frequency of the pipe, to keep the lumped inductance model valid. The relevant natural frequency of the hydraulic transmission line is called $\lambda/4$-resonance which is characterised by

$$f_{\lambda/4} \quad = \quad \frac{c_0}{4 l_p}. \tag{2.39}$$

Thus, the ratio between switching frequency and first natural frequency of the pipe reads

$$\frac{f_S}{f_{\lambda/4}} \lessapprox \frac{2}{5} \tag{2.40}$$

[2]Of course, an inductance represents a sort of inertia and, thus, large values can be achieved by using the inertia of mass loaded hydraulic rotary motors. But in this study only a simple and, thus, low cost concept of the HBC is intended.

at least in the case of $l_{p_{max}}$. However, the main task is to define an appropriate value of the inductance, which in hydraulics is defined by

$$L = \frac{4\rho l_p}{d_p^2 \pi} \tag{2.41}$$

with the pipe hydraulic diameter d_p, the pipe length l_p, and the fluid density ρ. Obviously, the smaller the pipe diameter the higher the inductance. On the other hand, a smaller diameter increases the pipe resistance tremendously. The static resistance of the pipe by Hagen-Poiseuille is defined by

$$R = \frac{8\rho\nu l_p}{\left(\frac{d_p}{2}\right)^4 \pi}, \tag{2.42}$$

with the viscosity ν as a further parameter. According to this simple model, the pipe diameter increases the resistance with the inverse of its fourth potency. So the inductance value cannot be designed arbitrarily large without running into severe loss problems due to pipe friction. A common way to fix the diameter of transmission lines is the evaluation of the turbulence criterion:

$$\begin{aligned} \mathrm{Re} &= \frac{v_p d_p}{\nu} = \frac{4\bar{Q}_{max}}{d_p \pi \nu} \\ &= \frac{4A_1}{d_p \pi \nu} \left| v_{max} \right| \leq \mathrm{Re}_{crit} \end{aligned} \tag{2.43}$$

with $\bar{Q}_{max}$ as the maximum flow rate defined by the load specifications. At the critical Reynold's number Re_{crit} the flow in the transmission line changes from laminar to turbulent, which leads to a dramatic increase of friction losses. Although the maximum instantaneous flow rates due to the switching process are higher than the average load flow rate $\bar{Q}_{max}$, the criterion of Eq. (2.43) is a good approximation, because experiments, e.g. by [1, 19], showed that strongly accelerated flows in straight pipes remain stable until Reynolds numbers far beyond the critical value of 2300. However, the Reynold's number $\mathrm{Re} = 2300$ is in accordance with the literature the lower stability boundary for decelerating laminar flows.

2.3.5. Accumulator

The working principle of the HBC intrinsically excites large flow rate fluctuations, which cause also large pressure pulsations at the load, if no pressure attenuation is provided. For a suitable control of the load these pressure ripples must be smoothened. For this purpose a sufficiently large accumulator is placed at the output of the converter. Basically, the accumulators not only provide pressure attenuation, but serve also other dynamical functions, namely the dynamical decoupling of the drive from the supply and tank lines.

2.3.5.1. Pressure Attenuation

The reason for the efficiency in pressure pulsation attenuation is the large capacity and the low inertia of the gas spring of an accumulator. A good model to assess the capacity of a gas spring is the polytropic change of state, which reads

$$p_{0_G} V_{0_G}^{\varkappa} = p_{OP} V_{OP}^{\varkappa} = \text{const} \tag{2.44}$$

with $\varkappa$ as the poly-tropic exponent, which can be assumed to be constant in common converter applications. Considering the accumulator at a certain operating pressure p_{OP} a pressure rise Δp due to a volume change ΔV calculates to

$$\Delta p = \frac{p_{0_G}}{\left(\left(\frac{p_{0_G}}{p_{OP}}\right)^{\frac{1}{\varkappa}} - \frac{\Delta V}{V_A}\right)^{\varkappa}} - p_{OP}. \tag{2.45}$$

Hence, presetting a maximum permitted pressure amplitude Δp_{max} the necessary volume V_A of the accumulator can be determined by solving Eq. (2.45) for V_A. It remains to define the volume change ΔV, that comes from the switching process of an HBC. The worst case operating point of the converter with respect to flow rate pulsations at the end of the main inductance has to be selected. This scenario takes place at the transition between flow control mode and pressure control mode, thus, at the transition duty ratio $\kappa^{\#}$ which depends, according to Eq. (2.7), on the load pressure p_A. Substituting $\kappa^{\#}$ from Eq. (2.7) into the flow rate equation of the inductance delivers

$$q\left(\kappa^{\#} T_P\right) = \frac{p_S - p_A}{R}\left(1 - \frac{(p_S - p_A)e^{-\frac{R}{L f_S}} + p_A - p_T}{p_S - p_T} e^{-\frac{R}{L f_S}}\right). \tag{2.46}$$

The maximum flow rate point results from the extremum value problem

$$\frac{\partial}{\partial p_A} q\left(\kappa^{\#} T_P\right) = 0. \tag{2.47}$$

If the static resistance is neglected, the load pressure results from Eq. (2.47) to

$$p_A = \frac{p_S + p_T}{2}. \tag{2.48}$$

The corresponding worst case swap ratio calculates to

$$\kappa^{\#} = \frac{1}{2}. \tag{2.49}$$

Assuming that the pressure in the attenuator is only rising during the acceleration of the flow rate in the main inductance of the HBC, the maximum differential volume ΔV can be approximated by

$$\begin{aligned} \Delta V &\approx \int_0^{\kappa \# T_P} \frac{(p_S - p_{OP})}{R} \left(1 - e^{-\frac{R}{L}t}\right) \mathrm{d}t \\ &= \frac{(p_S + p_T)}{2R} \left(\frac{1}{2f_S} + \frac{L}{R} \left(e^{-\frac{R}{L}\frac{1}{2f_S}} - 1 \right) \right). \end{aligned} \tag{2.50}$$

It has to be remarked, that this approximation is only valid, if the fluctuations of the operating pressure p_{OP} are small relative to the supply pressure p_S and, thus, Δp_{max} is sufficiently low. L and R are again the characteristic parameters of the main inductance of the HBC.

2.3.5.2. Decoupling from Supply Lines

To reduce the influence of the inertia of long supply lines, accumulators are used for decoupling and to sustain fairly constant pressures. As explained in Subsection 2.2.3.3 the accumulator must provide the necessary fluid needed by the load until the inertia of the supply line is overcome. The design of such a decoupling accumulator is carried out according to Eq. (2.45). Of course, in this case the essential volume ΔV has to be specified by the individual load requirements. However, the decoupling accumulator and the supply- or tank line, respectively, create a Helmholtz resonator, which is schematically depicted in Fig. 2.23. For the purpose of a low supply pressure fluctuation, the natural

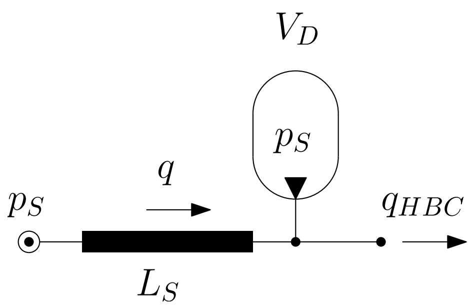

Figure 2.23.: Decoupling resonator on supply side

frequency of this resonator has to be much lower than the frequency of the load cycles (ω_A). In accordance with Fig. 2.23 this frequency can be estimated by

$$\begin{aligned} \omega_H &= \sqrt{\frac{1}{L_S C_D}} \\ &= \sqrt{\frac{d_S^2 \pi \varkappa p_S}{4 \rho l_S V_D \left(\frac{p_{0_G}}{p_S}\right)^{\left(\frac{1}{\varkappa}\right)}}} \end{aligned} \tag{2.51}$$

for the supply line and the tank line with the corresponding parameters.

2.3.5.3. Accumulators for Fast Switching Hydraulics

The standard device for pressure attenuation and decoupling in hydraulic systems with a high dynamics is a membrane accumulator like depicted in Fig. 2.24. Basically, the

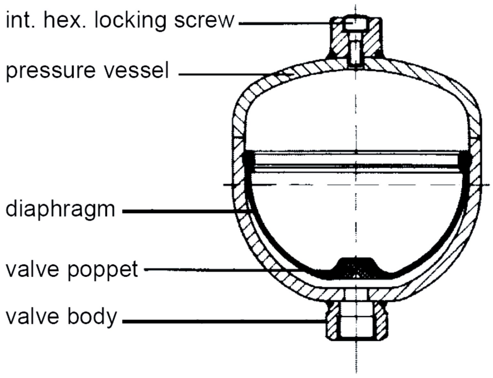

Figure 2.24.: Membrane accumulator (source: `www.hydac.com`)

low mass of the diaphragm in comparison to its effective cross-section area enables an effective exploitation of the capacity of the gas spring. Another reason for their common use is that such accumulators are commercially available at low costs. One drawback of such a membrane accumulator is the sensitivity of the diaphragm, a second the limited ratio between pre-pressure and maximum pressure which is a restriction of the operating range, and third a limited cross-section of the inlet port which prevents a damage of the diaphragm at a touch down of the valve poppet when the operating pressure falls below the pre-pressure. In contrast to the third drawback, the accumulator for pressure attenuation at the output of an HBC should be able to operate in the full range between tank pressure and supply pressure. Furthermore, for an appropriate attenuation of the large pressure pulsations due to the switching process a very fast response is required. One possibility to avoid the mentioned shortcomings of a membrane accumulator is to use a piston accumulator, like depicted in Fig. 2.25. This robust accumulator design has no

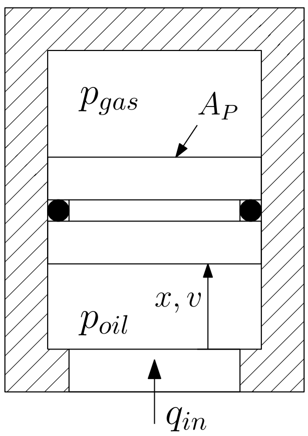

Figure 2.25.: Piston accumulator

restrictions concerning the pre-pressure to operating pressure ratio. In this context it has to be proven, that the mass of the piston does not impair the dynamics of the accumulator. To assess this a dynamical model of the dominating dynamics of the accumulator is set up. The corresponding state space representation is given by

$$\begin{bmatrix} \dot{x} \\ \dot{v} \\ \dot{p} \end{bmatrix} = \begin{bmatrix} v \\ \frac{1}{m_P}\left(\left(p - p_{0_G}\left(\frac{V_{0_G}}{V_{0_G} - A_P x}\right)^{\varkappa}\right) A_P - d_v v\right) \\ \frac{E_{oil}}{V_0 + A_P x}\left(q_{in} - A_P v\right) \end{bmatrix}. \tag{2.52}$$

The steady state values of piston position, velocity, pressure and flow rate are

$$\begin{bmatrix} x_{OP} \\ v_{OP} \\ p_{OP} \\ q_{in_{OP}} \end{bmatrix} = \begin{bmatrix} \frac{V_{0_G}}{A_P}\left(1 - \left(\frac{p_{OP}}{p_{0_G}}\right)^{\frac{1}{\varkappa}}\right) \\ 0 \\ p_{OP} \\ 0 \end{bmatrix}. \tag{2.53}$$

Linearising Eq. (2.52) at an equilibrium point leads to the following system matrix

$$\mathbf{A}_{PA} = \begin{bmatrix} 0 & 1 & 0 \\ -\frac{p_{0_G}\left(\frac{V_{0_G}}{V_{0_G} - A_P x_{OP}}\right)^{\varkappa} A_P^2}{m_P\left(V_{0_G} - A_P x_{OP}\right)} & -\frac{d_v}{m_P} & \frac{A_P}{m_P} \\ -\frac{E_{oil} A_P\left(q_{in_{OP}} - A_P v_{OP}\right)}{\left(V_0 + A_P x_{OP}\right)^2} & -\frac{E_{oil} A_P}{V_0 + A_P x_{OP}} & 0 \end{bmatrix}. \tag{2.54}$$

Reducing the linearised dynamics to the partial system consisting of the piston mass and the gas spring and further substituting Eq. (2.53) leads to the relevant dynamics matrix for the movement of the piston

$$\mathbf{A}_{PA_{red}} = \begin{bmatrix} 0 & 1 \\ -\frac{p_{OP}^{\frac{\varkappa+1}{\varkappa}} \varkappa A_P^2 p_{0_G}^{-\frac{1}{\varkappa}}}{m_P V_{0_G}} & -\frac{d_v}{m_P} \end{bmatrix} \tag{2.55}$$

with the resulting natural frequency

$$\omega_{PA} = \Im\left\{\sqrt{\frac{d_v^2}{4m_P^2} - \frac{A_P^2 \varkappa}{m_P V_{0_G}} p_{0_G}^{-\frac{1}{\varkappa}} p_{OP}^{\frac{\varkappa+1}{\varkappa}}}\right\}, \tag{2.56}$$

where $\Im$ indicates the imaginary part. Assuming, that the gas volume at the pre-pressure p_{0_G} has cylindrical form $V_{0_G} = A_P l_A = \frac{d_P^2 \pi}{4} l_A$, with l_A as the length of the volume. Furthermore, it is assumed that the length of the piston equals its diameter d_P, thus, the mass of the piston reads $m_P = \frac{d_P^2 \pi}{4} l_P \rho_P$. Then, the natural frequency of the piston movement follows to

$$\omega_{PA} = \Im\left\{\sqrt{\frac{d_v^2}{4d_P^4\pi^2 l_P^2\rho_P^2} - \frac{p_{OP}\varkappa}{l_P l_A \rho_P}\left(\frac{p_{OP}}{p_{0_G}}\right)^{-\frac{1}{\varkappa}}}\right\}, \tag{2.57}$$

which has to be sufficiently above the switching frequency f_S in order to exploit the capacity of the accumulator effectively. To get an idea of the natural frequency of that spring mass oscillator, a numeric calculation was carried out. The natural frequency of a $0.3\,l$ accumulator was investigated, by varying the piston diameter d_P and the operating pressure p_{OP}. The specific parameters of the simulation are listed in Tab. 2.3 and the result is illustrated in Fig. 2.26. It shows, that the natural frequencies are in most cases

Parameter	Value
Volume	$V_A = 0.3\,l$
Polytropic exponent	$n = 1.3$
Piston diameter	$d_P = 0.01, \ldots, 0.1\,mm$
Piston material, Aluminum	$\rho_{Al} = 3000\frac{kg}{m^3}$
Viscous damping of piston	$d_v = 500\frac{Ns}{m}$
Gas pre-pressure	$p_{0_G} = 10\,bar$
Operating pressures	$p_{OP} = p_{0_G}, \ldots, 300\,bar$
Switching frequency	$f_S = 100\,Hz$

Table 2.3.: Numeric parameters of piston accumulator

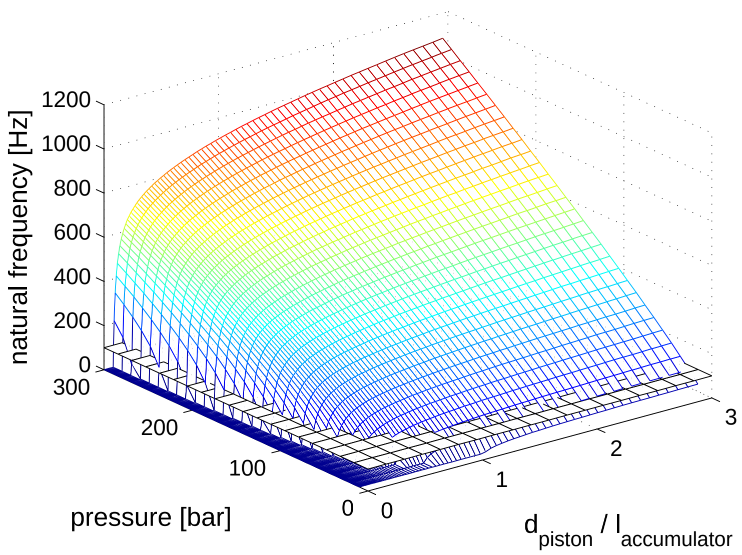

Figure 2.26.: Natural frequency depending on working pressure and geometry of the accumulator

of the considered parameter variations sufficiently above the switching frequency which is represented by the meshed horizontal plane at 100 Hz. Thus, a properly designed piston accumulator can be used for pressure attenuation of high frequency pulsations.

Misleadingly, a hydraulic accumulator is often called pulsation damper. This is actually not true, because the gas spring itself is not a dissipative element at all. Certainly, the resistance at the entry of a conventional accumulator, like depicted in Fig. 2.24, dampens some energy of the pulsations. But, if very high flow rate amplitudes should be attenuated by the accumulator the inlet throttle is counter-productive. Its high pressure losses degrade the attenuation performance, since these losses cause a pressure fluctuation which conflicts the requirements for the attenuation function. But the inlet throttle of membrane accumulators is necessary to avoid the destruction of the membrane, if the operating pressure falls quickly below the gas pressure in the accumulator. Also in this respect a piston accumulator has a better performance because of its robustness and the large inlet dimension. The main disadvantage of the piston accumulator is definitely, that the gas spring is not perfectly sealed from the fluid chamber. That could make some gas re-fill necessary. Also the costs are higher than those of conventional membrane accumulators.

Another promising type of accumulators for fast switching hydraulic systems is the metal bellow accumulator as shown by a technical drawing in Fig. 2.27. This accumulator design

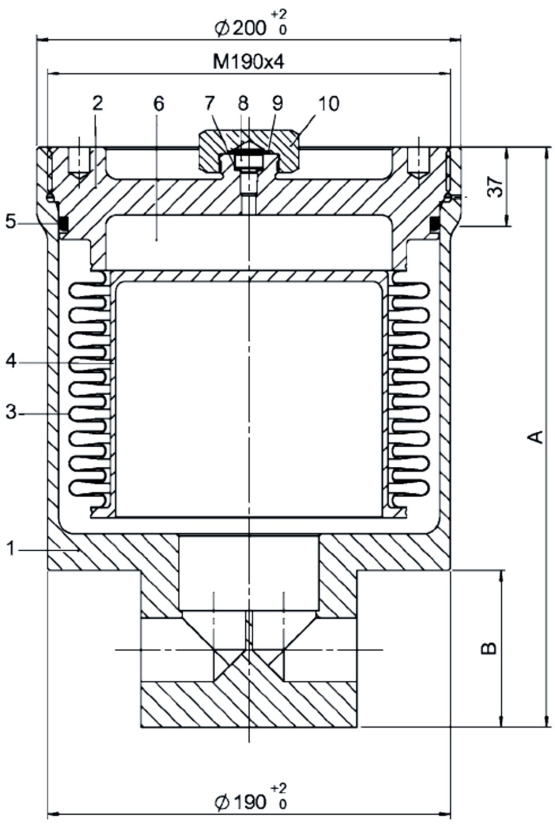

Figure 2.27.: Metal bellow accumulator (source: `www.hydac.com`)

is absolutely gas proof and is also very robust concerning different operating pressure levels. The main drawbacks at this time are its high cost and low compactness, since the operating volume ((6) in Fig. 2.27) is small compared to its size.

2.3.6. Basic Design Procedure of an HBC

Based on the considerations in the previous Subsections 2.3.1 to 2.3.5 the following design procedure is proposed:

1. Depending on the required dynamics at the load the maximum size of the accumulator V_A and the necessary switching frequency f_S can be desired from Eqs. (2.36) and (2.37).
2. Based on the switching frequency f_S, a qualified switching valve with the nominal flow rate Q_N at the nominal pressure drop Δp_N must be chosen. The switching time of the valve must be sufficiently low to realise a PWM switching.
3. To realise a proper PWM signal the maximum pressure drop over the switching valve must not exceed a certain level Δp_{max}. Thus, the maximum occurring flow rate through the converter can be estimated by

$$\hat{Q}_{max} \approx \frac{Q_N}{\sqrt{\Delta p_N}} \sqrt{\Delta p_{max}}. \tag{2.58}$$

This peak flow rate $\hat{Q}_{max}$ occurs at a duty ratio of 50% and a load pressure $p_A \approx \frac{p_S}{2}$. In this operating point the flow rate peak is about twice the maximum mean flow rate at the load. Based on the Reynold's relation and under the condition of a laminar flow during the acceleration of the fluid (for instance estimated by $Re_{max} \leq 5000$), the minimum pipe diameter can be assessed by

$$d_{p_{min}} \approx \frac{4\hat{Q}_{max}}{Re_{max}\pi\nu}. \tag{2.59}$$

4. Finally, the length of the inductance pipe is determined by the relation

$$l_p \approx \frac{d_{p_{min}}^2 \pi}{4\rho_{oil}\hat{Q}_{max}} \frac{p_S}{2} \frac{0.5}{f_S} \tag{2.60}$$

based on the lossless differential equation of the flow through a lumped parameter pipe. This leads in some cases to a quite long pipe, at least at high supply pressures. In such cases it is recommended to take the smaller value of Eqs. (2.60) and (2.38) to avoid unwanted wave propagation effects.

This design sequence leads to an appropriate design of an HBC, at least in many cases. Sometimes the different steps of the proposed procedure must be carried out iteratively until the design of the converter succeeds.

2.3.7. Block Design

Besides keeping the mentioned parasitic effects as low as possible, some other requirements have to be considered in the hydraulic block design of an HBC. In contrast to a conventional proportional valve, which houses only a solenoid controlled spool, a block of an hydraulic buck converter has to incorporate at least two switching valves, two check valves and two decoupling attenuators. Depending on the available space, the inductance can be realised as a straight pipe or as a coil. Of course, for maximum efficiency the inductance should be realised as a straight pipe, but especially at mobile applications space is often rare. Depending on the geometric constraints of the application, the output port of the converter and, thus, the pressure attenuator can be situated either at the switching block or at a certain distance to the switching block. In Fig. 2.28 a block design is proposed, where the converter output is directly situated at the valve block. The inductance must be at least a single loop. To save more space, the inductance can be

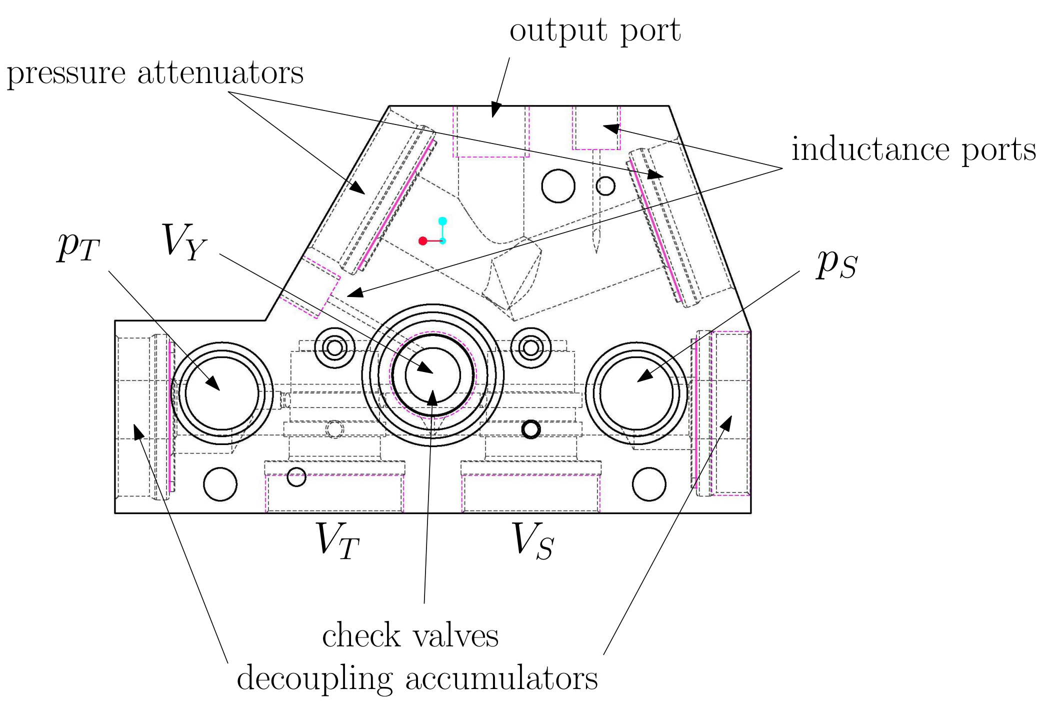

Figure 2.28.: Compact block design

formed to a coil with more windings at the cost of lower efficiency. The design from Fig. 2.28 is for an HBC for low power applications in the range of $1\,kW$. Low power systems have generally a bad power to size ratio. So, an HBC's size for higher power will not grow at the same rate as the output power. In this block design, the active switching valves are mounted from the bottom. The two bores left and right of the block are the supply and the tank line, respectively. The bore in the middle of the block contains both check valves, which are situated one after another. The node volume V_Y is between the two check valves and the small skew bore to the upper left is the connection to the inductance pipe. The bigger two skew bores are the connections to the pressure attenuators at the output of the converter, since here two attenuators at the output are intended. In the exploded view of Fig. 2.29 all different components including the inductance are shown. The introduced design of the converter allows a multiple arrangement of several HBCs in

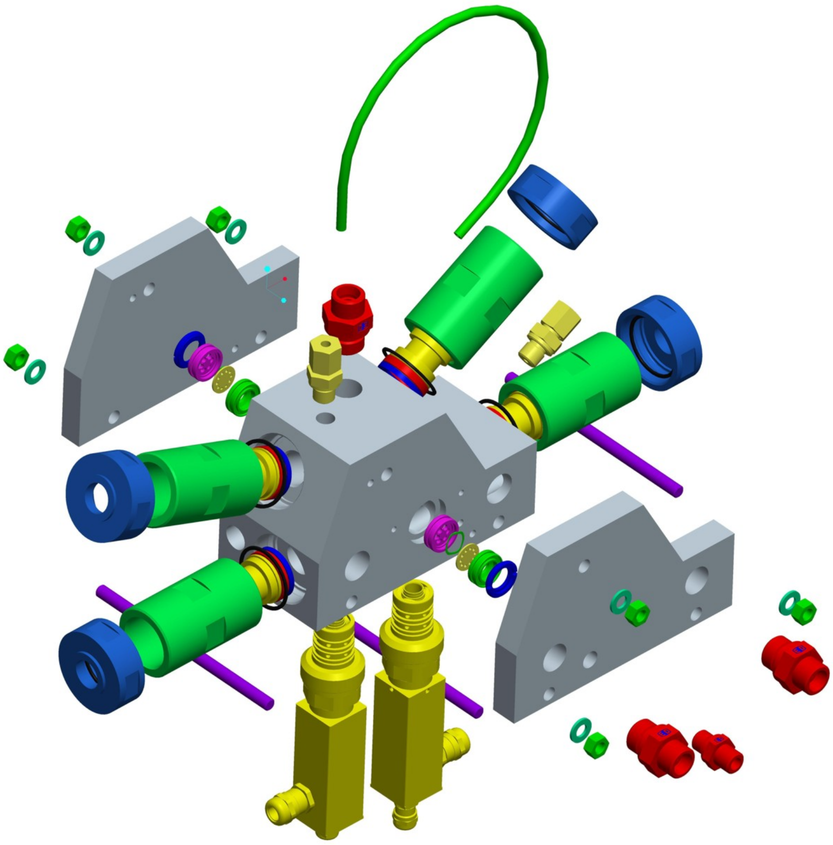

Figure 2.29.: Exploded view of the compact converter design

the form of a stack like in Fig. 2.30, which shows the potential for a compact control unit for several actuators.

2.3.8. Auxiliary Equipment

Fast switching hydraulic systems require some additional equipment to enable energy saving and recuperation, respectively. First, the tank system has to be pre-pressurised to avoid cavitation during the suction phase. Therefore, a certain tank pressure above the ambient pressure has to be provided. One possibility of realisation would be the use of a simple pressure relief valve, like depicted in Fig. 1.13. The dynamics of this relief valve has to be much slower than the switching frequency to avoid oscillating effects due to the switching process. Its size depends on the waste flow rate, i.e., the difference between the released and the flow drawn in the suction phase. The realisation of the tank pressure by a pressure relief valve is not sufficient for energy saving cycles, because a certain amount

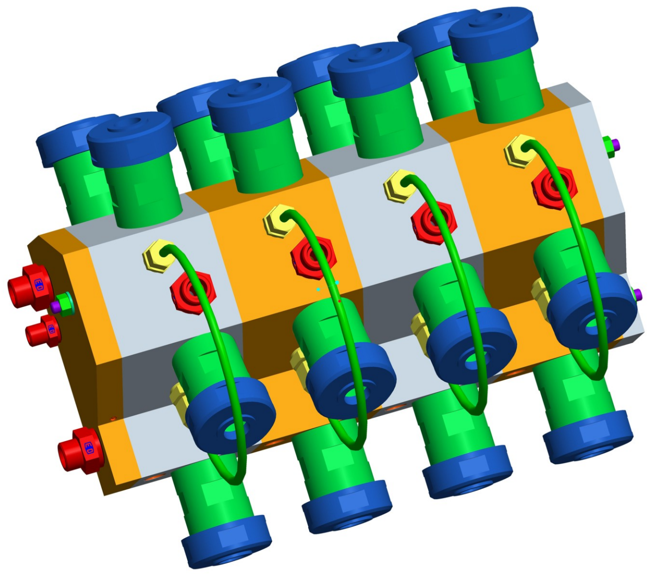

Figure 2.30.: Stack of several converters

of fluid has to be provided in the suction phase. For this purpose at least one additional accumulator in the tank line must be installed. If the amount of fluid in the corresponding decoupling accumulator is sufficient for the largest load cycle, no further accumulator has to be spent. However, in this case the occurring pressure descent during emptying phases must not fall below a permitted value, to prevent an underrun of the pressure below the pre-loaded gas pressure. But not only on the tank side additional capacity has to be provided, also at the supply pressure side additional volume is needed for collecting the returned amount of fluid in the recuperation phase.

2.4. Pressure Attenuators

The major drawback of the use of gas loaded accumulators for pressure attenuation is the loss of stiffness in hydraulic systems, which constitutes a great advantage of hydraulic drives. One possibility to compensate this disadvantage are control strategies to overcome the softness of the system, at least partially. Another option is to replace the accumulator by another compensator device, that is stiffer than a gas spring, but which provides the same degree of pressure attenuation. To give an idea how this could happen a short overview about common hydraulic compensators will be presented in the following. The attenuators presented in this section have to be tuned to a certain frequency and, thus, they are basically qualified for pressure attenuation in PWM controlled switching systems with a nearly constant switching frequency.

2.4.1. Helmholtz Resonator

The device illustrated in Fig. 2.31 is called a Helmholtz resonator, which is a very simple method for compensating pressure pulsations at a certain frequency. By the neglect of

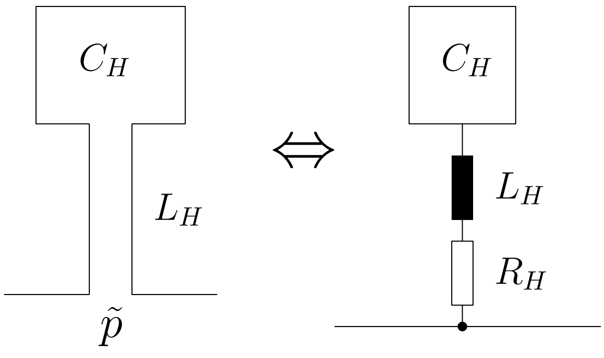

Figure 2.31.: Helmholtz resonator

the static pipe resistance R_H the operating frequency is determined by

$$\begin{aligned} \omega_H &= \sqrt{\frac{1}{L_H C_H}} \\ &= \sqrt{\frac{E_{oil} d_H^2 \pi}{4 V_H \rho l_H}} \end{aligned} \tag{2.61}$$

with the major design parameter V_H the volume of the resonator chamber, d_H the diameter and l_H the length of the inductance pipe. The degree of pressure attenuation has to be adjusted by the capacity, i.e., the volume of the resonator. A minimum limit for the volume C_H is the under-run of the cavitation level of the pressure in the mentioned cavity due to the occurring pulsations. Since the resonator is based on concentrated hydraulic elements, the fulfillment of the necessary assumptions for an adequate lumped modelling have to be checked properly.

2.4.2. Vibration Compensator

The concept of the vibration compensator, as depicted in Fig. 2.32, was introduced in [27] and its operating principle is quite similar to the Helmholtz resonator. The main

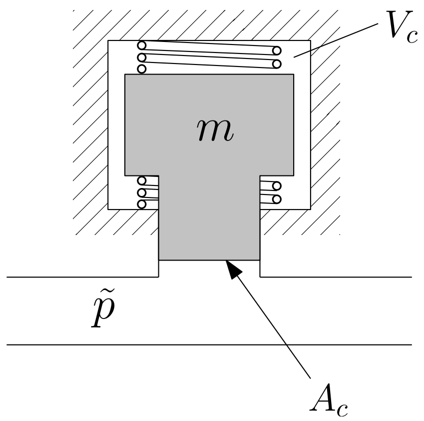

Figure 2.32.: Vibration compensator

difference is that the inertia is not realised by a hydraulic pipe, but by a high density solid body. This offers a more compact realisation of the compensator. The relevant spring of the oscillator is represented by a hydraulic cavity $C_c = \frac{V_c}{E_{oil}}$. Both mechanical springs in Fig. 2.32 are just for centering the mass in a defined rest position. The very basic design is determined by

$$\omega_c = \sqrt{\frac{A_c^2 E_{oil}}{V_c m}}. \tag{2.62}$$

Also the degree of attenuation has to be adjusted by the parameters and avoidance of cavitation has to be assured.

2.4.3. $\lambda/4$ - Compensator

The most simple compensator is the $\lambda/4$-side-branch resonator as depicted in Fig. 2.33, which consists only of a well dimensioned pipe line. The concept utilises the wave propagation effect in a hydraulic transmission line at its first natural frequency

$$f_{\lambda/4} = \frac{\sqrt{\frac{E_{oil}}{\rho_{oil}}}}{4 l_p}. \tag{2.63}$$

Thus the operating frequency is only determined by the length of the pipe l_p, since the remaining parameters are preset. The degree of attenuation can be determined by the

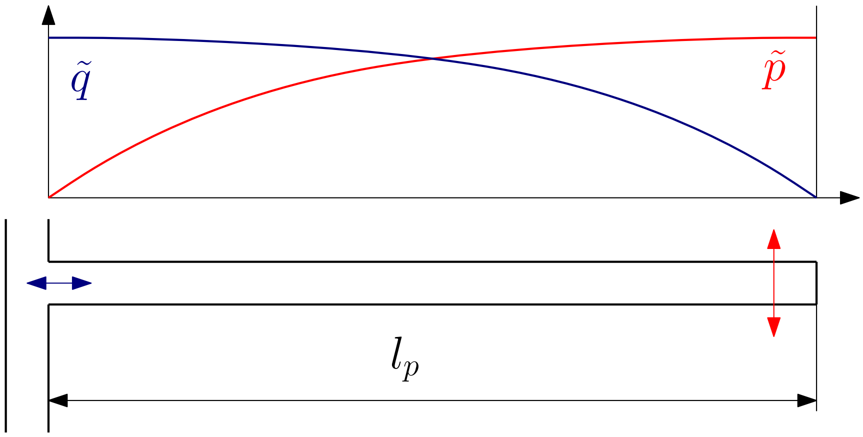

Figure 2.33.: $\lambda/4$-side-branch resonator

pipe diameter d_p, which influences the impedance

$$Z_0 = 4\frac{\sqrt{E_{oil}\rho_{oil}}}{d_p^2\pi}, \tag{2.64}$$

at least in case of neglecting the pipe friction. To avoid cavitation the pipe diameter must be sufficiently large. But, the striking simplicity of the $\lambda/4$-side-branch resonator is contrasted by its dimension. In today's feasible switching frequencies of about $100\,Hz$, a quite unhandy pipe length in the range of about $3\,m$ would be required.

3. Basic Experiments

The first series of experiments deals with the verification of the basic operating principle of the hydraulic buck converter. The main intention was to show the potential for energy saving and to collect experience for further development steps. Three different prototypes were under investigation, which were named *HBC010*, *HBC020* and *HBC030*. The prototype *HBC020* was consecutively improved in two further developing steps. The names of the corresponding subversions are *HBC021* and *HBC022*. In the following sections the experiments focusing on the efficiency gain of these different converter prototypes are reported.

3.1. First Prototype

The very first experiments were carried out with a converter according to Fig. 2.4. The converter was operating at a switching frequency of $50\,Hz$ and the load was an orifice, adjustable by hand. The configuration was designed only for forward flow direction. The corresponding test stand is illustrated in Fig. 3.1 and detailed information can be found in [23]. The switching valves of the *HBC010* were so called comb valves, which had been

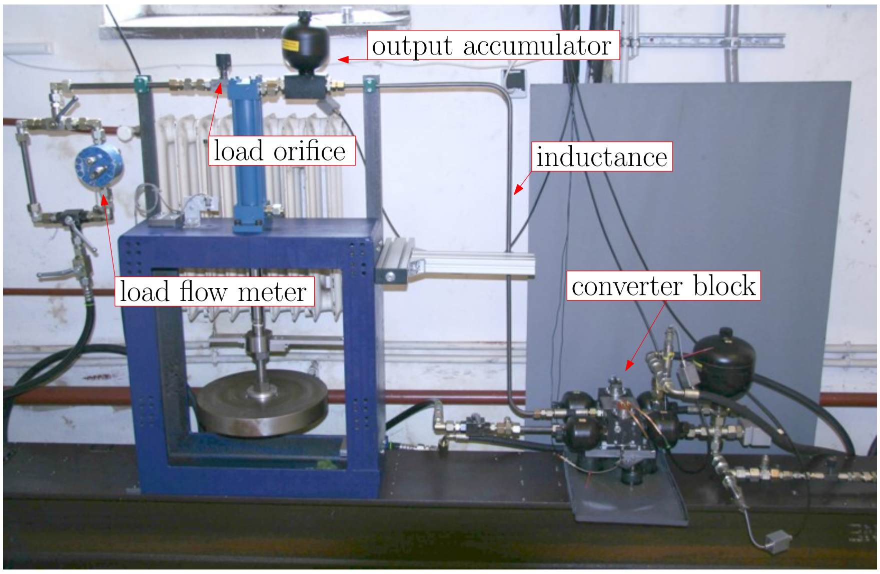

Figure 3.1.: Test stand of the *HBC010*

introduced before and are depicted in Fig. 2.19. This prototype of the HBC did not have any check valves, thus, both switching valves had to be pulsed alternately. For a correct timing of the switching the measurement of the spool positions of both valves was necessary. The original valves did not provide a spool measurement, thus, they had to be equipped with such a measurement device. In Fig. 3.2 the configuration for calibrating the position sensors of the valves is illustrated. The spool stroke of the used valves was

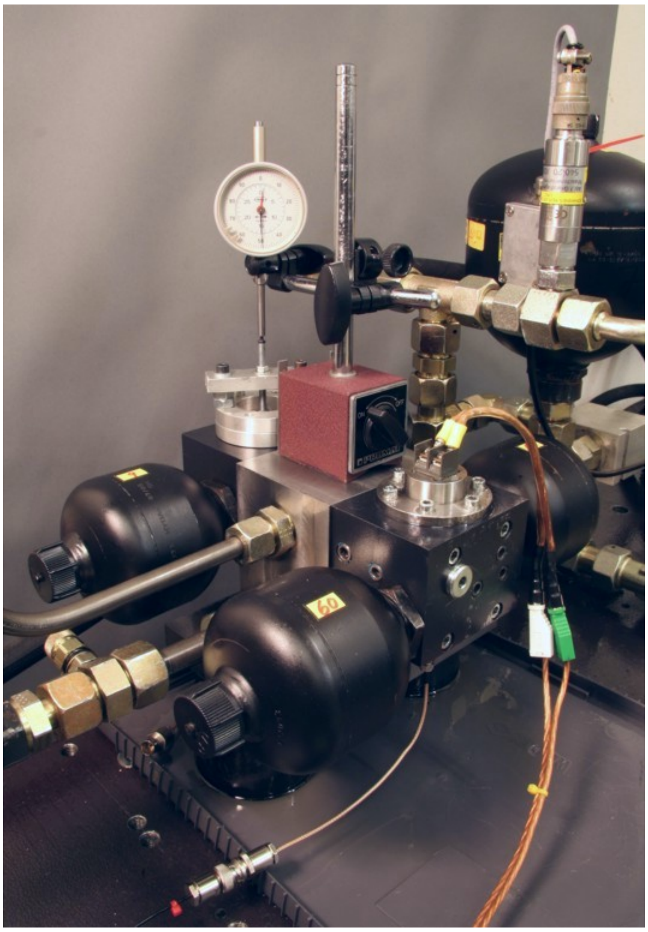

Figure 3.2.: Calibration of the spool position measurement at the *HBC010*

$0.5\,mm$ and the valve overlap was 50% of the full spool stroke. For an optimal operation of the converter both switching valves had to be synchronised accurately, such that when the metering edge of one valve comes into overlap, the metering edge of the other valve has to get out of overlap. It was very important to assure, that both valves were not closed at the same time to prevent cavitation at the beginning of the suction phase. On the other hand also a short circuiting should be prevented, i.e., when both valves are out of their overlap at the same time. In such a case a large cross flow occurs, which result in a dramatic loss of efficiency. Such a tuning of the valves is quite difficult, because the accurate timing of the switching is a fairly sensitive process. In Fig. 3.3 the valve opening and the current of the solenoid at a duty ratio of $\kappa = 50\%$ are illustrated. In the upper diagram a certain boost current can be identified, which is necessary to achieve a fast

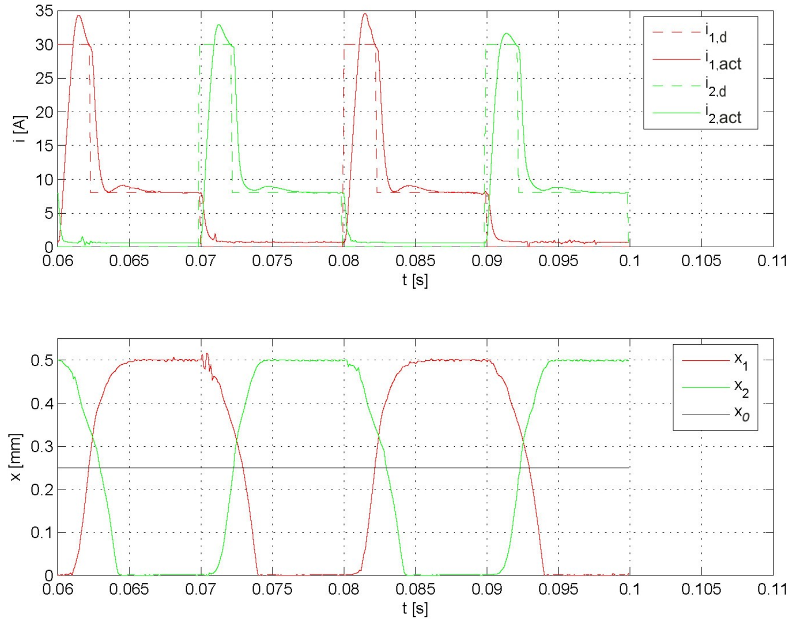

Figure 3.3.: Valve currents and spool positions

movement of the spool and, thus, a short switching time. When the valve is completely open, the current is reduced to a minimum to provide the necessary magnetic force to keep the valve open for the intended duty ratio. It is a matter of fact, that both switching valves must be pulsed alternately, since this prototype does not employ check valves for energy saving and recuperation. But it is remarkable, that the total electric power consumption of both valves is independent of the duty ratio κ, because at every point in time at least one switching valve is magnetically actuated. But on the other hand, if higher switching frequencies are intended, the electric power consumption will grow linear with frequency, which scales with the number of spool movements and, thus, the current boosts of the solenoids. For an alternating operation of the valves like depicted in Fig. 3.3 at a switching frequency of $50\,Hz$ an electric power of about $300\,W$ is necessary, which is too high for a reasonable application. Thus, also a reduction of the electric power consumption is a major objective of further switching valve generations.

For efficiency investigations the measurements of supply pressure, tank pressure and load pressure and, furthermore, the flow rates from pressure supply and to the load were necessary. Since the valve block of the HBC is representing a Kirchhoff node, the corresponding mean flow rate from the tank could be calculated by

$$q_T = q_L - q_S. \tag{3.1}$$

It was assumed, that the load flow rate always exceeds the flow rate from the supply line. The corresponding parameters and conditions of the test stand are listed in Tab. 3.1. In the following, the procedure of the efficiency measurements will be explained. The measurements were carried out at a constant duty ratio. Then the load orifice was

Parameter	Value
switching frequency	$f_S = 50\,Hz$
duty ratio	$\kappa = 50\,\%$
nominal flow rate of switching valves	$Q_N = 45\frac{l}{min}@5bar$
pipe length	$l_p \approx 1.8\,m$
attenuator size	$V_A = 0.75\,l$
pre-pressure of attenuator	$p_{0_G} \approx 50\,bar$
supply pressure	$p_S = 100\,bar$
tank pressure	$p_T = 30\,bar$

Table 3.1.: System parameter and conditions of measurements with the *HBC010*

opened by hand and thus the flow rate through the converter increased. The load orifice was opened in several steps by hand, such that in each step a quasi steady state of the converter could be observed. At a certain opening of the load orifice, a suction from the tank could be verified, because the measured flow rate at the load exceeded the flow rate from the pressure supply line. In this phase, a certain amount of fluid is drawn from the tank line and, thus, was raised from a lower to a higher pressure level by the surplus of kinetic energy in the main inductance of the converter. In such a case the HBC operates at a higher efficiency than a proportional drive. On the other hand, when the flow rate through the supply line is larger than the load flow rate, then a cross flow rate of the difference of both flow rates directly from pressure supply to tank occurs, which is a very inefficient operating area. The efficiency of the converter was calculated by the actual input to output steady state power ratio. With Eq. (3.1) this is represented by the following formula

$$\begin{aligned}\eta_{PWM} &= \frac{p_A q_L}{p_S q_S + p_T q_T} \\ &= \frac{p_A q_L}{p_S q_S + p_T\left(q_L - q_S\right)}.\end{aligned} \tag{3.2}$$

The corresponding efficiency of the resistance control reads

$$\eta_{prop} = \frac{p_A}{p_S}. \tag{3.3}$$

The results of this very basic experiment can be examined in Fig. 3.4, where the measured flow rates, the pressure signals and the actual efficiency are illustrated. The depicted signals are quite noisy due to the switching of the valves. For an improvement of the signal quality all measured signals will have to be filtered or, at least, they have to be averaged over one switching cycle, which is not done here, but at later experiments.

The investigations showed an improvement of the efficiency in a certain operating range, hence proved, that a basic goal of this switching converter is achieved. But, a converter

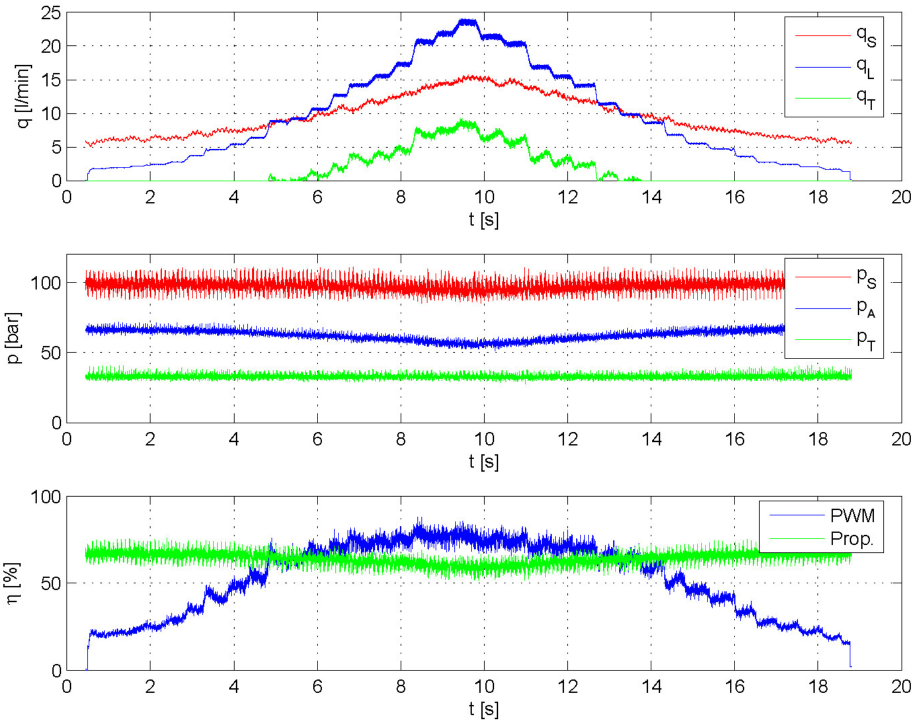

Figure 3.4.: Basic results of the first experiments

of this type, i.e., an HBC with two alternately pulsed valves, is not appropriate for industrial applications. The large efforts for valve timing, which requires spool position measurement, and the efficiency reduction due to cross flow at lower load flow rates ask for an improvement of the converter. Furthermore, the mentioned electric power consumption of the switching valves must be reduced. Both drawbacks can be decisively reduced by the use of fast check valves, which will be introduced in the following section.

The *HBC010* always operates in pressure control mode. If this property is essential for a certain application, then the converter should not be realised with two separate switching valves, but with a configuration according to Fig. 3.5, where the timing of the synchronous switching of both valve is enforced mechanically by the valve design.

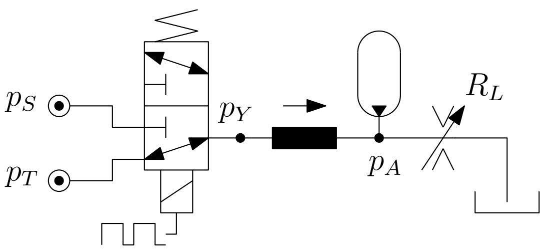

Figure 3.5.: HBC employing a 3/2-switching valve for pressure control

3.2. Improved Test Rig

The next prototype generation *HBC02x* was based on the experiences with the *HBC010*. The HBC *02*-series of hydraulic buck converters is characterised by the use of passive check valves for energy saving and recuperation. Therefore, no tuning of the switching edges of the valves and, thus, no measurement of the spool position is necessary. This improvement is an important step towards industrial applicability. Furthermore, with this design a number of parasitic effects could be decisively reduced. One knowingly remaining parasitic effect, the big node volume V_Y, can be adjusted in some range to measure its effect experimentally, to confirm in this way theoretical results and to obtain a save knowledge for an optimal converter design concerning this design parameter's influence.

3.2.1. Design of an HBC with Check Valves

The converter housing basically consists of three separated blocks, like depicted in Fig. 3.6. The transparent block in the middle comprises the node point Y. The two remaining

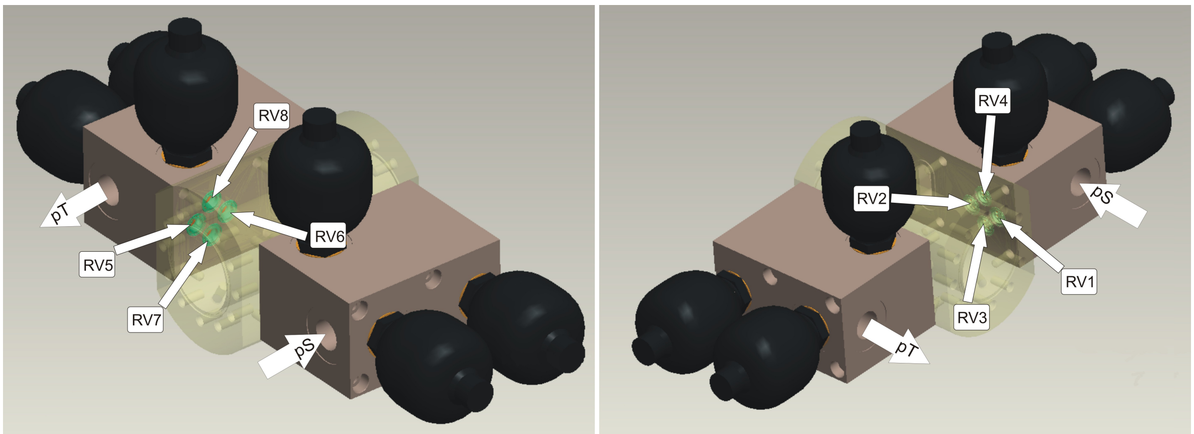

Figure 3.6.: 3D CAD drawings of the HBC with check valves

valve blocks incorporate all corresponding switching valves. They connect the converter to supply and tank pressure. The active switching valves are the same of the first HBC prototype, but they are implemented as a valve cartridge. In contrast to the first prototype this design uses a number of check valves ($RV1, \ldots, RV8$) for energy saving issues. The applied check valves follow the design by [29], which is depicted in Fig. 2.22. There are 4 parallel arranged check valves in each valve block, i.e. in total 8, to obtain a sufficiently high overall nominal flow rate. The inductance is realised by a straight pipe, which is connected to the front of the central converter block. In fact, this form of the inductance increases the overall space requirements, but its flow conditions are relatively simple and well understood. Existing dynamic mathematical models of a laminar flow through straight transmission lines can be used for simulation and parameter identification, respectively. At each valve block three separate ports are provided for decoupling by pulsation attenuation accumulators. It is not intended to place an accumulator at each of those provided ports, but the many ports just offer to study the role of accumulator positioning for an optimal operation. The experiments taught, that in most cases one accumulator is sufficient. In this context it is has to be mentioned, that the inlet of the used membrane accumulators was rebored to get a sufficiently large inlet bore for high frequency attenuation. At the output of the converter another effective bladder attenuator was placed to smoothen the pressure ripples due to switching since no adequate piston accumulators were available at that time. A schematic of the experiments is depicted in Fig. 3.7. The test rig offers the possibility to select either a flow control valve or a differential

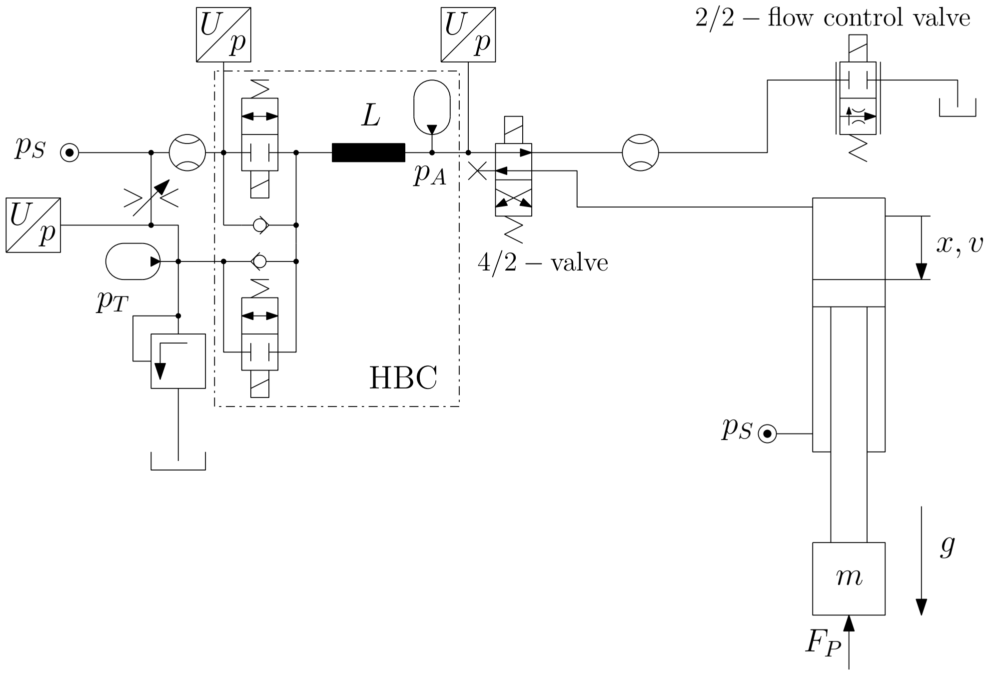

Figure 3.7.: Test rig diagram of *HBC020*

cylinder in plunger a mode as converter load. Switching between these two loads was done by a 4/2-switching valve, which was large enough, to prevent relevant pressure loss. Thus, on the one hand the performance characteristics of the converter can be investigated by presetting different working points by the flow control valve, and on the other hand drive experiments with a differential cylinder can be carried out. The test stand is illustrated in Fig. 3.8 and the used components with the corresponding major parameters are listed in Tab. 3.2. At this point it has to be remarked, that the supply pressure of 150 *bar* was limited by the design of the converter block. A deficiency of the construction provoked a damage of the *O*-ring seal between the supply pressure sided valve block and the central converter block due to a deficient, i.e. too soft bolted connection. This effect appeared at least if the supply pressure was higher than 150 *bar*. The necessary improvements to avoid this shortcoming were considered at later prototypes.

The first experiment with the *HBC020* prototype was the recording of the characteristic

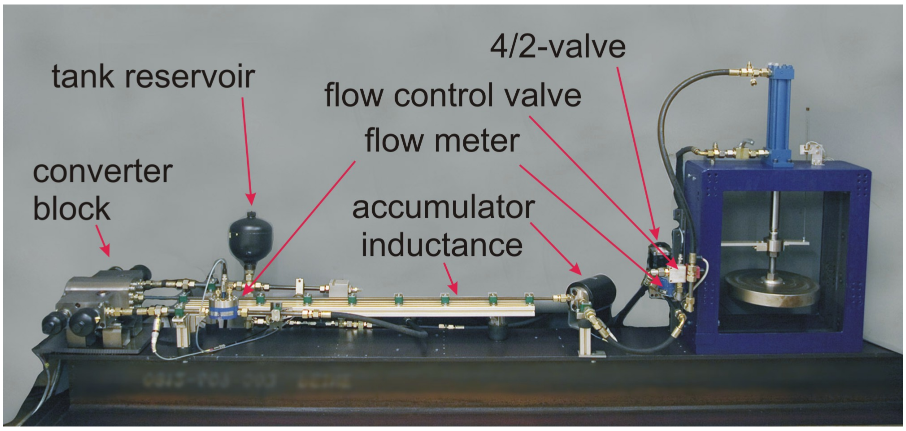

Figure 3.8.: Test rig of *HBC020*

Parameter	Value	Remark
switching frequency	$f_S = 50\,Hz$	
duty ratio	$\kappa = 20,\ldots,50\,\%$	
nominal flow rate of switching valves	$Q_N = 45\frac{l}{min}@5bar$	[50], cartridge
nominal flow rate of check valves	$Q_N = 4\times 30\frac{l}{min}@5bar$	[29]
pipe length	$l_p \approx 1.7\,m$	straight
attenuator size	$V_A = 0.6\,l$	`www.pulseguard.com`
pre-pressure of attenuator	$p_{0_G} \approx 50\,bar$	
supply pressure	$p_S = 150\,bar$	limited by design
tank pressure	$p_T = 15\,bar$	
ratio of cross-sections of the cylinder	$\frac{A_1}{A_2} = 2$	Rexroth
dead mass	$m \approx 50\,kg$	

Table 3.2.: Relevant parameters of the experiments on the *HBC020*

diagram of the converter in the forward flow direction. The flow control valve was selected as the corresponding load. For the experiment a grid of several operating points had been defined. A single working point is characterised by a duty ratio κ, a flow rate q_L - preset at the flow control valve - and the corresponding load pressure p_A. The characteristics were measured under steady state conditions by setting a constant duty ratio κ and a constant preset of the flow control valve. For the analysis of the converter characteristics the pressures p_S, p_T and p_A and the flow rates q_S and q_L had to be measured. The tank sided flow rate was evaluated in accordance to Eq. (3.1). Hence, the efficiency of the HBC can be calculated according to Eq. (2.11) by averaging the relevant signals over one switching period. For an adequate comparison a fictive proportional drive was opposed to the measurements of the HBC. The relevant pressure signals of the switching configuration were used to calculate the corresponding efficiency according to Eq. (2.14) of a proportional drive, which would provide the same power and flow rate. For correctness of the analysis, also the efficiency of the proportional drive had to be averaged over one switching period. The significant increase of efficiency and, thus, the potential benefits of this switching technology is clearly pointed out by Fig. 3.9. There, the main results are summed up by four diagrams, at least in the investigated operating range. In the

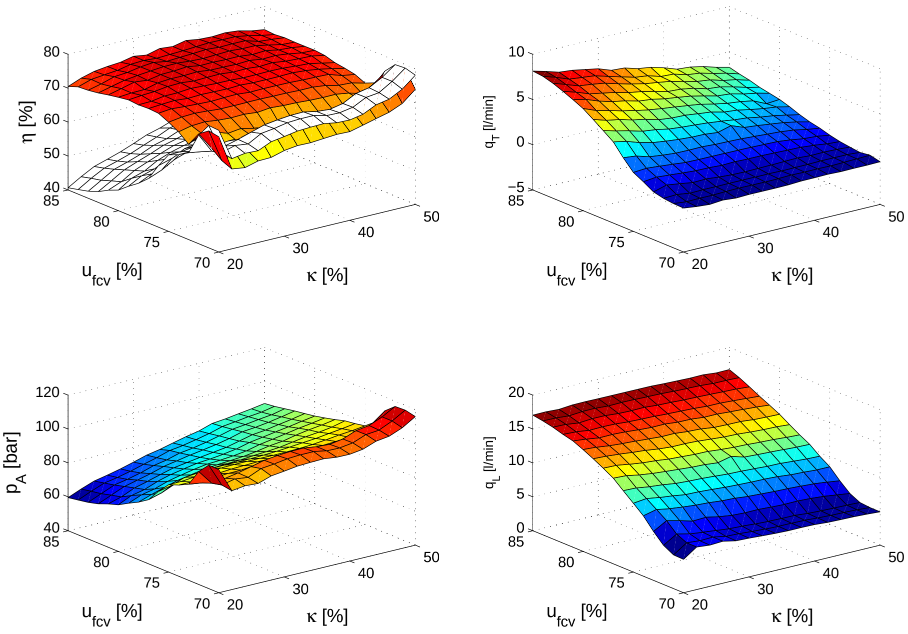

Figure 3.9.: Characteristics of the *HBC020*

upper left diagram a comparison between the efficiency of the HBC (coloured surface) and a corresponding proportional drive (white surface) is shown. Since the proportional efficiency is simply the quotient of the load pressure to the supply pressure (compare Eq. (3.3)), the corresponding white surface is simply scaled to the surface of the occurring load pressures, which is depicted in the lower left diagram, of course under the assumption of a constant supply pressure. In both diagrams on the right the suction flow rate from tank and the load flow rate are illustrated. The limit of the operating area was bounded by the permitted minimum load pressure due to the gas pre-pressure of the accumulator at the output of the converter. At the experiments a maximum efficiency improvement of 30 % occurred. The deficiency in both left diagrams at low load flow rates is caused by the poor controllability of the load sided flow control valve, at least in this operating area.

The next experiment considers the performance of a differential cylinder with a dead load, which is controlled by an HBC. A representative step response of the piston velocity is illustrated in Fig. 3.10. In the lower diagram the actual efficiencies of the HBC and the corresponding fictive proportional drive are opposed. Due to the accumulator at the output of the converter, the resulting system is rather soft. Thus, the comparison is only valid after the transient acceleration effect, i.e., in a steady state velocity of the piston. However, an increase of the efficiency of more than 20 % could be demonstrated, at least

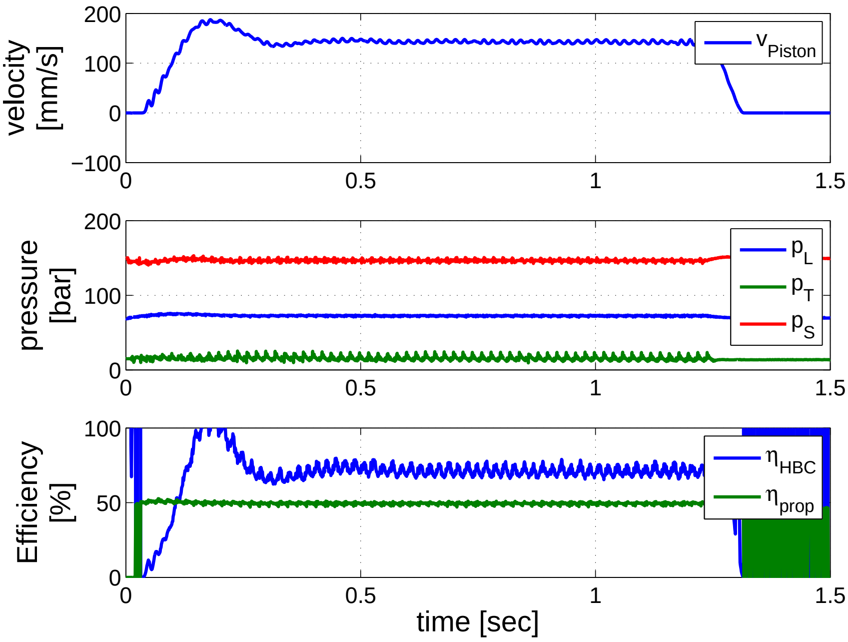

Figure 3.10.: Extending cylinder movement with *HBC020*

in this working point, which corresponds to an extending motion of the cylinder without any load force. Further details concerning the experiments with this test stand can be found in [5, 13].

3.2.2. Analysis of Different Inductance Geometries

For an industrial realisation not only efficiency is relevant, but also the converter's overall size. Especially for mobile applications the installation space is limited. Thus it is important to design a converter as compact as possible at maximum efficiency performance. The most unhandy component of the HBC, the inductance, is critical for efficiency.

The following considerations show the results of investigations on different inductance geometries. The least compact inductance is the straight pipe like depicted in Fig. 3.8. A more compact design of the inductance is a single loop. The number of windings can be increased further to improve compactness. Four different coil geometries were investigated, as depicted in the Figures 3.11 to 3.14. To obtain a relevant comparison between the different coils, they must have about the same length as the straight pipe. Thus, the difference in performance is only influenced by the curvature of the individual coil. In fact, an increase of the resistance of the inductance and, hence, of the losses is expected. The purpose of the experiments is to quantify these losses and to determine the trade off between compactness and efficiency. In the following, the results of each coil are assigned to a different colour as listed in Tab. 3.3. The experiments were carried out under identical conditions like the characteristic measurements described in the previous section. Thus, the working points were defined by the duty ratio κ and the load flow rate q_A. In

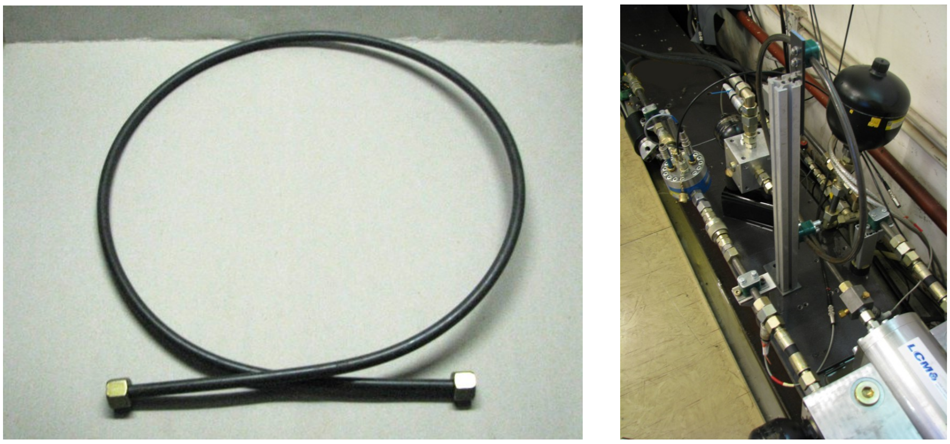

Figure 3.11.: Coil with one winding

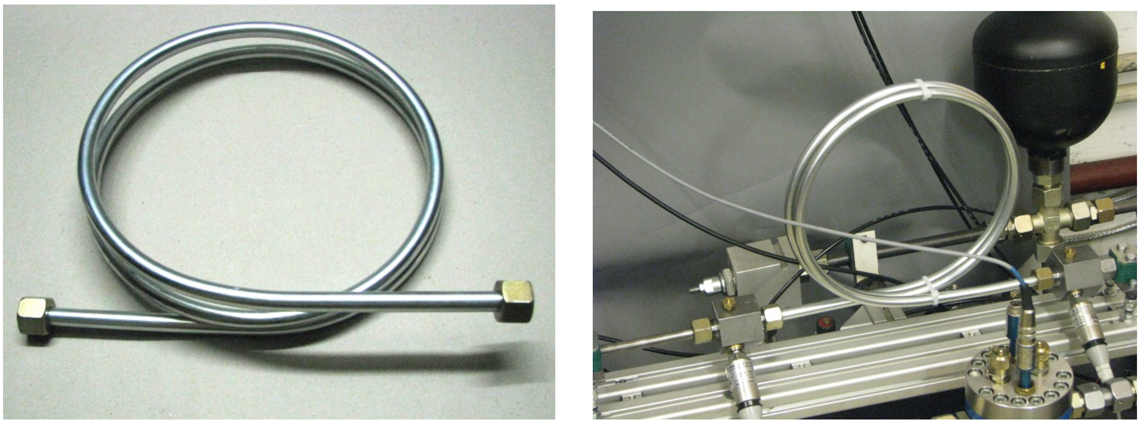

Figure 3.12.: Coil with two windings

contrast to the measurements before, the load flow rate was closed loop controlled by a PI-controller. With a controlled load flow rate and a measured load pressure the analysis of the different power characteristics was possible. The relevant grid of operating points was determined by the configuration with the largest pressure losses over the inductance, where the load pressure approaches the pre-pressure of the accumulator at the converter output. This boundary was kept equal for all the measurements. But, this does not mean that the investigated maximum flow rate is a limit at all. This simply depends on the necessary load pressures and, thus, on the pre-pressure of the load attenuator. For the experiments the same accumulators were used as for the measurements with the straight pipe inductance, because piston accumulators were not available at that time.

The resulting efficiency characteristics are depicted in Fig. 3.15. The absolute efficiency values of the different coils are illustrated in the left diagram. The measurements confirm the expectation, that the straight pipe achieves the maximum efficiency, followed by the coil with one winding. It is noteworthy, that the coil with 7 windings could achieve a higher efficiency than the coils with 2 or 4 windings. But, in fact, the effective length of the 7-windings coil was unfortunately a bit shorter than the remaining coils due to

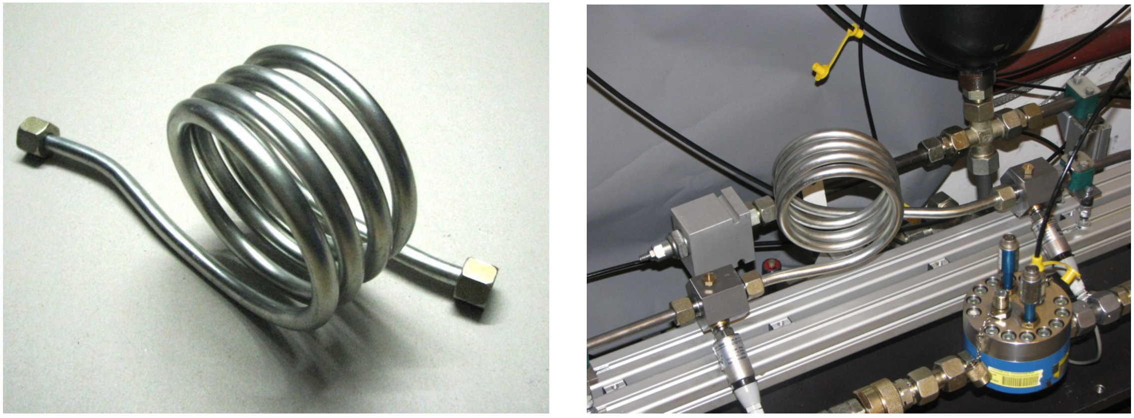

Figure 3.13.: Coil with four windings

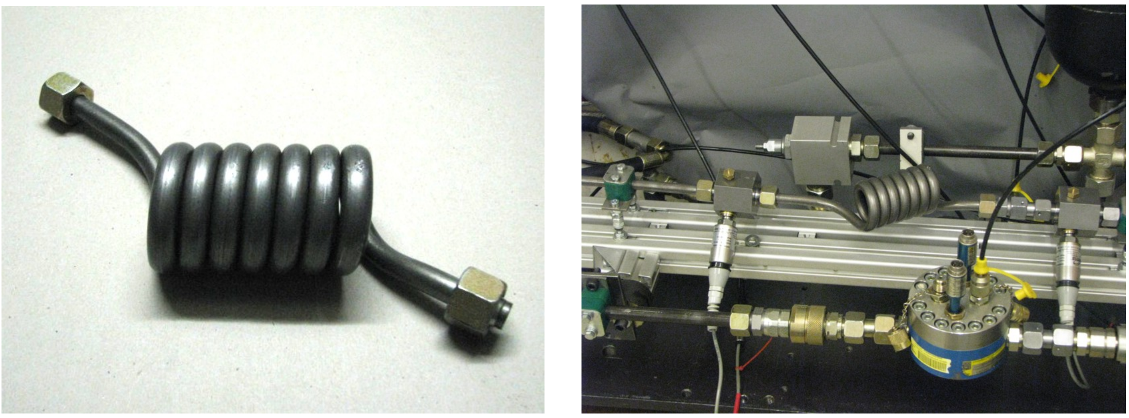

Figure 3.14.: Coil with seven windings

some complications in the spooling process. Even more remarkable is the fact, that the deviation of the coils with 2, 4 and 7 windings is quite low. Actually, the right diagram is more relevant, where the efficiency improvement in comparison to the corresponding proportional hydraulics of each measurement is depicted. As expected, the straight pipe delivers the highest improvement and, as remarked before, the coils with 2, 4 and 7 windings achieve nearly the same efficiency improvement.

The left diagram of Fig. 3.15 also reflects the influence of the node capacity C_Y on the efficiency. Since all measurements were carried out with the same converter block configuration, also the node volume V_Y was the same. The sharp bends in the different efficiency surfaces indicate the transition between pure throttling and an energy saving operation of the converter. In the latter case the mean flow rate through the converter and, thus, the impulse of the inductance, are high enough to discharge the node volume below the tank pressure within the available time of the switching process. The converter was designed for a number of different experiments and had to be flexible enough for the installation of other inductances, like a coil inductance which was integrated in the block[1]. Therefore, the node volume is rather high and in turn its parasitic effect. Basically it is

[1] This will be considered later in Subsection 3.2.3.

Configuration	Windings	Coil Diameter	Colour
1	0	∞	green
2	1	$\approx 60\ cm$	blue
3	2	$\approx 25\ cm$	cyan
4	4	$\approx 8\ cm$	magenta
5	7	$\approx 3\ cm$	red

Table 3.3.: Colour assignments of different coils

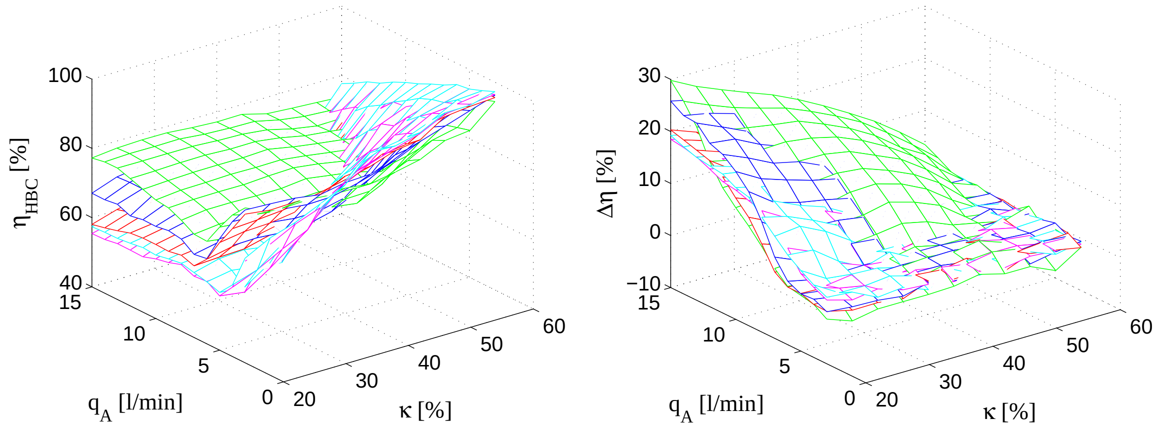

Figure 3.15.: Resulting efficiencies with different coils

not difficult to design a converter with a lower node volume for a better efficiency.

In Fig. 3.15 the efficiency of the different configurations is shown as a function of the load flow rate q_A and the duty ratio κ. Due to the fact, that the load flow rate was closed loop controlled, the efficiency can also be specified by the characteristic power dimensions p_A and q_A. In Fig. 3.16 the efficiency-map of the investigated operating points is depicted as a function of load pressure and load flow rate and, thus, of the output power of the converter. There, the black mesh represents the efficiency of a proportional valve. Unfortunately many operating points suffer from the large node volume as mentioned above and are consequently lying on the proportional surface. By a reduction of the node capacity one can expect higher efficiencies at higher power ratios. Another illustration of the power characteristics of the different configurations is depicted in Fig. 3.17, where the load flow rate is a function of the load pressure. The different lines of the characteristic fields represent the load power at a constant duty ratio κ. In this figure the transition from pure throttling to energy saving operation is indicated by the sharp bend in the characteristics of each configuration.

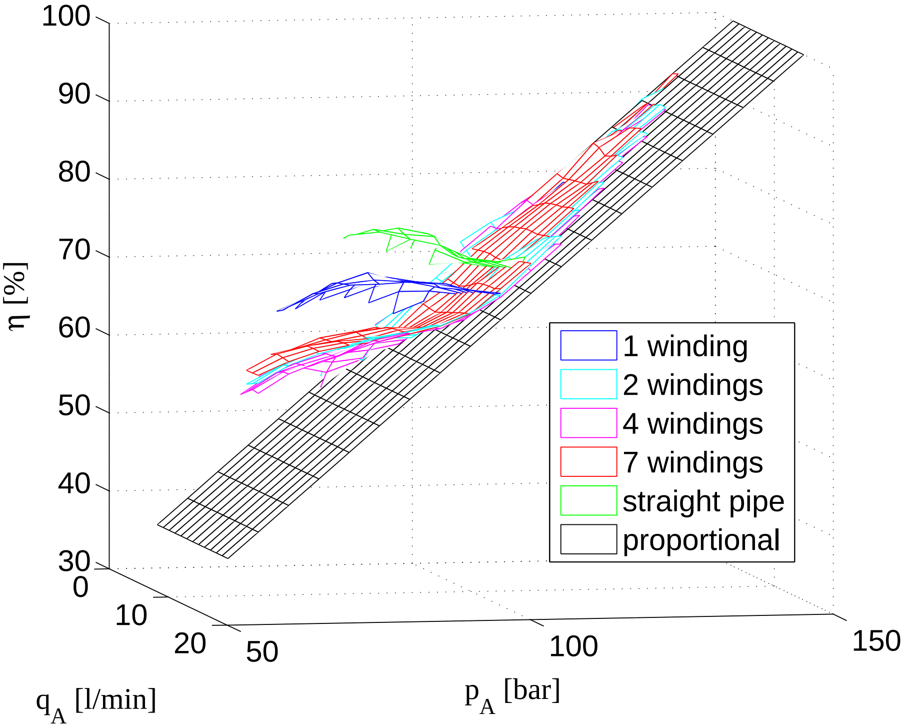

Figure 3.16.: Characteristic diagram of the different coil geometries

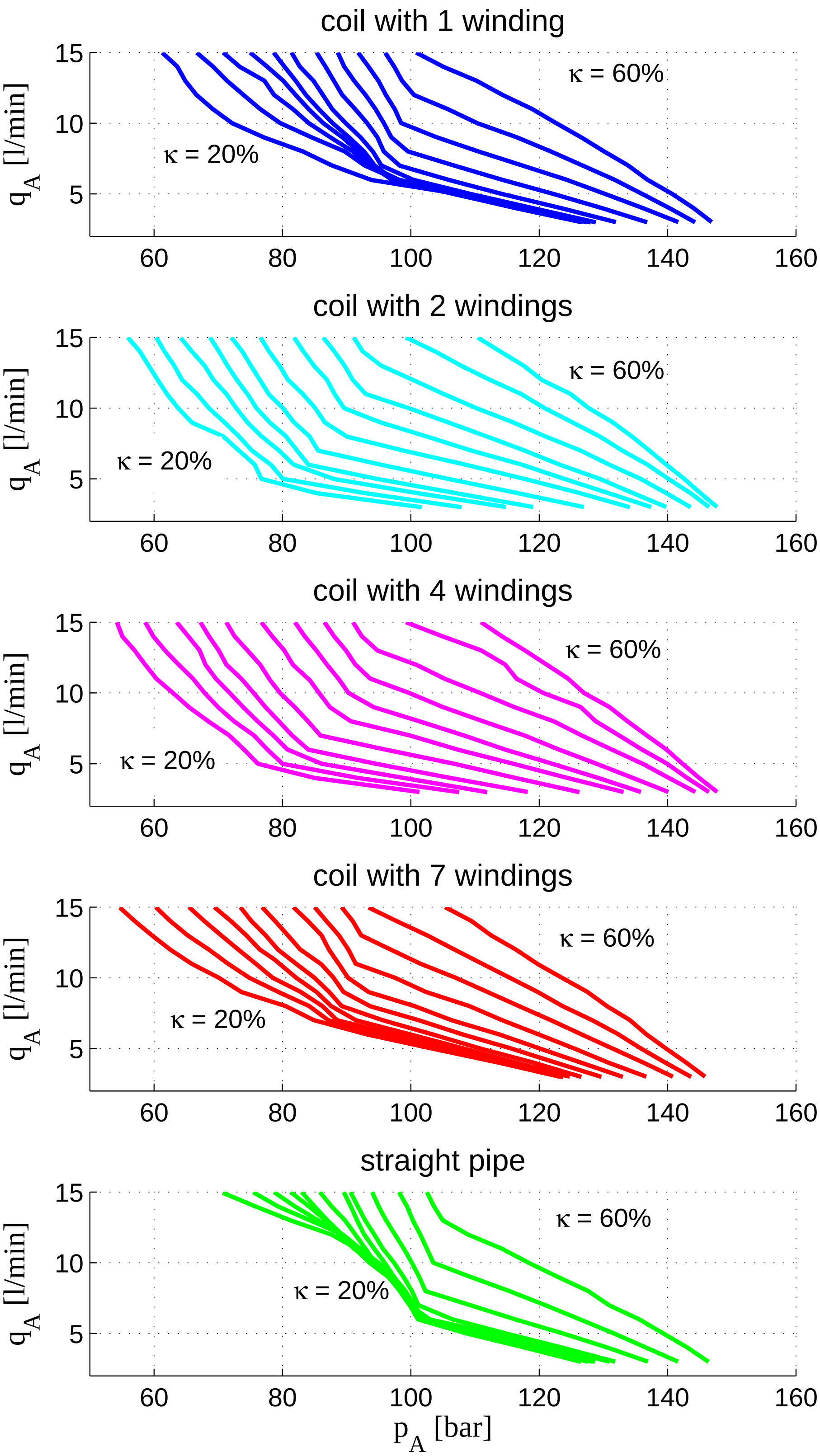

Figure 3.17.: Resulting power characteristics of the investigated coils

3.2.3. Compact Design of the Inductance

The converter block of the *HBC02x*-series was designed in a way, that a housing of the inductance is basically possible to achieve a most compact arrangement. In the following, two different realisations are presented, a threaded spindle and a compact coil inductance.

3.2.3.1. Threaded Spindle Inductance

The threaded spindle inductance is the characterising component of the prototype *HBC021*, which is depicted in Fig. 3.18. A thread (yellow) is situated inside a sleeve (green), which

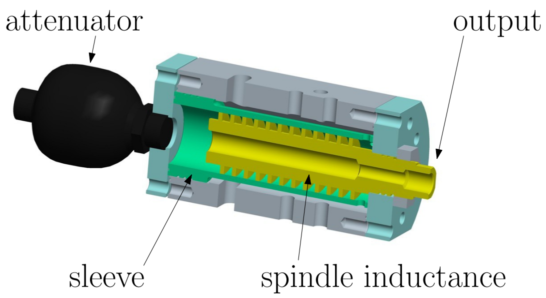

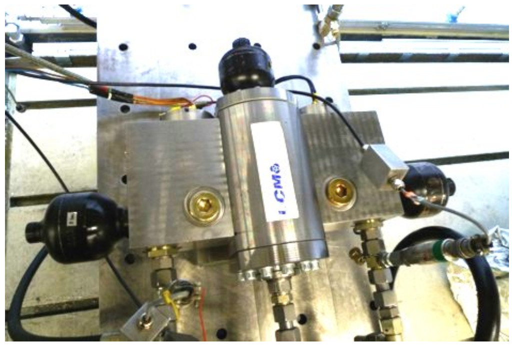

Figure 3.18.: Prototype *HBC021* with threaded spindle inside the valve block

is placed inside the converter block. The volume surrounding the sleeve is the node capacity C_Y, which is connected to all the switching valves. The node volume of this configuration is as large as of the *HBC020*. On the right end of the sleeve several bores provide the entry to the inductance. In forward flow direction the inductance thread ends at the pressure attenuator (black). A bore through the spindle directs to the output, which is connected to the consumer. The threaded spindle itself is put into the sleeve without any seals, because the gap resistance between the thread and the sleeve is much higher than the hydraulic resistance of one thread pitch. This fact enables a very comfortable assembling of the converter. The characteristic measurements on the *HBC021* were done as explained in Section 3.2.1 of the *HBC020*. The corresponding characteristics are illustrated in Fig. 3.19, where a maximum efficiency increase of 20 % in comparison to resistance control could be identified. Thus, a compact realisation of the inductance and, hence, a compact design of the converter is basically feasible, but is traded-off by a significant efficiency reduction. At this point it has to be mentioned, that the absolute values of the efficiency are certainly depending on the temperature of the oil. At higher oil temperatures the viscosity and, thus, the resistance will be lower. All illustrated measurements have been conducted at an operating state temperature of about 40°C.

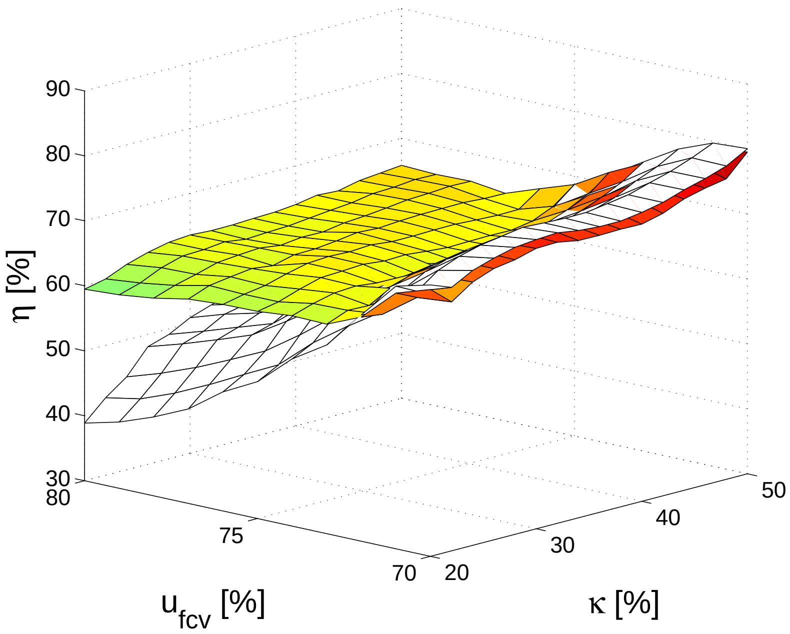

Figure 3.19.: Efficiency of *HBC021* with threaded spindle inductance

3.2.3.2. Coil Inductance

The application of a threaded spindle inductance promised a compact design of the converter. But the production of such a threaded inductance is quite expensive. To reduce the effort for mechanical production of the inductance, a pipe was coiled around a thorn on a lathe, to shape the inductance of the prototype *HBC022*. Afterwards, the coil was connected to the assembling shaft by hard-soldering. The resulting coil inductance is shown by Fig. 3.20. The coil was assembled in the same way as the thread of the *HBC021* inside

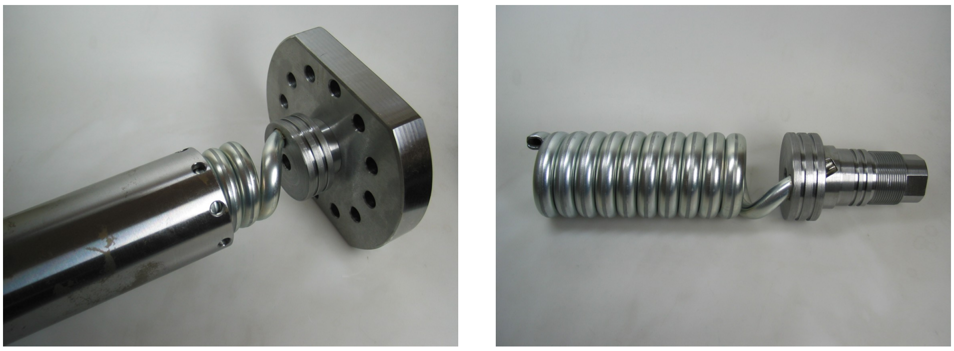

Figure 3.20.: Compact coil inductance of the *HBC022*

the sleeve, as illustrated in the left picture. The measured characteristics of the *HBC022* are depicted in Fig. 3.21. Comparing these results with those of the threaded spindle inductance in Fig. 3.19, the coil shows an even smaller efficiency. The difference of both characteristics is caused by the different hydraulic cross-section shapes of the inductances, since all other parameters and the conditions at both experiments were identical.

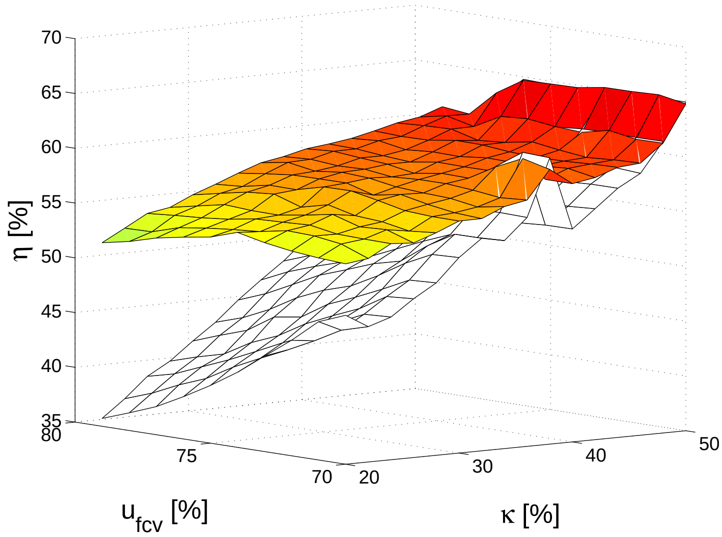

Figure 3.21.: Efficiency of the *HBC022* with compact coil inductance

3.3. Re-Design for Low Power Applications

In a next step a buck converter prototype for approximately 1.5 kW was developed, which was named *HBC030*. Low power hydraulic drives generally suffer from lower efficiency conditions than larger drives, because dissipative effects scale differently with power rating than productive effects. Also the relation between power and overall size is very disadvantageous at small scales. Therefore, this prototype's performance will be worse compared to larger power converters and constitutes a lower performance limit for properly designed systems. But, there exist a number of applications with the need of a small and energy efficient drive like autonomous robots as pointed out, for instance, in [10]. A possible design of such an HBC is introduced in Fig. 3.22, which was already discussed by [4]. The main functional specifications of this prototype are listed in Tab. 3.4. Certain properties

Parameter	Value	Remark
supply pressure	$p_S = 130\,bar$	supply power $P_S = 1.5\,kW$
tank pressure	$p_T = 5\,bar$	pressure relief valve
oil viscosity	$\nu \approx 20\,cSt$	Shell T 20
accumulators	$V_A = 0.04\,l$	piston type, Fig. 3.24
maximum load flow rate	$\bar{q}_{A_{max}} = 5\frac{l}{min}$	
inductance length	$l_p = 1.15\,m$	coil with 2 windings
hydraulic diameter of inductance	$d_p = 3\,mm$	
switching valves	$Q_{N_{SV}} = 10\frac{l}{min}@5bar$	Fig. 2.20
check valves	$Q_{N_{CV}} = 20\frac{l}{min}@5bar$	Fig. 3.23
switching frequency	$f_S = 100\,Hz$	

Table 3.4.: Functional specifications of the *HBC030*

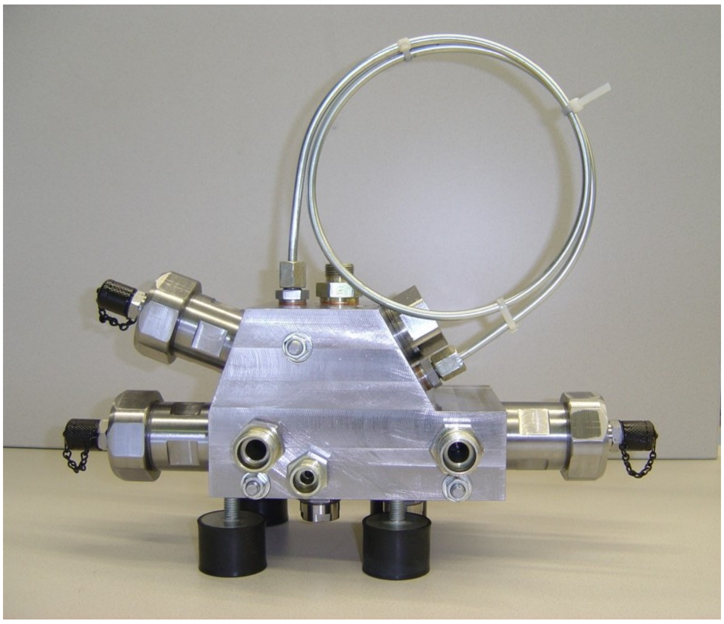

Figure 3.22.: The prototype *HBC030*

of the block design of this prototype have been already introduced in Subsection 2.3.7. A major design goal was a compact arrangement of all the valves to keep the node volume small. Furthermore, to achieve a lumped drive unit all components as valves, inductance, and pressure attenuator were required to be placed on the same block. This requires the inductance to have at least one winding. Moreover, the design should enable a multiple arrangement of several converters in a cluster, as already depicted in Fig. 2.30.

For this prototype also a new type of a plate check valve was tested. The previously mentioned check valve (see Fig. 2.22) turned out not to be very robust. Due to the extreme flow conditions in an HBC the spring arm of the check valve broke in several experiments with the previous prototypes. The requirement to manufacture the plate and the spring out of one piece was dropped. The resulting design was a separate valve plate actuated by a corrugated spring. The essential components of this check valve are depicted in Fig. 3.23. Due to its smaller power category, this converter operates at a

Figure 3.23.: Check valves for energy saving and recuperation of the *HBC030*

switching frequency of $f_S = 100\,Hz$, which is twice that of the previously investigated prototypes. Thus, also the check valves had to switch sufficiently fast. Due to a lack of experience, the dynamic response of this new type of check valves was not thoroughly known, at that time. If the check valves do not switch sufficiently fast, a drawback in efficiency had to be expected.

Another innovation in design of the *HBC030* was the use of piston accumulators, which can be examined in Fig. 3.24. This accumulator type is very simple and turned out to

Figure 3.24.: Piston attenuator of the *HBC030*

work properly. All expected advantages mentioned in Subsection 2.3.5 were confirmed by this prototype. Also the gas tightness was satisfying at least during all the test phases so far. Also when the test stand was out of operation for several weeks, the gas pre-pressure did not fall off noticeably. The main results of the basic measurements are illustrated in the Figures 3.25 to 3.28. A maximum efficiency improvement of more than 30% in the forward flow direction could be proved. Moreover, the recuperation power in the back flow direction was measured, which is depicted in Fig. 3.27. Furthermore, in Fig. 3.28 the resulting recuperation efficiency characteristics is illustrated. A certain loss of efficiency at the converter characteristics at low flow rates is depicted in Fig. 3.25. There, the efficiency of the HBC is even below the performance of resistance control. As suspected in the previous paragraph, this may be attributed to a too slow dynamics of the check valves. In this operating area it is possible, that a certain cross flow to the tank occurs, which lowers the efficiency.

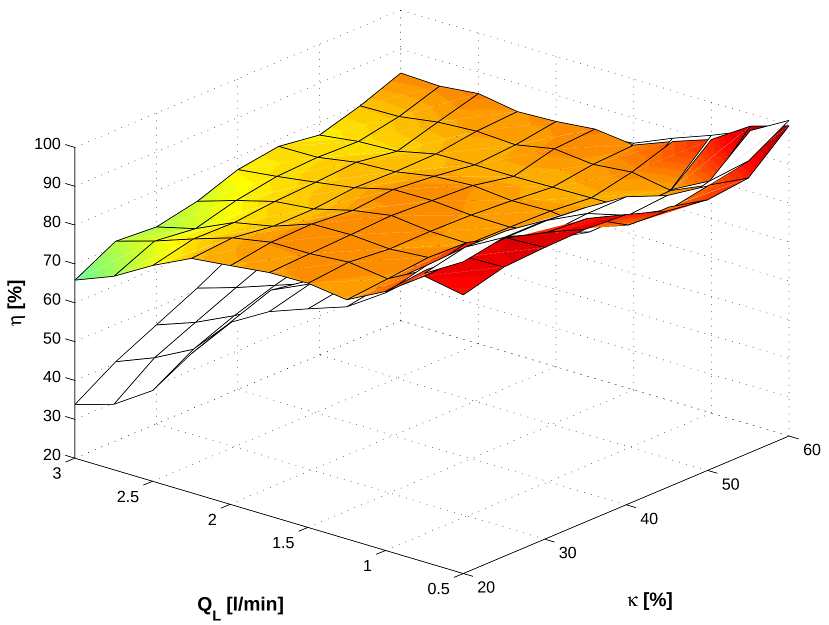

Figure 3.25.: Efficiency measurements of the *HBC030*

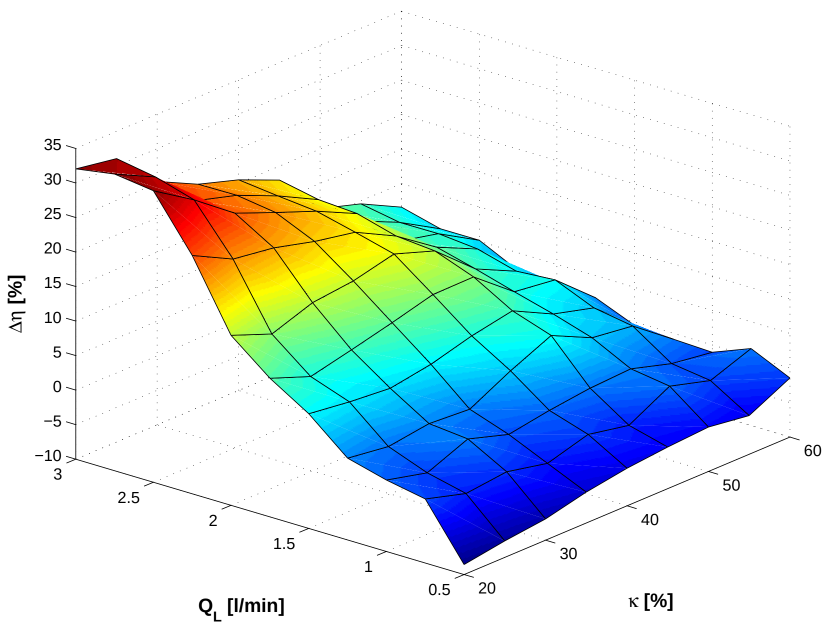

Figure 3.26.: Efficiency improvement of the *HBC030*

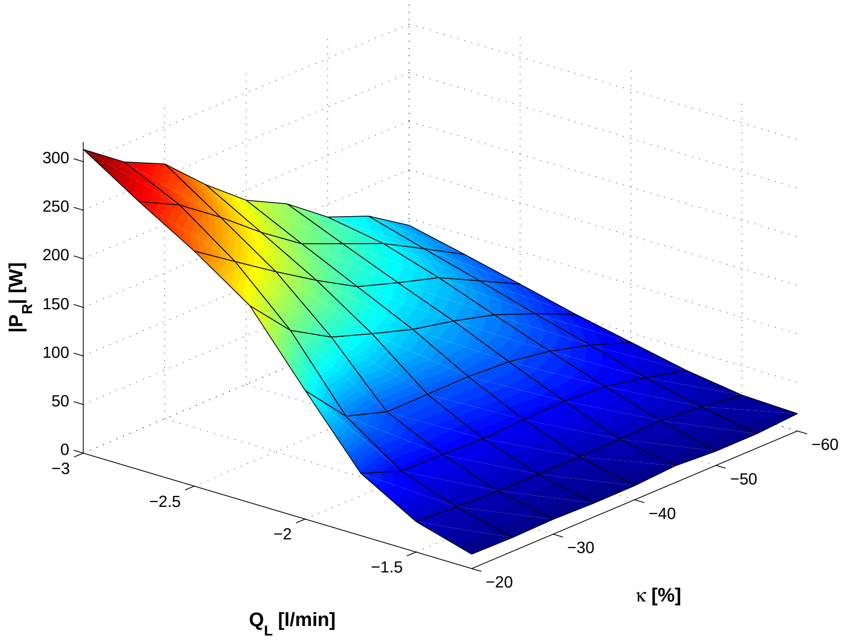

Figure 3.27.: Recuperation power of the *HBC030*

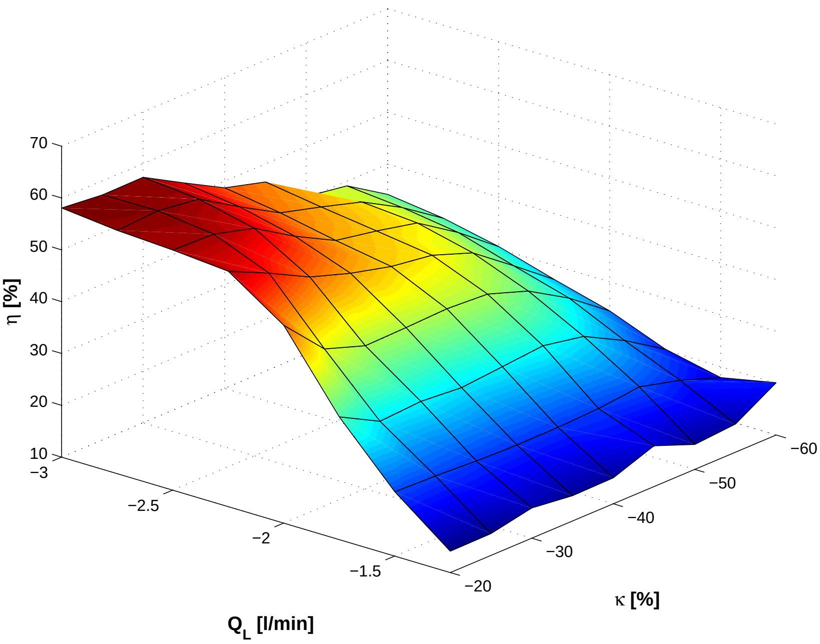

Figure 3.28.: Efficiency in recuperation mode of the *HBC030*

3.4. Theory versus Measurements

A sound knowledge of the system behaviour is important for the control and design issues. Thus, the accuracy of the model plays an outstanding role in the development of technical equipment. In case of the HBC, the considerations in Chapter 2 led to the theoretic converter characteristics depicted in Fig. 2.5. It had been already mentioned there, that some non-idealities of the real system let expect a certain deviation to the simple models of Section 2.1. To get an idea about the quality of the simple model approach, a comparison between the ideal characteristics and a measured power characteristics was worked out. In Fig. 3.29 the theoretic and the measured characteristics of the *HBC020* are opposed. The obviously poor agreement between the two performance maps implies, that

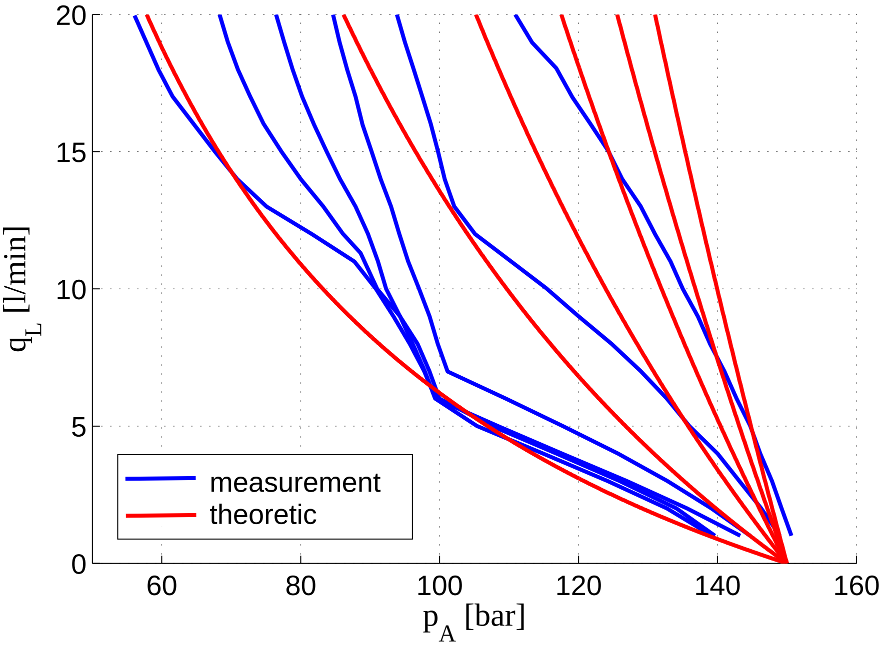

Figure 3.29.: Comparison of theoretic and measured characteristics

a number of non-idealities must be taken into account for an adequate modelling of the HBC. The main effects, that have to be considered are the nominal pressure drop of the switching valve, the parasitic capacity of the node volume V_Y, and wave propagation. As pointed out before (Subsection 3.2.1), the prototype *HBC020* was realised with a straight pipe inductance for an appropriate system analysis. This inductance geometry enables a proper description of the dynamic laminar flow through the pipe by the established models. For this reason the *HBC020* forms the basis for an advanced modelling of the relevant non-idealities, which will be considered in the following chapter.

4. Advanced Dynamic Modelling and Simulation

Due to the large deviations between the theoretical characteristics and the measurements, as depicted in Fig. 3.29, an advanced model that regards for some important non-idealities and parasitic effects is required for a thorough analysis. An adequate model of the converter is also necessary to derive a controller with a suitable performance, if advanced controller concepts are applied. In this chapter an advanced modelling of the HBC will be introduced, where the following effects are considered:

- wave propagation in the main inductance
- nonlinear valve characteristics
- valve dynamics
- finite capacity of the accumulator at the output
- parasitic capacity in the nodal point Y of the converter.

The schematic of the investigated system is depicted in Fig. 4.1. To obtain meaningful

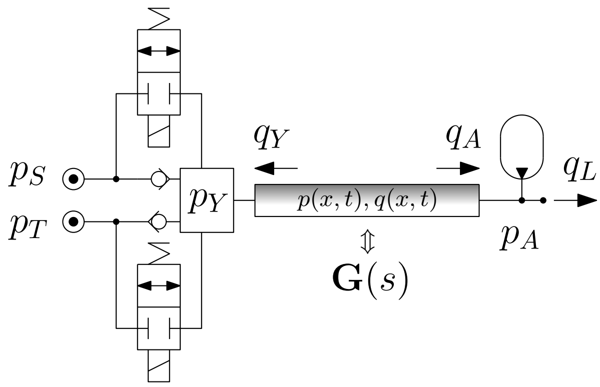

Figure 4.1.: Considered system

results, all other parasitic effects of a real converter have to be kept small by a proper design. The modelling of wave propagation is related to a straight pipe inductance. Thus, a comparison of the following results with measurements is only valid for the prototype *HBC020*, which employs such a straight pipe inductance.

The investigations are focused on a quasi steady state of the converter. Hence, strictly periodic processes are considered. In this case, wave propagation can be efficiently calculated in the frequency domain. Thus, a wave propagation model in accordance with Subsection 2.2.2 is used for the main inductance pipe. Therefore, laminar pipe flow and moderate pressure levels are assumed.

Due to certain nonlinearities, like valve characteristics and the behaviour of the gas spring, an overall analysis in the frequency domain is not possible. A common method would be a numeric simulation in time domain. Appropriate time domain simulation models of transmission lines are reported, for instance, in [24]. Since the investigations are focused on the steady state behaviour of the converter, a numeric integration of the system dynamics in the time domain is not suggested. To reach steady state, very long simulation times would have to be expected, even for a single steady state working point. The calculation time for a complete characteristic diagram would be correspondingly high. Thus, the method of a Time-Frequency-Domain-Iteration (TFDI) will be employed for the simulation of nonlinear periodic processes. The TFDI unifies the benefits of both calculation domains. Thereby, the nonlinear effects are considered in time domain and the effect of linear wave propagation will be calculated in frequency domain, respectively. This method is based on [2], another application of the TFDI can be found in [25].

4.1. Time Domain Models

The nonlinear effects in the considered HBC model according to Fig. 4.1 are represented by orifice equations of the different switching valves and the state equation of the gas spring in the accumulator. Also the single direction characteristic of the check valves represents a nonlinear effect. Appropriate mathematical descriptions of those mentioned nonlinearities are derived in the following.

4.1.1. The Orifice Equation

As pointed out in established literature (e.g. [26]), the flow through a valve exhibits mostly a quadratic pressure loss characteristic. If so, the flow rate relates to the well known orifice equation

$$q = K_V \sqrt{\Delta p} \tag{4.1}$$

with the orifice coefficient K_V and the pressure drop over the valve Δp. But, the orifice equation (4.1) causes a numerical problem at $\Delta p = 0$. To show this, the pressure build up of a hydraulic capacity of size 1, which is fed by the flow through an orifice with the flow coefficient 1, is studied. The state equation reads[1]

$$\dot{\Delta p} = -\sqrt{\Delta p}. \tag{4.2}$$

Just one flow direction is considered. For the initial condition $\Delta p_0 = 0$ two solutions

$$\Delta p = 0 \text{ and } \Delta p = \frac{t^2}{4} \tag{4.3}$$

of the differential equation (4.2) exist[2]. This means, that the solution of Eq. (4.2) is not unique at the point $\Delta p = 0$, due to a violation of the Lipschitz criterion (see e.g. [12]). This property of the orifice equation causes serious problems in numerical simulations, if the flow through an orifice crosses zero. To overcome this deficiency the orifice model of Eq. (4.1) has to be adapted in the neighbourhood of $\Delta p = 0$. According to [24] a reasonable model of an orifice is given by

$$q = \frac{Q_N}{\sqrt{p_N}} \sqrt[\vee]{\Delta p}, \tag{4.4}$$

with the nominal flow rate Q_N of the orifice at the nominal pressure drop p_N and with the *orifice-root*-function

$$\sqrt[\vee]{\Delta p} = \begin{cases} -\sqrt{|\Delta p|} & \Delta p \leq -\Gamma \\ \frac{1}{2}\sqrt{\Gamma}\left(\frac{3\Delta p}{\Gamma} + \frac{(\Delta p)^2}{\Gamma^2}\right) & -\Gamma < \Delta p < 0 \\ 0 & \Delta p = 0 \\ \frac{1}{2}\sqrt{\Gamma}\left(\frac{3\Delta p}{\Gamma} - \frac{(\Delta p)^2}{\Gamma^2}\right) & 0 < \Delta p < \Gamma \\ \sqrt{\Delta p} & \Delta p \geq \Gamma, \end{cases} \tag{4.5}$$

with $\Gamma > 0$. In Eq. (4.5) at lower pressure drops ($|\Delta p| < \Gamma$) the flow rate characteristics is approximated by a polynomial. At higher pressure drops, beyond Γ, the orifice model behaves according to the *sqrt*-function. The polynomial function at lower pressure drops ($|\Delta p| < \Gamma$) in Eq. (4.5) is designed such that the function value of the *orifice-root*-function at Γ equals the value of the *sqrt*-function. Furthermore, the same is valid for the first derivative with respect to Δp, which can be simplified to

$$\frac{\partial}{\partial(\Delta p)}\left(\sqrt[\vee]{\Delta p}\right) = \begin{cases} \frac{1}{2}\sqrt{\Gamma}\left(\frac{3}{\Gamma} - 2\frac{|\Delta p|}{\Gamma^2}\right) & 0 \leq |\Delta p| < \Gamma \\ \frac{1}{2\sqrt{|\Delta p|}} & |\Delta p| \geq \Gamma, \end{cases} \tag{4.6}$$

[1]A familiar formulation would be $\dot{p}(t) = \sqrt{p_S - p(t)}$, but this is equivalent due to the coordinate transformation $\Delta p = p_S - p(t)$.

[2]For a detailed calculation see Section A.2 in the Appendix.

and, which is bounded for all $\varDelta p \in \mathbb{R}$. This limited slope of the *orifice-root*-function guarantees the solvability of a differential equation of the form

$$\dot{\varDelta p} = -\frac{Q_N}{\sqrt{p_N}} \sqrt[\substack{\vee\\\wedge}]{\varDelta p}. \tag{4.7}$$

In Fig. 4.2 the *sqrt*- and the *orifice-root*-function are opposed. The limited slope of Eq.

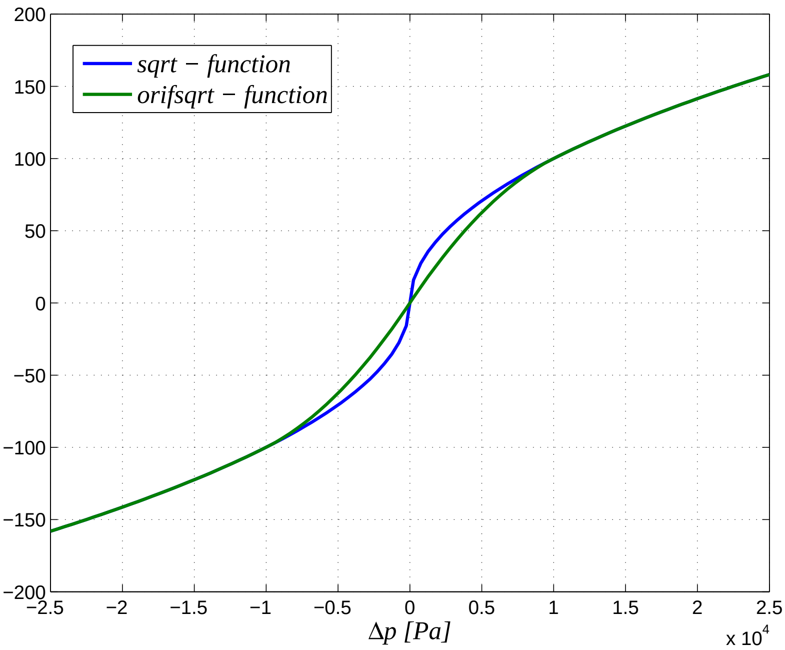

Figure 4.2.: Comparison of the *square-root* with the *orifice-root*-function

(4.5) at the origin has also a physical equivalence, because at low pressure drops the flow rate through an orifice is laminar. But, in most cases the square-root characteristics dominates the flow through an orifice and, thus, the coefficient $\varGamma$ is very small compared to common pressure drops at hydraulic valves. In most cases, the concrete value of $\varGamma$ does not play a significant role in systems identification, but the resulting polynomial characteristics is necessary for an efficient numeric simulation of hydraulic systems involving orifices.

A check valve enables a flow in only one direction. This characteristics can be realised by the so called *directed identity*, which reads

$$\mathrm{sgI}\,(x) = \begin{cases} 0 & x \leq 0 \\ x & x > 0 \end{cases} . \tag{4.8}$$

Applying this function to Eq. (4.4), the flow through a check valve is given by

$$q_{CV} = \frac{Q_N}{\sqrt{p_N}} \mathrm{sgI}\left(\sqrt[\substack{\vee\\\wedge}]{\varDelta p} \right). \tag{4.9}$$

In many hydraulic simulations proportional valves are considered. Thus, the metering of the valve edge must be taken into account. The characteristic flow through a fully opened valve calculates to

$$\frac{Q_N}{\sqrt{p_N}} = \alpha_O D_S \pi \sqrt{\frac{2}{\rho}} \xi_{max}, \tag{4.10}$$

where α_O, D_S, ρ and ξ_{max} stand for the contraction coefficient, the spool diameter, the fluid density and the maximum spool stroke of the valve. In metering case, the flow rate is described by

$$\frac{\xi_s}{\xi_{max}} \frac{Q_N}{\sqrt{p_N}} = \alpha_O D_s \pi \sqrt{\frac{2}{\rho}} \xi_s \tag{4.11}$$

with the actual spool position ξ_s.

4.1.2. Accumulator

To keep the equations of the TFDI simple, also a simple model of a hydraulic accumulator is desired. For this purpose, the dynamic equation of a hydraulic accumulator is derived and simplified successively. The different stages of simplification are comparatively evaluated. To avoid a higher order model, the inertia and the dissipation of the separating element between the oil and the gas is completely neglected, which corresponds to a membrane or a bladder accumulator.

The pressure build up equation in a hydraulic accumulator is based on the mass balance equation[3]

$$\dot{m}_{oil} = \rho q_{in}, \tag{4.12}$$

with m_{oil} as the oil mass, ρ the density of the fluid and the input flow rate q_{in}. With the relation $m_{oil} = \rho V_{oil}$, Eq. (4.12) can be written as

$$\dot{\rho} V_{oil} + \rho \dot{V}_{oil} = \rho q_{in}. \tag{4.13}$$

In the established literature, e.g. [26], the relation

$$\left(\frac{\partial \rho}{\rho} = \frac{\partial p}{E_{oil}} \right) \Bigg|_{T=const} \tag{4.14}$$

at a constant temperature T is applied, which is an acceptable simplification in common hydraulic systems. The assumption of a constant bulk modulus E_{oil} is also valid for many hydraulic applications, at least at moderate pressure rates. Assuming, that no air is entrained in the fluid, the density of the oil ρ in dependence of the pressure p follows to

$$\rho = \rho_0 e^{\frac{p-p_0}{E_{oil}}}, \tag{4.15}$$

[3]The argument t is omitted, at least if no confusion is possible.

with the fluid density ρ_0 at reference pressure p_0. The amount of fluid in the accumulator V_{oil} due to a polytropic change of state in the gas spring reads

$$V_{oil} = V_A \left(1 - \left(\frac{p_{0_G}}{p}\right)^{\frac{1}{\varkappa}}\right) \tag{4.16}$$

with the accumulator volume V_A, the pre-pressure of the gas spring p_{0_G} and the polytropic exponent $\varkappa$, which is assumed to be constant at the occurring pressure levels. With equations (4.13) to (4.16), the mass balance of Eq. (4.12) can be transformed into the pressure build up equation

$$\frac{\mathrm{d}p}{\mathrm{d}t} = \frac{E_{oil}}{V_A \left(1 + \left(\frac{E_{oil}}{p\varkappa} - 1\right)\left(\frac{p_{0_G}}{p}\right)^{\frac{1}{\varkappa}}\right)} q_{in}, \tag{4.17}$$

which constitutes the basic model of the accumulator. Assuming, that $E_{oil} \gg \varkappa p$, which is valid in common hydraulic systems, the pressure build up equation can be simplified to

$$\frac{\mathrm{d}p}{\mathrm{d}t} = \frac{E_{oil}}{V_A \left(1 + \frac{E_{oil}}{p\varkappa}\left(\frac{p_{0_G}}{p}\right)^{\frac{1}{\varkappa}}\right)} q_{in}. \tag{4.18}$$

With the assumption, that the oil is much stiffer than the gas spring at considered pressure levels, the simplification of $E \to \infty$ leads to the most simple model[4]

$$\frac{\mathrm{d}p}{\mathrm{d}t} = \frac{p\varkappa}{V_A \left(\frac{p_{0_G}}{p}\right)^{\frac{1}{\varkappa}}} q_{in}. \tag{4.19}$$

In Fig. 4.3 the pressure responses of the different models from Eq. (4.17) to Eq. (4.19) due to a sinusoidal input flow rate are opposed. Furthermore, the dynamic model of a piston accumulator according to Eq. (2.52) is compared to the other models. The responses of the different models are named *model 1,...,4*. The basis for comparison is given by *model 1*. The first simplification (*model 2*) makes the accumulator softer and neglecting the oil compressibility yields the stiffest *model 3*. Due to the fact, that the equation of the piston accumulator (Eq. (2.52)) accounts for an additional oil volume V_0, the *model 4* shows a slightly higher capacity than *model 1*, which represents an additional softness.

[4]This model can be exactly linearised by the transformation $p = \Pi^{-\varkappa}$ - see Section A.3.

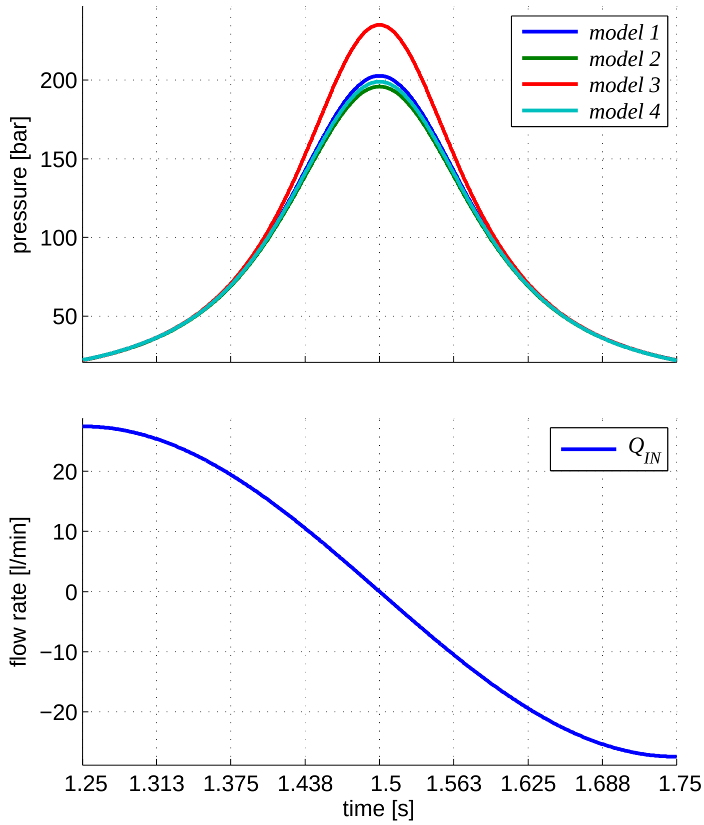

Figure 4.3.: Comparison of the different accumulator models (*model 1*→Eq. (4.17), *model 2*→Eq. (4.18), *model 3*→Eq. (4.19), *model 4*→Eq. (2.52))

Since most simple equations are intended for the TFDI, *model 3* was selected for the further considerations. But it has to be remarked, that the difference between *model 3* and *model 1* will grow with higher pressure rates. Thus, for a reasonable simulation of the HBC it must be assured, that the operating pressures remain in a certain range. On the other hand, the application of *model 3* leads to the maximum pulsation responses at the output of the converter and, thus, represents a worst case scenario due to its higher stiffness.

4.2. Time-Frequency-Domain-Iteration

The combined time-frequency-domain-iteration (TFDI) provides an efficient numeric calculation of periodic solutions of nonlinear dynamic systems. The basic idea of the TFDI will be explained in the following by its application to the dynamic modelling of the HBC according to Fig. 4.1. The system has two dynamic pressure states p_Y and p_A in the time domain. A certain operating point of the converter is determined by a constant duty ratio κ and the load flow rate q_L, which is a T_P-periodical signal. Thus, the differential equation of the pressure states has the following form

$$\begin{bmatrix} \dot{p}_Y \\ \dot{p}_A \end{bmatrix} = \mathbf{f}\left(p_Y, p_A, \kappa, q_L\right). \tag{4.20}$$

Both pressure states of Eq. (4.20) are linked by the main inductance of the converter, which is modelled in frequency domain by Eq. (2.25). Due to the periodicity of the switching process, the solution of the considered system is restricted to a finite time interval. Thus, the solution of Eq. (4.20) has the following from

$$p_i(t) = a_{0,i} + \sum_{k=1}^{\infty} \left\{a_{k,i} \cos\left(k\omega_0 t\right) + b_{k,i} \sin\left(k\omega_0 t\right)\right\}, \tag{4.21}$$

with $\omega_0 = \frac{2\pi}{T_P}$ and the indices $i = A, Y$, which indicate the different ends of the pipe inductance[5]. The considered time interval is defined by $T_P = \frac{1}{f_S}$. Since a numeric simulation is intended, the continuous time interval $[0, T_P[$ is sampled at a constant sample time T_S, with $\frac{T_P}{T_S} = N \in \mathbb{N}^+$. Thus, the discretised time interval consists of N equidistant samples. Since the differential equation (4.20) is valid for every point in time, it is also valid at each sample point. In the discretised version, every numeric periodic solution of the problem is represented by a vector

$$\begin{bmatrix} \mathbf{p}_Y \\ \mathbf{p}_A \end{bmatrix} = \left[p_{Y,0}, \ldots, p_{Y,N-1}, p_{A,0}, \ldots, p_{A,N-1}\right]^{\mathsf{T}} \tag{4.22}$$

of dimension $2N$. Due to this discretisation and the periodicity both solutions of the pressure states have the form

$$p_i(t) = a_{0,i} + \sum_{k=1}^{\frac{N-1}{2}} \left\{a_{k,i} \cos\left(k\omega_0 t\right) + b_{k,i} \sin\left(k\omega_0 t\right)\right\}, \text{ with } i = A, Y. \tag{4.23}$$

The $2N$ real valued coefficients[6] $a_{0,i}$, $a_{k,i}$ and $b_{k,i}$ represent the pressure offset, the real- and

[5]The index A stands for the pipe end with the *accumulator* and Y for the end at the *node point*.
[6]In the considered case of Eq. (4.23) N is uneven. If N is an even number, then $b_{\frac{N}{2},i}$ is identical zero.

the imaginary-part of the spectral components in frequency domain. This means, that the solution is well defined in each calculation domain. Thus, the solution in the time domain can be easily transformed to frequency domain by the Fast-Fourier-Transformation (FFT). Applying the pipe model of Eq. (2.25) in accordance with Fig. 4.1, the dynamic time domain flow rates q_Y and q_A at both ends of the main inductance can be calculated in frequency domain to $\hat{q}_Y$ and $\hat{q}_A$. The transformation back to time domain is carried out by the Inverse-Fast-Fourier-Transformation (IFFT). In this way, wave propagation in the main inductance is taken into account.

It remains to find an algebraic expression of the left hand side of Eq. (4.20). Using Eq. (4.23) the derivatives with respect to time read

$$\frac{\mathrm{d}}{\mathrm{d}t} p_i(t) = \sum_{k=1}^{\frac{N-1}{2}} \left\{ b_{k,i} k\omega_0 \cos\left(k\omega_0 t\right) - a_{k,i} k\omega_0 \sin\left(k\omega_0 t\right) \right\}, \text{ with } i = A, Y, \tag{4.24}$$

which converts Eq. (4.20) from a differential equation to a set of $2N$ nonlinear algebraic equations with $2N$ unknowns, which can be solved by adequate algorithms. But, at higher values of N, which are intended for a satisfying resolution of the problem, the numerical stability of the TFDI is lost, unfortunately. Probably, the factors $k\omega_0$ of the higher spectral components in Eq. (4.24) influence the numerical stability of the TFDI in a negative way, at least in the investigated cases. So, the derivatives with respect to time were approximated by means of a differential quotient in time domain, which is valid as well, if a proper discretisation of the problem is assumed. Thus, Eq. (4.20) is approximated by a system of nonlinear algebraic equations with $2N$ unknowns. The pressure states can be written as vectors $\mathbf{p}_Y$ and $\mathbf{p}_A$, consisting each of N unknowns, respectively. Hence, the resulting problem for the analysis of one periodic cycle in the time domain and at a certain operating point (κ, q_L) reads

$$\mathbf{F}\left(\mathbf{p}_A, \mathbf{p}_Y\right) = \mathbf{0}, \tag{4.25}$$

which can be solved by established iteration algorithms.

4.2.1. Formulation of the Problem

In the following, the detailed equations for the system according to Fig. 4.1 are formulated. In accordance with Section 4.1 the individual pressure build up equations in the node volume and in the accumulator from Eq. (4.20) read

$$\dot{p}_Y \frac{V_Y}{E_{oil}} = q_Y + q_{VS} - q_{VT} - q_{CS} + q_{CT} \tag{4.26}$$

$$\dot{p}_A \frac{V_A \left(\frac{p_{0G}}{p_A}\right)^{\frac{1}{\varkappa}}}{p_A \varkappa} = q_A - q_L \tag{4.27}$$

with the flow rates

$$q_{VS} = \mathrm{sgI}\left(\xi_{s_S}(\kappa, t)\right) \frac{Q_{N_{SV}}}{\sqrt{p_{N_{SV}}}} \sqrt[\veebar]{p_S - p_Y} \tag{4.28}$$

$$q_{VT} = \mathrm{sgI}\left(\xi_{s_T}(\kappa, t)\right) \frac{Q_{N_{SV}}}{\sqrt{p_{N_{SV}}}} \sqrt[\veebar]{p_Y - p_T} \tag{4.29}$$

through the supply sided and the tank sided switching valve. The actual spool positions of the valves are considered by ξ_{s_k}, with $k = S, T$ for the supply side and the tank side, respectively. The dynamic movement of the different valve spools is approximated by

$$\xi_{s_k}(t) = \left(\frac{1}{2} + \frac{o_V}{100}\right)\left(\tanh\left(\frac{2\pi\,(t - t_{off})}{t_r}\right) - \tanh\left(\frac{2\pi\,(t - t_{off} - \kappa_k T_P)}{t_f}\right)\right) - 2\frac{o_V}{100}. \tag{4.30}$$

In Eq. (4.30) the parameters t_r and t_f denote the rise and the fall time of the valves. Furthermore, the valve overlap is accounted for by o_V in a percentage of the full spool stroke. The duty ratios κ_k with respect to the cycle time T_P represent the inputs of Eq. (4.26). The mechanical movement of the spool is modelled by two complementary and staggered *tanh*-functions, where $0 < \xi_s < 1$ defines a hydraulic metering of the orifice. At $\xi_s = 1$ the valve is fully open. Negative values of ξ_s describe a movement behind the valve overlap. Since this area is not of hydraulic relevance it is omitted by the *directed identity* function of Eq. (4.8). The time offset t_{off} enables an arbitrary shift of the switching pulse along the cycle time interval for implementation reasons. The described relations are illustrated in Fig. 4.4 for a certain parameter set and a duty ratio of $\kappa = 25\%$. Both active switching valves have a nominal flow rate $Q_{N_{SV}}$ at the nominal pressure drop $p_{N_{SV}}$. In the same manner, the individual flow rates through the check valves read

$$q_{CS} = \frac{Q_{N_{CV}}}{\sqrt{p_{N_{CV}}}} \mathrm{sgI}\left(\sqrt[\veebar]{p_Y - p_S}\right) \tag{4.31}$$

$$q_{CT} = \frac{Q_{N_{CV}}}{\sqrt{p_{N_{CV}}}} \mathrm{sgI}\left(\sqrt[\veebar]{p_T - p_Y}\right). \tag{4.32}$$

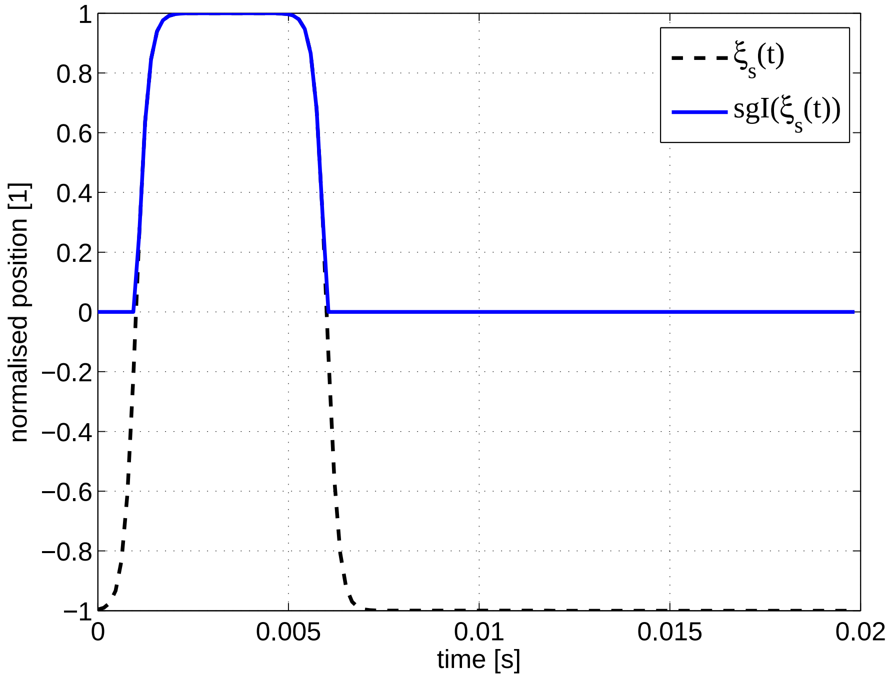

Figure 4.4.: Spool movement and opening of an active switching valve

For simplicity, the response dynamics of the check valves is not accounted for in Eq. (4.31) and (4.32). Due to the passive behaviour of check valves, further degrees of freedom for the movement of the poppet would have to be spent, which was not done here for simplicity reasons.

4.2.2. Discretisation and Restriction to the Switching Interval

Since the solutions of system (4.20) are periodic with respect to the switching period $T_P = \frac{1}{f_S}$ the considered discretised time interval reads

$$\mathbf{t} = \frac{T_P}{N}\,[0, 1, \ldots, N-1]^\mathsf{T} \tag{4.33}$$

with $N \in \{2k-1 | k \in \mathbb{N}^+\}$ being the number of samples per switching period. The uneven number of samples is not restricted in general, but the implementation of the iteration process in this work requires this constraint to avoid a significant loss of accuracy at the Discrete-Fourier-Transformation (DFT) between both calculation domains. However, for the desired resolution of the considered dynamic process, N is determined by Nyquist's criterion $\omega_{max} = \frac{\pi}{T_S} = \frac{N\pi}{T_P}$, where ω_{max} denotes the maximum frequency of the spectral components in frequency domain. In time domain the different pressure states are defined and discretised on the considered time interval,

$$\mathbf{p}_Y = p_Y(\mathbf{t}) = [p_{Y,0}, \ldots, p_{Y,N-1}]^\mathsf{T}, \text{ with } p_{Y,0} = p_{Y,N} \tag{4.34}$$

and

$$\mathbf{p}_A = p_A(\mathbf{t}) = [p_{A,0}, \ldots, p_{A,N-1}]^\mathsf{T}, \text{ with } p_{A,0} = p_{A,N}. \tag{4.35}$$

The desired set of nonlinear equations for the iteration process must have the following form

$$\mathbf{e}(\mathbf{p}_Y, \mathbf{p}_A) = \begin{bmatrix} \mathbf{e}_{\mathbf{p}_Y} \\ \mathbf{e}_{\mathbf{p}_A} \end{bmatrix} \stackrel{!}{=} \mathbf{0}, \tag{4.36}$$

where $\mathbf{e}_{\mathbf{p}_Y}$ and $\mathbf{e}_{\mathbf{p}_A}$ stand for the residual vectors of the discretised equations (4.26) and (4.27), respectively. They read

$$\mathbf{e}_{\mathbf{p}_Y} = -\frac{V_Y}{E_{oil}}\frac{\Delta \mathbf{p}_Y}{\Delta t} + (\mathbf{q}_Y + \mathbf{q}_{VS} - \mathbf{q}_{VT} - \mathbf{q}_{CS} + \mathbf{q}_{CT}) \tag{4.37}$$

and

$$\mathbf{e}_{\mathbf{p}_A} = -\frac{V_A p_{0_G}^{\frac{1}{\varkappa}}}{\varkappa} \mathrm{diag}\{\mathbf{p}_A\}^{-\frac{\varkappa+1}{\varkappa}} \frac{\Delta \mathbf{p}_A}{\Delta t} + (\mathbf{q}_A - \mathbf{q}_L) \tag{4.38}$$

under the assumption of $p_A \geq p_{0_G} > 0$ for every sampling point within the considered time interval. The derivatives of the periodic pressure vectors with respect to time are approximated by the central differential quotient

$$\frac{\Delta \mathbf{p}_i}{\Delta t} = \frac{1}{2T_S}\left(\begin{bmatrix} p_{i,N-1} \\ p_{i,0} \\ \vdots \\ p_{i,N-2} \end{bmatrix} - \begin{bmatrix} p_{i,1} \\ \vdots \\ p_{i,N-1} \\ p_{i,0} \end{bmatrix} \right) = \frac{1}{2T_S}\left(\mathbf{T}_{SH} - \mathbf{T}_{SH}^\top\right)\mathbf{p}_i, \; i = A, Y \tag{4.39}$$

with the sampling time T_S and the shifting matrix

$$\mathbf{T}_{SH} = \begin{bmatrix} 0 & 1 & 0 & \cdots & 0 \\ \vdots & \ddots & \ddots & \ddots & \vdots \\ \vdots & \ddots & \ddots & \ddots & 0 \\ 0 & 0 & \ddots & \ddots & 1 \\ 1 & 0 & \cdots & \cdots & 0 \end{bmatrix}. \tag{4.40}$$

The flow rate vectors of the active switching valves read

$$\mathbf{q}_{VS} = \frac{Q_{N_{SV}}}{\sqrt{p_{N_{SV}}}} \mathrm{diag}\left\{\mathrm{sgI}\left(\xi_{s_S}(\mathbf{t})\right)\right\} \sqrt[\veebar]{p_S - \mathbf{p}_Y} \tag{4.41}$$

$$\mathbf{q}_{VT} = \frac{Q_{N_{SV}}}{\sqrt{p_{N_{SV}}}} \mathrm{diag}\left\{\mathrm{sgI}\left(\xi_{s_T}(\mathbf{t})\right)\right\} \sqrt[\veebar]{\mathbf{p}_Y - p_T} \tag{4.42}$$

and the flow rate vectors of the check valves follow to

$$\mathbf{q}_{CS} = \frac{Q_{N_{CV}}}{\sqrt{p_{N_{CV}}}} \mathrm{sgI}\left(\sqrt[\veebar]{\mathbf{p}_Y - p_S}\right) \tag{4.43}$$

$$\mathbf{q}_{CT} = \frac{Q_{N_{CV}}}{\sqrt{p_{N_{CV}}}} \mathrm{sgI}\left(\sqrt[\veebar]{p_T - \mathbf{p}_Y}\right). \tag{4.44}$$

The flow rate vectors $\mathbf{q}_Y$ and $\mathbf{q}_A$ at the different pipe ends are calculated in frequency domain. Introducing the abbreviations $G_{ik}\left(j\omega\right),\ i,k = 1,2$ with respect to Eq. (2.25) and using the Fourier transformation

$$\hat{p}_i\left(j\omega\right) = \mathcal{F}\left\{p_i\left(t\right)\right\} \tag{4.45}$$

with $i = A, Y$, the dynamic flow rates calculate to

$$\begin{bmatrix} \hat{q}_Y\left(j\omega\right) \\ \hat{q}_A\left(j\omega\right) \end{bmatrix} = \begin{bmatrix} G_{11}\left(j\omega\right) & G_{12}\left(j\omega\right) \\ G_{21}\left(j\omega\right) & G_{22}\left(j\omega\right) \end{bmatrix} \begin{bmatrix} \hat{p}_Y\left(j\omega\right) \\ \hat{p}_A\left(j\omega\right) \end{bmatrix}. \tag{4.46}$$

Applying the inverse Fourier transformation the flow rates in the time domain read

$$q_i(t) = \mathcal{F}^{-1}\left\{q_i\left(j\omega\right)\right\},\ i = A, Y. \tag{4.47}$$

Considering the periodicity on the discretised time interval the Fourier transform corresponds to the Discrete Fourier Transform (DFT) and its inverse, respectively. The numeric implementation of the DFT is also called Fast-Fourier-Transform (FFT) and Inverse-Fast-Fourier-Transform (IFFT), respectively. Thus, the flow rate vectors at both ends of the inductance pipe in time domain calculate to

$$\mathbf{q}_Y = \mathrm{ifft}\left\{\mathbf{G}_{11}\left(j\boldsymbol{\omega}\right)\mathrm{fft}\left\{\mathbf{p}_Y\right\} + \mathbf{G}_{12}\left(j\boldsymbol{\omega}\right)\mathrm{fft}\left\{\mathbf{p}_A\right\}\right\} \tag{4.48}$$

$$\mathbf{q}_A = \mathrm{ifft}\left\{\mathbf{G}_{21}\left(j\boldsymbol{\omega}\right)\mathrm{fft}\left\{\mathbf{p}_Y\right\} + \mathbf{G}_{22}\left(j\boldsymbol{\omega}\right)\mathrm{fft}\left\{\mathbf{p}_A\right\}\right\}, \tag{4.49}$$

where the transfer functions $G_{ik}\left(j\omega\right),\ i,k = 1,2$ of Eq. (4.46) are replaced by the discretised transfer matrices

$$\mathbf{G}_{ik}\left(j\boldsymbol{\omega}\right) = \mathrm{diag}\left\{G_{ik}(j\boldsymbol{\omega})\right\},\ i,k = 1,2 \tag{4.50}$$

accounting for wave propagation. The vector of the discrete angular frequencies reads

$$\boldsymbol{\omega} = \omega_0 \left[0, 1, 2, \ldots, \frac{N-1}{2}, -\frac{N-1}{2}, -\frac{N-1}{2}+1, -\frac{N-1}{2}+2, \ldots, -1\right] \tag{4.51}$$

with

$$\omega_0 = \frac{2\pi}{T_P}. \tag{4.52}$$

The load flow rate vector $\mathbf{q}_L$ in Eq. (4.38) represents an input vector, which has the following form

$$\mathbf{q}_L = q_L \left[1, \ldots, 1\right]^\intercal, \tag{4.53}$$

where q_L is assumed to be constant during one switching cycle, at least in the considered case. In general, this is not necessary, but $\mathbf{q}_L$ must be at least periodical with T_P.

The discretised equations (4.37) and (4.38) represent a system of nonlinear equations, which cannot be solved directly. Hence, the problem has to be solved iteratively by appropriate algorithms, for instance, by *fsolve* in *Matlab*$^{\text{TM}}$. The convergence of such iteration algorithms depends, besides other specific parameters, strongly on the initial conditions $\mathbf{p}_{Y_0}$ and $\mathbf{p}_{A_0}$. In the simulations carried out, the choice

$$\mathbf{p}_{i_0} = \frac{p_S + p_T}{2} \left[1, \ldots, 1\right]^\intercal, \; i = A, Y \tag{4.54}$$

yielded always physically reasonable results. But no statement on the uniqueness of the obtained solution can be given.

4.2.3. Improvement of the Calculation Performance

The method introduced in the previous subsection represents a type of fixed-point iteration. The corresponding calculation time suffers from a large number of iterations until the convergence criterion is fulfilled. To improve the calculation performance, it is useful to evaluate the Jacobian matrix of Eq. (4.36), which reads in the considered case

$$\mathbf{J} = \begin{bmatrix} \frac{\partial}{\partial \mathbf{p}_Y}\mathbf{e}_{p_Y} & \frac{\partial}{\partial \mathbf{p}_A}\mathbf{q}_Y \\ \frac{\partial}{\partial \mathbf{p}_Y}\mathbf{q}_A & \frac{\partial}{\partial \mathbf{p}_A}\mathbf{e}_{p_A} \end{bmatrix} \tag{4.55}$$

with

$$\begin{aligned} \frac{\partial}{\partial \mathbf{p}_Y}\mathbf{e}_{p_Y} \quad &= \quad -\frac{\partial}{\partial \mathbf{p}_Y}\left(\frac{\Delta \mathbf{p}_Y}{\Delta t}\right)\frac{V_Y}{E_{oil}} + \\ &\quad + \frac{\partial}{\partial \mathbf{p}_Y}\left(\mathbf{q}_{VS} - \mathbf{q}_{VT} - \mathbf{q}_{CS} + \mathbf{q}_{CT}\right) + \frac{\partial}{\partial \mathbf{p}_Y}\mathbf{q}_Y \end{aligned} \tag{4.56}$$

$$\begin{aligned}\frac{\partial}{\partial \mathbf{p}_A}\mathbf{e}_{p_A} &= -\frac{V_A p_{0_G}^{\frac{1}{\varkappa}}}{\varkappa}\operatorname{diag}\left\{\mathbf{p}_A\right\}^{-\frac{\varkappa+1}{\varkappa}}\frac{\partial}{\partial \mathbf{p}_A}\left(\frac{\Delta \mathbf{p}_A}{\Delta t}\right)+\frac{\partial}{\partial \mathbf{p}_A}\mathbf{q}_A+\\ &+\frac{V_A p_{0_G}^{\frac{1}{\varkappa}}}{\varkappa}\left(1+\frac{1}{\varkappa}\right)\operatorname{diag}\left\{\mathbf{p}_A\right\}^{-\frac{2\varkappa+1}{\varkappa}}\operatorname{diag}\left\{\frac{\Delta \mathbf{p}_A}{\Delta t}\right\} \qquad (4.57)\end{aligned}$$

and

$$\frac{\partial}{\partial \mathbf{p}_i}\left(\frac{\Delta \mathbf{p}_i}{\Delta t}\right)=\frac{1}{2T_S}\left(\mathbf{T}_{SH}-\mathbf{T}_{SH}^{\top}\right). \qquad (4.58)$$

The influence of the different pressure states on the corresponding flow rates at both ends of the pipe inductance read

$$\frac{\partial}{\partial \mathbf{p}_Y}\mathbf{q}_Y = \operatorname{ifft}\left\{\mathbf{G}_{11}\left(j\boldsymbol{\omega}\right)\operatorname{fft}\left\{\mathbf{I}\right\}\right\} \qquad (4.59)$$

$$\frac{\partial}{\partial \mathbf{p}_A}\mathbf{q}_Y = \operatorname{ifft}\left\{\mathbf{G}_{12}\left(j\boldsymbol{\omega}\right)\operatorname{fft}\left\{\mathbf{I}\right\}\right\} \qquad (4.60)$$

$$\frac{\partial}{\partial \mathbf{p}_Y}\mathbf{q}_A = \operatorname{ifft}\left\{\mathbf{G}_{21}\left(j\boldsymbol{\omega}\right)\operatorname{fft}\left\{\mathbf{I}\right\}\right\} \qquad (4.61)$$

$$\frac{\partial}{\partial \mathbf{p}_A}\mathbf{q}_A = \operatorname{ifft}\left\{\mathbf{G}_{22}\left(j\boldsymbol{\omega}\right)\operatorname{fft}\left\{\mathbf{I}\right\}\right\}. \qquad (4.62)$$

Considering the Jacobian matrix, the convergence performance can be improved significantly. With a parallelised implementation on a multi core processor engine the calculation time can be reduced further.

4.3. Simulation

Exploiting the method of the TFDI, a comprehensive steady state analysis of the HBC is possible and the converter characteristics can be calculated efficiently. The obtained results will be compared with the measurements of the *HBC020* from Section 3.2.1. If a sufficient agreement of simulation and measurements is obtained, a comprehensive study of the converter performance in dependence of the system parameters can be carried out. All dynamic pressure states and the dynamic flow rates, respectively, in different operating points can be investigated over one switching cycle. Thus, a reasonable analysis of the role of the design parameters of an HBC is possible.

4.3.1. Model Verification

The first step in the analysis of the obtained results is a comparison with corresponding measurements. The converter characteristics of an HBC with the parameters like the prototype *HBC020* were calculated with the TFDI. An optimisation process for the identification of the real system parameters was carried out in *Matlab*™ with the *lsqnonlin*-algorithm, which is explained in Subsection A.4.1. The result of this parameter identification is depicted in Fig. 4.5. Obviously, the dominating effects are captured sufficiently

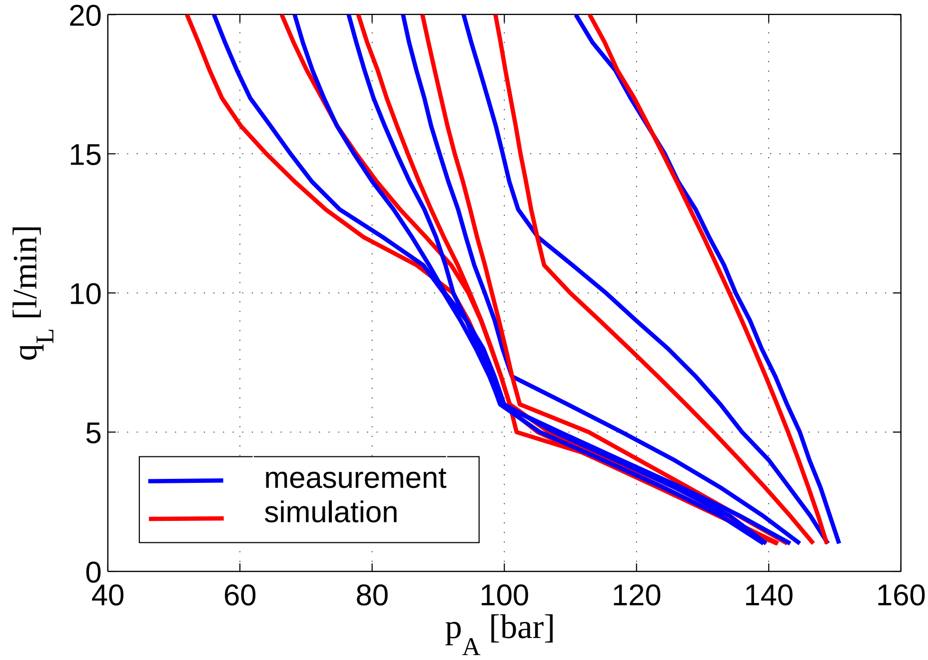

Figure 4.5.: Comparison of measurement and simulation

by the system model according to Fig. 4.1. The deviations between the measurements and the simulation result from effects that are not yet included in the model, like the check valves' dynamic response or some cavitation. But, the identified parameters agree quite satisfyingly with the expected values or allow a reasonable interpretation. The identified system parameters are listed in Tab. A.2.

4.3.2. Analysis of a certain working point

The results of the previous subsection allow a meaningful analysis of a certain operating point of the converter. A steady state working point of the HBC is defined by the duty ratio κ and a constant load flow rate q_L. The system parameters of the converter are listed in Tab. A.4. The configuration of the applied solution algorithm for the TFDI is documented in Tab. A.5. The corresponding simulation results of the HBC at an operating point are illustrated in Fig. 4.6. The upper diagram shows the opening of the supply sided active switching valve at the duty ratio $\kappa_S = 20\%$. In the second diagram both dynamic pressure states p_Y and p_A are depicted. Moreover, the pressures of the supply and the tank system are illustrated. When the valve opens, the node volume V_Y is fed by the flow rate through the supply sided switching valve. Thus, p_Y rises up to the supply pressure level and the flow rate through the main inductance increases. The

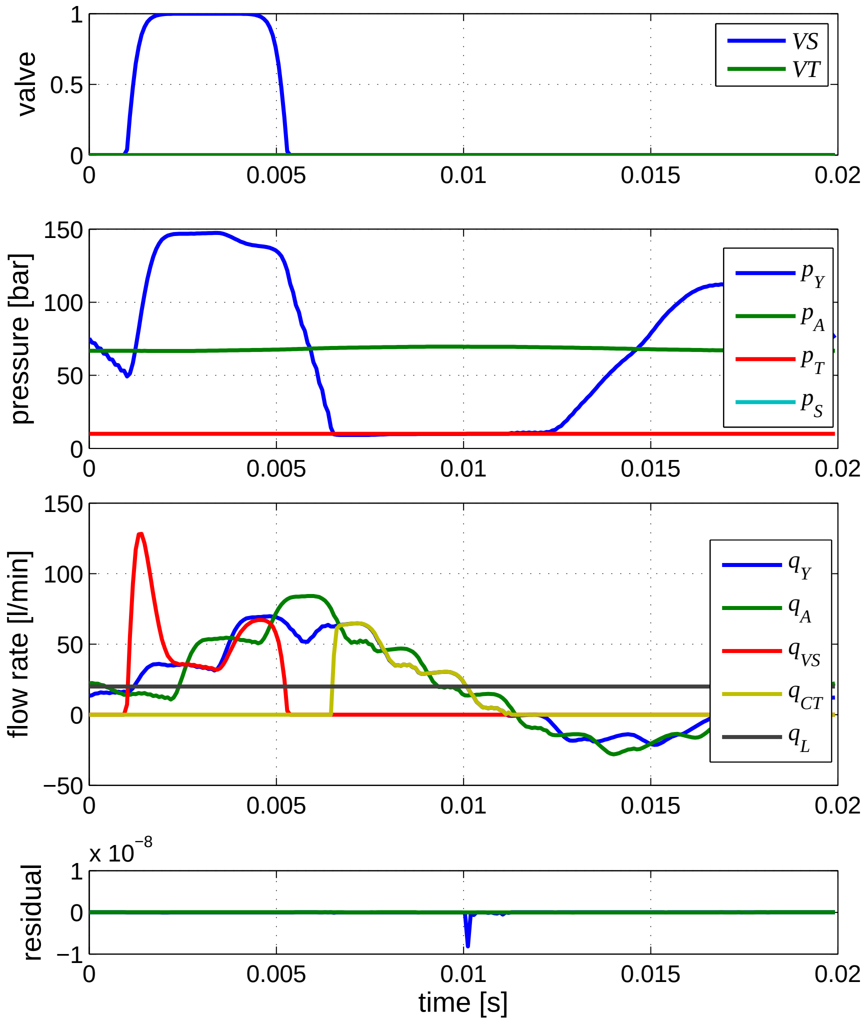

Figure 4.6.: Simulation of the steady state behaviour of the HBC

smooth characteristics of the load pressure p_A confirms, that the size of the accumulator at the output of the converter is sufficiently large. The third diagram represents the different dynamic flow rates of the configuration. Beside the duty ratio κ_S, another system input is defined by the constant load flow rate q_L (black line in the third subplot). The red line represents the flow rate through the active switching valve q_{VS}. The large peak of q_{VS} at the beginning of the valve opening results from charging the node volume. In the considered case this node volume is determined with $V_Y = 0.15\,l$. The gap between q_{VS} (red line) and q_{CT} (yellow line) after the closing of the switching valve is explained by the discharging of the node volume. When the node volume is discharged below the tank pressure the suction phase is initiated. As mentioned in Subsection 2.2.3, both effects, the large flow rate peak and the suction gap can be reduced by a smaller node volume. The ripples in the different flow rates are caused by wave propagation in the main inductance of the converter. At a certain time of the switching cycle, the suction flow rate through the tank sided check valve vanishes. Thus, the converter operates in flow control mode, at least in this case. After the suction phase, the pressure p_Y rises again and oscillates around the load pressure p_A until the next switching cycle starts. This oscillation represents a transient resonance effect of the Helmholtz resonator consisting of the node volume and the main inductance. For completeness, in the lower diagram the residuals of Eq. (4.37) and Eq. (4.38) at the final iteration step of the TFDI are illustrated.

4.3.3. Converter Characteristics

The satisfying accuracy of the simulation model (see Fig. 4.5) enables an adequate study of the converter behaviour in steady state. Furthermore, the TFDI is a time efficient method for the calculation of a comprehensive steady state characteristic diagram of an HBC within reasonable simulation times. In Fig. 4.7 the calculated efficiency characteristics of the HBC in the forward flow direction is depicted. The coloured surface corresponds to the

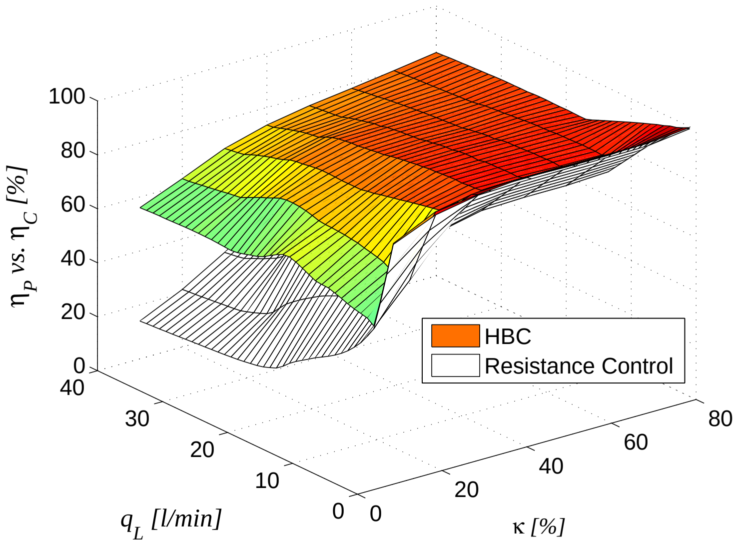

Figure 4.7.: Efficiency characteristics

efficiency performance of the HBC and the white surface to resistance control, respectively. The different working points were defined by the load flow rate $q_L = 0, \ldots, 40\frac{l}{min}$ and the duty ratio $\kappa = 0, \ldots, 80\%$. The parameters of the HBC correspond again to the prototype *HBC020*. The characteristics shown in Fig. 4.7, which are related to κ and q_L, are directly obtained from the simulation algorithm. A more convenient representation can be examined in Fig. 4.8, where the same simulation results are depicted in relation of the output power quantities p_A and q_L. In the left diagram the efficiency characteristics are illustrated. In the right diagram the efficiency improvement can be examined. The blue markers represent the simulated working points from Fig. 4.7. The different surfaces

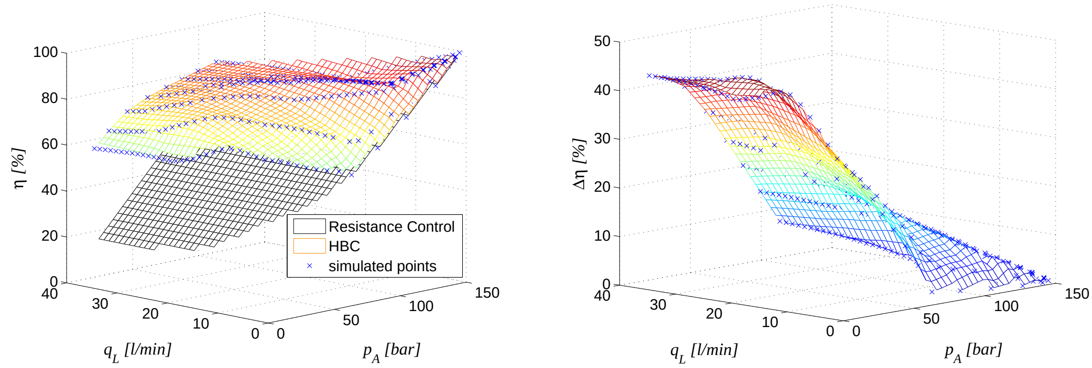

(a) Efficiency $\eta\,(q_L, p_A)$ (b) Efficiency improvement $\Delta\eta\,(q_L, p_A)$

Figure 4.8.: Efficiency characteristics depending on output power ($V_Y = 0.15\,l$)

are interpolated by the algorithm *griddata* in *Matlab*™. The considered configuration accounts for a large node volume of $V_Y = 0.15\,l$. In Fig. 4.9 the characteristic of basically the same converter configuration, but with a smaller node volume ($V_Y = 0.015\,l$), is illustrated. It can be seen, that the efficiency balance is much better with a smaller node

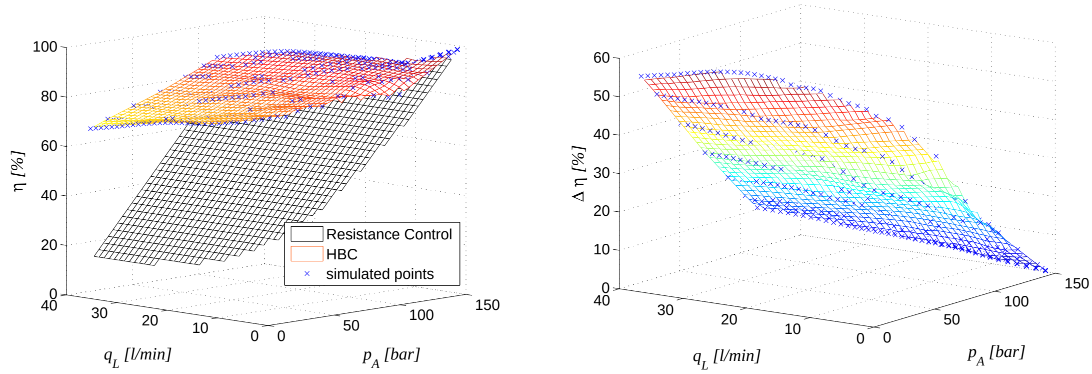

(a) Efficiency $\eta\,(q_L, p_A)$ (b) Efficiency improvement $\Delta\eta\,(q_L, p_A)$

Figure 4.9.: Efficiency characteristics depending on output power ($V_Y = 0.015\,l$)

volume, because this configuration does not suffer from such high charging losses as the converter with the larger node capacity. In Fig. 4.10 the corresponding two different power characteristics of the investigated configurations are depicted. The thick lines represent the characteristics obtained from the TFDI at a constant duty ratio κ. The thinner lines correspond to the ideal characteristics from Subsection 2.1.3. In contrast to the theoretical characteristics, the advanced model considers the valve characteristics and, hence, in both diagrams basically a higher resistance of the TFDI-characteristics can be observed. In Fig. 4.10a the sharp bend in the characteristics at $p_A \approx 120\,bar$ indicates the border to the energy saving area of operation. At pressure levels below this border energy saving takes place and, beyond just pure throttling occurs. Since the theoretical characteristics (thinner lines) do not consider a node capacity, the deviations

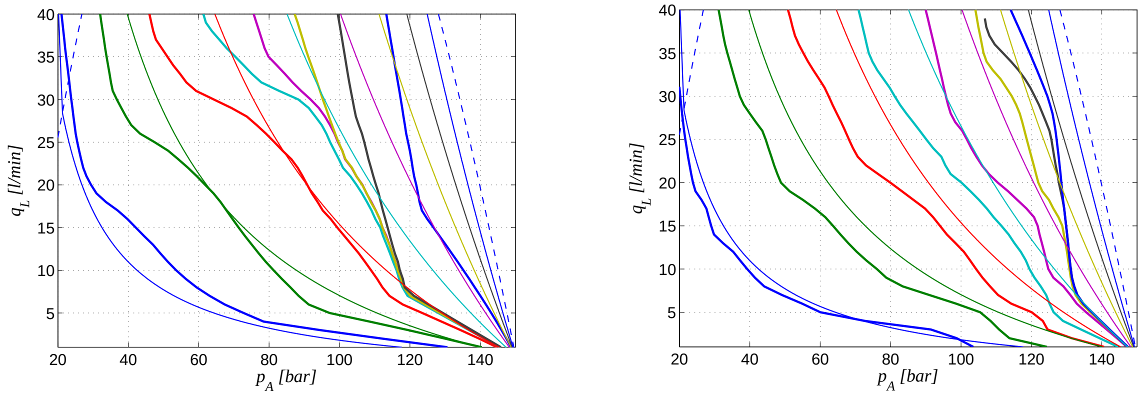

(a) $V_Y = 0.15l$ (b) $V_Y = 0.015l$

Figure 4.10.: Different power characteristics

to the simulation results obtained by the TFDI are very large in the throttling area. Below the border of $p_A \approx 120\,bar$ the deviation between the theoretical and the TFDI-results are mainly caused by the resistance of the valves and by oscillations of the Helmholtz resonator consisting of the main inductance and the node volume. In Fig. 4.10b the border between throttling and energy saving occurs at higher pressure levels, like $p_A \approx 130 bar$, due to the smaller node capacity. The deviations in the energy saving area are also smaller than at the configuration with a larger node volume, because the natural frequency of the mentioned Helmholtz resonator is higher due to the smaller node volume. Thus, the transient response effects of this resonator have less influence on the characteristics, as illustrated in Fig 4.11 and Fig. 4.12.

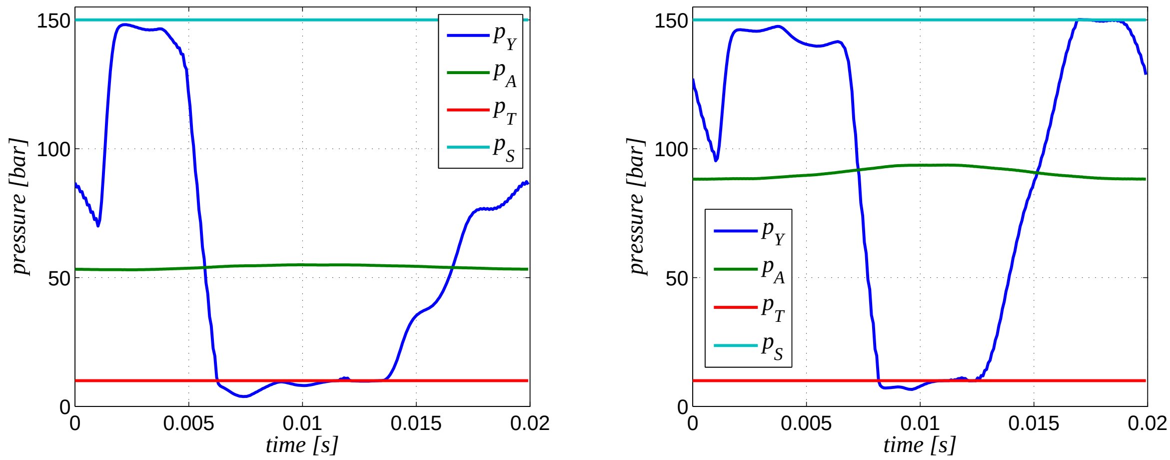

(a) $\kappa = 20\%$ (b) $\kappa = 30\%$

Figure 4.11.: Transient response of p_Y with $V_Y = 0.15\,l$ and $q_L = 20\frac{l}{min}$

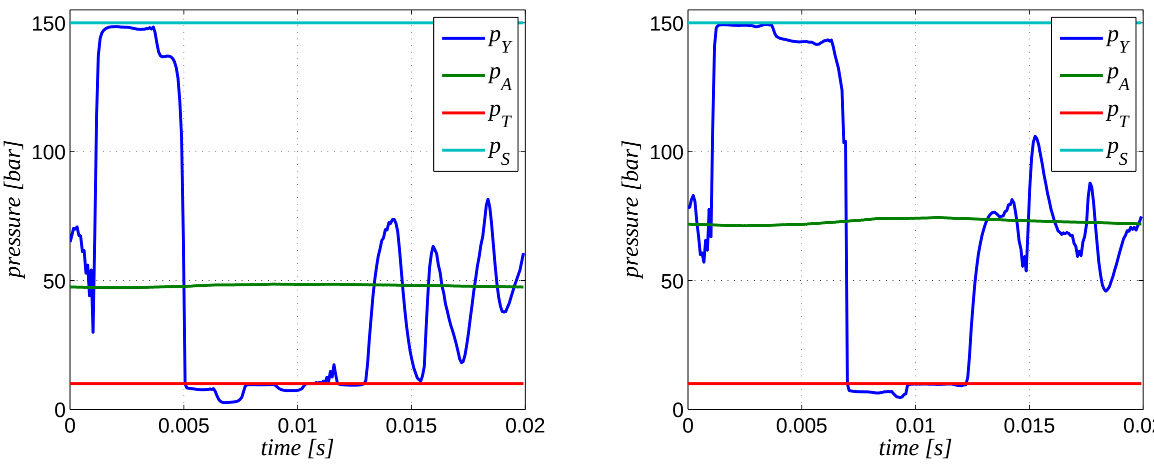

(a) $\kappa = 20\%$ (b) $\kappa = 30\%$

Figure 4.12.: Transient response of p_Y with $V_Y = 0.015\,l$ and $q_L = 20\frac{l}{min}$

Comparing Fig. 4.8 with Fig. 4.9 makes clear, that a smaller node volume is important for low charging losses and, thus, for high efficiency. But, an analysis of selected pressure signals at different locations along the main inductance shows a remarkable resonance effect. In the following, the pressure signals in the main inductance were investigated at three equidistant locations between both ends of the main inductance pipe, like depicted in Fig. 4.13. In Fig. 4.14 the distributed pressure signals in a certain working point

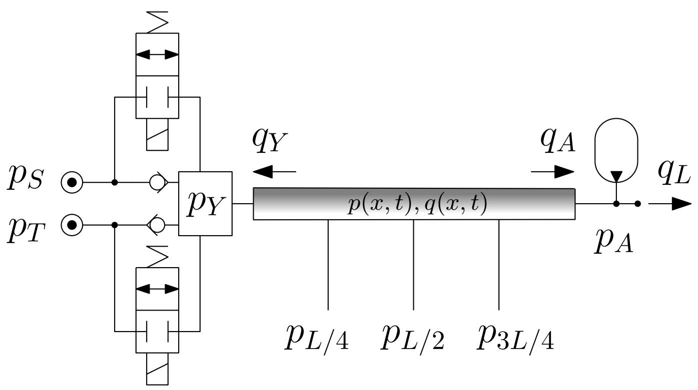

Figure 4.13.: Pressure signals at different locations

of the configurations with different node volumes are illustrated. In the right diagram - where a small node volume is considered - tremendous negative pressure values occur within the different pipe ends, while at the end of the pipe no cavitation appears. Of course, the negative amplitudes must not be interpreted as negative pressure levels, but the linear wave propagation model leads to this result. However, cavitation, bad noise and additional mechanical stress of the pipe may be expected. Obviously, the small node volume enables a sharp broad band excitation for the main inductance and, thus, pressure

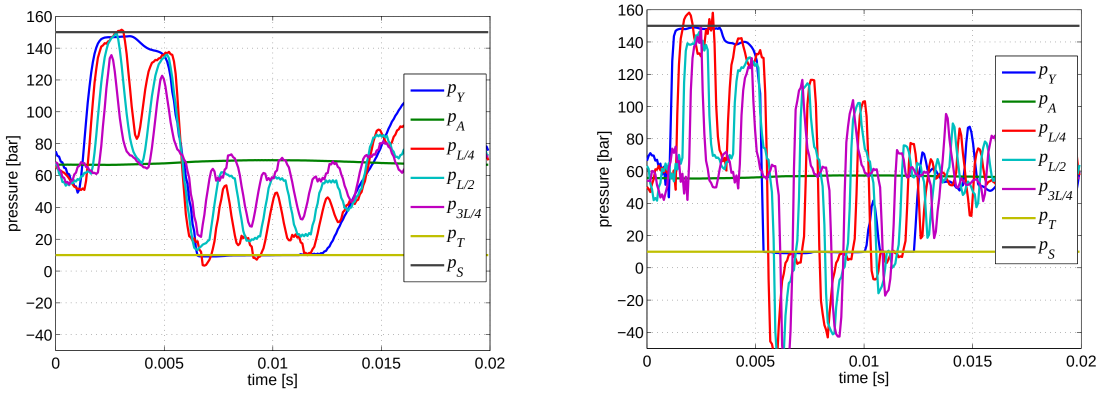

(a) $V_Y = 0.15l$ (b) $V_Y = 0.015l$

Figure 4.14.: Distributed pressure simulations

waves of very high magnitude are travelling through the pipe. Comparing both results of Fig. 4.14 the oscillations at the different locations show the same phase shift. Thus, this phenomenon represents the $\lambda/2$-resonance of the inductance pipe as illustrated in Fig. 4.15. This resonance effect occurs at the second natural frequency

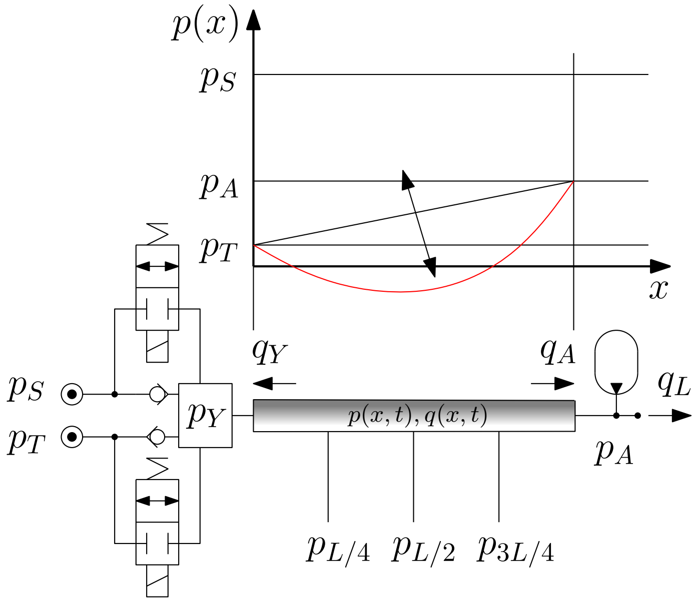

Figure 4.15.: $\lambda/2$-resonance in the main inductance

$$f_{\lambda/2} = \frac{c_0}{2L} \tag{4.63}$$

of the pipe, which is strictly determined by the length of the pipe line and the fluid parameters. The $\lambda/2$-resonance is usually much higher than the switching frequency, but the broad band excitation due to switching in combination with a small node volume provokes this resonance effect. Basically, there exist two different possibilities to reduce the $\lambda/2$-resonance. On the one hand, the diameter of the inductance can be reduced to achieve a higher damping in the pipe inductance. But this also affects the main resistance of the pipe and, thus, the efficiency will be decreased. On the other hand, a larger node volume prevents a high frequency excitation due to its high capacity, which results in a low pass characteristics. But this will cause a reduction of the efficiency due to the rising charging losses. Thus, a trade-off between both mentioned methods may be intended. Possibly, there exist further strategies to cope with the cavitation problem in the pipe inductance, but an investigation of such strategies was not carried out in this work.

For a convenient control of a hydraulic drive as depicted in Fig. 1.13 the converter characteristics have to be compensated. Therefore, the calculations must be carried out in both flow directions. In Fig. 4.16 the simulation results of both flow rate directions are illustrated, where p_A is a function of the duty ratio κ and the load flow rate q_L. For a reasonable compensation, the characteristics of Fig. 4.16 must be transformed to

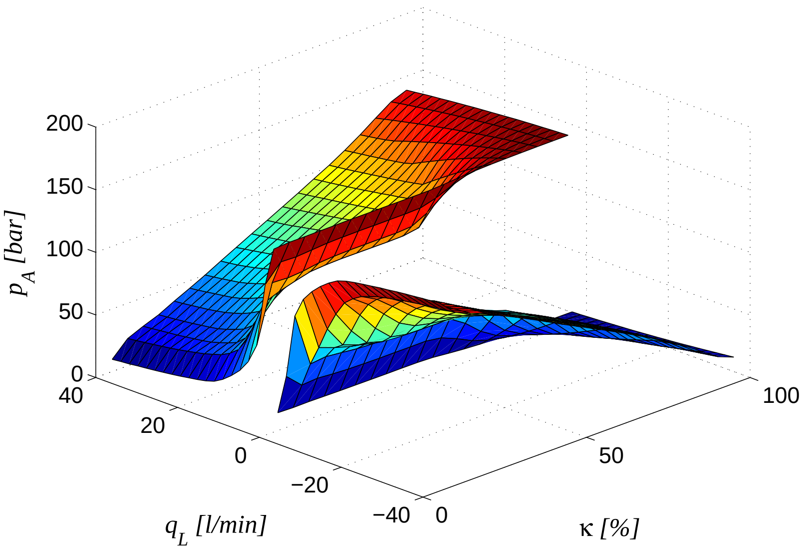

Figure 4.16.: Full converter characteristics $p_A = f(\kappa, q_L)$

the form of κ as a function of p_A and q_L, as depicted in Fig. 4.17. In other words the necessary duty ratio κ for the required power at the load is determined. The sign of κ corresponds to the direction of the flow rate at the load and thus through the converter. The characteristics shown in Fig. 4.17 are used for the implementation of appropriate control strategies, which will be considered in the following chapter.

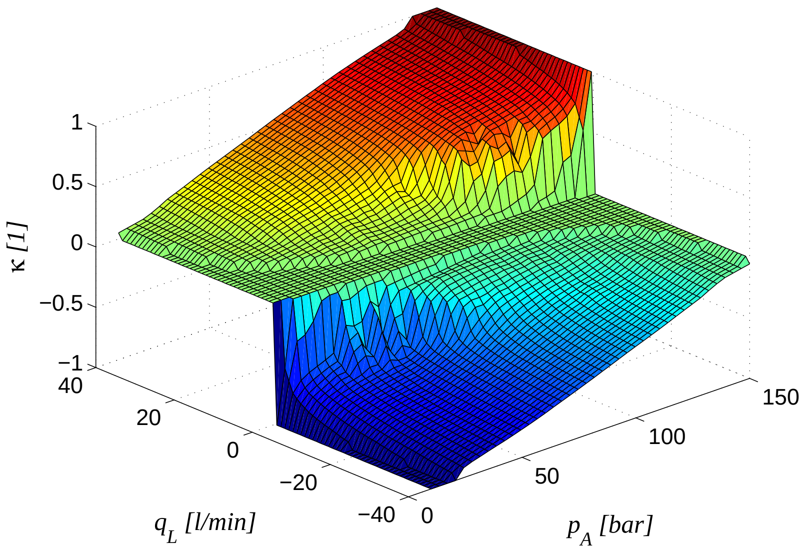

Figure 4.17.: Full converter characteristics $\kappa = f\left(q_L, p_A\right)$

5. Controller Design

A representative test case of an HBC is the position control of a linear hydraulic drive according to Fig. 5.1. This drive controls the vertical position of a dead load m under

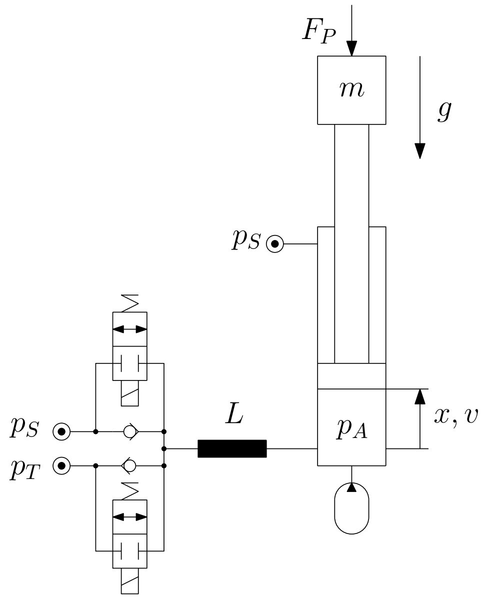

Figure 5.1.: HBC-controlled linear drive

a stepwise process force F_P. The differential cylinder operates in plunger mode, which means, that its annulus chamber is permanently connected to supply pressure. The HBC is connected to the piston sided chamber. For simplicity, the converter is directly mounted to the cylinder. Thus, the pressure attenuator of the HBC is directly connected to the piston chamber. Assuming an accumulator qualified for fast switching hydraulic systems, i.e., with a large enough cross-section area at its inlet, the pressure in the accumulator equals the pressure in the cylinder. The pressure attenuator at the output of the converter is a critical component of the configuration, since it makes the hydraulic system soft. This property lowers the natural frequency of the hydraulic drive, which makes a common industrial controller design inadequate. Moreover, the gas spring of the accumulator has a highly nonlinear characteristic if a large part of the pressure range is actually used. For those reasons different control strategies will be considered in this chapter. At first the performance of a P-controller is presented, which is the most simple and, thus, most common controlling method. Since it has strong deficiencies more sophisticated controller designs will be investigated. Most promising is a nonlinear flatness based controller.

5.1. Model for Synthesis

For a suitable control of the linear drive the pressure fluctuation in the cylinder due to the switching process must be negligibly low. For this reason the accumulator has to be designed sufficiently large, which makes the load system soft. If the drive is designed properly, the resonator consisting of the dead load m and the gas spring in the accumulator has a natural frequency, which is much lower than the switching frequency of the converter. This frequency gap allows to split up the configuration from Fig. 5.1 into two subsystems with fairly different time constants, as depicted in Fig. 5.2. Since the partial system of the

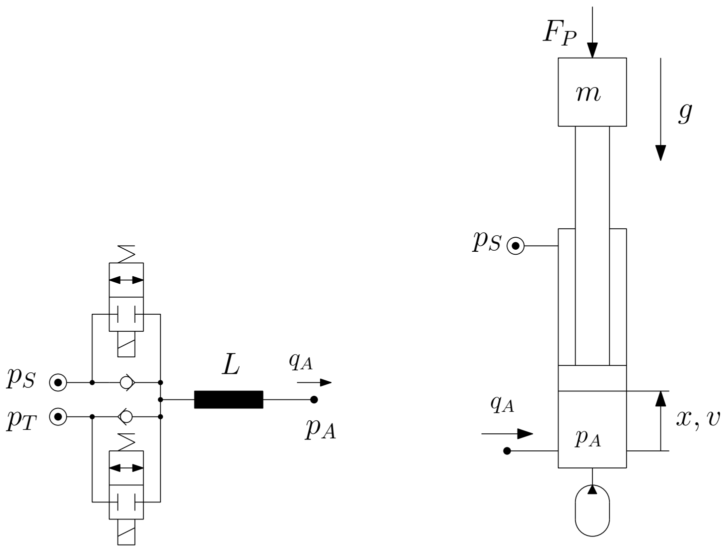

(a) Converter system (b) Load system

Figure 5.2.: System segmentation

converter according to Fig. 5.2a represents a much faster system than the load system, the dynamics of the converter can be neglected and the mean value of flow rate q_A in Fig. 5.2b can be assumed to be constant over one switching cycle. The characteristics of the converter must be compensated by the steady state characteristics shown in Fig. 4.17. Thus, the dynamic model for the synthesis of the drive is reduced to the configuration depicted in Fig. 5.2b. Using the momentum balance of the mechanical part of the system and, applying the accumulator model according to Eq. (4.19), the resulting nonlinear autonomous dynamic system reads

$$\begin{bmatrix} \dot{x} \\ \dot{v} \\ \dot{p}_A \end{bmatrix} = \begin{bmatrix} v \\ \frac{1}{m}\left(p_A A_1 - p_S A_2 - mg - d_v v - F_P\right) \\ \frac{p_A \varkappa}{V_A \left(\frac{p_{0_G}}{p_A}\right)^{\frac{1}{\varkappa}}}\left(-A_1 v + q_A\right) \end{bmatrix}, \tag{5.1}$$

with the state vector

$$\mathbf{x} = \begin{bmatrix} x \\ v \\ p_A \end{bmatrix} \tag{5.2}$$

and the control input q_A. The equilibrium point of the system calculates to

$$\begin{bmatrix} v_{OP} \\ p_{A_{OP}} \\ q_{A_{OP}} \end{bmatrix} = \begin{bmatrix} 0 \\ \frac{1}{A_1}\left(p_S A_2 + mg + F_P\right) \\ 0 \end{bmatrix} \tag{5.3}$$

under the assumption, that the process force F_P is known. Examining Eq. (5.1) it becomes clear, that in fact the capacity of a large accumulator (V_A) for pressure attenuation makes the system soft; but this deficiency can be compensated, at least by an advanced controller concept.

5.2. Models for Simulation

Due to the simplifications, which were made in the modelling process, the performance of the different controller designs have to be analysed in a number of simulation experiments. The major simplification is represented by the averaging of the converter dynamics. Hence, the performance of the closed loop system has to be tested in fact on a PWM-controlled simulation model, i.e., on a switching model. Since the dynamic system of Eq. (5.1) accounts only for a linear viscous friction, also an advanced friction model is applied for the simulation tests. Furthermore, the HBC-controlled linear drive shall be compared with a conventional proportional drive. For this purpose a simulation model of an equivalent resistance controlled differential cylinder drive will be derived in this section.

5.2.1. Simulation Model of the HBC

For the simulations, which are presented in the following sections, the dynamics of the HBC is modelled in the time domain. All modelled physical effects of the converter are considered in accordance with Chapter 4. The different switching valves are controlled with respect to the actual duty ratio κ at a constant switching frequency. Thereby, the duty ratio remains constant for one switching period T_P. After each period, κ is updated by the actual set value of the controller. The switching dynamics of the valves is modelled by a ramp having the same effective switching time as the real valves. Furthermore, a valve overlap of 50% of the full spool stroke is considered. The dynamics of the check valves is neglected, as already pointed out in Chapter 4. The effect of wave propagation in the converter inductance is modelled by a linear method of characteristics (MOC) according to [24]. The load model - Fig. 5.2b - comprising the dead load, the cylinder and the accumulator is basically modelled according to Eq. (5.1), but with the difference, that the compressibility of the oil in the piston sided chamber and in the accumulator is taken into account. Moreover, the term of the friction force $F_F = d_v v$ is replaced by a static friction model according to [18], which reads

$$F_F = d_v v + \mathrm{sign}(v) \left(d_c + (r_H - d_c)\, e^{-\left(\frac{v}{v_0}\right)^2} \right), \tag{5.4}$$

where d_v and d_c denote the viscous and the Coulomb friction, and, r_H the stiction coefficient. The parameter v_0 represents the reference velocity of the Stribeck-effect. The friction force F_F from Eq. (5.4) is illustrated in Fig. 5.3 at an exemplary parameter set. Furthermore, the stick-slip effect of the piston movement is modelled by the structural

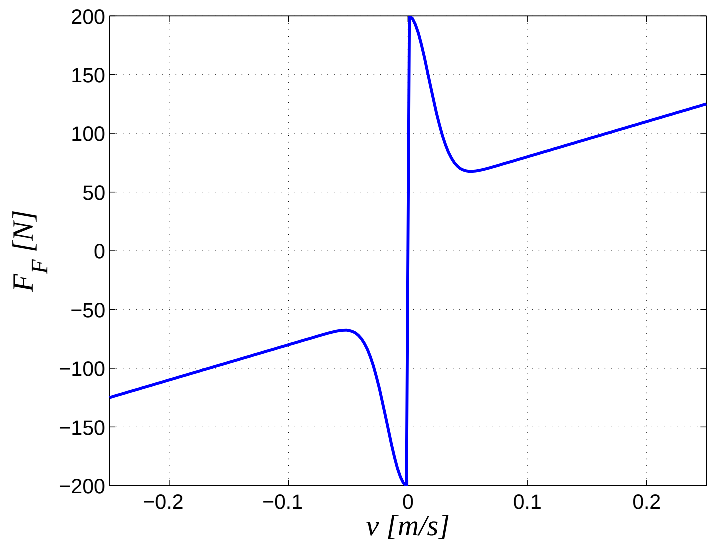

Figure 5.3.: Static friction model

change of state in the stiction case[1]. The main simulation parameters of the HBC are equal to the parameters of the TFDI simulations, as listed in Tab. A.4. The cross-section ratio of the differential cylinder is approximately 2 : 1. Hence, in case of equilibrium and without external forces the pressure in the piston sided chamber is half of the supply pressure in the annulus chamber. Thus, the difference between the pressure p_A and either

[1]See Section A.5.2.

the tank pressure or the supply pressure is nearly equal. This pressure symmetry provides best conditions for a good energetic performance in forward and recuperation mode. In case of an a priori known process force the cross-section ratio must be adapted to provide best conditions for an efficient operation in both flow directions. The simulation parameters of the differential cylinder, the dead load and the friction model are summed up in Tab. A.6. All simulations were carried out in *Matlab/Simulink*™. The block diagram of the HBC simulation model is depicted in Fig. 5.4.

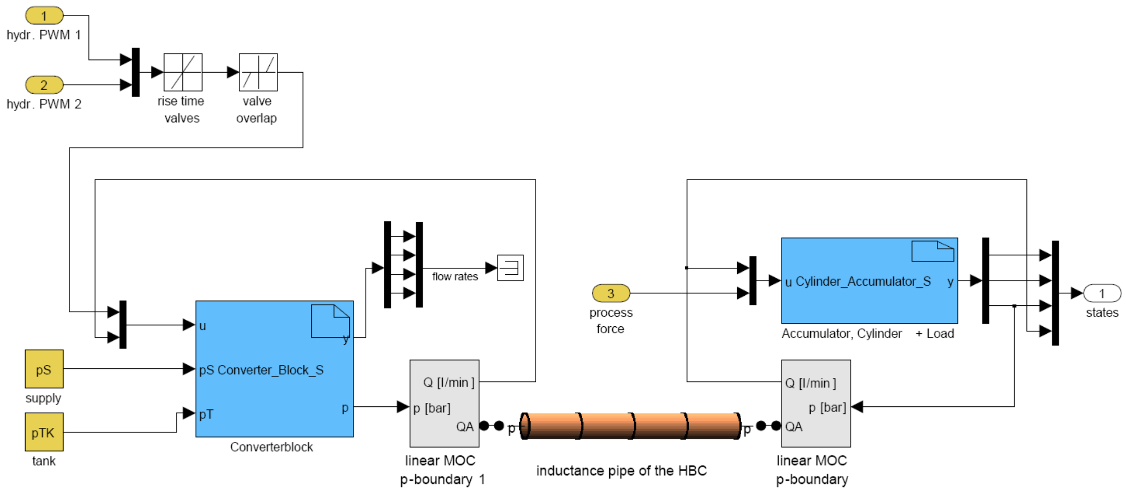

Figure 5.4.: Simulation model of the HBC in *Simulink*™

5.2.2. Model for Comparison

As pointed out in Subsection 2.1.4, the considered HBC configuration acts basically as a 3/3-proportional valve, but at higher efficiency. For this reason the performance of the HBC will be compared to a hydraulic proportional drive (HPD) according to Fig. 5.5. The dynamics of the cylinder is identical to the simulation model described in the previous Subsection 5.2.1. Also the same friction model of the piston is taken in to account. Furthermore, the dynamics of the proportional valve is considered by a *PT-2* behaviour with a cut-off frequency of about $f_c \approx 30\,Hz$. This dynamic valve response is common for lower-cost proportional valves, but of course not for modern advanced servo valves. The annulus chamber of the cylinder is also connected to supply pressure permanently. Since the pressure in the piston sided chamber is proportionally controlled, i.e., by metering of the valve edge, the size of the valve does not play any role in the simulations, at least if no saturation effects occur, what is assumed in this analysis.

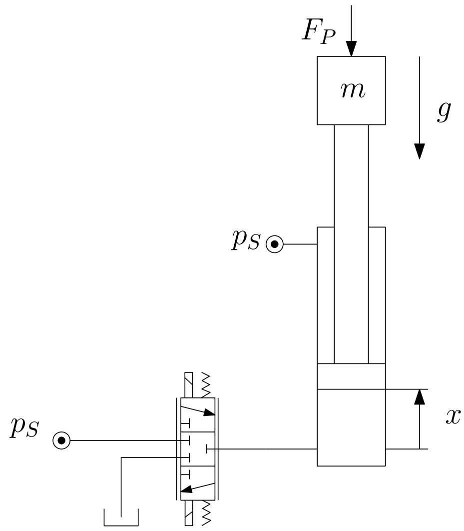

Figure 5.5.: Hydraulic proportional drive

5.3. Linear Controller Design

In the following section two different controller designs are investigated. The first concept is the most simple and, thus, most common controller design in industrial applications, the P-controller. The second approach is based on frequency domain methods, which accounts for some linearised dynamic effects of the plant. Today, most of such linear controllers are implemented on digital signal processing units. The theory of linear control systems provides the possibility to design time discrete controllers for a proper implementation on such industrial computers. However, since in this section just the dynamic behaviour of the closed loop system is investigated it is sufficient to treat the continuous case for simulations.

5.3.1. P-Controller

The proportional controller according to Fig. 5.6 is the most simple closed loop controller for the investigated system. But, the proportional controller does not use any information of the dynamics of the plant. If the plant is a nonlinear system, the closed loop dynamics is nonlinear too. For instance, to obtain an almost linear dynamic performance of the considered drive the controller gain would have to be adapted depending on the pressure p_A for each direction of movement. So, in most cases the design of the controller is carried out empirically, as also in the considered case. The controller gain was increased until the stability border of the closed loop was crossed, i.e., where the system starts to oscillate. In Fig. 5.7 the simulation results of the tracking performance of the P-controller at a $0.5\,Hz$ sinusoidal trajectory are illustrated.

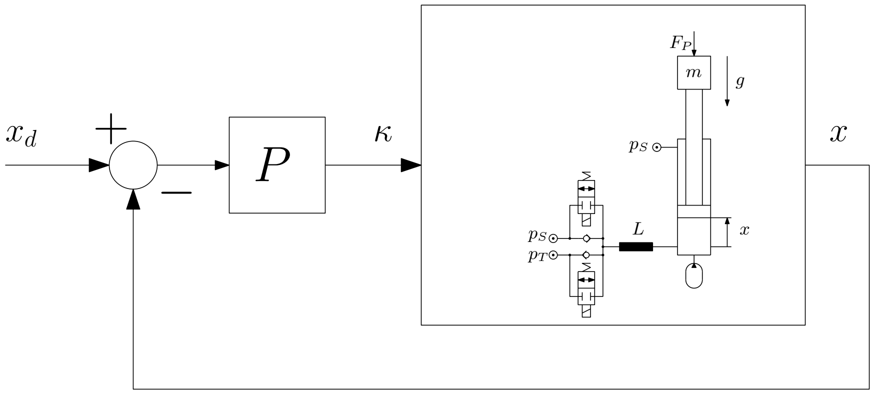

Figure 5.6.: Control scheme with P-controller

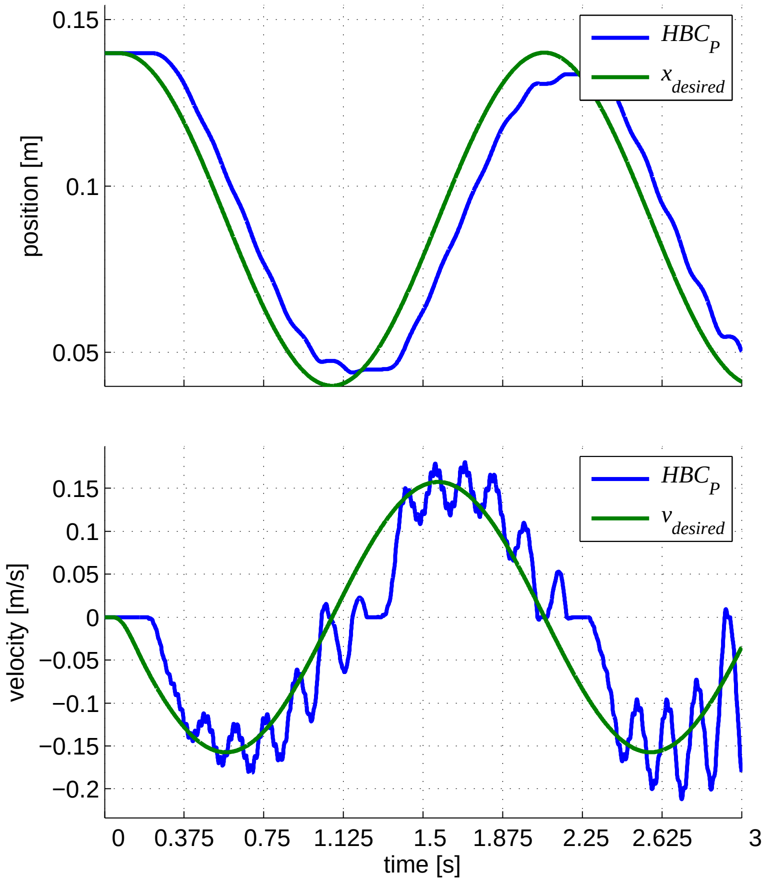

Figure 5.7.: Simulation of sinusoidal trajectory with P-controller

The poor performance of this configuration can be examined especially from the velocity signal in the lower diagram of Fig. 5.7. The considerable oscillations in the piston velocity occur due to the softness of the gas spring mass oscillator and also stick slip effects are present. If the controller gain is lowered to avoid the oscillations, the tracking performance is worsened.

But not only the results of the trajectory tracking are poor. In case of a certain process force a large deviation of the desired position is expected due to the softness of the closed loop system, if a P-controller is applied to the HBC. The corresponding simulation results are depicted in Fig. 5.8. There, the performance of the HBC is compared to a conventional

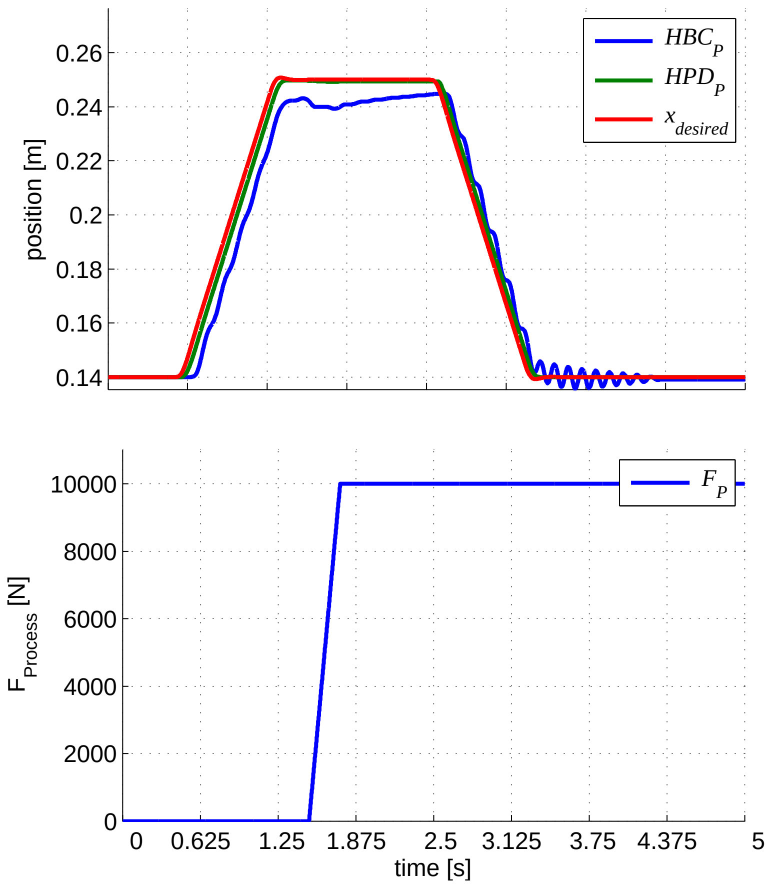

Figure 5.8.: Simulation of applied process force with P-controller

hydraulic proportional drive (HPD) according to Section 5.2.2. Also the HPD is only P-controlled. But due to the high stiffness of the HPD no relevant deviation of the desired position can be examined, even if a process force is applied.

5.3.2. Compensation Controller

In order to improve the closed loop response of the HBC controlled linear drive an advanced linear concept is investigated in the following. The main intention is to compensate the natural frequency of the drive system by a linear compensation controller, which is based on frequency shaping methods. For this purpose the system must be linearised around a certain operating point to obtain a linear transfer function of the considered system. This linearisation of the system dynamics according to Eq. (5.1) reads

$$\dot{\mathbf{x}} = \mathbf{A}\mathbf{x} + \mathbf{b}q_A \tag{5.5}$$

$$y = \mathbf{c}^\top \mathbf{x} \tag{5.6}$$

with

$$\mathbf{A} = \begin{bmatrix} 0 & 1 & 0 \\ 0 & -\frac{d_v}{m} & \frac{A_1}{m} \\ 0 & -\frac{A_1\left(\frac{p_{0_G}}{p_{A_{OP}}}\right)^{-\frac{1}{\varkappa}} \varkappa p_{A_{OP}}}{V_A} & 0 \end{bmatrix}, \tag{5.7}$$

$$\mathbf{b} = \begin{bmatrix} 0 \\ 0 \\ \frac{\left(\frac{p_{0_G}}{p_{A_{OP}}}\right)^{-\frac{1}{\varkappa}} \varkappa p_{A_{OP}}}{V_A} \end{bmatrix}, \tag{5.8}$$

$$\mathbf{c}^\top = \begin{bmatrix} 1 & 0 & 0 \end{bmatrix}, \tag{5.9}$$

and, the state vector $\mathbf{x} = [x \; v \; p_A]^\top$. Selecting the equilibrium of Eq. (5.3) as operating point, the linear transfer function of the drive calculates to

$$\begin{aligned} G_{LD}(s) &= \mathbf{c}^\top (s\mathbf{I} - \mathbf{A})^{-1} \mathbf{b} \\ &= \frac{1}{A_1} \frac{1}{s\left(s^2 \frac{V_A m \left(p_{0_G} A_1\right)^{\frac{1}{\varkappa}}}{A_1 \varkappa (p_S A_2 + mg + F_P)^{\frac{\varkappa+1}{\varkappa}}} + s \frac{d_v V_A \left(p_{0_G} A_1\right)^{\frac{1}{\varkappa}}}{A_1 \varkappa (p_S A_2 + mg + F_P)^{\frac{\varkappa+1}{\varkappa}}} + 1\right)} \end{aligned} \tag{5.10}$$

with the identity matrix $\mathbf{I}$. Since $G_{LD}(s)$ is a simple type transfer function a common frequency shaping method can be applied. The simple compensation controller results in

$$R(s) = \frac{V_C A_1 \left(s^2 \frac{V_A m \left(p_{0_G} A_1\right)^{\frac{1}{\varkappa}}}{A_1 \varkappa (p_S A_2 + mg + F_P)^{\frac{\varkappa+1}{\varkappa}}} + s \frac{d_v V_A \left(p_{0_G} A_1\right)^{\frac{1}{\varkappa}}}{A_1 \varkappa (p_S A_2 + mg + F_P)^{\frac{\varkappa+1}{\varkappa}}} + 1\right)}{\frac{s^2}{\omega_C^2} + 2\zeta_C \frac{s}{\omega_C} + 1}, \tag{5.11}$$

with ω_C, ζ_C and V_C as the major design parameters. Of course, the expectation to compensate exactly the resonance frequency of the transfer function $G_{LD}(s)$ from Eq. (5.10) in practice is quite optimistic. But for simulation experiments this compensation can be done. In Fig. 5.9 the relevant transfer functions of the controller design are illustrated as well as the transfer function of the closed loop system

$$\begin{aligned} T_{y/r} &= \frac{R(s) G_{LD}(s)}{1 + R(s) G_{LD}(s)} \\ &= \frac{V_C}{\frac{s^3}{\omega_C^2} + 2\zeta_C \frac{s^2}{\omega_C} + s + V_C}. \end{aligned} \tag{5.12}$$

The controller parameters were designed to assure the stability of the closed loop system,

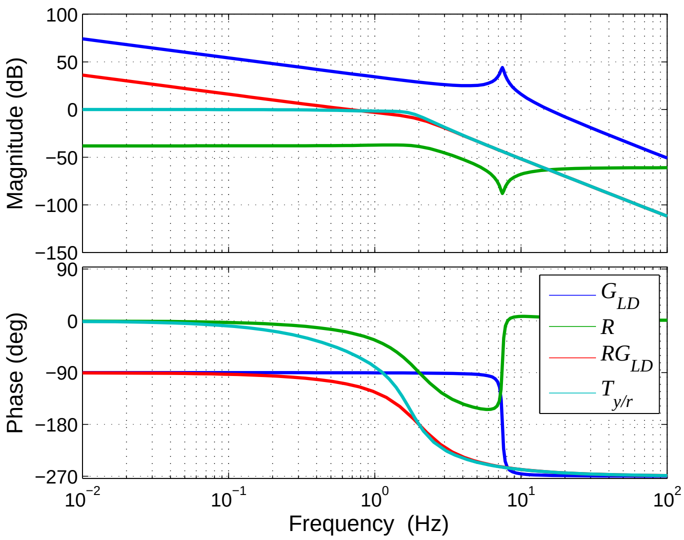

Figure 5.9.: Bode plots of the compensation controller design

i.e., that the phase margin at the gain cross over frequency is sufficiently large. This results in a much slower dynamics of the closed loop system than the compensated natural frequency of $G_{LD}(s)$.

The block diagram of the linear compensation controller is illustrated in Fig. 5.10. The

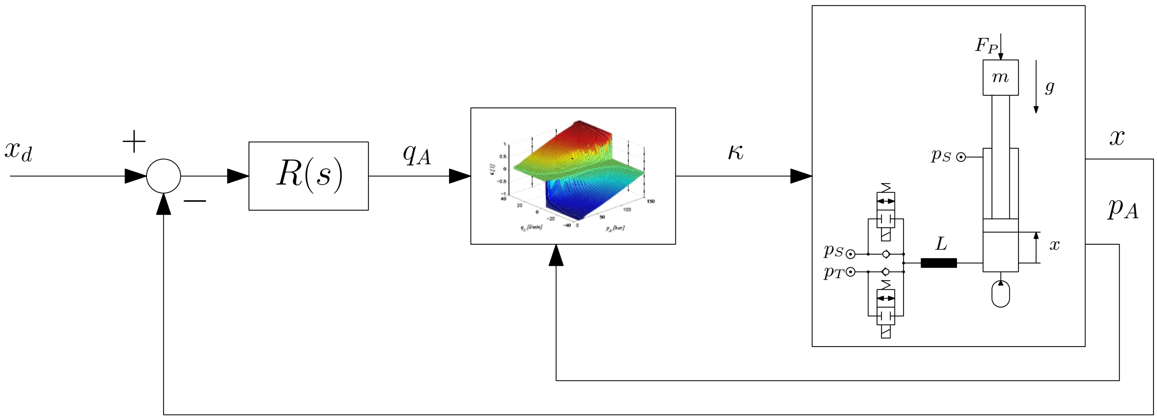

Figure 5.10.: Control scheme of the compensation controller

control input of the system (5.5) and, thus, the output of the controller is the flow rate q_A. The control input of the HBC is the duty ratio κ. To transform the output of the controller to the input of the HBC the inverted static converter characteristics according to Fig. 4.17 of Subsection 4.3.3 have to be applied. At this point it has to be remarked, that the pressure p_A in the cylinder must be measured for the correct compensation of the converter characteristics. The main simulation results are depicted in Fig. 5.11, where the system response with the different controller concepts introduced so far are compared. The performance of the linear compensation controller shows explicitly lower oscillations,

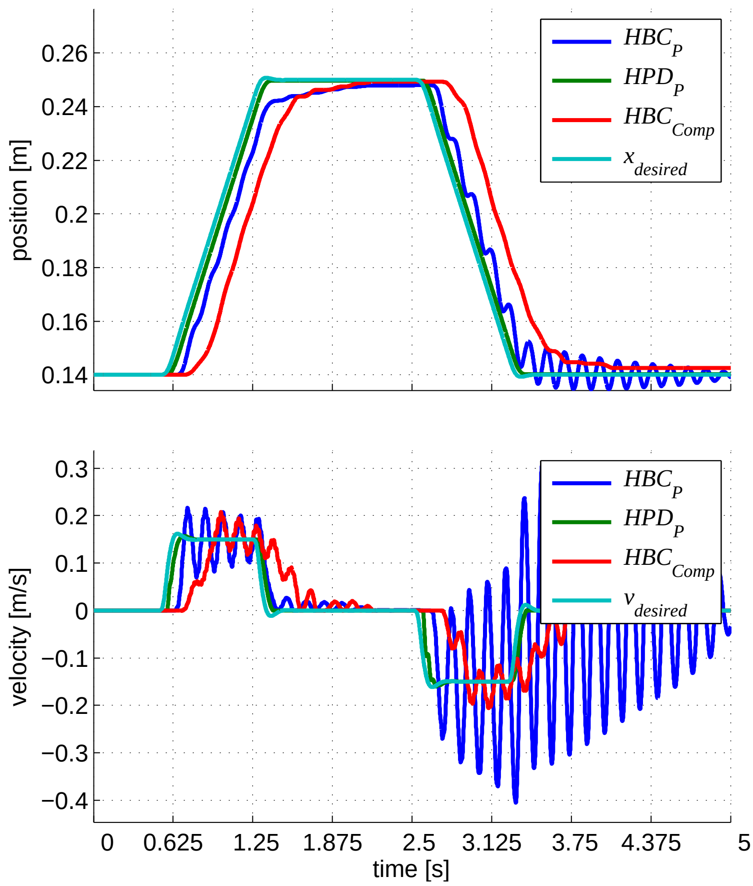

Figure 5.11.: Simulation results with compensation controller

but the response time is worse than of the P-controller for the already mentioned reasons. Although the natural frequency of the drive was exactly compensated by the controller, the oscillation could not be eliminated. This can be explained by the fact, that the natural frequency of the nonlinear system in this working point does not correspond exactly to the linearised system due to the switching, the stick slip effect and other nonlinearities. Another reason for the remaining oscillations is, that the stability of the control error and, thus, the compensation of the natural frequency are only guaranteed in rest positions. Possibly, the performance could be improved by a linear time invariant state controller, but also with this approach the stability of the closed loop system can only be proven in certain operating points. But this would not be feasible for trajectory tracking.

Another possibility would be a state controller based on the linearisation along a certain trajectory. In fact this would improve the performance and the accuracy, but this would also lead to a time variant system of state space equations. The effort for implementation of such a controller would be nearly the same as of a nonlinear controller, which will be presented in the following section.

5.4. Flatness Based Control

The control of nonlinear systems along certain trajectories with linear methods results sometimes in a meager performance concerning accuracy. Furthermore, in most cases the stability of the tracking error can not be proven. The gas spring of the pulsation damper at the output of the converter represents a nonlinearity, which cannot be compensated with linear controllers, at least if a linearisation around a certain working is applied. In the following it will be shown, that the considered differential cylinder driven by an HBC belongs to the special class of flat systems. This property allows a comprehensive analysis and the design of a powerful controller.

The concept of flatness was introduced by M. Fliess et al. in the 1990ies, see for instance [6]. The basic awareness was the classification of certain nonlinear systems, that behave like linear ones by applying a special type of state feedback. This property of dynamic systems is tightly related to the method of input-output linearisation of nonlinear systems, which can be found, e.g., in [11]. Another access to flatness is the dynamical invertibility of flat systems. A flat system can be inverted by a feedforward control - depending on the flat output and its derivatives with respect to time - which controls the system along the desired trajectories at least if no disturbances occur. For a comprehensive treatment of the concept of flatness, some knowledge in differential geometry is necessary. But, in this thesis only the basic definition of flatness and at least some applied mathematical terms are presented in accordance with the literature. To keep the analysis simple, the following considerations focus more on the physical view than on mathematical theory.

The application of the flatness based approach can be separated into three major design steps, which are presented in the following subsections. First, a feedforward control will be calculated, which enables an exact inversion of the system (5.1). Hence, in case of no disturbances the output of the system follows the desired trajectory. Therefore, a flat output y must be found, which allows the intended inversion of the system. Second, due to disturbances certain deflections from the desired motion are expected. Thus, a state feedback control will be designed to assure that the system follows the desired trajectories. And third, the state feedback control requires the knowledge of the complete system state. Since only certain state quantities can be measured a state observer must be designed.

The theoretical background for the flatness considerations in this thesis stems from [33, 34, 37]. Further interesting literature concerning flatness is given, for instance, by [22, 35].

5.4.1. Flat Output and Feedforward Control

In a flat system the control input can be formulated as a function of the flat output and a finite number of its derivatives with respect to time. With this relation between output and control input, the search of the flat output can be started at the differential equation for the pressure p_A

$$\dot{p}_A = \frac{p_A \varkappa}{V_A \left(\frac{p_{0_G}}{p_A}\right)^{\frac{1}{\varkappa}}} \left(-A_1 v + q_A\right), \tag{5.13}$$

which contains the input q_A of system (5.1). In the following, the individual differential equations of system (5.1) are considered as a sort of conditional equations. Thus, Eq. (5.13) represents such an equation for the pressure p_A, which in turn has influence on the mechanical momentum equation

$$m\dot{v} = p_A A_1 - p_S A_2 - mg - d_v v - F_P. \tag{5.14}$$

This equation represents another conditional equation for the velocity v. In Eq. (5.14) the unknown process force F_P is another input variable of the system, which is assumed to be constant since no further information about F_P is available. The momentum equation (5.14) determines the velocity v, which is conditional for the remaining system equation

$$\dot{x} = v. \tag{5.15}$$

Since no further conditional development is possible, a flat output is given by

$$y = x. \tag{5.16}$$

In the concrete case, a possible interpretation of the flat output would be, that x is the state variable with the largest dynamical distance with respect to the input q_A.

The next step is the calculation of a feedforward control, which must be a function of the flat output and its derivatives with respect to time. Considering system (5.1) and the chosen output (5.16) the first and the second derivative with respect to time read

$$\dot{y} = \frac{\partial y}{\partial \mathbf{x}} \dot{\mathbf{x}} = v \tag{5.17}$$

$$\ddot{y} = \frac{\partial v}{\partial \mathbf{x}} \dot{\mathbf{x}} = \frac{1}{m} \left(p_A A_1 - p_S A_2 - mg - d_v v - F_P\right), \tag{5.18}$$

where all variables of the system state $\mathbf{x}$ are present. Using Eqs. (5.16) to (5.18) the components of the state $\mathbf{x}$ calculate to

$$
\begin{aligned}
\begin{bmatrix} x \\ v \\ p_A \end{bmatrix} &= \begin{bmatrix} y \\ \dot{y} \\ \frac{1}{A_1}\left(\ddot{y}m + p_S A_2 + mg + d_v \dot{y} + F_P\right) \end{bmatrix} \\
&= \boldsymbol{\psi}_1\left(y, \dot{y}, \ddot{y}\right)
\end{aligned} \tag{5.19}
$$

depending only on the flat output and its derivatives, which is another important property of flat systems. With $\mathbf{u} = [q_A\ F_P]^\top$ the third derivative of y with respect to time reads

$$
\dddot{y} = \frac{\partial \ddot{y}}{\partial \mathbf{x}}\dot{\mathbf{x}} + \frac{\partial \ddot{y}}{\partial \mathbf{u}}\dot{\mathbf{u}} = \frac{1}{m}\left(\dot{p}_A A_1 - d_v \dot{v} - \dot{F}_P\right) \tag{5.20}
$$

$$
= \frac{1}{m}\left(\frac{p_A \varkappa A_1\left(-A_1 v + q_A\right)}{V_A\left(\frac{p_{0_G}}{p_A}\right)^{\frac{1}{\varkappa}}} - \frac{d_v}{m}\left(p_A A_1 - p_S A_2 - mg - d_v v - F_P\right) - \dot{F}_P\right), \tag{5.21}
$$

where the input q_A appears. Since the process force is assumed to be constant $\dot{F}_P$ is zero. At this point it has to be mentioned, that if information about the process force is available this information should be used at all to achieve a better the performance of the feedforward control. But, in this first step of the analysis the linear drive is considered without of a process force, i.e. $F_P = \dot{F}_P = 0$. Thus, solving Eq. (5.21) for q_A leads to the flatness based feedforward control

$$
\begin{aligned}
q_A &= A_1 \dot{y} + \frac{\left(m\dddot{y} + d_v \ddot{y}\right) V_A \left(\frac{p_{0_G} A_1}{p_S A_2 + d_v \dot{y} + m\ddot{y} + mg}\right)^{\frac{1}{\varkappa}}}{\varkappa\left(p_S A_2 + d_v \dot{y} + m\ddot{y} + mg\right)} \\
&= \psi_2\left(y, \dot{y}, \ddot{y}, \dddot{y}\right).
\end{aligned} \tag{5.22}
$$

With the conditions of Eq. (5.16), Eq. (5.19) and Eq. (5.22) it could be shown, that the considered system (5.1) is flat.

The feedforward control from Eq. (5.22) provides an exact inversion of system (5.1), like depicted in Fig. 5.12, at least if no disturbances influence the system.

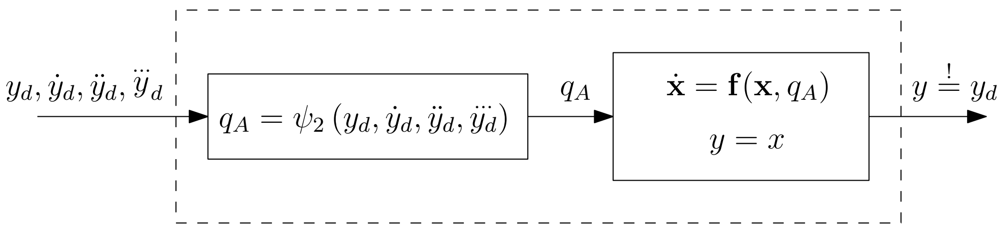

Figure 5.12.: Inversion of system (5.1) with the flatness based feedforward control (5.22)

5.4.2. Controller Design

The flat output and its derivatives from Eqs. (5.16) to (5.18) can be written as

$$\begin{aligned}\begin{bmatrix} y \\ \dot{y} \\ \ddot{y} \end{bmatrix} &= \begin{bmatrix} x \\ v \\ \frac{1}{m}\left(p_A A_1 - p_S A_2 - mg - d_v v - F_P\right) \end{bmatrix} \\ &= \boldsymbol{\psi}_1^{-1}\left(\mathbf{x}\right). \end{aligned} \tag{5.23}$$

This means, that if the state $\mathbf{x}$ is known, the actual flat output y and its derivatives with respect to time are known too. Thus, Eq. (5.23) can be used for a static state feedback. Therefore, the transformed state (5.23) is applied to Eq. (5.22), which results in a state feedback

$$q_A = \widetilde{\psi}_2\left(\mathbf{x}, v_C\right), \tag{5.24}$$

with a new input v_C, which is related to the third derivative of the flat output with respect to time. Furthermore, the trajectory error is defined by

$$\begin{bmatrix} e \\ \dot{e} \\ \ddot{e} \\ \dddot{e} \end{bmatrix} = \begin{bmatrix} y_d - y \\ \dot{y}_d - \dot{y} \\ \ddot{y}_d - \ddot{y} \\ \dddot{y}_d - v_C \end{bmatrix} \tag{5.25}$$

with the input variable v_C of the state feedback (5.24). Hence, with $y = x$ the dynamics of the position error $e = y_d - x$ can be written as

$$\begin{aligned} 0 &= \begin{bmatrix} \gamma_0 & \gamma_1 & \gamma_2 & 1 \end{bmatrix} \begin{bmatrix} y_d - y \\ \dot{y}_d - \dot{y} \\ \ddot{y}_d - \ddot{y} \\ \dddot{y}_d - v_C \end{bmatrix} \\ &= \dddot{y}_d - v_C + \gamma_2 \ddot{e} + \gamma_1 \dot{e} + \gamma_0 e, \end{aligned} \tag{5.26}$$

which represents a linear differential equation. The coefficients γ_0, γ_1 and γ_2 must guarantee asymptotic stability. Extracting v_C from Eq. (5.26) the resulting control law reads

$$v_C = \dddot{y}_d + \gamma_2 \ddot{e} + \gamma_1 \dot{e} + \gamma_0 e \tag{5.27}$$

with the parameters $\gamma_i,\ i = 0, 1, 2$. The block diagram of this flatness based control is depicted in Fig. 5.13. To assure asymptotic stability of the trajectory error all poles of Eq. (5.26) must have negative real parts. Hence, the roots of the cubical characteristic

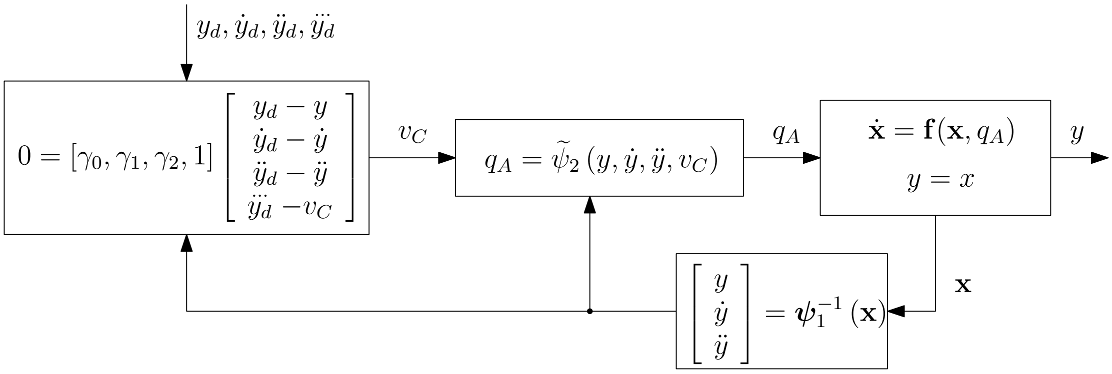

Figure 5.13.: Flatness based control of system (5.1)

polynomial

$$s^3 + \gamma_2 s^2 + \gamma_1 s + \gamma_0 = 0 \tag{5.28}$$

must be investigated. Since a cubic equation has at least one real root, Eq. (5.28) can be written either as

$$(s + \beta_1)(s + \beta_2)(s + \beta_3) = 0 \tag{5.29}$$

or as

$$(s + \beta_3)\left(s^2 + \beta_2 s + \beta_1\right) = 0 \tag{5.30}$$

with the parameters $\beta_i > 0$. In case of three real roots (Eq. (5.29)) of the characteristic polynomial the controller parameters read

$$\begin{bmatrix} \gamma_0 \\ \gamma_1 \\ \gamma_2 \end{bmatrix} = \begin{bmatrix} \beta_1\beta_2\beta_3 \\ \beta_1\beta_2 + \beta_1\beta_3 + \beta_2\beta_3 \\ \beta_1 + \beta_2 + \beta_3 \end{bmatrix}. \tag{5.31}$$

Since the linearisation around a certain operating point of system (5.1) leads to a characteristic polynomial according to Eq. (5.30), i.e. with complex roots, the controller parameters can be designed to

$$\begin{bmatrix} \gamma_0 \\ \gamma_1 \\ \gamma_2 \end{bmatrix} = \begin{bmatrix} \beta_1\beta_3 \\ \beta_1 + \beta_2\beta_3 \\ \beta_2 + \beta_3 \end{bmatrix} \tag{5.32}$$

with the resulting poles

$$s_{1,2} = -\frac{1}{2}\beta_2 \pm \sqrt{\frac{\beta_2^2}{4} - \beta_1} \tag{5.33}$$

$$s_3 = -\beta_3, \tag{5.34}$$

according to the dynamics of the linearised system (5.5). Since the flat output $y = x$ represents a position, its third derivative $\dddot{y}$ has the unit $\frac{m}{s^3}$. Thus, the units of γ_0, γ_1 and γ_2 read $\frac{1}{s^3}$, $\frac{1}{s^2}$ and $\frac{1}{s}$, respectively. Hence, the choice of the poles for the closed loop system allows a physical interpretation as a PDDD-controller for the position of the linear hydraulic drive.

5.4.3. Observer Design

The static state feedback (5.23) requires the knowledge of the complete state $\mathbf{x}$ of system (5.1). But in common industrial applications no measurement of the piston velocity is provided. Furthermore, for cost reasons it is better to avoid the measurement of the pressure p_A. Hence, the whole system state cannot be measured and, thus, a dynamic state observer has to be designed. The following considerations are carried out in accordance with [7, 34].

Since the investigated system (5.1) is nonlinear, an observer of the form

$$\dot{\hat{\mathbf{x}}} = \mathbf{f}\left(\hat{\mathbf{x}}, \hat{u}\right) + \mathbf{L}(t)\left(\eta - h(\hat{\mathbf{x}})\right), \ \hat{\mathbf{x}}(0) = \hat{\mathbf{x}}_0 \tag{5.35}$$

with the estimated state $\hat{\mathbf{x}}$, the generally time varying observer gain $\mathbf{L}(t)$, and the measured quantity η, is intended. Under the assumption that the flatness based control keeps the system state sufficiently close to the desired trajectories $\hat{u} = \hat{q}_A$ represents the input of the closed loop system. The intended flatness based control with a nonlinear observer is depicted in Fig. 5.14.

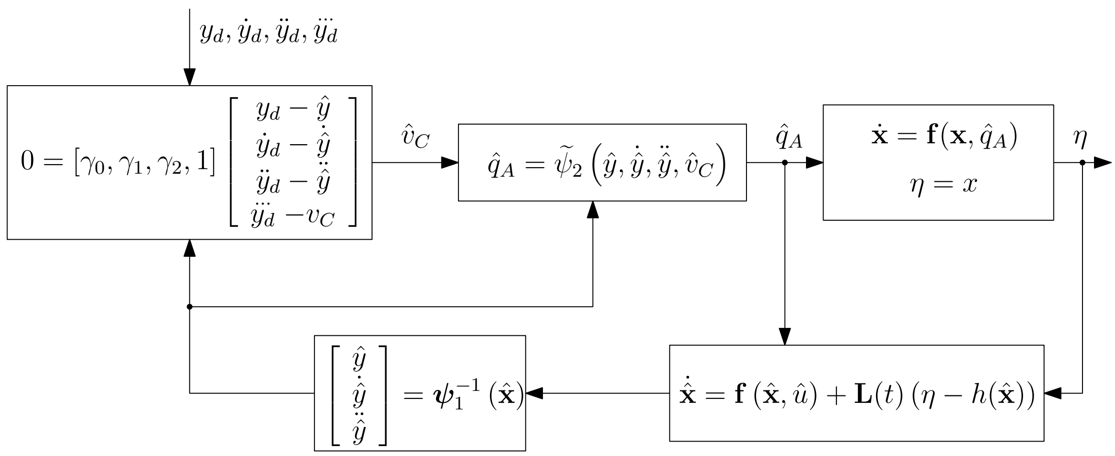

Figure 5.14.: Block diagram of the intended control exploiting a nonlinear observer

The dynamics of the estimation error $\hat{\mathbf{e}} = \hat{\mathbf{x}} - \mathbf{x}$ reads

$$\dot{\hat{\mathbf{e}}} = \mathbf{f}\left(\hat{\mathbf{x}}, \hat{u}\right) - \mathbf{f}\left(\mathbf{x}, \hat{u}\right) + \mathbf{L}(t)\left(h(\mathbf{x}) - h(\hat{\mathbf{x}})\right), \tag{5.36}$$

which represents a system of nonlinear differential equations. For a convenient analysis Eq. (5.36) must be linearised. Since the hydraulic drive is designed to move certain loads a linearisation around a working point is not sufficient. Thus, the nonlinear estimation error system (5.36) can be linearised around the desired trajectories under the assumption that the control keeps the system state sufficiently close to the desired trajectories. This assumption leads to a linear time varying design problem. The linearisation of Eq. (5.36) along the desired trajectory calculates to

$$\dot{\hat{\mathbf{e}}} = \underbrace{\left[\mathbf{A}\left(t\right)\widehat{\Delta\mathbf{x}} + \mathbf{b}\left(t\right)\Delta u + \mathbf{L}(t)\left(\mathbf{c}^{\top}\Delta\mathbf{x} - \mathbf{c}^{\top}\widehat{\Delta\mathbf{x}}\right)\right]}_{\text{observer}} - \underbrace{\left[\mathbf{A}\left(t\right)\Delta\mathbf{x} + \mathbf{b}\left(t\right)\Delta u\right]}_{\text{system}} \tag{5.37}$$

with

$$\mathbf{A}(t) = \left.\frac{\partial}{\partial\mathbf{x}}\mathbf{f}\left(\mathbf{x},u\right)\right|_{\mathbf{x}_d(t),u_d(t)}, \tag{5.38}$$

$$\mathbf{b}(t) = \left.\frac{\partial}{\partial u}\mathbf{f}\left(\mathbf{x},u\right)\right|_{\mathbf{x}_d(t),u_d(t)}, \tag{5.39}$$

$$\mathbf{c}^{\top} = \left.\frac{\partial}{\partial\mathbf{x}}h\left(\mathbf{x}\right)\right|_{\mathbf{x}_d(t),u_d(t)} \tag{5.40}$$

and the output equation $y = h\left(\mathbf{x}\right)$ of the original nonlinear system. Substituting $\widehat{\Delta\mathbf{x}} = \hat{\mathbf{x}} - \mathbf{x}_d$, $\Delta\mathbf{x} = \mathbf{x} - \mathbf{x}_d$, $\hat{\mathbf{e}} = \hat{\mathbf{x}} - \mathbf{x}$ and $\Delta u = \hat{u} - u_d$ into Eq. (5.37) the linearised observer dynamics of Eq. (5.36) follows to

$$\dot{\hat{\mathbf{e}}} = \left(\mathbf{A}(t) - \mathbf{L}(t)\mathbf{c}^{\top}\right)\hat{\mathbf{e}}. \tag{5.41}$$

The time varying observer gain $\mathbf{L}(t)$ in Eq. (5.41) has to be designed for asymptotic stability of the estimation error $\hat{\mathbf{e}}$. But, before the observer can be designed, the observability of system (5.1) must be checked. The output equation of the nonlinear system reads

$$\eta = y = h(\mathbf{x}) = x, \tag{5.42}$$

which is generally a function of the system state $\mathbf{x}$. According to Subsection 5.4.1 the system (5.1) is flat, which means, that the state $\mathbf{x}$ is a function of the flat output and its derivatives with respect to time. The time derivatives of the output equation (5.42) read

$$\dot{\eta} = \frac{\partial h(\mathbf{x})}{\partial\mathbf{x}}\mathbf{f}(\mathbf{x},u) = v \tag{5.43}$$

$$\ddot{\eta} = \frac{1}{m}\left(p_A A_1 - p_S A_2 - mg - d_v v - F_P\right) \tag{5.44}$$

and, thus, the complete system state $\mathbf{x}$ can be calculated from the measured output and its derivatives. This means, that the system (5.1) is, at least locally, observable[2]. The requirement for solvability of equations (5.42) to (5.44) for the state $\mathbf{x}$ is identical to the observability of the system

$$\mathit{\Delta}\dot{\mathbf{x}} = \mathbf{A}(t)\mathit{\Delta}\mathbf{x} + \mathbf{b}(t)\mathit{\Delta}u \tag{5.45}$$

$$\mathit{\Delta}\eta = \mathbf{c}^\top \mathit{\Delta}\mathbf{x} \tag{5.46}$$

linearised along the desired trajectories. For observability it is necessary, that the components of the state $\mathit{\Delta}\mathbf{x}$ can be calculated from the output $\mathit{\Delta}\eta$ and its derivatives with respect to time. This is only possible if the following expressions

$$\mathit{\Delta}\eta = \mathbf{c}^\top \mathit{\Delta}\mathbf{x} \tag{5.47}$$

$$\mathit{\Delta}\dot{\eta} = \left[\frac{\mathrm{d}}{\mathrm{d}t}\mathbf{c}^\top + \mathbf{c}^\top \mathbf{A}(t)\right]\mathit{\Delta}\mathbf{x} = \left[\left(\mathbf{A}^\top(t) + \frac{\mathrm{d}}{\mathrm{d}t}\right)\mathbf{c}\right]^\top \mathit{\Delta}\mathbf{x} \tag{5.48}$$

$$\begin{aligned}\mathit{\Delta}\ddot{\eta} &= \frac{\mathrm{d}}{\mathrm{d}t}\left[\frac{\mathrm{d}}{\mathrm{d}t}\mathbf{c}^\top + \mathbf{c}^\top \mathbf{A}(t)\right]\mathit{\Delta}\mathbf{x} + \left[\frac{\mathrm{d}}{\mathrm{d}t}\mathbf{c}^\top + \mathbf{c}^\top \mathbf{A}(t)\right]\mathbf{A}(t)\mathit{\Delta}\mathbf{x}\\ &= \left[\left(\mathbf{A}^\top(t) + \frac{\mathrm{d}}{\mathrm{d}t}\right)^2 \mathbf{c}\right]^\top \mathit{\Delta}\mathbf{x},\end{aligned} \tag{5.49}$$

can be calculated, i.e., the observability matrix

$$\mathbf{Q}\left(t\right) = \begin{bmatrix} \mathbf{c}^\top \\ M_{\mathbf{A}(t)}\mathbf{c}^\top \\ M^2_{\mathbf{A}(t)}\mathbf{c}^\top \end{bmatrix} \tag{5.50}$$

must have full rank, where $M_{\mathbf{A}(t)}$ represents a differential operator

$$M_{\mathbf{A}(t)}\mathbf{t}_1^\top = \mathbf{t}_1^\top \mathbf{A}(t) + \dot{\mathbf{t}}_1^\top,\ M^{k+1}_{\mathbf{A}(t)}\mathbf{t}_1^\top = M_{\mathbf{A}(t)}\left(M^k_{\mathbf{A}(t)}\mathbf{t}_1^\top\right),\ k > 0,\ M^0_{\mathbf{A}(t)}\mathbf{t}_1^\top = \mathbf{t}_1^\top \tag{5.51}$$

for time dependent[3] row vectors $\mathbf{t}_1^\intercal$ and the matrix $\mathbf{A}(t)$. But, even if system (5.45) is observable it is not sufficient to design the eigenvalues of the error dynamics (5.41) with negative real parts, since it is a time varying system. To assure the stability of the estimation error the time variance must be compensated, which can be done in the observability canonical form. The necessary change of coordinates reads

$$\boldsymbol{\zeta} = \boldsymbol{\Theta}(t)\mathbf{x}, \tag{5.52}$$

which is a regular[4] transformation. In Eq. (5.52) the vector $\boldsymbol{\zeta}$ represents the state in

[2] According to the definition of flatness this is understandable without any calculation, that a flat system is observable, if the flat output is measured.

[3] For better readability the argument t of the time dependent vectors $\mathbf{t}_1^\intercal$ is omitted.

[4] The proof for invertibility of $\boldsymbol{\Theta}\left(t\right)$ is not shown in this work.

coordinates of the observability canonical form. The calculation of $\boldsymbol{\Theta}(t)$ requires the use of the following differential operator $N_{\mathbf{A}(t)}$

$$N_{\mathbf{A}(t)}\mathbf{b} = \mathbf{A}(t)\mathbf{b} - \dot{\mathbf{b}},\ N^{k+1}_{\mathbf{A}(t)}\mathbf{b} = N_{\mathbf{A}(t)}\left(N^{k}_{\mathbf{A}(t)}\mathbf{b}\right),\ k > 0,\ N^{0}_{\mathbf{A}(t)}\mathbf{b} = \mathbf{b} \tag{5.53}$$

for column vectors $\mathbf{b}$ applied to the matrix $\mathbf{A}(t)$.

In the following three different observer designs - the complete, the disturbance, and, the reduced observer - will be presented. The resulting performance of the different observer designs will be immediately verified by simulations in *Matlab/Simulink*$^{\mathrm{TM}}$ in each case.

5.4.3.1. Complete Observer

The first observer type estimates the full system state, even though at least one state variable

$$\eta = h(\mathbf{x}) = x, \tag{5.54}$$

the position of the dead load, is measured. As pointed out before, the linearisation of system (5.1) along the trajectory leads to a linear time varying dynamical system with

$$\mathbf{A}(t) = \begin{bmatrix} 0 & 1 & 0 \\ 0 & -\frac{d_v}{m} & \frac{A_1}{m} \\ 0 & -\frac{A_1 \varkappa p_A(t)}{V_A\left(\frac{p_{0G}}{p_A(t)}\right)^{\frac{1}{\varkappa}}} & \frac{(-A_1 v(t) + q_A(t))(\varkappa+1)}{V_A\left(\frac{p_{0G}}{p_A(t)}\right)^{\frac{1}{\varkappa}}} \end{bmatrix} \tag{5.55}$$

$$\mathbf{c}^\top = \begin{bmatrix} 1 & 0 & 0 \end{bmatrix}. \tag{5.56}$$

For better readability, the entries of the matrix $\mathbf{A}(t)$ are abbreviated, as

$$\mathbf{A}(t) = \begin{bmatrix} 0 & 1 & 0 \\ 0 & a_{22} & a_{23} \\ 0 & a_{32}(t) & a_{33}(t) \end{bmatrix}. \tag{5.57}$$

Before the observer is designed, the observability has to be checked by the calculation of the observability matrix

$$\begin{aligned} \mathbf{Q} &= \begin{bmatrix} \mathbf{c}^\top \\ M_{\mathbf{A}(t)}\mathbf{c}^\top \\ M^2_{\mathbf{A}(t)}\mathbf{c}^\top \end{bmatrix} \\ &= \begin{bmatrix} 1 & 0 & 0 \\ 0 & 1 & 0 \\ 0 & a_{22} & a_{23} \end{bmatrix}. \end{aligned} \tag{5.58}$$

This matrix has full rank for every point in time and, thus, the linearised system is observable. The time varying state transformation to the observability canonical form calculates to

$$\begin{aligned}\boldsymbol{\Theta}^{-1}(t) &= \begin{bmatrix} \boldsymbol{\theta} & N_{\mathbf{A}(t)}\boldsymbol{\theta} & N^2_{\mathbf{A}(t)}\boldsymbol{\theta} \end{bmatrix} \\ &= \begin{bmatrix} 0 & 0 & 1 \\ 0 & 1 & a_{22} + a_{33}(t) \\ \frac{1}{a_{23}} & \frac{a_{33}(t)}{a_{23}} & a_{32(t)} + \frac{a_{33}^2(t)}{a_{23}} + \frac{\frac{\mathrm{d}}{\mathrm{d}t}a_{33}(t)}{a_{23}} \end{bmatrix}\end{aligned} \tag{5.59}$$

with

$$\boldsymbol{\theta} = \mathbf{Q}^{-1} \begin{bmatrix} 0 \\ 0 \\ 1 \end{bmatrix} \tag{5.60}$$

and $N_{\mathbf{A}(t)}$ according to Eq. (5.53). With Eq. (5.59) the desired canonical form follows to

$$\begin{aligned}\mathbf{A}^{\star}(t) &= \left(\frac{\mathrm{d}}{\mathrm{d}t}\boldsymbol{\Theta}(t) + \boldsymbol{\Theta}(t)\mathbf{A}(t)\right)\boldsymbol{\Theta}^{-1}(t) \\ &= \begin{bmatrix} 0 & 0 & a_{22}\frac{\mathrm{d}}{\mathrm{d}t}a_{33}(t) + \frac{\mathrm{d}^2}{\mathrm{d}t^2}a_{33}(t) - a_{23}\frac{\mathrm{d}}{\mathrm{d}t}a_{32}(t) \\ 1 & 0 & a_{23}a_{32}(t) - a_{33}(t)a_{22} - 2\frac{\mathrm{d}}{\mathrm{d}t}a_{33}(t) \\ 0 & 1 & a_{32}(t) + a_{33}(t) \end{bmatrix}.\end{aligned} \tag{5.61}$$

The time varying entries of Eq. (5.61) can be compensated in this canonical form by the design vector

$$\mathbf{L}^{\star}(t) = \begin{bmatrix} \alpha_0 + a_{22}\frac{\mathrm{d}}{\mathrm{d}t}a_{33}(t) + \frac{\mathrm{d}^2}{\mathrm{d}t^2}a_{33}(t) - a_{23}\frac{\mathrm{d}}{\mathrm{d}t}a_{32}(t) \\ \alpha_1 + a_{23}a_{32(t)} - a_{33}(t)a_{22} - 2\frac{\mathrm{d}}{\mathrm{d}t}a_{33}(t) \\ +\alpha_2 + a_{32}(t) + a_{33}(t) \end{bmatrix}, \tag{5.62}$$

which leads to the dynamic matrix of the observer

$$\mathbf{A}^{\star}(t) - \mathbf{L}^{\star}(t)\begin{bmatrix} 0 & 0 & 1 \end{bmatrix} = \begin{bmatrix} 0 & 0 & -\alpha_0 \\ 1 & 0 & -\alpha_1 \\ 0 & 1 & -\alpha_2 \end{bmatrix} \tag{5.63}$$

with the characteristic polynomial of the observation error

$$s^3 + \alpha_2 s^2 + \alpha_1 s + \alpha_0 = 0, \tag{5.64}$$

which must be a Hurwitz-Polynomial[5] in s. Similarly as before in Subsection 5.4.2, the observer parameters $\alpha_i,\ i = 0, 1, 2$ must be adjusted properly for asymptotic stability.

[5]All roots of a Hurwitz-Polynomial have negative real parts.

In original coordinates the flatness based complete observer reads

$$
\begin{aligned}
\dot{\hat{\mathbf{x}}} &= \mathbf{f}(\hat{\mathbf{x}}, \hat{u}) + \boldsymbol{\Theta}^{-1}(t)\mathbf{L}^{\star}(t)(\eta - h(\hat{\mathbf{x}})) \qquad (5.65)\\
&= \begin{bmatrix} \hat{v} \\ \frac{1}{m}\left(\hat{p}_A A_1 - p_S A_2 - mg - d_v \hat{v}\right) \\ \frac{\hat{p}_A \varkappa}{V_A \left(\frac{p_{0_G}}{\hat{p}_A}\right)^{\frac{1}{\varkappa}}} \left(-A_1 \hat{v} + \hat{q}_A\right) \end{bmatrix} \\
&+ \begin{bmatrix} \left(\alpha_2 - \frac{d_v}{m} + \vartheta(t)\right)(x - \hat{x}) \\ \left(\alpha_1 - 2\frac{\mathrm{d}\vartheta(t)}{\mathrm{d}t} - \frac{d_v \vartheta(t) + \varsigma(t) A_1 - d_v \alpha_2 + d_v^2}{m} + \vartheta(t)\alpha_2 + \vartheta^2(t)\right)(x - \hat{x}) \\ \Upsilon(t)\,(x - \hat{x}) \end{bmatrix}
\end{aligned}
$$

with

$$
\begin{aligned}
\Upsilon(t) &= \frac{m\alpha_0}{A_1} - \frac{\mathrm{d}\varsigma(t)}{\mathrm{d}t} + \frac{m\frac{\mathrm{d}^2\vartheta(t)}{\mathrm{d}t^2} + \vartheta(t) m \alpha_1 - 3\vartheta(t) m \frac{\mathrm{d}\vartheta(t)}{\mathrm{d}t}}{A_1} \\
&\quad + 2\vartheta(t)\varsigma(t) + \alpha_2 \varsigma(t) - \frac{\varsigma(t) d_v}{m} \\
&\quad + \frac{\vartheta(t)^2 m \alpha_2 + \vartheta(t)^3 m - \frac{\mathrm{d}\vartheta(t)}{\mathrm{d}t}\alpha_2 m}{A_1}, \qquad (5.66)
\end{aligned}
$$

$$
\begin{aligned}
\varsigma(t) &= -\frac{A_1 p_{A_d} \varkappa}{V_A \left(\frac{p_{0_G}}{p_{A_d}}\right)^{\frac{1}{\varkappa}}}, \qquad (5.67)\\
\vartheta(t) &= -\frac{(\varkappa + 1)\left(A_1 v_d - q_{A_d}\right)}{V_A \left(\frac{p_{0_G}}{p_{A_d}}\right)^{\frac{1}{\varkappa}}}, \qquad (5.68)
\end{aligned}
$$

where $\eta = x$ denotes the measured position of the dead load and $\hat{\mathbf{x}} = [\hat{x}\ \hat{v}\ \hat{p}_A]^\top$ represents the state of the observer. It is important to mention, that the observer (5.65) requires the knowledge of the desired trajectories $\mathbf{x}_d$ and u_d. Since in the concrete case the flatness based control is a sort of a PDDD-controller, the desired trajectory of the flat output and, further, a number of its derivatives with respect to time have to be provided. Furthermore, this flatness based observer requires the fourth and fifth derivative of the flat output according to Eq. (5.66), which must be provided by an adequate trajectory generation. This can be realised either offline by pre-processing or by the implementation of a certain pre-filter, which will be discussed in Subsection 5.4.4.

The block diagram of the flatness based control (FBC) employing a complete observer is illustrated in Fig. 5.15, where the advantage of this observer type becomes clear. The nonlinear observer estimates the whole system state $\hat{\mathbf{x}} = [\hat{x}\ \hat{v}\ \hat{p}_A]^\top$, which is necessary for the FBC, just by measuring the position of the load x. This is a large benefit in the view of a low-cost implementation, because no additional pressure sensor must be spent. The

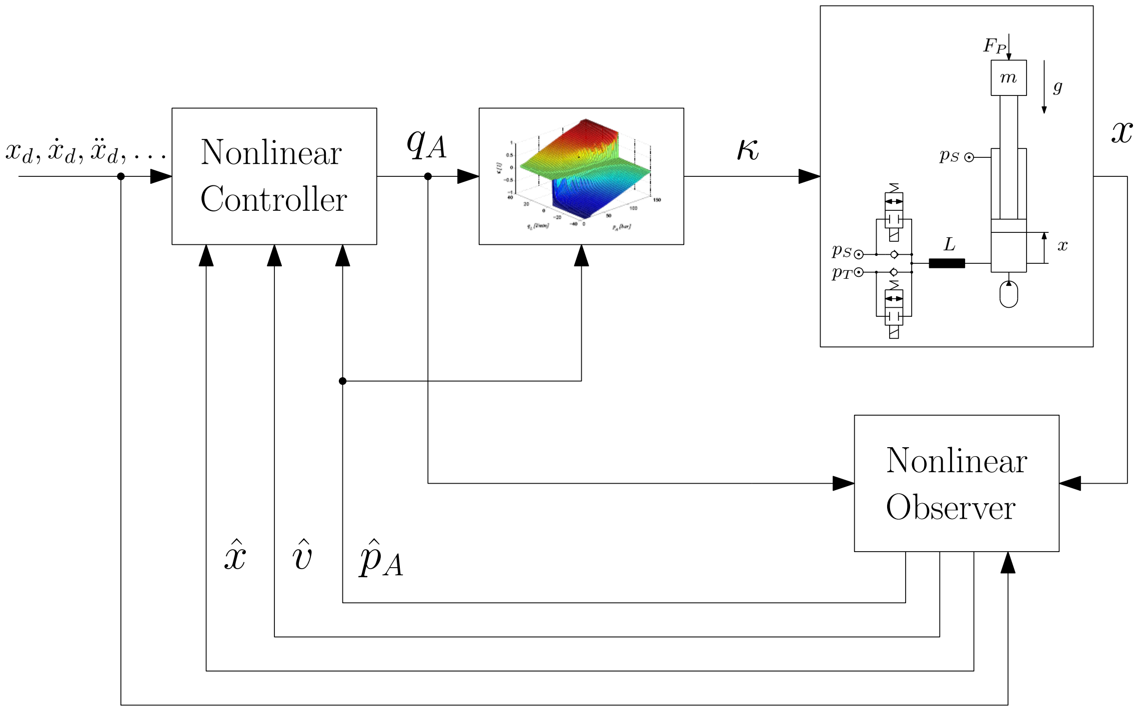

Figure 5.15.: Flatness based control of a linear hydraulic drive applying a complete observer

set variable of the nonlinear controller is the flow rate q_A, which must be transformed to a duty ratio κ by the static converter characteristics according to Subsection 4.3.3. The performance of this configuration will be analysed by simulations in the following.

The first simulation case considers a ramp in both moving directions with a constant slope of $v_d = 150\frac{mm}{s}$. No external load force is applied to the piston, thus, $F_P = 0$ is assumed. The corresponding results are illustrated in Fig. 5.16, where the flatness based control is compared to a conventional HPD according to Subsection 5.2.2. In contrast to the performance of the linear controllers according to Fig. 5.11 a remarkable improvement can be achieved with the FBC. Beside some fluctuations in the piston velocity, the trajectory of the HBC is even closer to the desired trajectory than the HPD with a P-controller. In Fig. 5.17 simulation results of a $2\,Hz$ sinusoidal trajectory are presented. In contrast to the HBC, the HPD shows a small phase shift between the desired and its actual position due to the performance restrictions caused by the ordinary P-controller and the limited dynamics of the proportional valve. Since the FBC uses the knowledge of the desired trajectory and further compensates the dynamics of the system, a better performance can be achieved. In the lower diagram the energy consumptions of both drive concepts are depicted. The HBC in combination with an FBC needs for an even better performance less than half of the power of the HPD in this specific case. It has to be pointed out, that the overall drive configuration represents a nonlinear system, which prevents an extrapolation of the illustrated results to other power dimensions. Also the specific load scenarios play

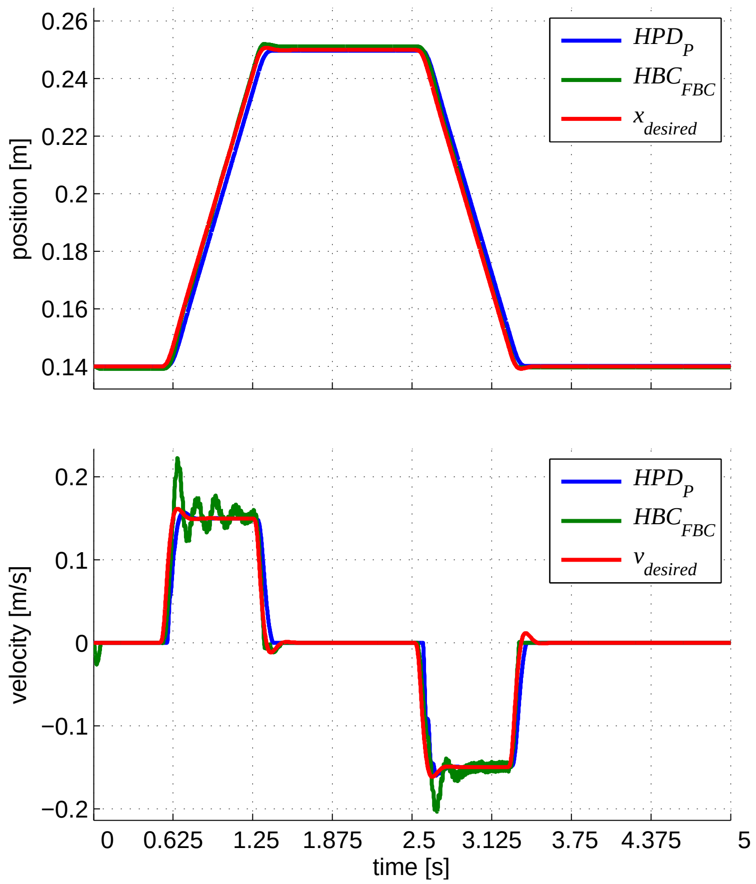

Figure 5.16.: Simulated trajectory tracking of the FBC

a significant role for the energy consumption of such drives.

In the simulation results of the flatness based control presented so far no external loads were applied. In most cases a hydraulic drive is designed to handle big loads and forces. The simulated performances of the HBC exploiting a flatness based control and an HPD under a nearly stepwise process force are presented in Fig. 5.18. The results show the big advantage of the conventional proportional hydraulics. Due to the stiffness of the HPD no relevant deviation in the piston position is noticeable despite of the applied process force. In contrast to that, the proposed controller for the HBC drive is not qualified for an adequate compensation of the deflection in the piston position resulting from the external force jump. To eliminate the difficulties to follow transient motions in case of load force disturbances, a more sophisticated observer design has to be applied, which will be derived in the following.

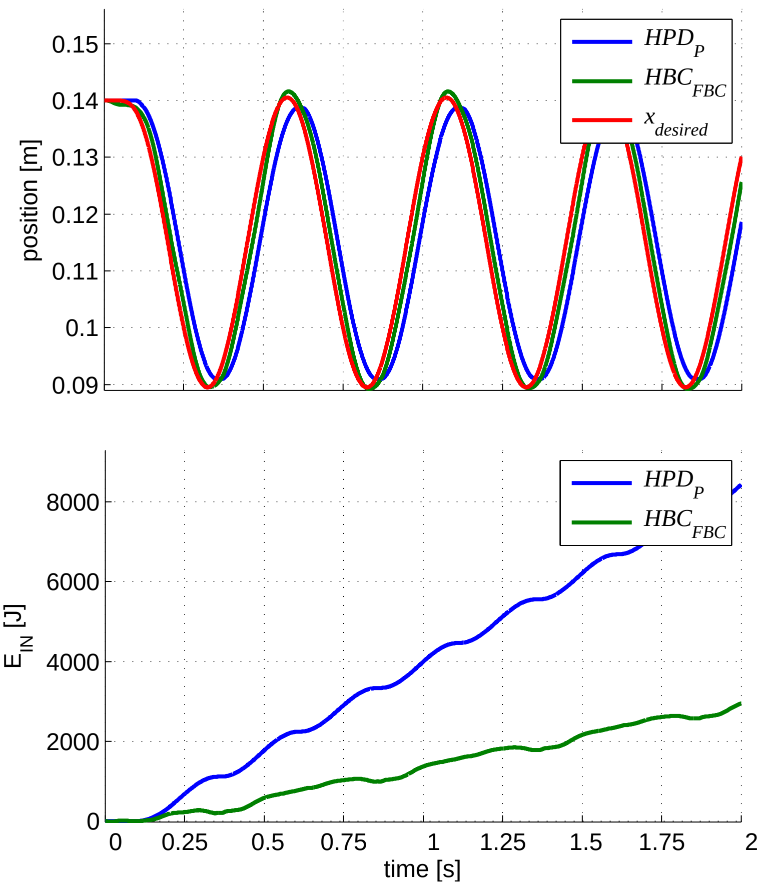

Figure 5.17.: Energy consumption of the FBC at trajectory tracking

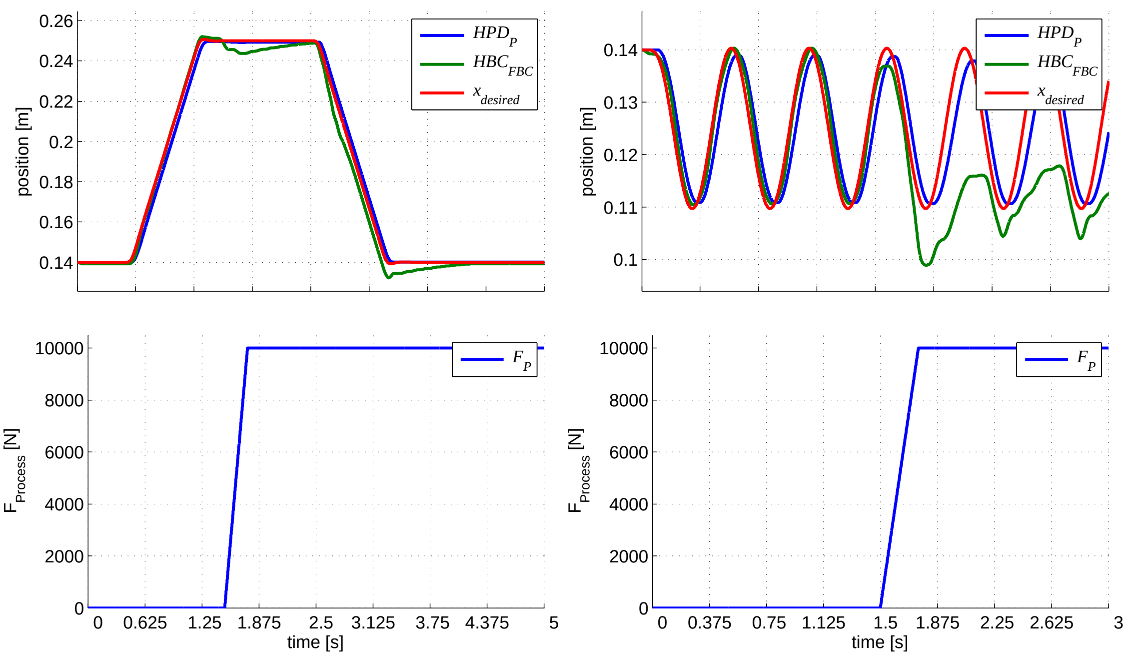

Figure 5.18.: Simulation results of the FBC with an applied process force

5.4.3.2. Load Observer

The ability to cope with unknown process forces is important for the soft HBC configuration in order to stay competitive with a correspondingly stiff HPD. A process force describes a disturbance for the considered system. The concept of flatness allows to estimate such a disturbing process force by the adaption of the observer design. For this purpose the control system must be extended to the form

$$\begin{bmatrix} \dot{x} \\ \dot{v} \\ \dot{p}_A \\ \dot{F}_P \end{bmatrix} = \begin{bmatrix} v \\ \frac{1}{m}\left(p_A A_1 - p_S A_2 - mg - d_v v - F_P\right) \\ \frac{p_A \varkappa}{V_A \left(\frac{p_{0_G}}{p_A}\right)^{\frac{1}{\varkappa}}}\left(-A_1 v + q_A\right) \\ 0 \end{bmatrix} \tag{5.69}$$

with the new system state $\mathbf{x} = [x\ v\ p_A\ F_P]^\top$. In Eq. (5.69) the process force F_P describes an integrator state, which means, that the process force is assumed to be constant since no further information is available.

Under the assumption that only the load position $\eta = x$ is measured the dynamic matrix and the output vector of the linearised system along the trajectory $(\mathbf{x}_d(t), u_d(t))$ read

$$\begin{aligned} \mathbf{A}(t) &= \begin{bmatrix} 0 & 1 & 0 & 0 \\ 0 & -\frac{d_v}{m} & \frac{A_1}{m} & -\frac{1}{m} \\ 0 & -\frac{A_1 \varkappa p_{A_d}(t)}{V_A\left(\frac{p_{0_G}}{p_{A_d}(t)}\right)^{\frac{1}{\varkappa}}} & \frac{\left(-A_1 v_d(t) + q_{A_d}(t)\right)(\varkappa + 1)}{V_A\left(\frac{p_{0_G}}{p_{A_d}(t)}\right)^{\frac{1}{\varkappa}}} & 0 \\ 0 & 0 & 0 & 0 \end{bmatrix} \\ &= \begin{bmatrix} 0 & 1 & 0 & 0 \\ 0 & a_{22} & a_{23} & a_{24} \\ 0 & a_{32}(t) & a_{33}(t) & 0 \\ 0 & 0 & 0 & 0 \end{bmatrix} \end{aligned} \tag{5.70}$$

$$\mathbf{c}^\top = \begin{bmatrix} 1 & 0 & 0 & 0 \end{bmatrix}. \tag{5.71}$$

and the observability matrix follows to

$$\mathbf{Q}(t) = \begin{bmatrix} \mathbf{c}^\top \\ M_{\mathbf{A}(t)}\mathbf{c}^\top \\ M^2_{\mathbf{A}(t)}\mathbf{c}^\top \\ M^3_{\mathbf{A}(t)}\mathbf{c}^\top \end{bmatrix} = \begin{bmatrix} 1 & 0 & 0 & 0 \\ 0 & 1 & 0 & 0 \\ 0 & a_{22} & a_{23} & a_{24} \\ 0 & a_{22}^2 + a_{32}(t)a_{23} & a_{22}a_{23} + a_{33}(t)a_{23} & a_{22}a_{24} \end{bmatrix}, \tag{5.72}$$

which is time dependent in this specific case. A correct observer design is only possible if the observability matrix is regular. This is checked by its determinant

$$\det\{\mathbf{Q}(t)\} = -a_{24}a_{23}a_{33}(t), \tag{5.73}$$

which is time varying due to $a_{33}(t)$. In this case, the observability matrix is not regular for certain trajectories, i.e., where $a_{33}(t) = 0$. Moreover, this is the case at every arbitrary rest position of the hydraulic drive. This can be easily seen from the fact, that if the drive is not accelerating, the pressure p_A and the process force F_P cannot be estimated at the same time, since no corresponding measurement is available. Hence, a further measurement - the pressure p_A - is used, which leads to the new linear measurement equation

$$\Delta\boldsymbol{\eta} = \mathbf{C}\Delta\mathbf{x} = \begin{bmatrix} \mathbf{c}_1^\top \\ \mathbf{c}_2^\top \end{bmatrix} \Delta\mathbf{x} = \begin{bmatrix} 1 & 0 & 0 & 0 \\ 0 & 0 & 1 & 0 \end{bmatrix} \begin{bmatrix} \Delta x \\ \Delta v \\ \Delta p_A \\ \Delta F_P \end{bmatrix} \tag{5.74}$$

$$= \begin{bmatrix} \Delta x \\ \Delta p_A \end{bmatrix}. \tag{5.75}$$

For a new calculation of the observability matrix, the influence of both measurements on the observability must be specified, which is basically not a unique process. In the concrete case the individual observability indices are chosen by

$$\mu_1 = 3 \text{ and } \mu_2 = 1, \tag{5.76}$$

which allow a decomposition of the original problem into simpler subsystems. Applying indices (5.76) the observability matrix calculates to

$$\begin{aligned} \mathbf{Q} &= \begin{bmatrix} M^0_{\mathbf{A}(t)}\mathbf{c}_1^\top \\ M^1_{\mathbf{A}(t)}\mathbf{c}_1^\top \\ M^{\mu_1-1}_{\mathbf{A}(t)}\mathbf{c}_1^\top \\ M^{\mu_2-1}_{\mathbf{A}(t)}\mathbf{c}_2^\top \end{bmatrix} \\ &= \begin{bmatrix} 1 & 0 & 0 & 0 \\ 0 & 1 & 0 & 0 \\ 0 & a_{22} & a_{23} & a_{24} \\ 0 & 0 & 1 & 0 \end{bmatrix}, \end{aligned} \tag{5.77}$$

which has now full rank for every point in time due to

$$\det\{\mathbf{Q}\} = -a_{24}. \tag{5.78}$$

The transformation into the canonical form requires the following matrix

$$\begin{aligned}
\boldsymbol{\theta} &= \mathbf{Q}^{-1}\begin{bmatrix} 0 & 0 \\ 0 & 0 \\ 1 & 0 \\ 0 & 1 \end{bmatrix} \\
&= \begin{bmatrix} \boldsymbol{\chi}_1 & \boldsymbol{\chi}_2 \end{bmatrix} && (5.79) \\
&= \begin{bmatrix} 0 & 0 \\ 0 & 0 \\ 0 & 0 \\ \frac{1}{a_{24}} & -\frac{a_{23}}{a_{24}} \end{bmatrix}, && (5.80)
\end{aligned}$$

which is necessary to calculate the time varying transformation matrix

$$\begin{aligned}
\boldsymbol{\Theta}^{-1}(t) &= \begin{bmatrix} \boldsymbol{\chi}_1 & N_{\mathbf{A}(t)}\boldsymbol{\chi}_1 & N^2_{\mathbf{A}(t)}\boldsymbol{\chi}_1 & \boldsymbol{\chi}_2 \end{bmatrix} \\
&= \begin{bmatrix} 0 & 0 & 1 & 0 \\ 0 & 1 & a_{22} & 0 \\ 0 & 0 & a_{32}(t) & 0 \\ \frac{1}{a_{24}} & 0 & 0 & -\frac{a_{23}}{a_{24}} \end{bmatrix}. && (5.81)
\end{aligned}$$

Thus, the dynamic matrix (5.70) in its canonical form reads

$$\begin{aligned}
\mathbf{A}^{\star}(t) &= \left(\frac{\mathrm{d}}{\mathrm{d}t}\boldsymbol{\Theta}(t) + \boldsymbol{\Theta}(t)\mathbf{A}(t)\right)\boldsymbol{\Theta}^{-1}(t) \\
&= \begin{bmatrix} 0 & 0 & a_{33}(t)a_{23}a_{32}(t) - \frac{\mathrm{d}}{\mathrm{d}t}a_{32}(t) - a_{23} & a_{33}(t)a_{23} \\ 1 & 0 & a_{23}a_{32}(t) & 0 \\ 0 & 1 & a_{22} & 0 \\ 0 & 0 & a_{33}(t)a_{32(t)} - \frac{\mathrm{d}}{\mathrm{d}t}a_{32}(t) & a_{33}(t) \end{bmatrix}. && (5.82)
\end{aligned}$$

According to Eq. (5.41), the observer matrix can be chosen by

$$\mathbf{L}^{\star}(t) = \begin{bmatrix} \alpha_0 + a_{33}(t)a_{23}a_{32}(t) - \frac{\mathrm{d}}{\mathrm{d}t}a_{32}(t) - a_{23} & a_{33}(t)a_{23} \\ \alpha_1 + a_{23}a_{32}(t) & 0 \\ \alpha_2 + a_{22} & 0 \\ a_{33}(t)a_{32(t)} - \frac{\mathrm{d}}{\mathrm{d}t}a_{32}(t) & \beta_0 + a_{33}(t) \end{bmatrix} \qquad (5.83)$$

to compensate the time varying entries of $\mathbf{A}^{\star}(t)$. The resulting dynamics of the observation error

$$\dot{\widehat{\Delta\mathbf{e}}}^{\star} = \begin{bmatrix} 0 & 0 & -\alpha_0 & 0 \\ 1 & 0 & -\alpha_1 & 0 \\ 0 & 1 & -\alpha_2 & 0 \\ 0 & 0 & 0 & -\beta_0 \end{bmatrix} \widehat{\Delta\mathbf{e}}^{\star} \tag{5.84}$$

has the characteristic polynomial

$$\left(s^3 + \alpha_2 s^2 + \alpha_1 s + \alpha_0\right)(s + \beta_0) = 0 \tag{5.85}$$

with the observer parameters α_i, $i = 0, 1, 2$ and β_0. Finally, the flatness based load observer in original coordinates calculates to

$$\begin{aligned} \dot{\hat{\mathbf{x}}} &= \mathbf{f}(\hat{\mathbf{x}}, \hat{u}) + \boldsymbol{\Theta}^{-1}(t)\mathbf{L}^{\star}(t)(\boldsymbol{\eta} - \mathbf{C}\hat{\mathbf{x}}) \qquad (5.86) \\ &= \begin{bmatrix} \hat{v} \\ \frac{1}{m}\left(\hat{p}_A A_1 - p_S A_2 - mg - d_v \hat{v} - \hat{F}_P\right) \\ \frac{\hat{p}_A \varkappa}{V_A \left(\frac{p_{0_G}}{\hat{p}_A}\right)^{\frac{1}{\varkappa}}} \left(-A_1 \hat{v} + \hat{q}_A\right) \\ 0 \end{bmatrix} \\ &+ \begin{bmatrix} -\left(\frac{d_v}{m} - \alpha_2\right)(x - \hat{x}) \\ -\left(\frac{d_v}{m}\alpha_2 - \frac{d_v^2}{m^2} - \frac{\vartheta(t) A_1}{m} - \alpha_1\right)(x - \hat{x}) \\ -\left(\frac{\vartheta(t) d_v}{m} + \frac{\mathrm{d}}{\mathrm{d}t}\vartheta(t) - \vartheta(t)\varsigma(t) - \vartheta(t)\alpha_2\right)(x - \hat{x}) + (\beta_0 + \varsigma(t))(p - \hat{p}) \\ -m\alpha_0 (x - \hat{x}) + A_1 \beta_0 (p - \hat{p}) \end{bmatrix} \end{aligned}$$

with

$$\vartheta(t) = \frac{A_1 \varkappa p_{A_d}}{V_A \left(\frac{p_{0_G}}{p_{A_d}}\right)^{\frac{1}{\varkappa}}} \tag{5.87}$$

$$\varsigma(t) = \frac{\left(-A_1 v_d + q_{A_d}\right)(\varkappa + 1)}{V_A \left(\frac{p_{0_G}}{p_{A_d}}\right)^{\frac{1}{\varkappa}}} \tag{5.88}$$

and the measurement vector $\boldsymbol{\eta} = [x \; p_A]^{\top}$. Due to the segmentation into two subsystems by the application of the observability indices (Eq. (5.76)) the disturbance observer is even simpler than the conventional observer derived above. Of course, this is possible due to the additional information provided by the pressure measurement.

The performance of the load observer is also studied by simulation experiments, which were carried out in accordance with Fig. 5.19. Beside the state of the control system (5.1), the observer also estimates the uncertain process force F_P. The estimated value $\hat{F}_P$ is used in the nonlinear controller to compensate its influence on the closed loop performance.

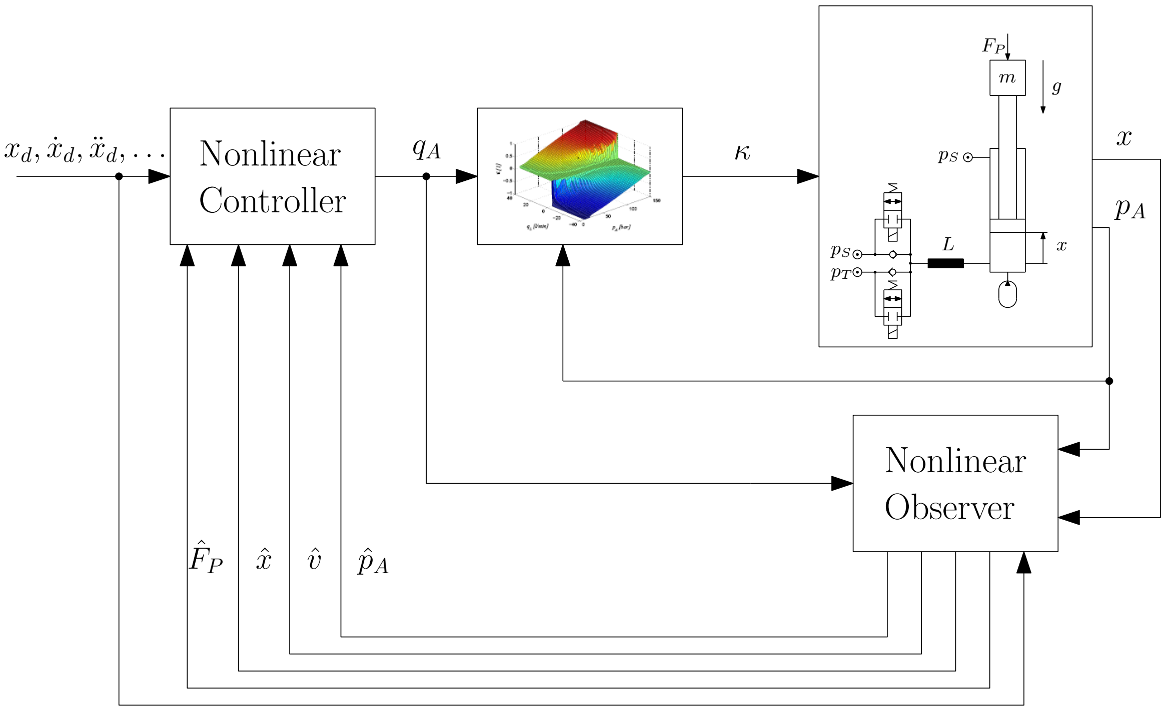

Figure 5.19.: Flatness based control of a linear hydraulic drive exploiting a load observer

The main improvements exploiting the load observer (5.86) can be examined in Fig. 5.20, where the simulation results of both flatness based controllers and the HPD are opposed. The process force $F_P = 10\,kN$ is applied as in the previous simulations at $t = 1.5\,s$ with a limited slope and remains constant for the rest of the simulation. In contrast to the conventional flatness based controller (HBC_{FBC}) the tracking performance of the HBC is improved significantly by the load observer[6] (HBC_{FBC_d}) and, thus, the softness could be nearly compensated. There remain still some deviations to the HPD during the moving phase, but for a number of applications this accuracy is sufficient. In the middle diagram of Fig. 5.20 the energy consumptions of the different configurations are depicted. It is noteworthy, that due to the potential energy of the process force in the retracting direction energy is recuperated by the HBC configurations, whereas the HPD dissipates nearly as much energy as in the deploying direction of movement.

In Fig. 5.21 the tracking performance of the mentioned configurations at a cyclic sinusoidal position reference at a frequency of 2 Hz is illustrated. In fact, the deviations in the position compared to the ramp simulations increase due to the process force. But the performance of the HBC with the load observer is much better than with the complete observer. The second diagram in Fig. 5.21 shows the energy consumption. In contrast to the HPD the HBC needs less than the half power for almost the same output performance. As a consequence, the power dimension of the hydraulic supply unit can be reduced

[6]Since the process force represents a sort of disturbance the sub-index d is used in the diagrams.

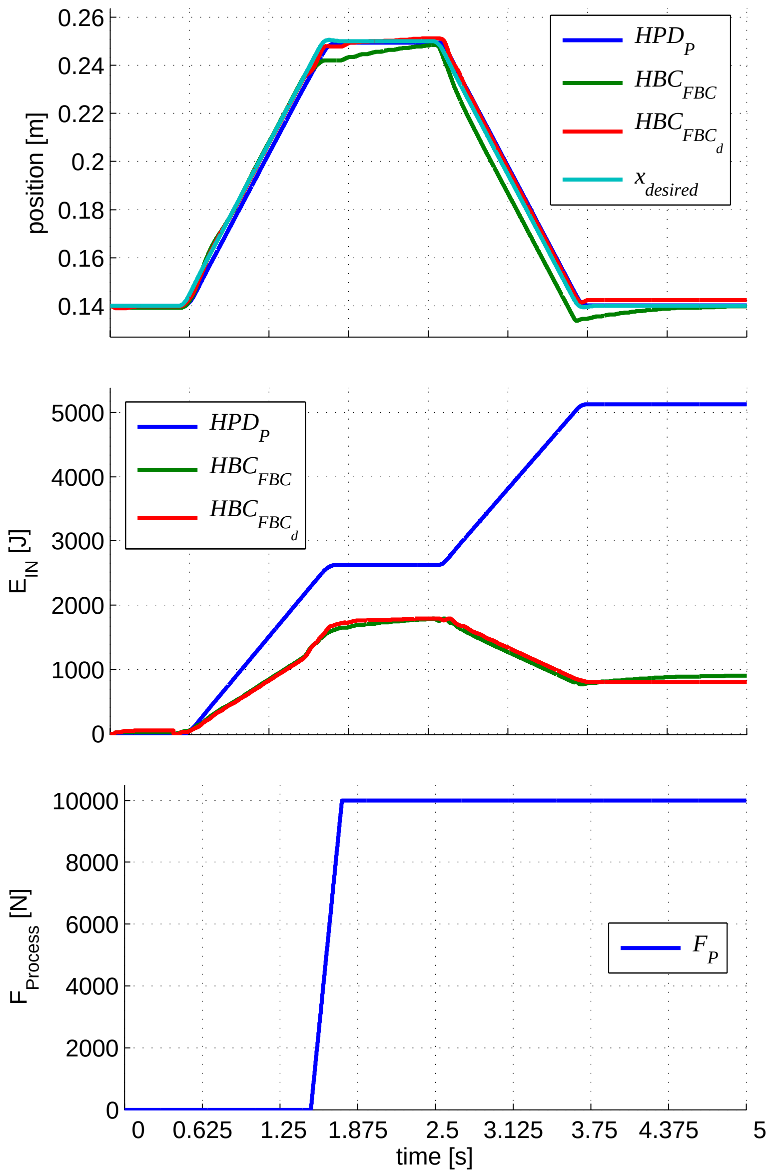

Figure 5.20.: Trajectory tracking and energy consumption of the FBC_d

dramatically, if an HBC is applied. Thus, not only the running energy costs would be lowered by the application of an HBC, but, also the costs for the supply unit could be reduced in industrial applications. For completeness the actual and the estimated process force are opposed in the lower diagram. It is noticeable, that the estimated process force shows certain ripples due to the cyclic movement of the drive. The small high frequency ripples result from a too large observer gain, where obviously the pressure fluctuations in the cylinder due to the switching process are not filtered properly by the observer. Hence, the choice of the observer parameters could be optimised for better accuracy, which was not done here.

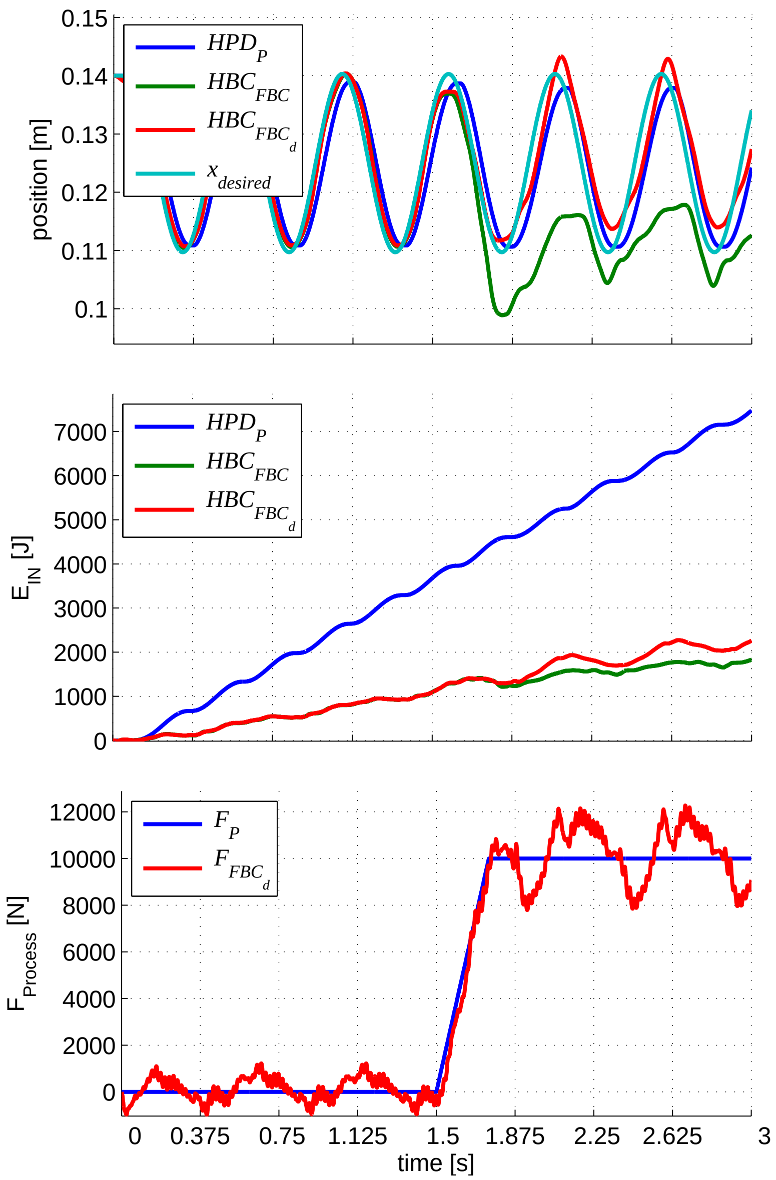

Figure 5.21.: Trajectory tracking, energy consumption and observed process force of the FBC_d

5.4.3.3. Reduced Observer

The two observers introduced above represent nonlinear differential equations, which have to be integrated with respect to time on a signal processing unit. For implementation on some industrial control units it would be easier to calculate just linear difference equations. The following concept of the reduced observer results in linear differential equations, which can be realised as difference equations on a low cost control unit. The necessary theoretical background will be given in the course of the derivations in accordance to [47].

From the previous section it is clear, that the measurement of the pressure is necessary for a satisfying performance if uncertain load forces occur. Since already two components of the system state are measured, it is plausible to consider a reduced observer for the estimation of the remaining unknown state quantities. This is studied in the following.

Assuming that the position x and the pressure p_A are measured, the equations of the considered system (5.70) have to be rearranged by applying the permutation matrix

$$\mathbf{P} = \begin{bmatrix} 1 & 0 & 0 & 0 \\ 0 & 0 & 1 & 0 \\ 0 & 1 & 0 & 0 \\ 0 & 0 & 0 & 1 \end{bmatrix} \tag{5.89}$$

for a transformation of the linearised system into sensor coordinates $\mathbf{x} = \begin{bmatrix}\mathbf{y}^\top & \mathbf{w}^\top\end{bmatrix}^\top$. The resulting system calculates to

$$\begin{aligned} \begin{bmatrix} \dot{\mathbf{y}} \\ \dot{\mathbf{w}} \end{bmatrix} &= \mathbf{P}\mathbf{A}(t)\mathbf{P}^{-1} \begin{bmatrix} \mathbf{y} \\ \mathbf{w} \end{bmatrix} + \mathbf{P}\mathbf{b}(t)\varDelta u \\ &= \begin{bmatrix} \bar{\mathbf{A}}_{11}(t) & \bar{\mathbf{A}}_{12}(t) \\ \bar{\mathbf{A}}_{21}(t) & \bar{\mathbf{A}}_{22}(t) \end{bmatrix} \begin{bmatrix} \mathbf{y} \\ \mathbf{w} \end{bmatrix} + \begin{bmatrix} \bar{\mathbf{b}}_1(t) \\ \bar{\mathbf{b}}_2(t) \end{bmatrix} \varDelta u \end{aligned} \tag{5.90}$$

$$\mathbf{y} = \begin{bmatrix} \mathbf{I} & \mathbf{0} \end{bmatrix} \begin{bmatrix} \mathbf{y} \\ \mathbf{w} \end{bmatrix}, \tag{5.91}$$

with the sub-states of the measurements $\mathbf{y} = [\varDelta x \ \varDelta p_A]^\top$, the estimated quantities $\mathbf{w} = [\varDelta v \ \varDelta F_P]^\top$, and, the identity matrix $\mathbf{I}$. Since the system (5.90) is linearised along a trajectory, the entries of $\mathbf{y}$ and $\mathbf{w}$ represent the deviations from their desired trajectories, which read

$$\varDelta x = x - x_d, \ \varDelta p_A = p_A - p_{A_d}, \ \varDelta v = v - v_d, \ \varDelta F_P = F_P - F_{P_d}. \tag{5.92}$$

The input of the system reads $\varDelta u = u - u_d$, which denotes the deviation between the actual and the desired set value due to linearisation. Since the system state is partially known, the estimation concentrates on the sub-state $\mathbf{w}$. Therefore, the auxiliary quantity

$$\mathbf{v} = \mathbf{w} + \mathbf{K}(t)\mathbf{y} \tag{5.93}$$

with the generally time variant matrix $\mathbf{K}(t)$ is introduced. The derivation with respect to time of Eq. (5.93) reads

$$\dot{\mathbf{v}} = \dot{\mathbf{w}} + \dot{\mathbf{K}}(t)\mathbf{y} + \mathbf{K}(t)\dot{\mathbf{y}} \tag{5.94}$$

and substituting Eq. (5.93) into (5.90) leads to

$$\begin{aligned}\dot{\mathbf{v}} = &\left(\bar{\mathbf{A}}_{22}(t) + \mathbf{K}(t)\bar{\mathbf{A}}_{12}(t)\right)\mathbf{v} + \left(\mathbf{K}(t)\bar{\mathbf{b}}_1(t) + \bar{\mathbf{b}}_2(t)\right)\Delta u\\ &+ \left(\dot{\mathbf{K}}(t) + \bar{\mathbf{A}}_{21}(t) + \mathbf{K}(t)\bar{\mathbf{A}}_{11}(t) - \bar{\mathbf{A}}_{22}(t)\mathbf{K}(t) - \mathbf{K}(t)\bar{\mathbf{A}}_{12}(t)\mathbf{K}(t)\right)\mathbf{y}.\end{aligned} \tag{5.95}$$

The output equation of the reduced observer according to Eq. (5.93) reads

$$\hat{\mathbf{w}} = \mathbf{v} - \mathbf{K}(t)\mathbf{y}. \tag{5.96}$$

With the design matrix $\mathbf{K}(t)$ the time variance of the dynamics of the estimation error $\hat{\mathbf{e}}_{RO} = \hat{\mathbf{w}} - \mathbf{w}$ must be compensated, and, the eigenvalues of the resulting system

$$\dot{\hat{\mathbf{e}}}_{RO} = \left(\bar{\mathbf{A}}_{22}(t) + \mathbf{K}(t)\bar{\mathbf{A}}_{12}(t)\right)\hat{\mathbf{e}}_{RO} = \mathbf{A}_{RO}\hat{\mathbf{e}}_{RO} \tag{5.97}$$

must guarantee asymptotic stability.

In the concrete case of the HBC controlled linear hydraulic drive, the individual dynamic matrices and input vectors read

$$\bar{\mathbf{A}}_{11}(t) = \begin{bmatrix} 0 & 0 \\ 0 & \frac{(-A_1 v(t) - q_A(t))(\varkappa+1)}{V_A\left(\frac{p_{0G}}{p_A(t)}\right)^{\frac{1}{\varkappa}}} \end{bmatrix} \tag{5.98}$$

$$\bar{\mathbf{A}}_{12}(t) = \begin{bmatrix} 1 & 0 \\ -\frac{A_1 \varkappa p_A(t)}{V_A\left(\frac{p_{0G}}{p_A(t)}\right)^{\frac{1}{\varkappa}}} & 0 \end{bmatrix} \tag{5.99}$$

$$\bar{\mathbf{A}}_{21} = \begin{bmatrix} 0 & \frac{A_1}{m} \\ 0 & 0 \end{bmatrix} \tag{5.100}$$

$$\bar{\mathbf{A}}_{22} = \begin{bmatrix} -\frac{d_v}{m} & -\frac{1}{m} \\ 0 & 0 \end{bmatrix} \tag{5.101}$$

$$\bar{\mathbf{b}}_1(t) = \begin{bmatrix} 0 \\ \frac{p_A(t)\varkappa}{V_A\left(\frac{p_{0G}}{p_A(t)}\right)^{\frac{1}{\varkappa}}} \end{bmatrix} \tag{5.102}$$

$$\bar{\mathbf{b}}_2 = \begin{bmatrix} 0 \\ 0 \end{bmatrix}. \tag{5.103}$$

The dynamic matrix of the observation error according to Eq. (5.97) reads

$$\bar{\mathbf{A}}_{22} + \mathbf{K}(t)\bar{\mathbf{A}}_{12}(t) = \begin{bmatrix} -\frac{d_v}{m} + k_{11}(t) - k_{12}(t)\frac{A_1 \varkappa p_A(t)}{V_A\left(\frac{p_{0_G}}{p_A(t)}\right)^{\frac{1}{\varkappa}}} & -\frac{1}{m} \\ k_{21}(t) - k_{22}(t)\frac{A_1 \varkappa p_A(t)}{V_A\left(\frac{p_{0_G}}{p_A(t)}\right)^{\frac{1}{\varkappa}}} & 0 \end{bmatrix} \tag{5.104}$$

with the observer parameters $k_{ij}(t),\ i,j = 1,2$. Now, the time variance of Eq. (5.104) can be compensated by the observer parameters $k_{ij}(t)$ and, the stability must be guaranteed. One strategy is to annihilate the time variance by $k_{12}(t) = k_{22}(t) = 0$, which leads to the time invariant design matrix

$$\mathbf{K} = \begin{bmatrix} \frac{d_v}{m} + k_{11} & 0 \\ k_{21} & 0 \end{bmatrix}, \tag{5.105}$$

where k_{11} and k_{21} are constants. Thus, the dynamics of the observation error calculates to

$$\dot{\hat{\mathbf{e}}}_{RO} = \begin{bmatrix} k_{11} & -\frac{1}{m} \\ k_{21} & 0 \end{bmatrix} \hat{\mathbf{e}}_{RO} \tag{5.106}$$

with the eigenvalues

$$\lambda_{1/2} = \frac{k_{11}}{2} \pm \frac{\sqrt{k_{11}^2 m^2 - 4k_{21}m}}{2m}. \tag{5.107}$$

For asymptotic stability of Eq. (5.106) the real part of Eq. (5.107) must be negative, which can be adjusted by the parameters k_{11} and k_{21}. The resulting differential equation of the reduced observer according to Eq. (5.95) reads

$$\dot{\mathbf{v}} = \left(\bar{\mathbf{A}}_{22} + \mathbf{K}\bar{\mathbf{A}}_{12}\right)\mathbf{v} + \left(\dot{\mathbf{K}} + \bar{\mathbf{A}}_{21} + \mathbf{K}\bar{\mathbf{A}}_{11} - \bar{\mathbf{A}}_{22}\mathbf{K} - \mathbf{K}\bar{\mathbf{A}}_{12}\mathbf{K}\right)\Delta\boldsymbol{\mu}, \tag{5.108}$$

where $\Delta\boldsymbol{\mu} = [\Delta x\ \Delta p_A]^\top$ denotes the deviations of the measured quantities from its desired trajectories. It must be remarked, that with the design matrix (5.105) the pressure measurement cannot be directly amplified by the observer parameters, unfortunately. Furthermore, in Eq. (5.108) the fluctuations of the set value Δu have no more influence on the observer due to the choice $k_{12} = k_{22} = 0$, and, thus

$$\mathbf{K}\bar{\mathbf{b}}_1 + \bar{\mathbf{b}}_2 = \begin{bmatrix} k_{12} \\ k_{22} \end{bmatrix} = \mathbf{0}. \tag{5.109}$$

But, for simplicity the considerations are continued with this configuration. Thus, the estimated system state reads

$$\hat{\mathbf{x}} = \begin{bmatrix} \boldsymbol{\mu} \\ \hat{\mathbf{w}} \end{bmatrix} = \begin{bmatrix} \boldsymbol{\mu} \\ \mathbf{w}_d + \mathbf{v} - \mathbf{K}\Delta\boldsymbol{\mu} \end{bmatrix}, \tag{5.110}$$

with the measurements $\boldsymbol{\mu} = [x\ p_A]^\top$ and the desired trajectories of the estimated state variables $\mathbf{w}_d$.

As mentioned before, the dynamics of the reduced observer is linear. Its performance in the nonlinear simulation model will be presented in the following. The implementation of the reduced observer is realised according to Fig. 5.22. In this case the measurements of x

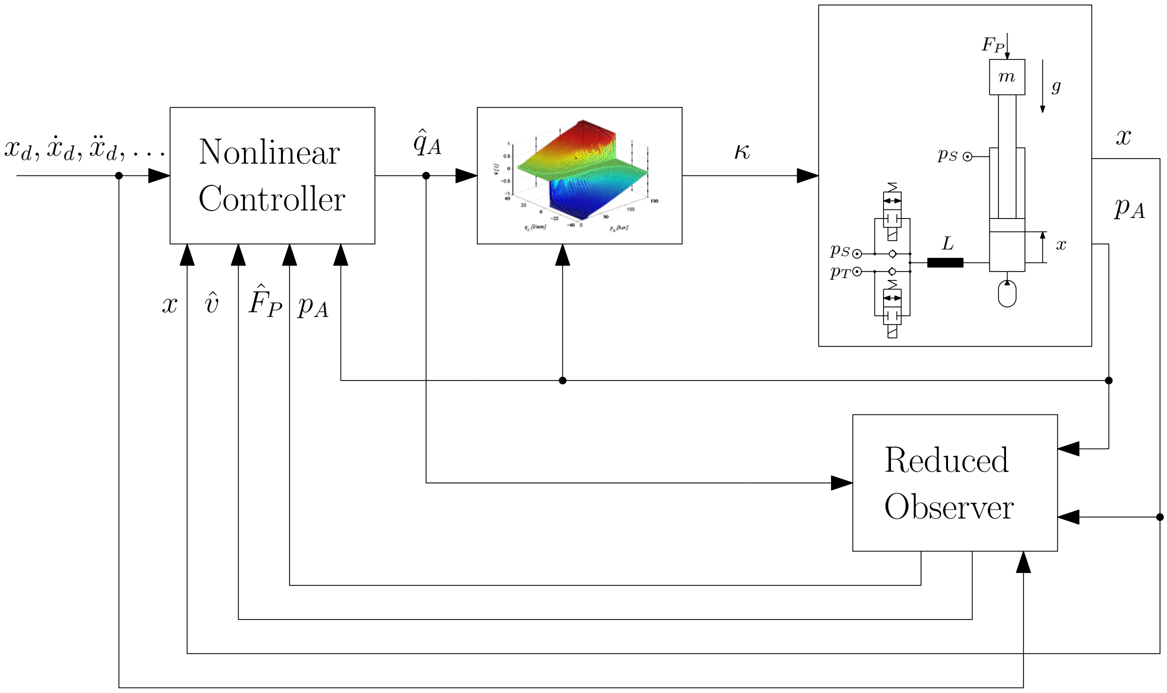

Figure 5.22.: Control scheme of the FBC in combination with a reduced observer

and p_A are directly used in the controller and the quantities $\hat{v}$ and $\hat{F}_P$ are estimated by the reduced observer. The rest of the circuitry is equal to the already discussed flatness based controllers. The tracking performance of the reduced observer is depicted in Fig. 5.23 for a position ramp with a slope of $100\frac{mm}{s}$. At $t = 1.5\,s$ a certain process force is applied to the configuration. Before the process force appears, the trajectory tracking is satisfying, but afterwards the deviation in the position of the load is too large. In Fig. 5.24 the performance at a $2\,Hz$ sinusoidal reference trajectory of the load position is illustrated. The closed loop system works properly until the process force occurs. From this point on, the deviations in the load position are also unacceptable. A possible reason for this behaviour is probably the fact, that with the design matrix (5.105) the information of the pressure measurement is lost. Thus, the choice of the design matrix (5.105) does not lead

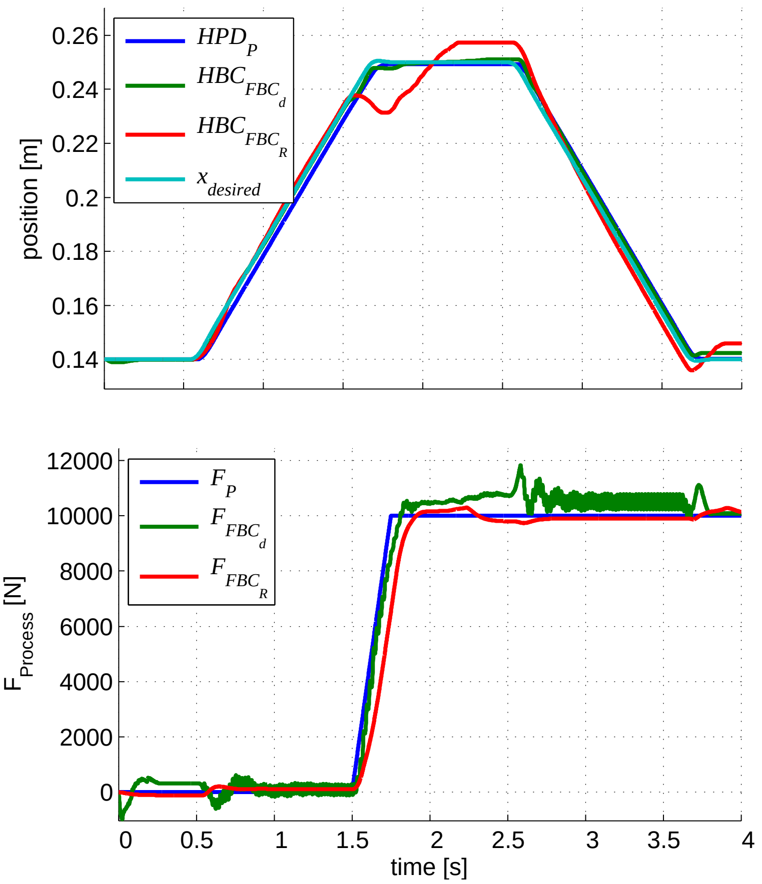

Figure 5.23.: Trajectory tracking of the FBC_R

to satisfying results. Probably better results could be achieved with an observer matrix

$$\mathbf{K}(t) = \begin{bmatrix} \frac{d_v}{m} + k_{11} & k_{12} \frac{V_A \left(\frac{p_{0_G}}{p_A(t)}\right)^{\frac{1}{\varkappa}}}{A_1 \varkappa p_A(t)} \\ k_{21} & k_{22} \frac{V_A \left(\frac{p_{0_G}}{p_A(t)}\right)^{\frac{1}{\varkappa}}}{A_1 \varkappa p_A(t)} \end{bmatrix}, \tag{5.111}$$

because in this case also the pressure information can be used to adjust the closed loop behaviour by the observer parameters. With such a configuration also a higher number of degrees of freedom for the observer parameterisation are available. The performance of the reduced observer with a design matrix (5.111) is not studied in this thesis, but will be investigated in future.

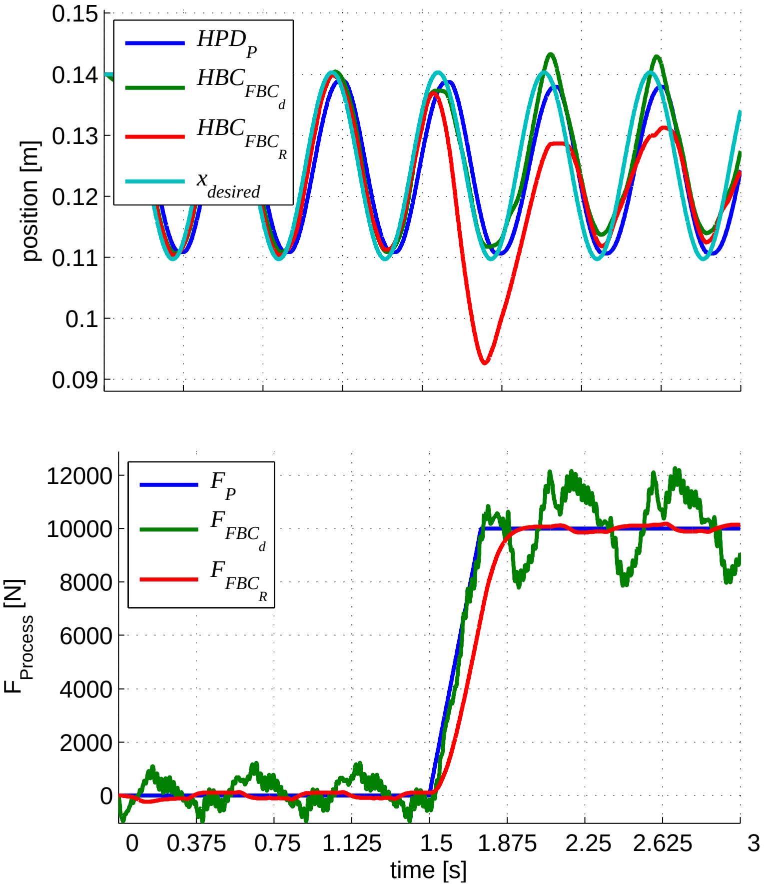

Figure 5.24.: Sinusoidal trajectory tracking of the FBC_R

5.4.4. Trajectory Planning

As pointed out in the previous sections the desired trajectory and a finite number of its derivatives with respect to time must be provided for the flatness based controller. Basically, there are two possibilities to fulfill this requirement. First, the trajectory can be planned by pre-processing in offline mode. Therefore, the intended motion of the system must be known and parameterised before the application goes into operation. In many cases the desired trajectory is uncertain itself, moreover it is governed by the operator of the drive during the working process. In such cases a second method is applicable. It uses a certain pre-filter, which delivers a trajectory with all its derivatives necessary for the controller. Since such a filter represents a sort of differentiator, this method only works in a certain dynamic operating range. However, one example for each strategy in planning a trajectory for a flatness based control will be outlined in the following.

5.4.4.1. Pre-Processing Method

The trajectory of the flat output has to fulfill the requirements

$$y(0) = y_0,\ y(t_{end}) = y_{end} \tag{5.112}$$

under the restrictions

$$\dot{y}(0) = \ddot{y}(0) = \ldots = \overset{(\sigma)}{y}(0) = 0 \tag{5.113}$$

and

$$\dot{y}(t_{end}) = \ddot{y}(t_{end}) = \ldots = \overset{(\sigma)}{y}(t_{end}) = 0, \tag{5.114}$$

where σ denotes the necessary number of derivatives, i.e., all derivatives of the flat output must vanish in each rest position. This can be realised for instance by a function

$$y_d = \begin{cases} 0, & t < 0 \\ \frac{1}{2} + \frac{1}{2}\tanh\left(\frac{2\left(2\frac{t}{t_{end}}-1\right)}{\left(4\frac{t}{t_{end}}\left(1-\frac{t}{t_{end}}\right)\right)^d}\right), & t \in [0, t_{end}] \\ 1, & t > t_{end} \end{cases}, \tag{5.115}$$

which belongs to a certain class of *Gevrey*-functions according to [36]. For instance, the function (5.115) is depicted in Fig. 5.25 for two different parameters d. Since the *tanh*-

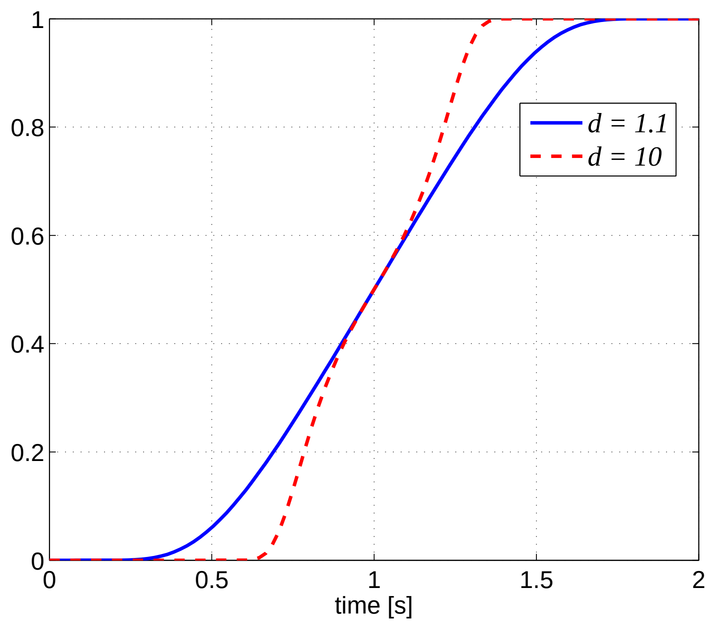

Figure 5.25.: Gevrey function

function is smooth, derivatives of all orders are available. Thus, such a *Gevrey*-function of Eq. (5.115) is qualified for a trajectory of the flat output. But it is not obligatory to use a function like Eq. (5.115) for trajectory planning, if only a finite number of derivatives is required. Thus, also an appropriate polynomial function of sufficient order is basically qualified for trajectory planning, if the polynomial fulfills the requirements of Eqs. (5.112) to (5.114).

5.4.4.2. Pre-Filter

In many cases the desired load position is given by the operator. Thus, trajectory planning by offline pre-processing is not advantageous. There exist a number of methods to calculate the necessary derivatives for a flatness based control in online mode, as for instance in [46]. As a simple example, the design of a digital filter according to [52] is outlined.

Basically, a transfer function of the form

$$G(s) = \frac{1}{\tau_\sigma s^\sigma + \ldots + \tau_1 s + 1}, \tag{5.116}$$

with σ as the number of necessary derivatives, is qualified for online trajectory planning. Such a filter can be, for instance, a *Bessel-*, *Butterworth* or any other low pass filter of sufficient order. The continuous transfer function (5.116) is equivalent to the controllable canonical form in state space

$$\begin{aligned} \dot{\mathbf{x}} &= \mathbf{A}_C \mathbf{x} + \mathbf{b}_C u \\ \mathbf{y} &= \mathbf{C}_C \mathbf{x} + \mathbf{d}_C u. \end{aligned} \tag{5.117}$$

In this canonical form the entries of the state $\mathbf{x}$ correspond to the derivatives of the filtered signal u. For implementation on a digital signal processing unit the continuous filter of Eq. (5.117) must be discretised with a constant sample time T_S. Therefore, the system (5.117) must be integrated on the time interval $[kT_S, (k+1)T_S]$, which leads to the system of difference equations

$$\begin{aligned} \mathbf{x}\left((k+1)T_S\right) &= \mathbf{A}_D \mathbf{x}(kT_S) + \mathbf{b}_D u(kT_S) \\ \mathbf{y}(kT_S) &= \mathbf{C}_D \mathbf{x}(kT_S) + \mathbf{d}_D u(kT_S), \end{aligned} \tag{5.118}$$

with

$$\mathbf{A}_D = e^{\mathbf{A}_C T_S} \mathbf{x}\left(kT_S\right) \tag{5.119}$$

$$\mathbf{b}_D u(kT_S) = \int_0^{T_S} e^{\mathbf{A}_C \tau} \mathbf{b}_C u\left(kT_S - \tau\right) \mathrm{d}\tau \tag{5.120}$$

$$\mathbf{C}_D = \mathbf{I} \text{ and } \mathbf{d}_D = \mathbf{0}. \tag{5.121}$$

The discrete dynamic matrix (5.119) can be calculated easily, but not Eq. (5.120) because of the unknown input values within the considered integration interval. The common method is to assume a constant input value in this integration interval, which corresponds to a zero order hold element. This is implemented in a number of discretising algorithms. In a more general representation of hold elements, the input values are approximated by a polynomial of the order r like

$$u\left(kT_S - \tau\right) \approx p\left(\tau\right) = \sum_{i=0}^{r} \kappa_i \left(\frac{\tau}{T_S}\right)^i, \tag{5.122}$$

which leads to

$$\mathbf{b}_D u(kT_S) = \sum_{i=0}^{r} \kappa_i \underbrace{\int_0^{T_S} e^{\mathbf{A}_C \tau} \mathbf{b}_C \left(\frac{\tau}{T_S}\right)^i \mathrm{d}\tau}_{\gamma_i}, \tag{5.123}$$

where the coefficient vector $\boldsymbol{\gamma}_i$ calculate to

$$\boldsymbol{\gamma}_i = \begin{cases} \mathbf{A}_C^{-1}\left(e^{\mathbf{A}_C T_S} - \mathbf{I}\right)\mathbf{b}_C & \text{for } i = 0 \\ \mathbf{A}_C^{-1}\left(e^{\mathbf{A}_C T_S}\mathbf{b}_C - \frac{i}{T_S}\gamma_{i-1}\right)\mathbf{b}_C & \text{for } i > 0, \end{cases} \tag{5.124}$$

if partial integration is applied several times. All $\boldsymbol{\gamma}_i$ can be collected in the matrix $\boldsymbol{\Gamma} = [\boldsymbol{\gamma}_0, \ldots, \boldsymbol{\gamma}_r]$. For the calculation of the remaining polynomial coefficients κ_i the requirement $p(\nu T_S) = u\left((k-\nu)\, T_S\right)$ for $\nu = 0, \ldots, r$ leads to the linear system of equations

$$\underbrace{\begin{bmatrix} 1 & 0 & \cdots & \cdots & 0 \\ 1 & 1 & 1^2 & \cdots & 1^r \\ 1 & 2 & 2^2 & \cdots & 2^r \\ \vdots & \vdots & \vdots & \ddots & \vdots \\ 1 & r & r^2 & \cdots & r^r \end{bmatrix}}_{\mathbf{V}} \begin{bmatrix} \kappa_0 \\ \kappa_1 \\ \vdots \\ \kappa_r \end{bmatrix} = \begin{bmatrix} u\left(kT_S\right) \\ u\left(kT_S - 1\right) \\ \vdots \\ u\left(kT_S - r\right) \end{bmatrix} = \mathbf{u}_k. \tag{5.125}$$

The solution of Eq. (5.125) for $\boldsymbol{\kappa}$ like[7]

$$\boldsymbol{\kappa} = \mathbf{V}^{-1}\mathbf{u}_k \tag{5.126}$$

leads finally to the discrete version of the continuous filter (5.117), which reads

$$\mathbf{x}_{k+1} = e^{\mathbf{A}_C T_S}\mathbf{x}_k + \boldsymbol{\Gamma}\mathbf{V}^{-1}\mathbf{u}_k \tag{5.127}$$

$$\mathbf{y}_d = \mathbf{I}\mathbf{x}_k \tag{5.128}$$

with the vector of the input values $\mathbf{u}_k = [u_k, \ldots, u_{k-r}]^\top$. The filter, which is parameterised for the flatness based control of the linear hydraulic drive powered by the HBC, is illus-

[7] It can be shown, that the Van-der-Monde matrix $\mathbf{V}$ is invertible.

trated in Fig. 5.26. Since an ideal differentiator is not realisable, the filter has a cut-off

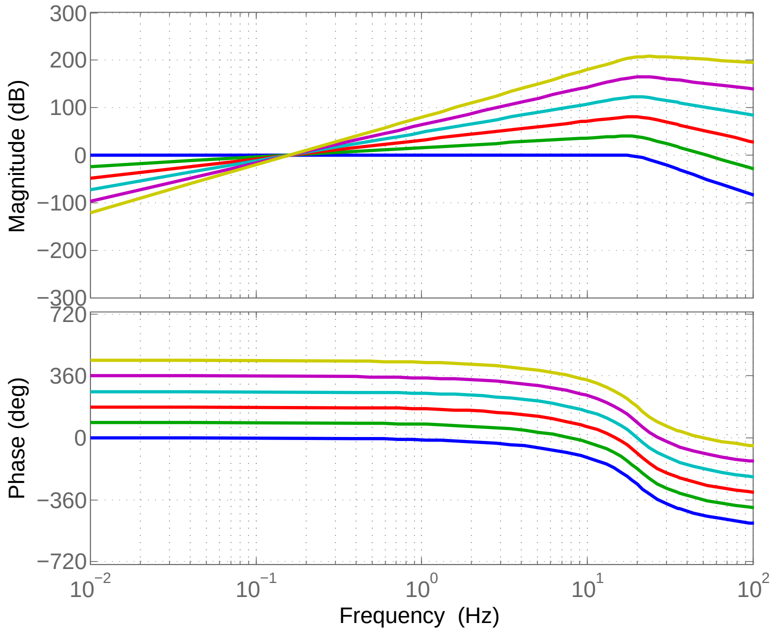

Figure 5.26.: Bode plots of a filter according to Eq. (5.118)

frequency. In this case the maximum frequency of the desired operating cycles is limited to approximately $10\,Hz$. In contrast to filters using a zero order hold element for the approximation of $u(kT - \tau)$ and, in accordance with [52], the presented filter shows a better behaviour beyond the cut-off frequency, if the order of the approximating polynomial r is not too high. But it has to be remarked, that the stability of such a filter - especially at higher orders r - must be checked in the z-domain, because the stability can only be proven in case of a zero order hold element in general. Finally, it is important to mention, that such filters only work on floating point units.

6. Advanced Experiments

The basic experiments according to Chapter 3 concerned the characteristic behaviour and the efficiency performance of the different HBC prototypes, but, so far, no closed loop control experiments were presented. In fact, the low energy consumption of the HBC compared to resistance control was shown theoretically and the control performance was investigated by simulations, but the verification of these results by appropriate experiments is still missing. In this chapter two different types of experiments will be reported. First, the energy performance of the HBC prototype *HBC030* is compared to resistance control and, second, the control performance of an HBC actuated hydraulic linear drive exploiting advanced controller concepts according to Chapter 5 will be presented.

6.1. Energy Comparison

The first experiment compares the energetic performance of the HBC and resistance control by a proportional valve. For this purpose a test stand according to the hydraulic circuitry of Fig. 6.1 was set up. The load is determined by the accumulator A_L on the right hand side with a size of $0.32\,l$ and a pre-pressure of $40\,bar$. The intention is to control the pressure p_L either via the proportional valve on top or with the HBC at the bottom of the figure. For a correct evaluation of the different energy consumptions the output power must be equal in both drive configurations. Only then the power consumption of both drives can be compared by measuring the supply pressure p_S and the corresponding supply flow rate Q_S. Thus, also the load flow rate Q_L is measured to reconstruct the power at the load. The tank pressure is realised by a pressure relief valve. The necessary amount of fluid needed in the suction phase is stored in the accumulator A_T. The tank pressure is provided by the adjustable orifice R_S, which is closed before the converter goes into operation. In fact, the tank pressure will be lowered when the HBC draws fluid from the tank, but in the recuperation mode of the converter the tank will be refilled. The smaller accumulators D_S and D_T are installed to decouple the converter from the surrounding pipe system. The accumulator A_O is designed for pressure attenuation at the output of the converter.

For a correct measurement of the individual power consumptions of each drive no leakage flow over the inactive part of the circuit - either the proportional valve or the HBC - must

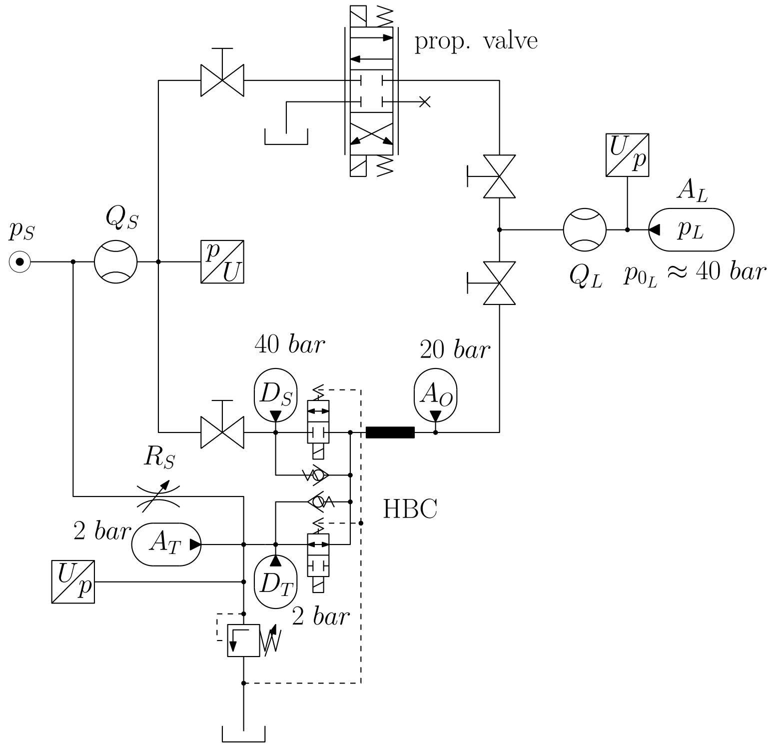

Figure 6.1.: Hydraulic circuitry for energy comparison

occur. This can be guaranteed by the different ball valves in the circuitry of Fig. 6.1, which enable - in right position - only a flow in the actual investigated system. Furthermore, the pipe systems of both configurations must have the same dimensions in order to assure equal losses by transmission lines. A photo of the setup is depicted in Fig. 6.2. The measurements are carried out with the converter prototype *HBC030*. Since this converter represents a low power converter the results are expected to be worse compared to larger converters, because the relative effect of dissipative processes become more dominant at small drives. So, one can expect a higher efficiency, if converters with a larger power ratio are considered. The used proportional valve is a 4/3 valve, which only acts as a 3/3-valve since only one output port of the valve is used for the intended pressure control. Thus, the flow is controlled by one metering edge. For this reason the size of the proportional valve is not relevant, at least if no saturation effects occur.

The desired trajectory of the load pressure p_L is a sinusoidal signal at a sufficiently low frequency in order to guarantee quasi-static conditions. Thus, the dynamics of the proportional valve and of the HBC can be neglected. The static characteristics of the converter are compensated according to Eqs. (2.4) and (A.3) for both flow directions by a corresponding static feed-forward. Actually, the direction of the flow rate should have been measured, because during the discharging cycle of the load accumulator A_L the HBC is expected to recuperate energy into the supply line and, thus, the direction of Q_S is relevant. Unfortunately, the applied sensor did not provide the sign of the flow direction. But, since the desired trajectory is well known and since no further dynamics occurs, the

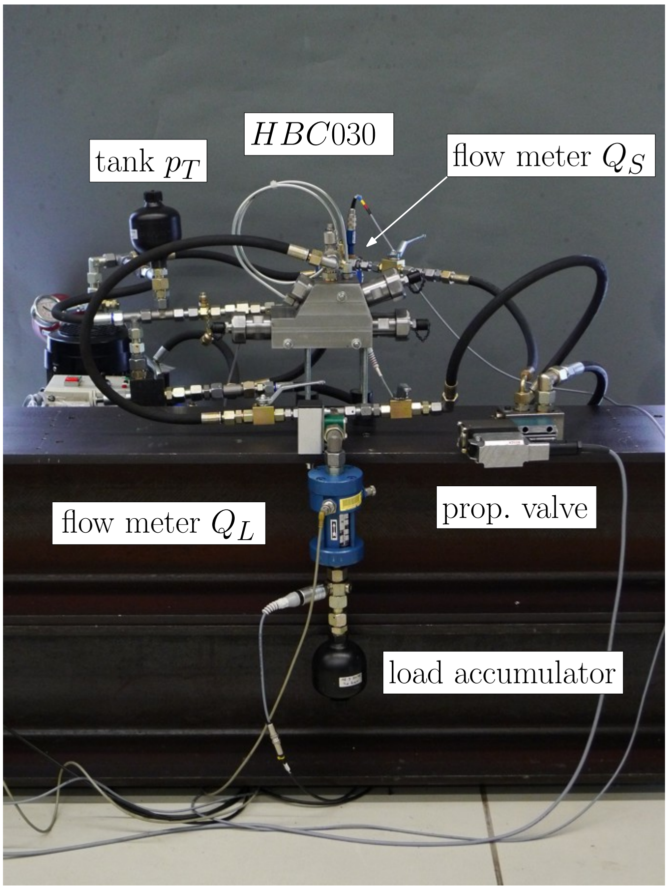

Figure 6.2.: Test stand for energy comparison

load flow rate under the assumption that the gas spring dominates the hydraulic capacity reads

$$Q_{L_d} = \dot{p}_{L_d} \frac{V_A \left(\frac{p_{0_L}}{p_{L_d}}\right)^{\frac{1}{\varkappa}}}{\varkappa p_{L_d}}. \tag{6.1}$$

The sign of the measured flow rates can be determined, if no phase shift between the measured load pressure and the desired trajectory occurs. The closed loop control is realised by a simple P-Controller, which is sufficient at such a low frequency of the trajectory. In Fig. 6.3 the results of the tracking control of both investigated configurations are illustrated. In the lower diagram the corresponding load pressures are opposed to the desired trajectory. The accuracy is satisfactory for the purpose of this experiment. In the upper diagram the load flow rates are depicted, where $Q_{L_{HBC}}$ of the converter exhibits some ripples, probably due to the switching process. But this amount of noise is acceptable for this experiment. Moreover, also the flow rate signal of the HPD shows some ripples at the point where the direction of the flow rate changes. This is possibly caused by the overlap of the proportional valve. However, the curves in Fig. 6.3 indicate, that both configurations accomplish almost the same power at the output, which is necessary for the analysis of the energy consumption. Thus, the comparison of the measured energy consumption can be carried out conveniently, which is shown in Fig. 6.4. In the lower

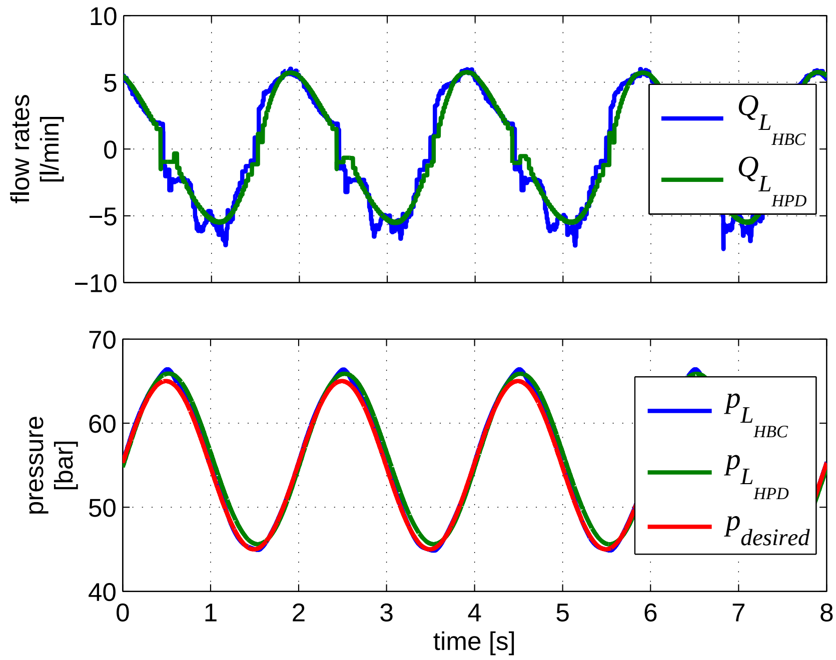

Figure 6.3.: Measurements at the load

diagram again the different load pressures like depicted in Fig. 6.3 are shown. Due to the simple P-controller a small phase shift between the desired and the measured trajectory arises. For this reason the change of the flow rate sign according to Eq. (6.1) may occur a little bit earlier than in reality. The corresponding supply flow rates are illustrated in the middle diagram of Fig. 6.4, where the mentioned sign problem is indicated by the negative peaks in the flow rate $Q_{S_{HBC}}$. Thus, the corresponding amount of seemingly recuperated energy falsifies the overall energy consumption of the HBC. However, a negative supply flow rate means that energy is recuperated. On the other hand, in the forward flow direction, when the load accumulator A_L is charged, the flow rate from the supply line $Q_{S_{HBC}}$ at the HBC configuration remains always below the flow rate $Q_{S_{HPD}}$ from the HPD. The difference between both flow rates is drawn from tank line and, thus, energy is saved. In the upper diagram the energy consumptions of both drives and, thus, the integrals with respect to time of the consumed power are presented. The slope of the HBC's energy curve is always lower than the curve of the HPD. In the phase of a descending load pressure the slope of the energy curve of the HBC is negative, i.e., energy is recuperated. In this diagram a mean reduction of the consumed energy of about one third over one working cycle can be observed. It should be mentioned, that this value may be little bit too high, because of the mentioned negative flow rate peaks due to the sign problem. Nevertheless, a significantly better efficiency of the HBC compared to resistance control could be verified, even at such small power ratios.

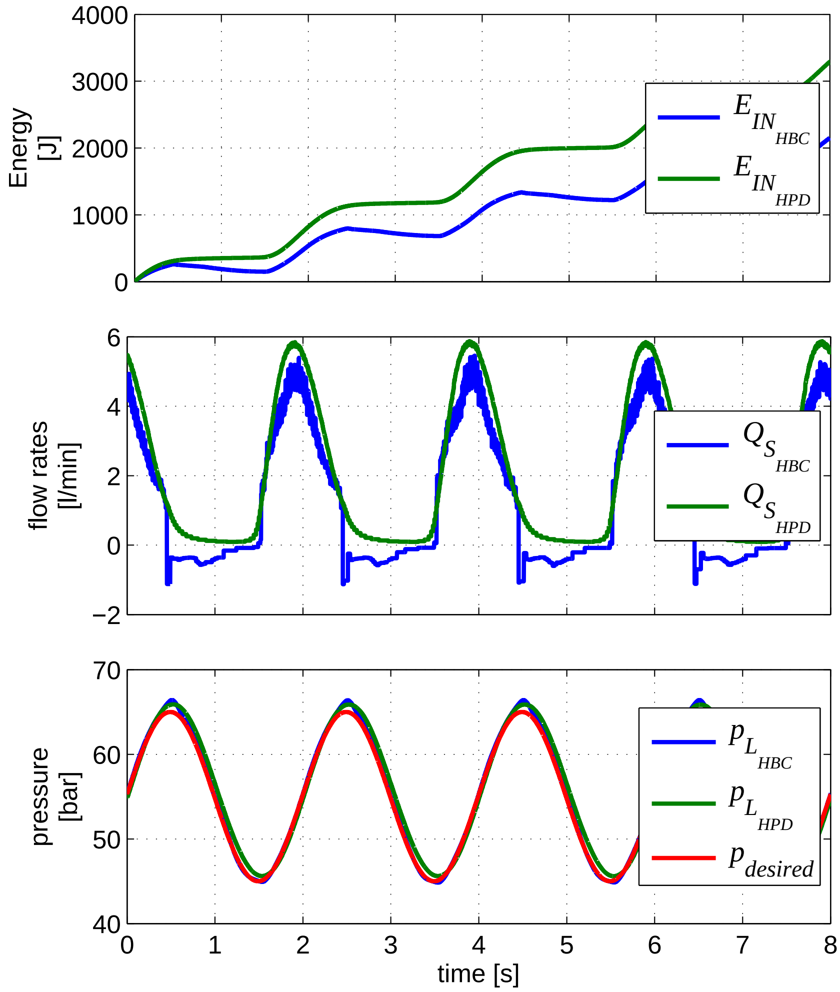

Figure 6.4.: Energy comparison of the different configurations

6.2. Linear Drive Control Experiments

The following investigations deal with the closed loop control performance of a linear hydraulic drive. As already pointed out in Chapter 5 the softness of the HBC due to the pressure attenuation capacitance at the output of the converter requires an advanced controller design for an acceptable control performance. Based on the considerations in Chapter 5, the shortcoming of the softness of the HBC can be at least partially compensated by a flatness based control, as has been already shown by simulations. The investigations documented in this section show the experimental control performance of a linear hydraulic drive controlled by an HBC employing a flatness based control. The experiments concentrate on a configuration like depicted in Fig. 6.5. The load is defined by

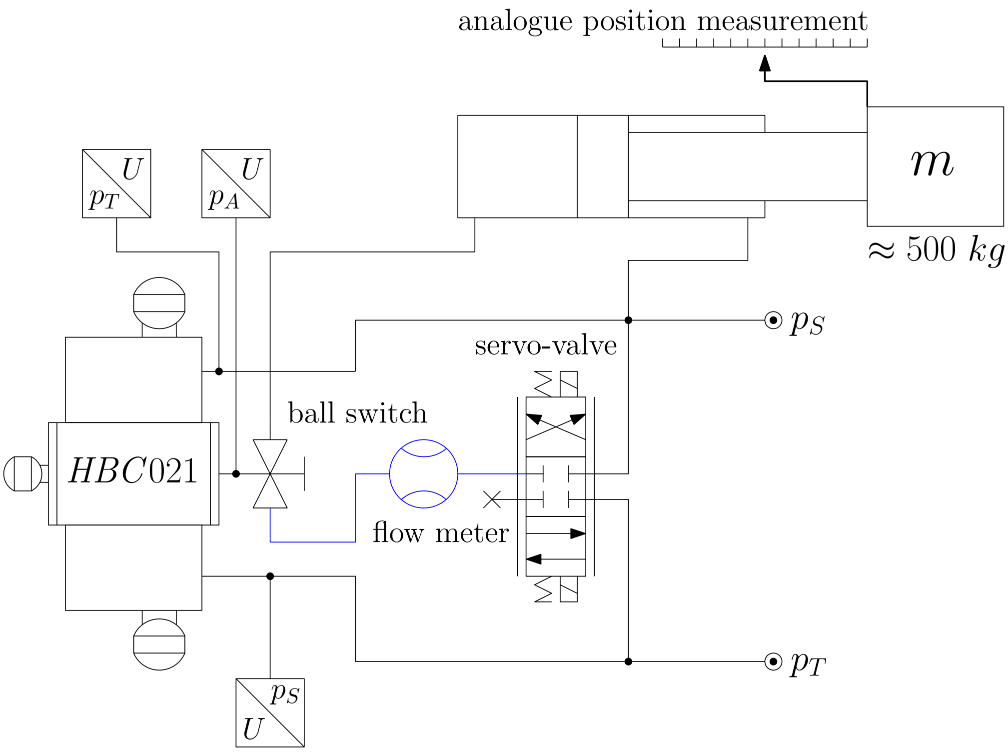

Figure 6.5.: Hydraulic circuit for control measurements

a differential cylinder, which operates in plunger mode according to the considerations in Chapter 5. At the end of the piston rod a dead load of approximately 500 kg is mounted. For control issues the position of the mass and the pressures p_S, p_T and p_A are measured. The investigations were carried out with the prototype *HBC021* already introduced in Section 3.2.3. For this reason the *HBC021* is only schematically depicted on the right hand side in Fig. 6.5. For an adequate application of the intended control strategies the static converter characteristics must be compensated as shown in Chapter 5 . For this purpose, the circuitry in Fig. 6.5 also involves a servo valve for the measurement of the actual characteristics of the used converter. The servo valve can be connected via a three port ball valve to the HBC. In the corresponding branch a flow meter is situated, which is necessary to control the load flow rate during the characteristic measurements. The second switching state of the ball valve connects the output of the converter to the piston sided chamber of the differential cylinder. It has to be remarked, that the servo valve in the circuitry serves only for characteristic measurements and, thus, no explicit comparison between the HBC and resistance control is intended with the following experiments. The real test bench according to the circuitry of Fig. 6.5 is depicted in Fig. 6.6.

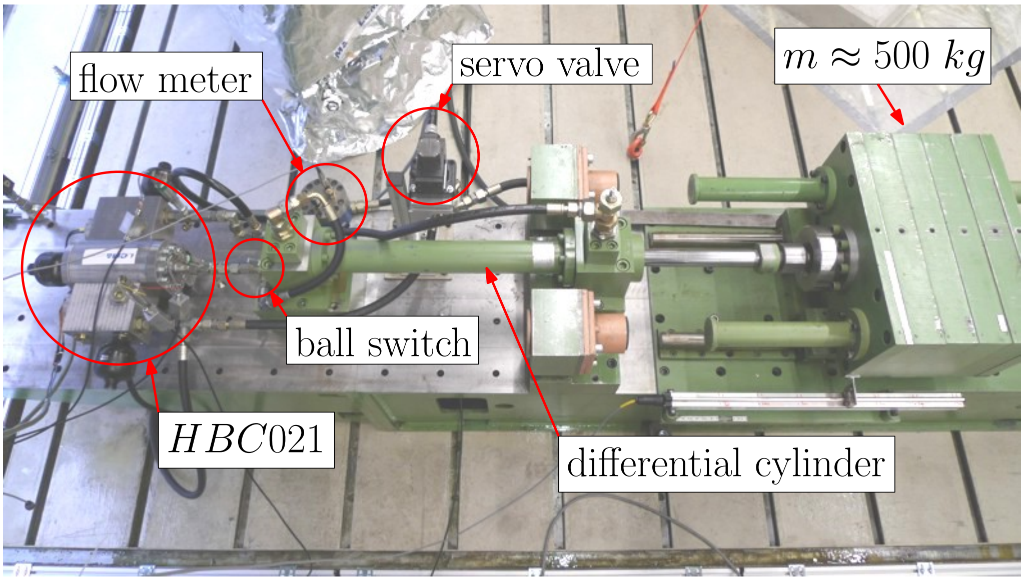

Figure 6.6.: Linear axis controlled by an HBC

6.2.1. Converter Characteristics

For a reasonable application of the flatness based control the characteristics of the converter must be compensated. The used HBC prototype is a converter with a threaded spindle inductance. Since the calculated characteristics from chapter 4 are only valid for a converter with a straight inductance pipe, the characteristics of the applied converter have to be identified from measurements. Therefore, a rectangular set of operating points concerning load flow rates and duty cycles was defined. Those points of operation are adjusted subsequently in the experiments and the corresponding load pressure was measured. The measured load pressure characteristics in dependence of the load flow rate and the duty ratio is depicted in Fig. 6.7. The HBC prototype employs a membrane accumulator at the output, which is pre-pressurised to $50\,bar$. To prevent a destruction of the diaphragm of the accumulator the load pressure must not fall below this pressure limit. Thus, if the pressure drop over the converter due to the increasing load flow rate leads to an output pressure lower than the limit of $60\,bar$, the remaining sub-series of operating points at this constant duty ratio was cancelled and the next row of the mesh

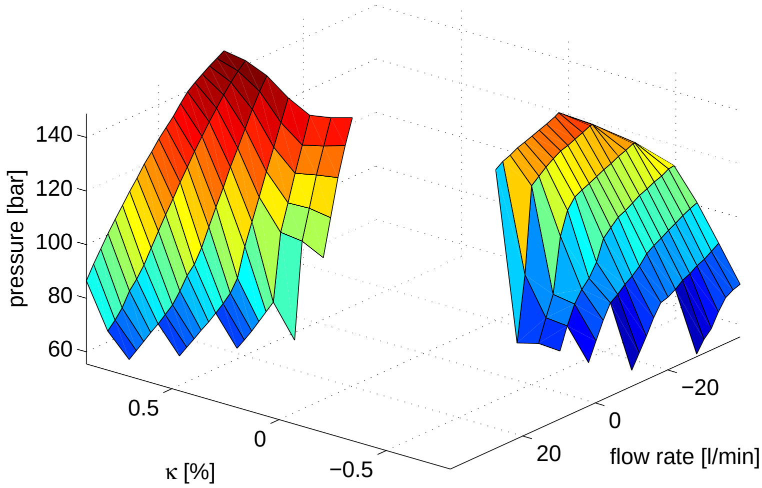

Figure 6.7.: Measured converter characteristics

grid was started. For this reason the sets of operating points in both flow directions in Fig. 6.7 are not rectangles.

The measured characteristics from Fig. 6.7 are not yet suitable for compensation. Remembering, that the output of the different controllers is not a duty ratio but represents a flow rate at the actual operating pressure, the characteristics for compensation must have the following form

$$\kappa = f\left(p_A, q_L\right). \tag{6.2}$$

Thus, the diagram of Fig. 6.7 has to be transformed to the desired structure of Eq. (6.2), which was performed in *Matlab*™ by the algorithm *griddata*. The resulting diagram of the converter characteristics for compensation is illustrated in Fig. 6.8. The measured operating points are indicated by the cross markers. The resulting surface was interpolated by the use of the command *griddata*. Additionally, a certain dead band around the zero flow rate line was created to avoid some limit cycles of the position control in rest positions. It must be remarked, that the accuracy in positioning the dead load is also influenced by this dead band. Due to this dead zone and the disadvantageous resolution of the equidistant mesh of operation points, the smoothness of the characteristic around the zero flow rate is corrupted. Thus, some problems at the position control in rest positions may be expected. Nevertheless, the control experiments, which are described in the following section are carried out with the characteristics of Fig. 6.8.

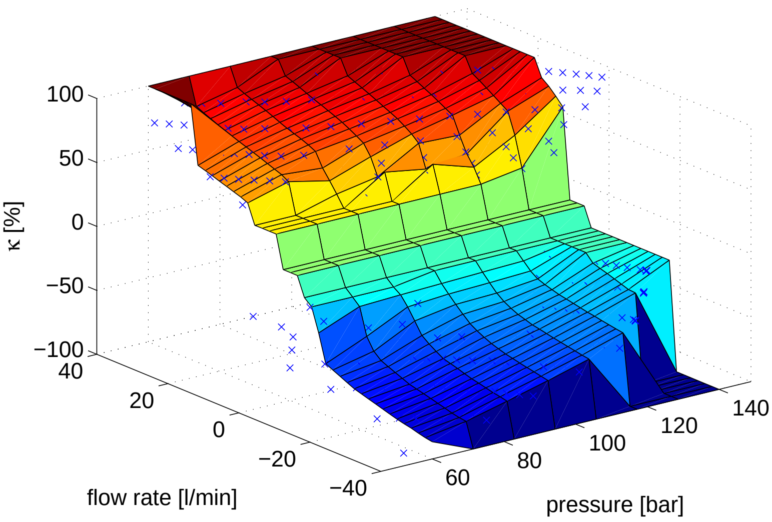

Figure 6.8.: Transformed converter characteristics

6.2.2. Position Control

In the following the tracking performance of three different position controllers are opposed in a number of different drive control experiments. The first controller type is the conventional P-Controller according to Fig. 5.6. Second, two different flatness based controllers according to Section 5.4 are tested, which differ only in the observer design. On the one hand the application of the complete observer design (FBC) in accordance with Subsection 5.4.3.1 will be demonstrated, which only uses the position of the dead load for the estimation of the system state. On the other hand the performance of the load observer (FBC-D) from Subsection 5.4.3.2 will be discussed, which additionally needs the measurement of the pressure at the output of the converter to estimate the process force F_P accurately. But, with the available test stand depicted in Fig. 6.6 no external process force could be applied. Thus, the load observer may compensate only some effects like friction of the load carriage guide way, which were neglected during the modelling process. The flatness based controller design with the reduced observer was not investigated by experiments.

The first two experiments represent the response due to a desired ramp with two different slopes in both directions of movement. The corresponding results are depicted in Fig. 6.9 and Fig. 6.10. As expected, the tracking performance of the empirically adjusted P-Controller is not acceptable. Due to the softness of the system large oscillations occur during the movement. Also the delay in the response time is too high. The performance of the two flatness based controllers are much better, remarking that no identification of the model parameters was carried out. The physical parameters of the nonlinear model for the synthesis were estimated only from design data. The dynamics of the flatness based controller and the different observers were adjusted empirically. Moreover, the controller

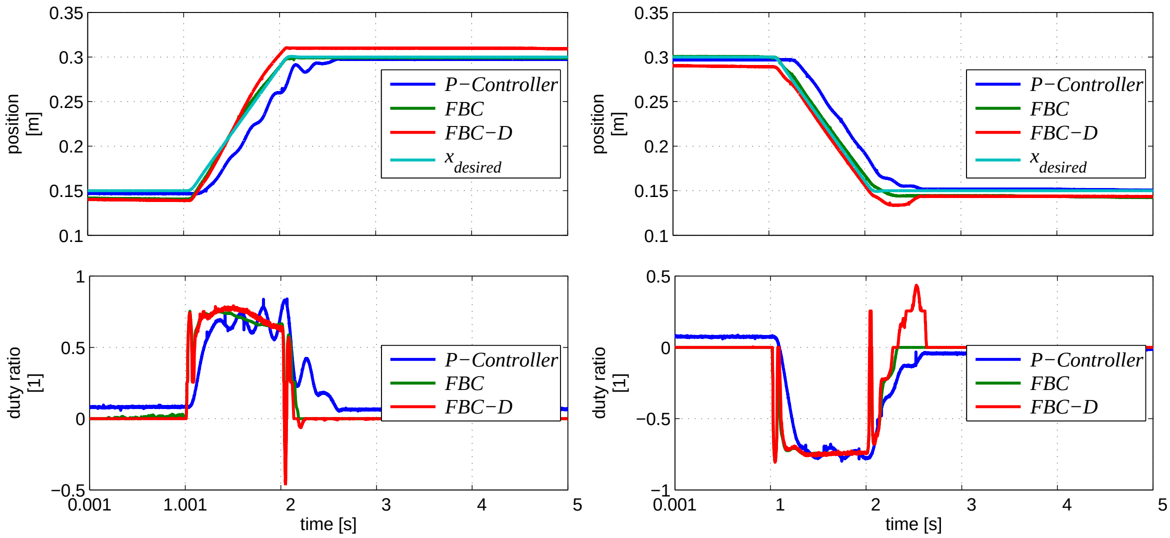

Figure 6.9.: Ramp $v_d = \pm 150 \frac{mm}{s}$

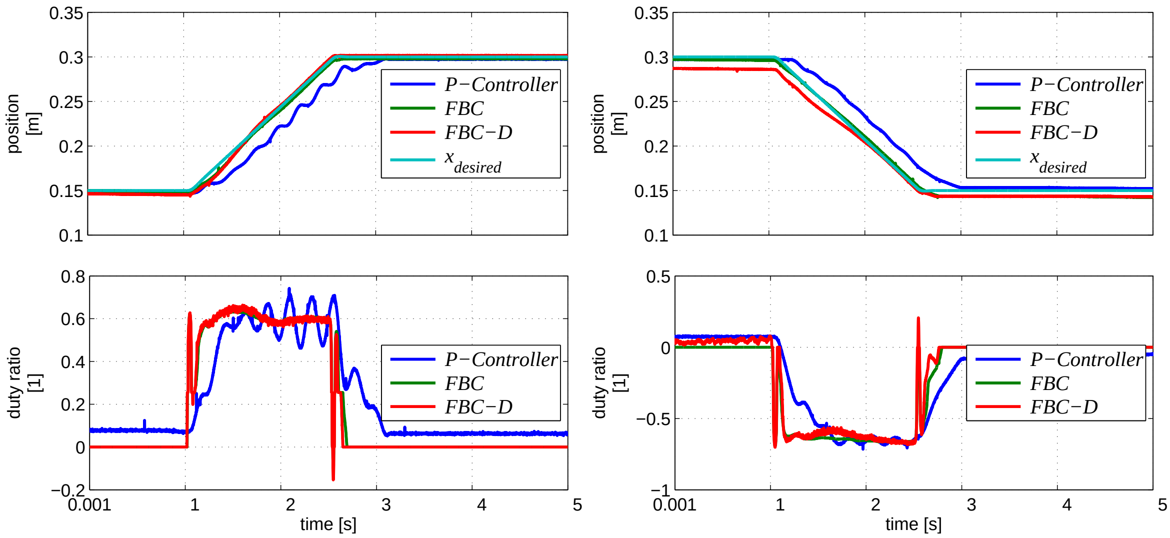

Figure 6.10.: Ramp $v_d = \pm 100 \frac{mm}{s}$

parameters remain constant for all other experiments. The deviations in the response of the flatness based controllers can be explained by the fact, that the tank sided switching valve had an unexpected high leakage due to a damage of the spool, which occurred during some other experiments before. The different deviations in the starting points can be explained by this fact. But beside this deficiencies the responses of the flatness based controllers coincide with the desired trajectory and, thus, the good performance of the flatness based concept could be verified.

As mentioned already in Subsection 6.2.1 the inaccurate characteristics in the area of zero flow rates leads to a bad tracking performance at lower piston velocities. This can be examined in the right diagram of Fig. 6.9, or as well in the left diagrams of Fig. 6.11, where a sinusoidal desired trajectory of the piston was commanded. On the right hand side of Fig. 6.11 the system response at an excitation frequency of $1\,Hz$ of the desired

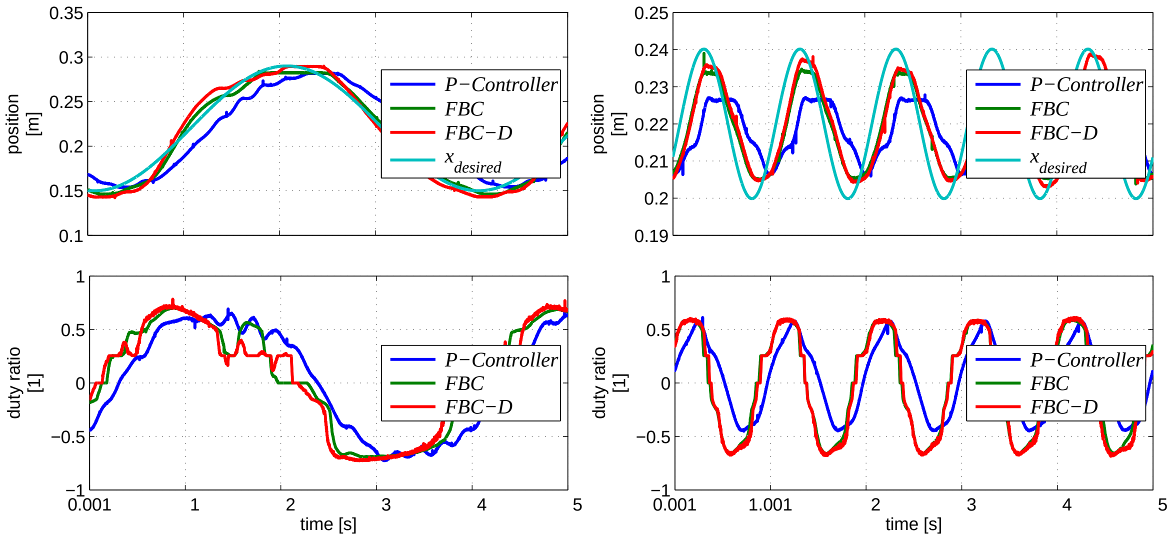

Figure 6.11.: Sinusoidal signal $f_{exc} = 0.25\,Hz$ (left) and $f_{exc} = 1\,Hz$ (right)

trajectory is depicted. In fact, the deviations in the system response are increasing, but remembering, that the controller parameters were kept constant at all experiments, i.e. they have not been optimised, the results are still acceptable. Moreover, the mentioned problem with the damaged switching valve and the rough measured characteristics of the converter let expect further improvements in the control performance of faultless drives.

The investigated configuration according to Fig. 6.6 has a natural frequency of

$$f_{axis} \approx \frac{1}{2\pi}\sqrt{\frac{\varkappa \bar{p}_A A_1^2}{V_A m}\left(\frac{p_{0_A}}{\bar{p}_A}\right)^{-\frac{1}{\varkappa}}} = 3.6\,Hz. \tag{6.3}$$

In the following, the closed loop performance at an operating frequency beyond the resonance frequency will be investigated. In Fig. 6.12 the system response at an excitation frequency of $5\,Hz$ is depicted. The flatness based controllers can follow the commanded signal at least dynamically. On the one hand, the offset in the response can be explained by saturation effects of the duty ratio, which can be seen in the lower left diagram in Fig. 6.12. Thus, for a dynamic response at such frequencies a larger converter would have to be applied to achieve a better accuracy. On the other hand, at such frequencies the model parameters must be very accurate and should have been identified by experiments. However, if the HBC and the control are designed properly also a high dynamic movement of the load can be realised, because of the high band width of the switching valves.

The experiments showed, that a linear hydraulic drive exploiting a hydraulic buck converter can achieve an acceptable accuracy at better efficiency. Furthermore, a fast switching drive can be realised cheaper than common proportional hydraulics, because the provided switching valves can be produced at much lower costs than proportional valves. All this proves the remarkable potential of the HBC.

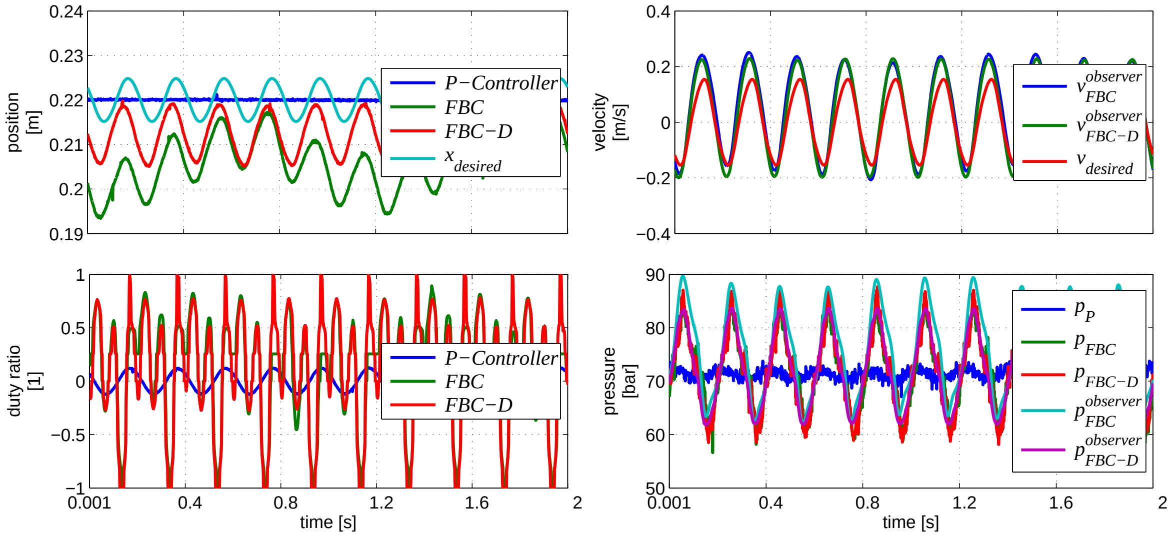

Figure 6.12.: Sinusoidal movement at $f_{exc} = 5\,Hz$

7. Future Prospects

In this work basic studies of the Hydraulic Buck Converter were presented. The investigations taught, that the efficiency of hydraulic drives can be improved dramatically with an HBC. Due to the simplicity of the used components a low cost manufacturing of such drives is possible. Such switching configurations are also expected to be very robust concerning oil contamination. Thus, it could be shown, that the HBC is an alternative to proportional control for a number of applications. In the following some ideas for some further development steps are proposed.

7.1. Efficient System Configuration

In many industrial and mobile applications the control elements, such as valves or even an HBC, are often situated far away from the cylinder. Thus, the fluid has to be transported via long pipes or hoses from the control units to the actuator and back again to tank line, as depicted in Fig. 7.1. The pipes' or hoses' dynamical responses are indicated

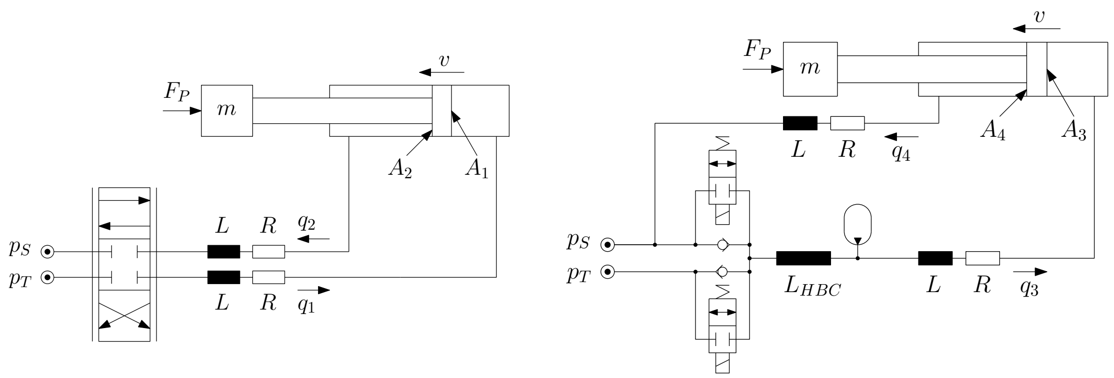

(a) 4/3-proportional valve (b) HBC in plunger configuration

Figure 7.1.: Equivalent force configurations

by lumped parameters L and R. For simplicity it is assumed, that both lines have the same dimension. Furthermore, the tank port of the 4/3-valve is assumed to be connected to a pre-pressurised tank, also for simplicity. The application of an HBC - at least as introduced in this work - requires a differential cylinder, which operates in plunger mode in accordance with Fig. 7.1b. To achieve the same force capacity with the HBC as the configuration according to Fig. 7.1a the cross-section ratio of the cylinder in Fig. 7.1b must fulfill the following relations

$$p_S A_1 - p_T A_2 = p_S A_3 - p_S A_4 \tag{7.1}$$
$$p_T A_1 - p_S A_2 = p_T A_3 - p_S A_4, \tag{7.2}$$

which leads to the new cross-sections of the plunger cylinder

$$A_3 = A_1 + A_2 \tag{7.3}$$
$$A_4 = A_2 \frac{p_T + p_S}{p_S}. \tag{7.4}$$

Thus, in fact, both configurations of Fig. 7.1 have the same force performance, but for the same velocity a different amount of oil must be provided at the cylinder. Without any judgment of the efficiency of the different control elements the power losses due to the static resistance R of the transmission lines read in case of the proportional drive

$$P_{V_{HPD}} = R\left(A_1^2 + A_2^2\right) v^2 \tag{7.5}$$

according to Fig. 7.1a and,

$$\begin{aligned} P_{V_{HBC}} &= R\left(A_3^2 + A_4^2\right) v^2 \\ &= R\left(A_2 \frac{p_T + p_S}{p_S} v\right)^2 + R\left(A_1 + A_2\right)^2 v^2 \\ &\approx R\left(A_2^2 + \left(A_1 + A_2\right)^2\right) v^2 \end{aligned} \tag{7.6}$$

for the HBC configuration from Fig. 7.1b. In case of the HBC, the transmission power losses are higher than the losses of the proportional drive due to the larger cross-sections. To avoid this drawback the converter must be situated directly at the cylinder, as depicted in Fig. 7.2. Thus, a reduction of the fluid transport losses over the supply lines is possible by the use of a differential flow from the annulus to the piston chamber for $v > 0$ and vice versa in recuperation mode of the converter. The flow rate through the converter reads

$$\begin{aligned} q_C &= q_A + q_S \\ A_4 v + q_S &= A_3 v - q_T. \end{aligned} \tag{7.7}$$

The flow rate through the supply line can be approximated by

$$\begin{aligned} q_S &= \left(A_1 + A_2\right) v - A_2 \frac{p_T + p_S}{p_S} v - q_T \\ &\approx \left(A_1 + A_2\right) v - A_2 v - q_T \end{aligned} \tag{7.8}$$

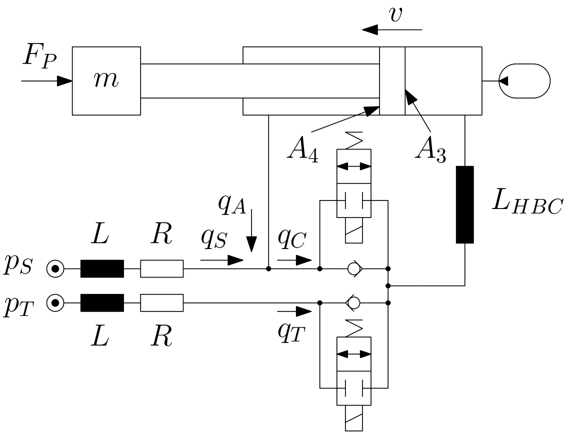

Figure 7.2.: Efficient plunger configuration

and, thus, the losses due to oil transport in the connection lines calculate to

$$\begin{aligned} P_{V_{HBC}} &= R\left(q_S^2 + q_T^2\right) \\ &= R\left(A_1 v - q_T\right)^2 + Rq_T^2 \\ &= R\left(A_1^2 v^2 - 2q_T A_1 v + q_T^2\right) + Rq_T^2 \\ &= R\left(A_1^2 v^2 - 2q_T A_1 v + 2q_T^2\right) < RA_1^2 v^2, \end{aligned} \tag{7.9}$$

under the assumption $A_1 v > q_T$, which is valid in most operating points of the HBC. Then, the transport losses of the configuration according to Fig. 7.2 are lower compared to Eq. (7.5), in spite of the adapted cross-section ratio of the cylinder. In fact, in some operating points this assumption is violated when, for instance, the converter is saturating and no more switching of the valves takes place. But, a properly designed hydraulic drive fulfills the maximum force requirements without operating in saturation mode.

The possibility to reduce the transport power losses using differential energy flow by the application of an HBC was the motivation to design the prototype *HBC041*, which can be directly mounted at the annulus port of a commercially available differential cylinder, like depicted in Fig. 7.3. In this case the inductance is realised as a straight pipe along the cylinder. In fact, this is the best configuration in view of losses in the inductance, but the value of the inductance and, thus, also the efficiency performance of the converter depends strongly on the length of the cylinder. Of course, there exist a number of possibilities for an advantageous placement of the inductance, for instance, to wind the pipe around the outside of the cylinder wall. But a threaded inductance pipe may exhibit higher losses. Such a configuration would have to be evaluated with respect to its energetic performance. The prototype according to Fig. 7.3 is still under development. Its realisation and measurements will be done in the near future.

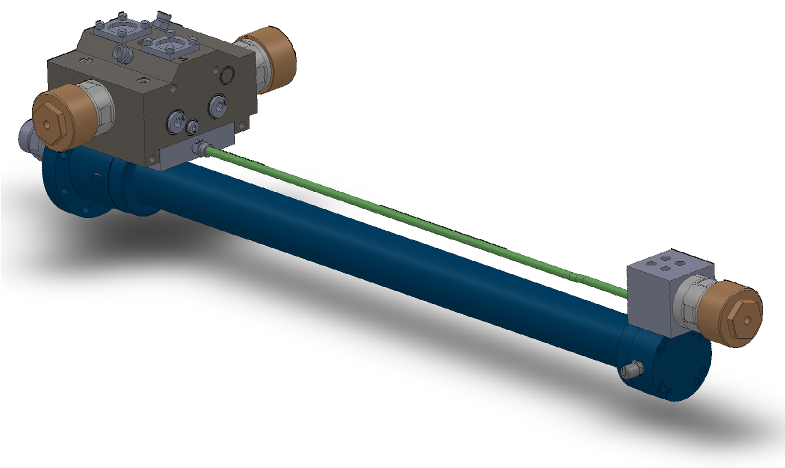

Figure 7.3.: CAD drawing of the *HBC041*

7.2. Components

For a convenient realisation of energy efficient fast switching hydraulic systems well designed and reliable components are needed. The experiments shown in this work taught, that in some cases a better energy performance could be achieved by improving certain deficiencies of essential components.

7.2.1. Digital Valves

A satisfying energy performance of an HBC requires the application of qualified digital switching valves. As mentioned in this thesis, such valves must have a large nominal flow rate and a high dynamic response. Today some active switching valves exist, which meet those necessary requirements for fast switching hydraulics. Furthermore, there exist a number of ideas for another promising valve concepts for hydraulic switching converters. Those ideas will be evaluated in the future.

For a proper design of energy efficient hydraulic drives not only active switching valves are important. Especially check valves play a crucial role for a good efficiency performance. The nowadays developed prototypes are in fact qualified for laboratory tests, but their dynamics and also their reliability are not yet satisfying for practical application at the moment. Hence, the development of highly dynamic, high flow and robust check valves constitutes an important research issue.

7.2.2. Inductance

The considerations in this thesis taught, that the best efficiency can be achieved with a straight pipe. But this geometry of the pipe inductance needs much space, which is often hardly available. To reduce the overall size of the converter four different coils with different winding diameters were investigated. The experiments showed, that the lower the coil diameter the lower the efficiency. But in Fig. 3.15 also a possible saturation trend could be supposed, where the losses do not increase anymore below a certain coil diameter. For a sound understanding of the flow through helical pipes appropriate dynamic models are necessary, which should be developed in future work.

Another possibility to increase the efficiency of the converter is to reduce the wall friction in the pipe. This can be possibly done by so called nano texturing, which is a special coating of the inside wall surface of the inductance pipe. Some results concerning nano texturing for hydraulic transmission lines can be found, for instance, in [42].

7.3. Exploiting the Load Capacitance

The additional capacity at the output of the converter is necessary to smoothen the pressure ripples at the load due to the switching process. In the considered cases of this thesis the capacity was realised by a gas loaded accumulator, which provides additional unwanted softness to the system. Furthermore, this additional component increases the installation and maintenance costs. Moreover, the nonlinear characteristic of the gas spring makes the controller design more sophisticated. But, there exist high force applications, which already provide a large capacity at the load as, for instance, high force cylinder drives. Due to the requirement of coping with process forces up to several mega Newtons, the cross-section of the piston is such large, that the volume in the piston sided chamber can smoothen the pressure ripples excited by the switching process of an HBC. Thus, no additional pressure attenuator device must be installed. Furthermore, the nonlinearities of a gas filled accumulator can be avoided.

In this thesis the control of HBC driven applications is based on the fact, that the natural frequency of the load system must be much lower than the switching frequency of the converter. But, due to the large cross-section of the piston the natural frequency of such drives is in many cases above the switching frequency. For instance, a high force cylinder has typically a piston diameter of about $1\,m$. The installed mass m is about several tons, e.g., $m \approx 20\,t$ and the piston position leads to a typical dead volume $V_P \approx 100\,l$. This parameter set and a bulk modulus of $E_{oil} \approx 14000\,bar$ leads to a natural frequency of

$$f_{axis} = \frac{1}{2\pi}\sqrt{\frac{E_{oil}A_P^2}{V_P m}} \approx 150\,Hz, \tag{7.10}$$

which is in the range of today realisable switching frequencies and, the necessary gap between the natural and the switching frequency cannot be maintained. Furthermore, a movement at higher velocities of drives with such large cross-sections requires conditionally huge flow rates, which cannot be provided by a single converter at reasonable efficiencies. Thus, an arrangement of several parallel HBCs can achieve the necessary flow rate, like depicted in Fig. 7.4. Moreover, in case of several parallel converters the

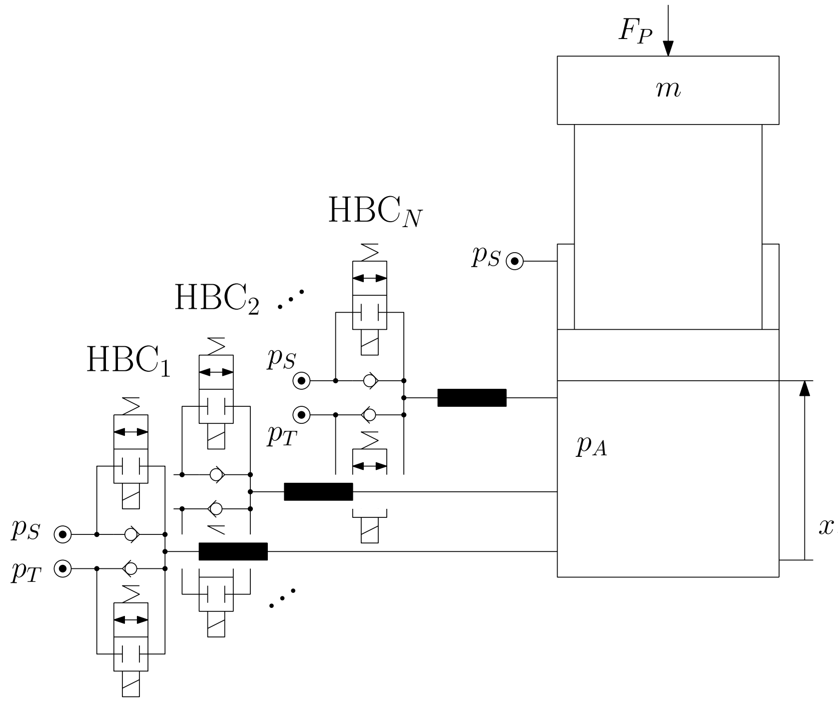

Figure 7.4.: Multiple HBC arrangement exploiting the load capacitance

pressure pulsations at the load due to the switching process can be reduced dramatically by a phase shifted control of the individual HBCs, because the effective switching frequency at the load is $f_S N$, which is again sufficiently above the natural frequency of Eq. (7.10). With a phase shifted approach also the noticed flow rate pulses are reduced, which result again in lower pressure pulsations at the load. Furthermore, the reliability of such a system is guaranteed even in a fault case of a single HBC, which is an important requirement in heavy duty industrial production processes.

7.4. Fast Switching Converters

The basic components of fast switching systems are fast switching valves, fast check valves and fast accumulators. It is a remarkable property of fast switching systems, that little different arrangement of the mentioned components leads to completely different behaviour. Thus, like in electrical engineering, a number of different converter types can be realised very easily. Two examples will be presented here.

At first the full hydraulic boost converter will be introduced, which is depicted in Fig. 7.5. This converter is basically very similar to the HBC, but with the difference that the

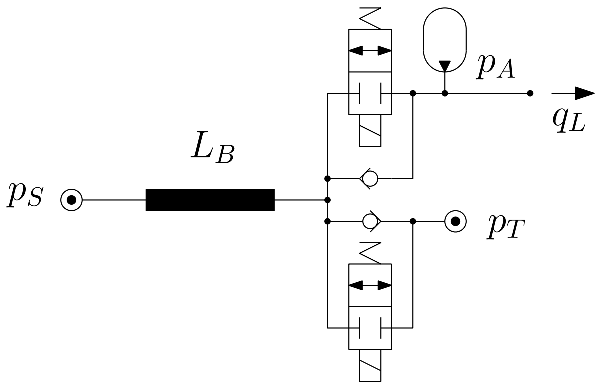

Figure 7.5.: Full Hydraulic Boost Converter

ports of p_S and p_A are exchanged. Due to the ability to boost the pressure, high forces can be achieved at the load. For instance, if only one actuator of a hydraulic system with many actuators requires high forces, the installed supply pressure can be kept small. It has to be mentioned, that the application pressure p_A cannot be lower than the supply pressure p_S. The hydraulic boost converter could be, for instance, an efficient method for the application of hydraulic micro supply units in combination with portable and handy actuators.

The second remarkable switching converter is the hydraulic boost buck converter, which is depicted in Fig. 7.6. As already mentioned in Chapter 1, this converter unifies the

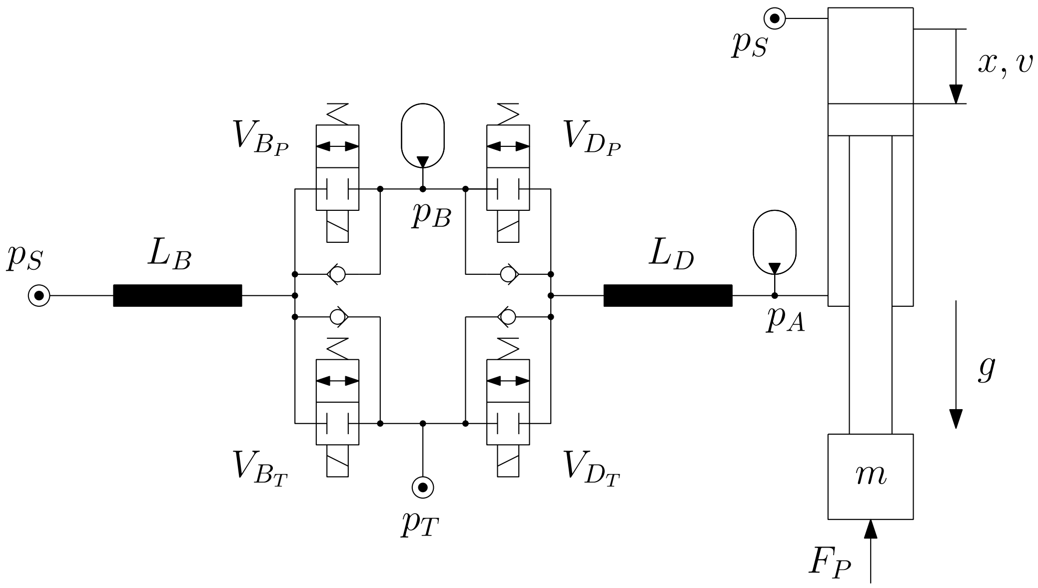

Figure 7.6.: Exemplary hydraulic boost buck converter configuration

benefits of the HBC and the hydraulic boost converter. In contrast to the boost buck converter mentioned in Subsection 1.6.3 the converter depicted in Fig. 7.6 enables a power flow in both directions. For an upward movement of the piston the diagonally situated valves V_{D_P} and V_{B_T} have to be switched simultaneously with the same duty ratio. In the down moving direction the corresponding valves V_{B_P} and V_{D_T} are pulsed. This arrangement avoids the force limitations of the HBC with a differential cylinder in plunger mode. Due to the ability to reduce and to boost the pressure at the load, the hydraulic boost buck converter can be connected to the annulus chamber. Consequently, the piston sided chamber is connected to supply pressure permanently and, thus, a larger load variability can be achieved.

A. Appendix

A.1. Theoretic Characteristics in Recuperation Mode

For completeness the theoretic characteristics of the HBC in recuperation mode are summarised in this section. The results are basically very similar to the considerations in forward flow direction according to Subsections 2.1.1 and 2.1.2.

The basic structure of the HBC in recuperation mode used for the following considerations is depicted in Fig. A.1.

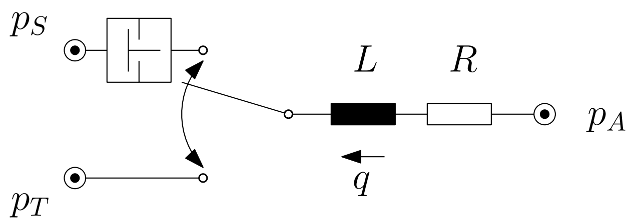

Figure A.1.: Basic principle of the HBC in recuperation mode

A.1.1. Flow Control Mode

The theoretic relations of pressure and flow rate in flow control mode are depicted in Fig. A.2 under the assumptions made in Section 2.1.

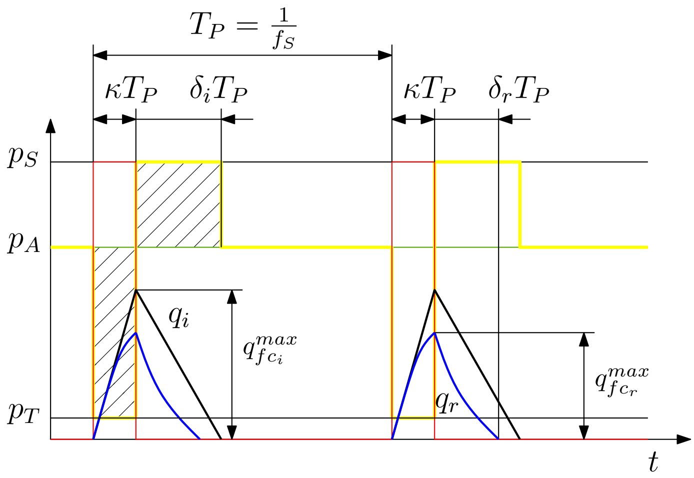

Figure A.2.: Flow control mode

The free-wheeling ratio neglecting the static resistance R reads

$$\delta_i^{rec} = \frac{p_A - p_T}{p_S - p_A}\kappa. \tag{A.1}$$

The free-wheeling ratio accounting for the static resistance R follows to

$$\delta_r^{rec} = -\frac{f_S L}{R} \ln\left(\frac{p_S - p_A}{p_S - p_T + (p_T - p_A)e^{(-\frac{R\kappa}{Lf_S})}}\right). \tag{A.2}$$

Using this result for the free-wheeling ratio δ_r^{rec}, the average flow rate in recuperation mode reads

$$\overline{q}_{fc}^{rec}(\kappa) \quad = \quad \left(\frac{f_S L(p_S - p_A)}{R^2}\right) \ln\left(\frac{p_S - p_A}{p_S - p_T + (p_T - p_A)e^{-\frac{R\kappa}{Lf_S}}}\right) + \frac{p_T - p_A}{R}\kappa. \tag{A.3}$$

The limiting process of R tending to zero delivers

$$\overline{q}_{fc}^{rec}(\kappa)\Big|_{R\to 0} = \frac{1}{2}\frac{(p_S p_T + p_A p_T - p_S p_A - p_T^2)}{(p_S - p_A)Lf_S}\kappa^2. \tag{A.4}$$

A.1.2. Pressure Control Mode

The swap ratio $\kappa^{\#}$ in recuperation mode calculates to

$$\kappa_{rec}^{\#} = \frac{1}{R}\left(\ln\left(\frac{(p_A - p_T)e^{-\frac{R}{Lf_S}} + p_S - p_A}{p_S - p_T}\right) Lf_S + R\right). \tag{A.5}$$

The limiting process of R tending towards zero delivers again

$$\kappa_{rec}^{\#}\Big|_{R\to 0} = \frac{p_S - p_A}{p_S - p_T}, \tag{A.6}$$

Also in recuperation mode the pressure control mode enforces an average pressure at the node point of the converter according to Fig. 2.3, which reads

$$p_N = p_T + (p_S - p_T)\,\kappa. \tag{A.7}$$

A.1.3. Characteristics

The theoretic characteristics for both flow directions are depicted in Fig. A.3. The corresponding numerical data of the considered HBC are listed in Tab. A.1.

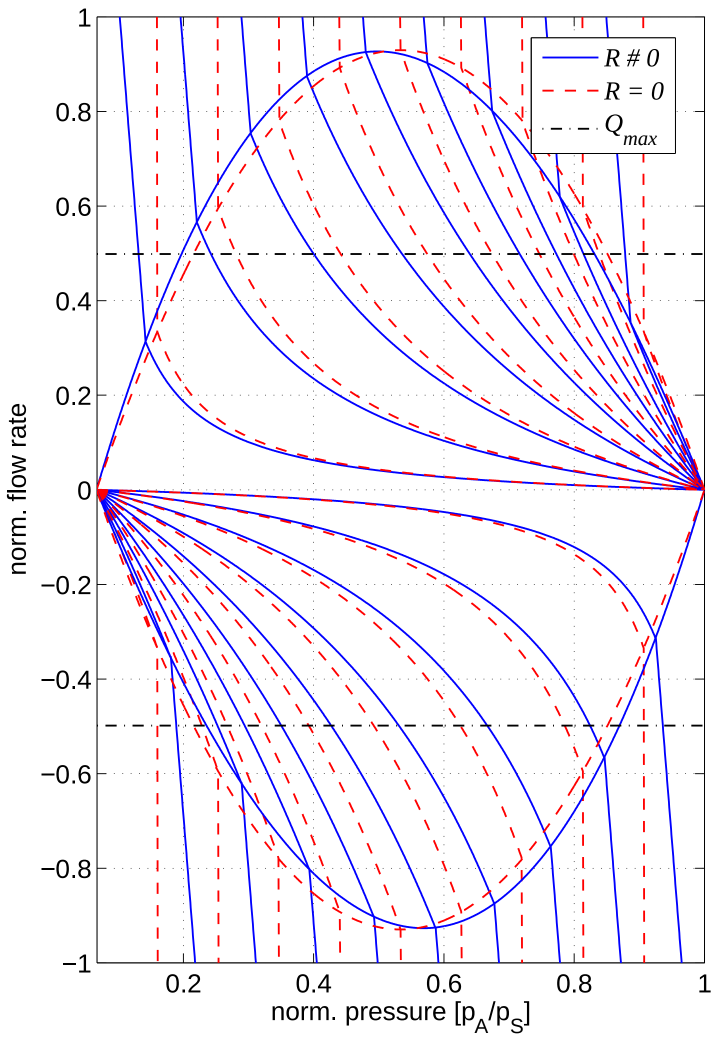

Figure A.3.: Theoretic characteristic diagram of the HBC

Parameter	Value
supply pressure	$p_S = 150\,bar$
tank pressure	$p_T = 10\,bar$
maximum load flow rate	$\lvert q_{max}\rvert = 80\frac{l}{min}$
density of the fluid	$\rho_{oil} = 860\,\frac{kg}{m^3}$
viscosity of the fluid	$\nu = 46\,\frac{mm^2}{s}$
switching frequency	$f_S = 50\,Hz$
length of inductance pipe	$l_p = 1.7\,m$
hydraulic diameter of inductance pipe	$d_p = 8\,mm$
Hagen-Poiseuille resistance	$R \approx 6.5 \cdot 10^8\,\frac{kg}{m^4 s}$
pipe inductance	$L \approx 2.8 \cdot 10^7\,\frac{kg}{m^4}$

Table A.1.: Numeric HBC data used for calculation of theoretic characteristics

It must be remarked, that with a parameter configuration according to Tab. A.1 a mean flow rate of $|\bar{q}| = 40\frac{l}{min}$ represents a transition to turbulent flow characteristics if the turbulence criterion with a Reynoldsnumber of

$$\mathrm{Re} = \frac{4|\bar{q}|}{d_p \pi \nu} \approx 2300 \tag{A.8}$$

is used. Thus, the theoretic characteristics beyond the normalised flow rate of $|\bar{q}| = 0.5$ in Fig. A.3 up to the maximum load flow rate $|q_{max}| = 80\frac{l}{min}$ represents an operating area, where additional resistance must be expected.

A.1.4. Efficiency

The mathematical expression of the theoretic efficiency in the reverse flow direction reads for flow control mode:

$$\eta_{fc}^{\leftarrow} = \frac{\frac{p_S f_S L}{R} \ln\left(\frac{p_S - p_A}{p_S - p_T - (p_A - p_T) e^{-\frac{R\kappa}{L f_S}}}\right) + \frac{p_T (p_A - p_T)\kappa}{(p_S - p_A)} + \frac{f_S L}{R}\left(1 - e^{-\frac{R\kappa}{L f_S}}\right)\frac{\left(p_S p_A - p_S p_T - p_A p_T + p_T^2\right)}{(p_S - p_A)}}{\left(\frac{f_S L}{R} \ln\left(\frac{p_S - p_A}{p_S - p_T - (p_A - p_T) e^{-\frac{R\kappa}{L f_S}}}\right) + \frac{(p_A - p_T)\kappa}{(p_S - p_A)}\right) p_A} \tag{A.9}$$

and, for pressure control mode, respectively

$$\eta_{pc}^{\leftarrow} = \frac{L\left(\frac{e^{\frac{R(1-\kappa)}{L f_S}} + e^{\frac{R\kappa}{L f_S}} - 2e^{\frac{R}{L f_S}}}{e^{\frac{R}{L f_S}} - 1} f_S \left(p_S - p_T\right)^2 + \frac{R}{L}\left((1-\kappa)\left(p_S - p_A\right) p_S - \kappa \left(p_A - p_T\right) p_T\right)\right)}{R\left((1-\kappa) p_S + \kappa p_T - p_A\right) p_A}. \tag{A.10}$$

The corresponding characteristic diagrams are depticted in Fig. 2.10.

A.2. Analytic Solution of Pressure Build Up Eq. (4.2)

For a better readability Δp will be substituted by p. Thus, the differential equation reads

$$\dot{p} = \frac{\mathrm{d}p}{\mathrm{d}t} = -\sqrt{p} \tag{A.11}$$

with the initial condition $p\,(0) = 0$. The first solution is obviously given by $p = 0$. The second solution can be calculated by a separation of the variables, like

$$-\frac{\mathrm{d}p}{\sqrt{p}} = \mathrm{d}t. \tag{A.12}$$

The integration of both sides with respect to time t leads to

$$\begin{aligned} \int_{p(0)}^{p(t)} \frac{\mathrm{d}p}{\sqrt{p}} &= -\int_0^t \mathrm{d}t \\ 2\sqrt{p}\Big|_0^p &= -t. \end{aligned}$$

Thus, the second solution of Eq. (A.11) is given by

$$p = \frac{t^2}{4}. \tag{A.13}$$

In accordance with the literature (see e.g. [12]), the right hand side of Eq. (A.11) and, thus, the function $f:\ [0,1] \to \mathbb{R}$ with $p \mapsto \sqrt{p}$ is not globally Lipschitz due to

$$\frac{|f\,(p) - f\,(0)\,|}{|p-0|} = \frac{1}{\sqrt{p}} \underset{\substack{\uparrow \\ p\to 0}}{=} \infty \nleq L. \tag{A.14}$$

A.3. A Linear Model for the Pressure Build Up in a Hydraulic Accumulator

According to Eq. (4.19) the simplified model for the pressure build up in a gas loaded accumulator reads

$$\dot{p} = \frac{p\varkappa}{V_A \left(\frac{p_{0_G}}{p}\right)^{\frac{1}{\varkappa}}} q_{in} = \frac{\varkappa}{V_A p_{0_G}^{\frac{1}{\varkappa}}} p^{\left(1+\frac{1}{\varkappa}\right)} q_{in} \tag{A.15}$$

with the pressure state p, the input flow rate q_{in}, the size of the accumulator V_A, the gas pre-pressure p_{0_G} and the polytropic exponent $\varkappa$. Applying the transformation

$$p = \Pi^{-\varkappa} \tag{A.16}$$

leads to

$$-\varkappa \Pi^{-(\varkappa+1)} \dot{\Pi} = \frac{\varkappa}{V_A p_{0_G}^{\frac{1}{\varkappa}}} \Pi^{-\varkappa\left(1+\frac{1}{\varkappa}\right)} q_{in} \tag{A.17}$$

which results in the linear integrator equation[1]

$$\dot{\Pi} = -\frac{1}{V_A p_{0_G}^{\frac{1}{\varkappa}}} q_{in} = \widetilde{C} q_{in}. \tag{A.18}$$

[1]Probably, with this linearisation the flatness based analysis according to Section 5.4 can be simplified significantly. But, this insight came up not until the consultation of the secondary auditor. Hence, this linearisation could not be duly applied in this thesis, but it will be investigated in future.

A.4. TFDI-Simulations

A.4.1. Identification

The parameter identification was carried out by an optimisation process under the application of *lsqnonlin* in *Matlab*™. This algorithm solves nonlinear least squares curve fitting problems of the form

$$\min_{\mathbf{z}} \|\mathbf{e}(\mathbf{z})\|_2^2 = \min_{\mathbf{z}} \left(e_1(\mathbf{z})^2 + e_1(\mathbf{z})^2 + \cdots + e_n(\mathbf{z})^2 \right) \tag{A.19}$$

with the residual vector $\mathbf{e}$ and the parameter vector $\mathbf{z}$. In the concrete case, the residual vector $\mathbf{e}$ consists of the difference between the measured quasi steady state characteristics according to Fig. 4.5 and the corresponding characteristics calculated with the TFDI. The vector $\mathbf{z}$ contains the parameters to be identified. The iteration process starts with appropriate initial values $\mathbf{z}_0$ and the algorithm finds a minimum of the sum of squares of the components of $\mathbf{e}$ according to Eq. (A.19). To obtain physically meaningful results upper and lower bounds of the individual parameters of $\mathbf{z}$ were defined. The identified parameters of the identification results presented in Subsection 4.3.1 are listed in Tab. A.2.

Parameter	Identified values $\mathbf{z}$	Initial values $\mathbf{z}_0$	Real values $\mathbf{z}_{\text{real}}$
pipe length	$l_p = 1.615\,m$	$l_{p0} = 1.7\,m$	$l_{p_r} = 1.7\,m$
pipe diameter	$d_p = 7.997\,mm$	$d_{p0} = 8\,mm$	$d_{p_r} = 8\,mm$
node volume	$V_Y = 0.3\,l$	$V_{Y_0} = 0.3\,l$	$V_{Y_r} = 0.25\,l$
oil viscosity	$\nu = 46.379\,cSt$	$\nu_0 = 46\,cSt$	$\nu_r = 46\,cSt$
switching valve	$Q_N = 30.9\,\frac{l}{min}@5bar$	$Q_{N_0} = 40\,\frac{l}{min}@5bar$	$Q_{N_r} = 45\,\frac{l}{min}@5bar$
check valve	$Q_N = 131.5\,\frac{l}{min}@5bar$	$Q_{N_0} = 120\,\frac{l}{min}@5bar$	$Q_{N_r} = 120\,\frac{l}{min}@5bar$
attenuator size	$V_A = 0.329\,l$	$V_{A_0} = 0.5\,l$	$V_{A_r} = 0.32\,l$
oil stiction	$\Delta_\kappa = 1.9\%$	$\Delta_{\kappa_0} = 0\%$	$\Delta_{\kappa_r} = ?\,\%$

Table A.2.: Identified Parameters

In the second column the identified parameters and the third column the initial values for the identification are listed. The deviation in the nominal flow rates of the switching valve can be explained by the fact, that due to pipe connections additional losses occur. The percentage value for the increase of the duty ratio due to oil stiction corresponds to

$$\Delta_\kappa = \frac{t_{\delta_c}}{T_P} \tag{A.20}$$

according to Fig. 2.11. Since no position measurement of the valve spool was provided, this value was actually not known, but a value was derived by identification.

Display	iter
MaxIter	500
MaxFuncEvals	5000
TolX	$1e^{-6}$
TolFun	$1e^{-6}$

Table A.3.: Configuration of the algorithm *lsqnonlin* in *Matlab*™ for parameter identification of the HBC

A.4.2. Simulation Analysis

In the following, the table data for the simulations carried out in Subsection 4.3.2 are provided. In Tab. A.4 the numeric parameters of the Time-Frequency-Domain-Iteration are listed. The used parameter set of the nonlinear solving algorithm *fsolve* in Matlab is listed in Tab. A.5.

Parameter	Value
supply pressure	$p_S = 150\,bar$
tank pressure	$p_T = 10\,bar$
node volume	$V_Y = 0.2\,l$
bulk modulus of the fluid	$E_{oil} = 14000\,bar$
density of the fluid	$\rho_{oil} = 860\,\frac{kg}{m^3}$
viscosity of the fluid	$\nu = 46\,\frac{mm^2}{s}$
nominal flow rate of switching valve	$Q_{N_{Sx}} = 45\frac{l}{min}@5bar$
nominal flow rate of check valve	$Q_{N_{Sx}} = 120\frac{l}{min}@5bar$
switching time	$t_r = t_f = 2\,ms$
valve covering	$c_V = 50\%$
switching frequency	$f_S = 50\,Hz$
length of inductance pipe	$l_p = 1.7\,m$
hydraulic diameter of inductance pipe	$d_p = 8\,mm$
volume of the accumulator	$V_A = 0.32\,l$
pre-pressure of accumulator	$p_{0_G} = 20\,bar$
polytropic exponent	$\varkappa = 1.3$

Table A.4.: HBC parameters for TFDI simulations

Display	iter
MaxIter	1500
MaxFuncEvals	15000
TolX	$1e^{-12}$
TolFun	$1e^{-12}$
Jacobian	on
DerivativeCheck	off

Table A.5.: Configuration of the algorithm *fsolve* in *Matlab*™

A.5. Control Simulations

The numerical parameters of the linear drive axis for simulation are listed in Tab. A.6, which correspond nearly to the real axis used for experiments according to Fig. 6.6.

A.5.1. Simulation Parameters

Parameter	Value
dead load	$m = 500\,kg$
diameter of the piston	$d_P = 63\,mm$
diameter of the rod	$d_R = 45\,mm$
viscous friction	$d_v = 1000\,\frac{Ns}{m}$
coulomb friction	$d_c = 100\,N$
stiction force	$F_H = 500\,N$
gravity	$g = 9.81\,\frac{m}{s^2}$
process force	$F_P = 10\,kN$
slope of process force	$\frac{\mathrm{d}}{\mathrm{d}t}F_P = 40\,\frac{kN}{s}$

Table A.6.: System parameters for control simulations

A.5.2. Implementation of the Cylinder Model

The simulation model according to Fig. 5.2b is implemented as a C-code S-function in *Matlab/Simulink*™. The dynamic equations are based on Eq. (5.1), where only viscous friction is assumed. But, in addition to Eq. (5.1) the simulation model accounts for a static friction model according to Eq. (5.4). In the following, the most important code listings are presented.

1. Parameter vector of the C-Code S-function:

```
Parameter_V = [pS ...  = Par[0],  /* supply pressure */
               pTK ... = Par[1],  /* tank pressure */
               AZ ...  = Par[2],  /* cross-section of piston */
               AK ...  = Par[3],  /* annulus cross-section area */
               MA ...  = Par[4],  /* dead mass */
               VZ0 ... = Par[5],  /* dead volume at x=0 */
               VSp ... = Par[6],  /* volume of attenuator */
               pSP ... = Par[7],  /* pre-pressure of attenuator */
               np ...  = Par[8],  /* polytropic exponent */
               rv ...  = Par[9],  /* viscous friction */
               dc ...  = Par[10], /* Coulomb' friction */
               v0 ...  = Par[11], /* Stribeck-velocity */
               FH ...  = Par[12], /* stiction force */
```

```
                    g... = Par[13], /* gravity */
                   Eo... = Par[14], /* bulk modulus of the fluid */
                   ro... = Par[15], /* density of the fluid */
                   ny... = Par[16], /* viscosity of the fluid */
                  KSV... = Par[17], /* flow coeff. switching valve*/
                  KCV... = Par[18], /* flow coeff. check valve*/
                  dpN... = Par[19], /* nominal pressure drop */
                   VK... = Par[20], /* node volume */
                   LD... = Par[21], /* transient pressure drop */
                   Ta... = Par[22] ]; /* sampling time */
```

2. Continuous state variables and definitions:

```
xC[0]; /* piston position */
xC[1]; /* piston velocity */
xC[2]; /* pressure in the cylinder */

#define dx0 dx[0] /*derivative of piston position*/
#define dx1 dx[1] /*derivative of piston velocity*/
#define dx2 dx[2] /*derivative of cylinder pressure*/
#define check_stick xD[4]
```

3. Discrete state variables:

```
xD[0]; /* velocity value of previous sampling step */
xD[1]; /* zero-crossing detection */
xD[2]; /* stiction flag */
xD[3]; /* end position of cylinder */
```

4. Continuous derivatives:

```
real_T   *xD = ssGetDiscStates(S);
#include <Include_Check_Stick_Force.c>

/* piston in end position? */
if (xD[3]==1) { xC[1]=0; xC[0]=0;};
if (xC[0]<=0 && xC[1] < 0 && xD[3]==0) {xD[3] = 1;};
if ((xD[3]==1 && check_stick > Par[12]) || xC[0] > 0) { xD[3] = 0; };

/* stick-Slip friction */
if (xD[1]==1 && (fabs(check_stick)<=Par[12])) { xD[2]=1; };
if (fabs(check_stick) > Par[12] && xD[2]==1)  { xD[2]=0; };

/* main differential equations */
```

```
if (xD[2]==1 || xD[3]==1)
    {       dx0 = 0;
            dx1 = 0;
            xC[1] = 0;   }
else
    {       #include <Include_Cyl_Acc_Derivatives_mech.c>  };

#include <Include_Cyl_Acc_Derivatives_hydr.c>
```

5. Content of the file *Include_Check_Stick_Force.c*:

```
check_stick = xC[2] * Par[2] - Par[0] * Par[3] - Par[4] * Par
[13] - u[1];
```

6. Content of the file *Include_Cyl_Acc_Derivatives_mech.c*:

```
dx0 = xC[1];
dx1 = 0.1e1 / Par[4] * (xC[2] * Par[2] - Par[0] * Par[3] - Par
[4] * Par[13] - u[1] - sgn(xC[1]) * ((Par[12] - Par[10]) * exp(-
pow(xC[1], 0.2e1) * pow(Par[11], -0.2e1)) + Par[10]) - Par[9] *
xC[1]);
```

7. Content of the file *Include_Cyl_Acc_Derivatives_hydr.c*:

```
dx2 = -Par[14] * Par[8] * xC[2] * (-Par[2] * xC[1] + u[0]) / (-
Par[8] * xC[2] * Par[6] + Par[8] * xC[2] * Par[6] * pow(Par[7] /
 xC[2], 0.1e1 / Par[8]) - Par[8] * xC[2] * Par[5] - Par[8] * xC
[2] * Par[2] * xC[0] - Par[14] * Par[6] * pow(Par[7] / xC[2],
0.1e1 / Par[8]));
```

8. The *sgn*-function:

```
double sgn(double q)
{
  if (q>0)
    return(1);
  else if (q<0)
    return (-1);
  else
    return(0);
}
```

9. Discrete Model Update:

```
real_T  *xC = ssGetContStates(S);
```

```
/* Zero-Crossing Detection */
if ((xD[0]>0 && xC[1]<0) || (xC[1]==0))
    { xD[1] = 1;}
else if ((xD[0]<0 && xC[1]>0) || (xC[1]==0))
    { xD[1] = 1;}
else
    { xD[1] = 0;};

xD[0]=xC[1]; /* save of velocity */
xD[2]=xD[2]; /* stiction flag */
xD[3]=xD[3]; /* end position x=0 */
xD[4]=xD[4]; /* check stiction force */
```

B. Bibliographical Notes

Chapter 1 The picture of the hydraulic ram by Easton & Amos in Fig. 1.2 was taken from Wikipedia. The statements concerning basic hydraulic switching control are based on the considerations of Heinz Gall and Kurt Senn according to [8]. The picture of the Wave Converter in Fig. 1.5 stems from [39] of the *Institute of Machine Design and Hydraulic Drives* (IMH) at the Johannes Kepler University. There, also the investigations of the Hydraulic Resonance Converter took place and the results are summed up in [9, 31, 32, 38]. The facts and figures concerning the Digital Hydraulics Concept were kindly provided by Matti Linjama of the Department for *Intelligent Hydraulics and Automation* (IHA) at the Technical University of Tampere in Finland [20, 21]. The basic information to the Hydraulic Buck Converter was already published by the author in [13].

Chapter 2 The theoretic investigations concerning the modes of operation were already presented by the author in [13]. The transmission line model in frequency domain is based on the considerations of D'Souza and Oldenburger according to [3] and was optimised by Zielke in [53] for numeric considerations. The assessment of the water hammer phenomenon can be found in [28], which is written in German by Hubertus Murrenhoff. The pictures of the different switching valves were kindly provided by the *Linz Center of Mechatronics* (LCM). Facts and figures of these valves are available in [29, 30, 49, 50]. The statements on the stability of accelerated fluids are based on [19, 1]. The sectional drawing of the membrane accumulator and the metal bellow accumulator were taken from the *hydac* website (`www.hydac.com`). The guide lines concerning the block design and the different pictures were developed during the diploma thesis of Michael Ehrentraut at the IMH and can be found in [4]. The concept of the vibration compensator was investigated by Josef Mikota during his doctoral studies at the IMH [27].

Chapter 3 The experiments with the prototype *HBC010* were carried out under the assistance of Markus Mairhofer in the framework of his diploma thesis. A conclusion can be found in [23]. The experiments considering the improved prototype *HBC020* were carried out by Johannes Falkner in his student's seminar [5] at the IMH. The valve block design was carried out by Thomas Richter during an internship at the IMH. The analysis of the different rail geometries was done at the IMH by Josef Schäffler during the student's project [41]. The *HBC030* was developed and investigated in the framework of the diploma thesis [4] of Michael Ehrentraut at the IMH.

Chapter 4 The *orifice square root function* was introduced by Bernhard Manhartsgruber and is implemented in the simulation toolbox *HydroLib* according to [24]. The method of the TFDI is based on the publications [2, 25].

Chapter 5 The basic considerations on flatness were introduced by Michel Fliess et al. according to e.g. [6]. Furthermore, Ralf Rothfuss provides essential contributions concerning flatness in [33, 34], which are written in German. Other helpful literature concering flatness was provided by Joachim Rudolph [37] - also written in German. Some applied mathematical definitions on differential geometry can be found, for instance, in [11] written by Alberto Isidori. Furthermore, helpful information concerning nonlinear dynamic systems were found in [12] written by H. K. Khalil. The time domain simulations were carried out in *Matlab/Simulink*™ with the application of the already mentioned *HydroLib* according to [24] developed by Bernhard Manhartsgruber and Rainer Haas. The design of the reduced observer is based on [47] written by Donald M. Wiberg. Worthy literature concering trajectory planning is given by Johannes von Löwis and Joachim Rudolph in [46, 36]. The presented filter design for online trajectory planning was carried out in accordance with [52].

Chapter 6 Some results of the advanced experiments were partially published by the author in [14].

Chapter 7 Informations concerning nano texturing are given in [42] published by Adam Steele.

C. Curriculum Vitae

Personal:	Name:	Helmut Kogler
	Date of Birth:	26. June 1977
	Place of Birth:	Linz, Austria
	Address:	Pöstlingbergstraße 110 A-4040 Linz

Educational:	2005 – 2012	Doctoral Studies at Johannes Kepler University, Linz
	1997 – 2004	Studies of Mechatronics at Johannes Kepler University, Linz
	1996 – 1997	Military Service
	1991 – 1996	Secondary Technical College for Mechanical Engineering *HTBLA II*, Linz
	1987 – 1991	Secondary School, BRG Linz Auhof
	1983 – 1987	Elementary School, Gramastetten

Professional:	Since 2012	Post-Doc Assistant, Institute of Machine Design and Hydraulic Drives, Johannes Kepler University, Linz
	Since 2011	Assistant Lecturer, Institute of Machine Design and Hydraulic Drives, Johannes Kepler University, Linz
	2008 – 2012	Research Assistant, Institute of Machine Design and Hydraulic Drives, Johannes Kepler University, Linz
	2004 – 2008	Research Engineer, Linz Center of Mechatronics GmbH

Musical:	Since 2008	Freelance Composer for Wind Orchestra
	Since 2005	Conductor of the *Musikverein Pöstlingberg*
	2008 – 2009	Course on Composition for Wind Orchestra
	2003 – 2007	Course on Conduction of Wind Orchestra
	1987 – 2003	Music School for French & Viennese Horn

	Languages:	German (mother tongue), English
	Further interests:	nature, sports

List of Figures

1.1 Resistance control . . . 1
1.2 Working principle of the hydraulic ram . . . 3
1.3 Hydraulic ram by Easton & Amos in 1851 . . . 4
1.4 Energy efficient positioning via free-wheeling valves . . . 4
1.5 The wave converter from [39] . . . 6
1.6 Electrical resonance converter . . . 7
1.7 Hydraulic resonance converter from [32] . . . 8
1.8 Digital hydraulic valve . . . 8
1.9 Different digital valve blocks from [20] . . . 9
1.10 Different quantisation levels of digital hydraulic valve systems . . . 10
1.11 Electrical buck converter . . . 11
1.12 Simple hydraulic buck converter . . . 11
1.13 Both-way hydraulic buck converter . . . 12
1.14 Hydraulic boost converter . . . 13
1.15 The hydraulic boost-buck converter . . . 14

2.1 Basic principle of the Hydraulic Buck Converter . . . 16
2.2 Flow control mode . . . 17
2.3 Pressure control mode . . . 19
2.4 HBC without check valves . . . 19
2.5 Characteristic diagram of the HBC . . . 20
2.6 Basic principle in recuperation mode . . . 21
2.7 Theoretical recuperation characteristics . . . 21
2.8 Full HBC and 3/3-valve . . . 22
2.9 Theoretic efficiency in the forward flow direction . . . 23
2.10 Theoretic recuperation efficiency . . . 24
2.11 Spool movement of a digital hydraulic valve . . . 25
2.12 Ballistic switching modes . . . 26
2.13 Different relations between intended (κ_i) and the hydraulic (κ_h) duty ratios 27
2.14 Straight pipe . . . 28
2.15 Parasitic effects in an HBC . . . 29
2.16 Parasitic effect of an inductance . . . 30
2.17 Parasitic capacity effect; numeric values for this configuration listed in Tab. A.4 . . . 32
2.18 Noise generation due to a broad band frequency excitation by switching ($f_S = 50\,Hz$; $\kappa = 20\%$) . . . 35
2.19 Comb valve . . . 38
2.20 Pilot valve . . . 39
2.21 Piloted multi poppet valve . . . 39

2.22 Fast plate check valve . . . 39
2.23 Decoupling resonator on supply side . . . 43
2.24 Membrane accumulator (source: `www.hydac.com`) . . . 44
2.25 Piston accumulator . . . 44
2.26 Natural frequency depending on working pressure and geometry of the accumulator . . . 46
2.27 Metal bellow accumulator (source: `www.hydac.com`) . . . 47
2.28 Compact block design . . . 49
2.29 Exploded view of the compact converter design . . . 50
2.30 Stack of several converters . . . 51
2.31 Helmholtz resonator . . . 52
2.32 Vibration compensator . . . 53
2.33 $\lambda/4$-side-branch resonator . . . 54

3.1 Test stand of the *HBC010* . . . 55
3.2 Calibration of the spool position measurement at the *HBC010* . . . 56
3.3 Valve currents and spool positions . . . 57
3.4 Basic results of the first experiments . . . 59
3.5 HBC employing a 3/2-switching valve for pressure control . . . 59
3.6 3D CAD drawings of the HBC with check valves . . . 60
3.7 Test rig diagram of *HBC020* . . . 61
3.8 Test rig of *HBC020* . . . 62
3.9 Characteristics of the *HBC020* . . . 63
3.10 Extending cylinder movement with *HBC020* . . . 64
3.11 Coil with one winding . . . 65
3.12 Coil with two windings . . . 65
3.13 Coil with four windings . . . 66
3.14 Coil with seven windings . . . 66
3.15 Resulting efficiencies with different coils . . . 67
3.16 Characteristic diagram of the different coil geometries . . . 68
3.17 Resulting power characteristics of the investigated coils . . . 69
3.18 Prototype *HBC021* with threaded spindle inside the valve block . . . 70
3.19 Efficiency of *HBC021* with threaded spindle inductance . . . 71
3.20 Compact coil inductance of the *HBC022* . . . 71
3.21 Efficiency of the *HBC022* with compact coil inductance . . . 72
3.22 The prototype *HBC030* . . . 73
3.23 Check valves for energy saving and recuperation of the *HBC030* . . . 73
3.24 Piston attenuator of the *HBC030* . . . 74
3.25 Efficiency measurements of the *HBC030* . . . 75
3.26 Efficiency improvement of the *HBC030* . . . 75
3.27 Recuperation power of the *HBC030* . . . 76
3.28 Efficiency in recuperation mode of the *HBC030* . . . 76
3.29 Comparison of theoretic and measured characteristics . . . 77

4.1 Considered system . . . 78
4.2 Comparison of the *square-root* with the *orifice-root*-function . . . 81
4.3 Comparison of the different accumulator models (*model 1*→Eq. (4.17), *model 2*→Eq. (4.18), *model 3*→Eq. (4.19), *model 4*→Eq. (2.52)) . . . 84
4.4 Spool movement and opening of an active switching valve . . . 88

4.5 Comparison of measurement and simulation 93
4.6 Simulation of the steady state behaviour of the HBC 94
4.7 Efficiency characteristics 95
4.8 Efficiency characteristics depending on output power ($V_Y = 0.15\,l$) 96
4.9 Efficiency characteristics depending on output power ($V_Y = 0.015\,l$) 96
4.10 Different power characteristics 97
4.11 Transient response of p_Y with $V_Y = 0.15\,l$ and $q_L = 20\frac{l}{min}$ 97
4.12 Transient response of p_Y with $V_Y = 0.015\,l$ and $q_L = 20\frac{l}{min}$ 98
4.13 Pressure signals at different locations 98
4.14 Distributed pressure simulations 99
4.15 $\lambda/2$-resonance in the main inductance 99
4.16 Full converter characteristics $p_A = f(\kappa, q_L)$ 100
4.17 Full converter characteristics $\kappa = f(q_L, p_A)$ 101

5.1 HBC-controlled linear drive 102
5.2 System segmentation 103
5.3 Static friction model 105
5.4 Simulation model of the HBC in *Simulink*™ 106
5.5 Hydraulic proportional drive 107
5.6 Control scheme with P-controller 108
5.7 Simulation of sinusoidal trajectory with P-controller 108
5.8 Simulation of applied process force with P-controller 109
5.9 Bode plots of the compensation controller design 111
5.10 Control scheme of the compensation controller 111
5.11 Simulation results with compensation controller 112
5.12 Inversion of system (5.1) with the flatness based feedforward control (5.22) 115
5.13 Flatness based control of system (5.1) 117
5.14 Block diagram of the intended control exploiting a nonlinear observer . . . 118
5.15 Flatness based control of a linear hydraulic drive applying a complete observer 124
5.16 Simulated trajectory tracking of the FBC 125
5.17 Energy consumption of the FBC at trajectory tracking 126
5.18 Simulation results of the FBC with an applied process force 126
5.19 Flatness based control of a linear hydraulic drive exploiting a load observer 131
5.20 Trajectory tracking and energy consumption of the FBC_d 132
5.21 Trajectory tracking, energy consumption and observed process force of the FBC_d 133
5.22 Control scheme of the FBC in combination with a reduced observer 137
5.23 Trajectory tracking of the FBC_R 138
5.24 Sinusoidal trajectory tracking of the FBC_R 139
5.25 Gevrey function 140
5.26 Bode plots of a filter according to Eq. (5.118) 143

6.1 Hydraulic circuitry for energy comparison 145
6.2 Test stand for energy comparison 146
6.3 Measurements at the load 147
6.4 Energy comparison of the different configurations 148
6.5 Hydraulic circuit for control measurements 149
6.6 Linear axis controlled by an HBC 150
6.7 Measured converter characteristics 151

6.8 Transformed converter characteristics 152
6.9 Ramp $v_d = \pm 150\frac{mm}{s}$ 153
6.10 Ramp $v_d = \pm 100\frac{mm}{s}$ 153
6.11 Sinusoidal signal $f_{exc} = 0.25\,Hz$ (left) and $f_{exc} = 1\,Hz$ (right) 154
6.12 Sinusoidal movement at $f_{exc} = 5\,Hz$ 155

7.1 Equivalent force configurations 156
7.2 Efficient plunger configuration 158
7.3 CAD drawing of the *HBC041* 159
7.4 Multiple HBC arrangement exploiting the load capacitance 161
7.5 Full Hydraulic Boost Converter 162
7.6 Exemplary hydraulic boost buck converter configuration 162

A.1 Basic principle of the HBC in recuperation mode 164
A.2 Flow control mode 165
A.3 Theoretic characteristic diagram of the HBC 166

List of Tables

1.1 Data of digital valve blocks from Fig. 1.9 9

2.1 Load specifications 36
2.2 Switching valves developed at the Linz Center of Mechatronics 38
2.3 Numeric parameters of piston accumulator 46

3.1 System parameter and conditions of measurements with the *HBC010* . . . 58
3.2 Relevant parameters of the experiments on the *HBC020* 62
3.3 Colour assignments of different coils 67
3.4 Functional specifications of the *HBC030* 72

A.1 Numeric HBC data used for calculation of theoretic characteristics 167
A.2 Identified Parameters 170
A.3 Configuration of the algorithm *lsqnonlin* in *Matlab*™ for parameter identification of the HBC 171
A.4 HBC parameters for TFDI simulations 171
A.5 Configuration of the algorithm *fsolve* in *Matlab*™ 171
A.6 System parameters for control simulations 172

Bibliography

[1] I. Annus, T. Koppel, and A. Vardy. Transition to Turbulence in Accelerating Pipe Flow. *Proceedings of the HYDRALAB III Joint User Meeting, Hannover*, 2010.

[2] T. M. Cameron and J. H. Griffin. An alternating frequency/time domain method for calculating the steady-state response of nonlinear dynamic systems. *Journal of Applied Mechanics*, 56:149–154, 1989.

[3] A. F. D'Souza and R. Oldenburger. Dynamic response of fluid lines. *Trans. ASME, J. Basic Engineering*, 86:589–598, 1964.

[4] M. Ehrentraut. Auslegung und Realisierung eines kompakten energieeffizienten hydraulischen Antriebes für kleine Leistungen. Master's thesis, Institute of Machine Design and Hydraulic Drives, Johannes Kepler University, Linz, 2010.

[5] J. Falkner. Aufbau und Wirkungsgradvermessung eines hydraulischen Buck Konverters. Seminar Work at the Institute of Machine Design and Hydraulic Drives, Johannes Kepler University, Linz, 2008.

[6] M. Fliess, J. Lévine, P. Martin, and P. Rouchon. Flatness and Defect of Nonlinear Systems: Introductory Theory and Examples. Technical report, Centre Automatique et Systèmes, 1994.

[7] M. Fliess and J. Rudolph. Local "tracking observers" for flat systems. In *Proceedings of the Symposium on Control, Optimization and Supervision, CESA '96 IMACS Multiconference, Lille, France*, pages 213–217, 1996.

[8] H. Gall and K. Senn. Freilaufventile - Ansteuerungskonzept zur Energieeinsparung bei hydraulischen Linearantrieben. *Ölhydraulik und Pneumatik*, 38:Nr. 1–2, 1994.

[9] M. Garstenauer. Modellbildung und experimentelle Untersuchung eines Resonanzkonverters in der Ölhydraulik. Master's thesis, Institute of Machine Design and Hydraulic Drives, Johannes Kepler University, Linz, 1996.

[10] E. Guglielmino, C. Semini, Y. Yang, D. G. Caldwell, R. Scheidl, and H. Kogler. Energy Efficient Fluid Power in Autonomous Legged Robots. In *Proceedings of the 2009 ASME Dynamic Systems and Control Conference, DSCC 2009, Renaissance Hollywood Hotel, October 12-14, Hollywood, California*, 2009.

[11] A. Isidori. *Nonlinear Control Systems.* $3^{rd} Edition, Springer, London, UK$, 1995.

[12] H. K. Khalil. *Nonlinear Systems.* Prentice Hall, 1996.

[13] H. Kogler and R. Scheidl. Two Basic Concepts of Hydraulic Switching Converters. In *Proceedings of the First Workshop on Digital Fluid Power, DFP08, Tampere, Finland*, 2008.

[14] H. Kogler, R. Scheidl, M. Ehrentraut, E. Guglielmino, C. Semini, and D. G. Caldwell. A Compact Hydraulic Switching Converter for Robotics Applications. In *Proceedings of the Bath/ASME Symposium on Fluid Power and Motion Control - FPMC2010, Sept. 11-17, Bath, UK.*, 2010.

[15] H. Kogler, B. Winkler, and R. Scheidl. Flatness based control of a fast switching hydraulic drive. In *Proceedings of the* 2^{nd} *International Conference on Computational Modelling in Fluid Power, Aalborg, Denmark*, 2006.

[16] A. Kugi. *Nichtlineare Regelung elektrischer Systeme.* PhD thesis, Johannes Kepler University, Linz, Austria, 1995.

[17] A. Kugi. *Nonlinear Control based on Physical Models.* Springer, 2001.

[18] A. Kugi. Regelungssysteme. Automation and Control Institute, Technical University Vienna, 2010. Lecture notes - in german.

[19] J. Kurokawa and M. Morikawa. Accelerated and Decelerated Flows in a Circular Pipe. Technical report, Japanese Society of Mechanical Engineering, 1986.

[20] M. Linjama. Digital Hydraulics Research at IHA. In *Proceedings of The* 1^{st} *Workshop on Digital Fluid Power,* 3^{rd} *October, Tampere, Finland*, 2008.

[21] M. Linjama and M. Vilenius. Digital Hydraulics - Towards Perfect Valve Technology. In *Proceedings of The* 10^{th} *Scandinavian Interational Conference on Fluid Power, SICFP'07, May 21-23, Tampere, Finland*, 2007.

[22] J. Lévine. *Analysis and Control of Nonlinear Systems: A Flatness-based Approach.* Springer, Berlin, 2009.

[23] M. Mairhofer. Theoretische und experimentelle Optimierung eines schnellschaltenden hydraulischen Antriebes. Master's thesis, Institute of Machine Design and Hydraulic Drives, Johannes Kepler University, Linz, 2007.

[24] B. Manhartsgruber, N. Krimbacher, and R. Haas. *HydroLib - A Simulink Toolbox for Hydraulic Simulation.* Institute of Machine Design and Hydraulic Drives, Johannes Kepler University, Altenberger Straße 69, 4040 Linz, Austria.

[25] B. Manhartsgruber, G. Mikota, and R. Scheidl. Modelling of a switching Control Hydraulic System. *Mathematical Computer Modelling of Dynamical Systems*, 11(3):329–344, 2005.

[26] H. E. Merritt. *Hydraulic Control Systems.* John Wiley & sons, 1967.

[27] J. Mikota. *Contributions to the developments of compact and tuneable vibration compensators for hydraulic systems.* PhD thesis, Johannes Kepler University, Linz, 2002.

[28] H. Murrenhoff. *Grundlagen der Fluidtechnik.* Verlag Mainz, Wissenschaftsverlag, Aachen, 1998.

[29] A. Plöckinger and R. Scheidl. Development and laboratory tests of a cheap, robust and fast check valve for industrial applications. In *Proceedings of the* 9^{th} *Scandinavian International Conference on Fluid Power, Linköping, Sweden*, 2005.

[30] A. Plöckinger, R. Scheidl, and B. Winkler. Development and Prototyping of a Compact, Fast 3/2 Way Switching Valve with Integrated Onboard Electronics. In *Proceedings of The* 11^{th} *Scandinavian International Conference on Fluid Power, SICFP'09, June 2-4, Linköping, Sweden*, 2009.

[31] G. Riha. *Beiträge zur Entwicklung eines energiesparenden hydraulischen Schaltkonverters.* PhD thesis, Institute of Machine Design and Hydraulic Drives, Johannes Kepler University, Linz, 1998.

[32] G. Riha and R. Scheidl. Energy efficient switching control by a hydraulic Resonance Converter. In *Proceedings of the Workshop on Power Transmission and Motion Control (PTMC '99), Sept 8-11, Bath*, September 1999.

[33] R. Rothfuß. Anwendung der flachheitsbasierten Analyse und Regelung nichtlinearer Mehrgrößensysteme. Technical report, Fortschr.-Ber. VDI Reihe 8 Nr. 664, Düsseldorf: VDI Verlag, Germany, 1997.

[34] R. Rothfuß, J. Rudolph, and M. Zeitz. Flachheit: Ein neuer Zugang zur Steuerung und Regelung nichtlinearer Systeme. *Automatisierungstechnik*, 45:517–525, 1997.

[35] P. Rouchon. Flatness based control of oscillators. Plenary Lecture presented at the 75^{th} Annual GAMM Conference, Dresden/Germany, March 2004.

[36] J. Rudolph. Planning Trajectories for a Class of Linear Partial Differential Equations: An Introduction. *Sciences et Technologies de l'Automatique (e-sta), J. électr. (http://www.e-sta.see.asso.fr)*, 1, 2004.

[37] J. Rudolph. Rekursiver Entwurf stabiler Regelkreise durch sukzessive Berücksichtigung von Integratoren und quasi-statische Rückführungen. *Automatisierungstechnik*, 53:389–399, 2005.

[38] R. Scheidl, M. Garstenauer, and S. Grammer. The Resonance Converter - A Novel Method for Hydraulic Fluid Power Control. In *Proceedings of Mechatronics '96, Guimaraes, Portugal, ISBN: 972-8063-0*, 1996.

[39] R. Scheidl and B. Manhartsgruber. State of the Art in Hydraulic Switching Control - Components, Systems, Applications. In *Proceedings of The* 9^{th} *Scandinavian International Conference on Fluid Power, SICFP '05, Linköping, Sweden, June 1-3*, 2005.

[40] R. Scheidl, D. Schindler, G. Riha, and W. Leitner. Basics for the Energy-Efficient Control of Hydraulic Drives by Switching Techniques. In *Proceedings of the* 3^{rd} *Conference on Mechatronics and Robots, ISBN: 3-519-02625-2, in J. Lückel*, 1995.

[41] J. Schäffler. Untersuchung verschiedener Geometrien als Induktivität bei einem Hydraulischen Buck Konverter. Seminar Work at the Institute of Machine Design and Hydraulic Drives, Johannes Kepler University, Linz, 2011.

[42] A. Steele, I. Bayer, and E. Loth. Inherently Superoleophobic Nanocomposite Coatings by Spray Atomization. *Aerospace Engineering Department, The University of Illinois at Urbana-Champaign*, 2008.

[43] K. Suzuki, T. Taketomi, and T. Sato. Improving Zielke's method of simulating frequency-dependent friction in laminar liquid pipe flow. *Transactions of the ASME, Journal of Fluid Engineering*, 1991.

[44] H. Theissen. *Die Berücksichtigung instationärer Rohrströmung bei der Simulation hydraulischer Anlagen.* PhD thesis, Rheinisch-Westfälische Technische Hochschule Aachen, 1983.

[45] U. Tietze and C. Schenk. *Halbleiter-Schaltungstechnik.* Springerverlag, 9^{th} Edition, 1990.

[46] J. von Löwis and J. Rudolph. Real-time trajectory generation for flat systems with constraints. In A. Zinober and D. Owens, editors, *Nonlinear and Adaptive Control*, pages 385–394. Springer Verlag Berlin Heidelberg, 2003.

[47] D. M. Wiberg. *Schaum's Outline of Theory and Problems of State Space and Linear Systems*. McGRAW-HILL Book Company, 1971.

[48] B. Winkler. Development of a fast low-cost switching valve for big flow rates. In *Proceedings of the* 3^{rd} *FPNI PhD Symposium on Fluid Power, Terassa, Spain*, 2004.

[49] B. Winkler, A. Plöckinger, and R. Scheidl. A novel piloted fast multi poppet valve. In *Proc. of The Second Workshop on Digital Fluid Power, ISBN 978-3-200-01713-9, pp. 116-128, DFP09, Linz, Austria*, 2009.

[50] B. Winkler and R. Scheidl. Optimization of a Fast Switching Valve for Big Flow Rates. In *Proceedings of the Bath Workshop on Power Transmission and Motion Control, PTMC 2006, Bath, England*, 2006.

[51] B. Winkler and R. Scheidl. Develpment of a Fast Seat Type Switching Valve for Big Flow Rates. In *Proceedings of the* 10^{th} *Scandinavian International Conference on Fluid Power, Tampere, Finland*, 2007.

[52] A. Wolfram and M. Vogt. Zeitdiskrete Filteralgorithmen zur Erzeugung zeitlicher Ableitungen. *at - Automatisierungstechnik*, 50:346 – 353, 2002.

[53] W. Zielke. Frequency-dependent friction in transient pipes. *ASME Journal of Basic Engineering*, 90(1):109–115, 1968.

Nomenclature

Abbreviations

CV	check valve
DFT	discrete Fourier transformation
FBC	flatness based control
FFT	fast Fourier transform
HBC	hydraulic buck converter
HBC	hydraulic buck converter
HPD	hydraulic proportional drive
HPD	hydraulic proportional drive
IFFT	inverse fast Fourier transform
LD	linear drive
max	maximum
MOC	method of characteristics
OP	operating point
PA	piston accumulator
red	reduced
RO	reduced observer
S	supply
SV	switching valve
T	tank
TFDI	time frequency domain iteration
TM	Trade Mark

Mathematical symbols

$\mathbf{A}$	time invariant matrix
$\bar{\mathbf{A}}_{ij}$	re-arranged sub matrix
$\lvert\cdot\rvert$	absolute value
$\mathbf{A}_C$	continuous dynamics matrix
$\mathbf{A}_D$	discrete dynamics matrix
α_i	i^{th} observer parameter
$\mathbf{b}$	input vector
$\bar{\mathbf{b}}_i$	re-arranged sub input vector
β_i	i^{th} controller parameter
$\mathbf{b}_C$	continuous input vector
$\mathbf{b}_D$	discrete input vector
$\mathbf{C}_C$	continuous output matrix
$\mathbf{C}_D$	discrete ouput matrix
$\boldsymbol{\chi}$	auxiliary vector
$\mathbf{c}^\mathsf{T}$	output vector
$\Delta\boldsymbol{\eta}$	deviation of measured quantities according to linearisation

$\Delta\boldsymbol{\mu}$	deviation of measurements to desired trajectory
Δu	deviation between actual and desired set value
$\Delta\mathbf{x}$	deviation between actual and desired state
$\widehat{\Delta\mathbf{x}}$	deviation between estimated and desired state
$\det\{\boldsymbol{.}\}$	determinante
$\mathrm{diag}\{\boldsymbol{.}\}$	diagonal matrix
$M_{\mathbf{A}(t)}\mathbf{t}_1^\intercal$	differential operator on the matrix $\mathbf{A}(t)$ and the row vector $\mathbf{t}_1^\intercal$
$N_{\mathbf{A}(t)}\mathbf{b}$	differential operator on the matrix $\mathbf{A}(t)$ and the column vector $\mathbf{b}$
$\mathbf{d}_C$	continuous direct feedthrough
$\mathbf{d}_D$	discrete direct feedthrough
e	error
$\mathbf{e}$	error vector
$\hat{\mathbf{e}}$	vector of estimation error
$\mathcal{F}\{\boldsymbol{.}\}$	Fourier transformation
$\mathcal{F}^{-1}\{\boldsymbol{.}\}$	inverse Fourier transformation
$\mathrm{fft}\{\boldsymbol{.}\}$	fast Fourier transform
$G(s)$	transfer function
$\boldsymbol{\Gamma}$	matrix of all vectors $\boldsymbol{\gamma}_i,\ i = 0, ..., r$
γ_i	i^{th} controller parameter
$\boldsymbol{\gamma}_i$	i^{th} integral vector
η	measured quantity
$\boldsymbol{\eta}$	vector of measured quantities
$\Im\{z\}$	imaginary part of the complex number z
$\mathbf{I}$	identity matrix
$\mathrm{ifft}\{\boldsymbol{.}\}$	inverse fast Fourier transform
$i,\ j,\ k$	counter variables
j	imaginary unit
$\mathbf{K}$	parameter matrix of reduced observer
k_{ij}	entry in i^{th} row and j^{th} column in parameter matrix $\mathbf{K}$ of reduced observer
λ	eigenvalue
$\mathbf{L}$	observer design matrix
μ_i	i^{th} observability index
$\sqrt[\vee]{\boldsymbol{.}}$	orifice root function
$\mathbf{P}$	permutation matrix
$\boldsymbol{\psi}_1$	state transformation
ψ_2	input transformation
$\widetilde{\psi}_2$	state feedback
$\mathbf{Q}$	observability matrix
s	laplace variable
$\mathrm{sgI}(\boldsymbol{.})$	directed identity
ς	auxiliary variable
$\mathrm{sign}(\boldsymbol{.})$	sign function
τ_i	i^{th} filter parameter
$\boldsymbol{\Theta}$	state transformation matrix into canonical form
$\boldsymbol{\theta}$	auxiliary matrix
ϑ	auxiliary variable

$\mathbf{u}_k$	discrete input vector at k^{th} sampling step
$\mathbf{V}$	Van der Monde matrix
$\mathbf{v}$	auxiliary state vector of reduced observer
$\mathbf{w}$	estimated state variable of reduced observer
$\mathbf{x}$	state vector
$\dot{x} = \frac{\mathrm{d}x}{\mathrm{d}t}$	derivative of x with respect to time
$\hat{\mathbf{x}}$	observer state vector
$\mathbf{x}_k$	discrete state vector at k^{th} sampling step
Υ	auxiliary variable
y	system output
y_d	desired output
$\mathbf{y}$	output vector
$\mathbf{y}_d$	vector of desired trajectories
$\boldsymbol{\zeta}$	state vector in canonical form

Indicators

A_L	accumulator at the load
A_O	pressure attenuator at output of the *HBC030*
A_T	tank reservoir of the *HBC030*
D_S	supply sided decoupling accumulator of the *HBC030*
D_T	tank sided decoupling accumulator of the *HBC030*
R_S	supply sided adjustable resistance
R_T	tank sided adjustable resistance

Greek symbols

α_O	contraction coefficient of an orifice	[1]
δ	free wheeling ratio	[1]
δ_i	ideal free wheeling ratio	[1]
δ_r	free-wheeling ratio accounting for a static resistance	[1]
Δp	pressure drop	$[Pa]$
Δp_0	initial pressure drop	$[Pa]$
Δp_{max}	maximum pressure difference	$[Pa]$
Δp_p	parasitic pressure drop	$[Pa]$
ΔV	volume difference	$[m^3]$
η	efficiency	[%]
$\eta_{HBC}^{\leftarrow}$	efficiency of the HBC in reverse flow direction	[%]
$\eta_{HBC}^{\rightarrow}$	efficiency of the HBC in forward flow direction	[%]
$\eta_{fc}^{\rightarrow}$	efficiency of the HBC in forward flow control mode	[%]
$\eta_{pc}^{\rightarrow}$	efficiency of the HBC in forward pressure control mode	[%]
$\eta_{HPD}^{\leftarrow}$	efficiency of the HPD in reverse flow direction	[%]
$\eta_{HPD}^{\rightarrow}$	efficiency of the HPD in forward flow direction	[%]
η_{prop}	efficiency of a proportional controlled configuration	[%]
η_{PWM}	efficiency of a PWM controlled configuration	[%]
Γ	transition pressure drop	$[Pa]$
$\gamma(s)$	wave propagation coefficient	$[\frac{1}{m}]$
κ	duty ratio	[1]
$\varkappa$	polytropic exponent	[1]
κ_h	hydraulic duty ratio	[1]

κ_i	ideal duty ratio	$[1]$
κ_S	duty ratio of supply sided valve	$[1]$
κ_T	duty ratio of tank sided valve	$[1]$
$\kappa^{\#}$	transition ratio	$[1]$
λ	wave length	$[m]$
ν	kinematic viscosity	$[\frac{m^2}{s}]$
ω_A	angular load frequency	$[\frac{rad}{s}]$
ω_H	natural angular frequency of a Helmholtz resonator	$[\frac{rad}{s}]$
C_A	capacity of an accumulator	$[\frac{m^3}{Pa}]$
ρ	density	$[\frac{kg}{m^3}]$
ρ_{oil}	density of oil	$[\frac{kg}{m^3}]$
ρ_P	density of piston material	$[\frac{kg}{m^3}]$
σ	number of derivatives with respect to time	$[1]$
τ	argument of convolution integral with respect to time	$[s]$
ξ	spool stroke	$[m]$
ξ_s	actual spool position	$[m]$

Roman symbols

A	area	$[m^2]$
A_1	piston sided cross-section of a differential cylinder	$[m^2]$
A_2	annulus cross-section of a differential cylinder	$[m^2]$
A_c	cross-section of the inlet of a vibration compensator	$[m^2]$
A_P	cross-section of piston	$[m^2]$
c_0	speed of sound	$[\frac{m}{s}]$
C_c	hydraulic capacity of a vibration compensator	$[\frac{m^3}{Pa}]$
C_D	decoupling capacity	$[\frac{m^3}{Pa}]$
C_H	hydraulic capacity of a Helmholtz resonator	$[\frac{m^3}{Pa}]$
C_Y	node capacity	$[\frac{m^3}{Pa}]$
d_c	coulomb friction coefficient	$[N]$
d_H	pipe diameter of a Helmholtz resonator	$[m]$
d_P	piston diameter	$[m]$
d_p	inner pipe diameter	$[m]$
D_s	spool diameter	$[m]$
d_S	inner diameter of supply line	$[m]$
d_v	viscous friction	$[\frac{Ns}{m}]$
E_{oil}	bulk modulus of oil	$[Pa]$
E'	respective bulk modulus	$[Pa]$
f_A	frequency at the load	$[s^{-1}]$
f_{axis}	natural frequency of linear axis	$[s^{-1}]$
f_c	cut off frequency	$[s^{-1}]$
F_F	friction force	$[N]$
$f_{\lambda/4}$	first pipe resonance frequency	$[s^{-1}]$
F_P	process force	$[N]$
f_S	switching frequency	$[s^{-1}]$
J_0	Bessel function of zero order and first kind	$[1]$
J_2	Bessel function of second order and first kind	$[1]$

K_V	valve flow constant	$[\sqrt{\frac{m^7}{kg}}]$
L	hydraulic inductance	$[\frac{kg}{m^4}]$
l_A	length of accumulator	$[m]$
L_H	inductance of a Helmholtz resonator	$[\frac{kg}{m^4}]$
l_H	pipe length of a Helmholtz resonator	$[m]$
L_p	parasitic inductance	$[\frac{kg}{m^4}]$
l_P	length of piston	$[m]$
l_p	pipe length	$[m]$
L_S	inductance of long supply line	$[\frac{kg}{m^4}]$
l_S	length of supply line	$[m]$
L_T	inductance of long tank line	$[\frac{kg}{m^4}]$
m	dead mass	$[kg]$
m_P	mass of piston	$[kg]$
N	number of samples	$[1]$
ω	angular velocity	$[\frac{rad}{s}]$
o_V	valve overlap	$[\%]$
p	pressure	$[Pa]$
p_0	ambient pressure	$[Pa]$
p_{0_G}	gas pre-pressure	$[Pa]$
$\hat{p}_0, \hat{p}_1$	pressure at different pipe ends in frequency domain	$[Pa]$
p_A	application pressure	$[Pa]$
$\bar{p}_A$	average application pressure	$[Pa]$
$\hat{P}_{C_Y}$	maximum node power loss	$[W]$
$\bar{P}_{C_Y}$	average node power loss	$[W]$
p_{L_d}	desired load pressure	$[Pa]$
p_N	nominal pressure drop	$[Pa]$
p_{OP}	pressure at operating point	$[Pa]$
p_S	supply pressure	$[Pa]$
p_T	tank pressure	$[Pa]$
p_Y	converter node pressure	$[Pa]$
q	flow rate	$[\frac{m^3}{s}]$
q_0	initial flow rate	$[\frac{m^3}{s}]$
$\hat{Q}_0, \hat{Q}_1$	flow rate at different pipe ends in frequency domain	$[\frac{m^3}{s}]$
q_A	application flow rate	$[\frac{m^3}{s}]$
q_S	supply flow rate	$[\frac{m^3}{s}]$
$\hat{q}_A$	applicaton flow rate in frequency domain	$[\frac{m^3}{s}]$
q_{CS}	flow rate through supply sided check valve	$[\frac{m^3}{s}]$
q_{CT}	flow rate through tank sided check valve	$[\frac{m^3}{s}]$
q_{CV}	flow through check valve	$[\frac{m^3}{s}]$
$\bar{q}_{fc}$	average flow rate in flow control mode	$[\frac{m^3}{s}]$
q_{in}	input flow rate	$[\frac{m^3}{s}]$
$q_{in_{OP}}$	input flow rate at operating point	$[\frac{m^3}{s}]$
q_L	load flow rate	$[\frac{m^3}{s}]$
Q_{L_d}	desired load flow rate	$[\frac{m^3}{s}]$

$\bar{Q}_{max}$	maximum flow rate	$[\frac{m^3}{s}]$
Q_N	nominal flow rate	$[\frac{m^3}{s}]$
q_T	tank flow rate	$[\frac{m^3}{s}]$
q_{VS}	flow rate through supply sided switching valve	$[\frac{m^3}{s}]$
q_{VT}	flow rate through tank sided switching valve	$[\frac{m^3}{s}]$
q_Y	flow into node volume	$[\frac{m^3}{s}]$
$\hat{q}_Y$	flow rate from node volume in frequency domain	$[\frac{m^3}{s}]$
R	Hagen Poiseuille resistance	$[\frac{kg}{m^4 s}]$
r	polynomial order	$[1]$
Re	Reynold's number	$[1]$
r_H	stiction coefficient	$[N]$
R_h	Hagen Poiseuille resistance of the main indunctance	$[\frac{kg}{m^4 s}]$
R_p	Hagen Poiseuille resistance of a parasitic inductance	$[\frac{kg}{m^4 s}]$
r_p	inner pipe radius	$[m]$
R^*	nondimensional friction radius	$[1]$
T	temperature	$[^\circ K]$
t	time	$[s]$
t_{δ_c}	closing delay time	$[s]$
t_{dec}	deceleration time	$[s]$
t_{δ_I}	delay time of current	$[s]$
t_{δ_o}	delay time due to hydraulic overlap	$[s]$
t_{end}	end time of trajectory	$[s]$
t_f	fall time	$[s]$
t_{f_h}	hydraulic fall time	$[s]$
t_{off}	time offset	$[s]$
T_P	duration of period	$[s]$
t_r	rise time	$[s]$
t_{r_m}	mechanical rise time	$[s]$
T_S	sampling time	$[s]$
t_{SW}	switching time	$[s]$
V	volume	$[m^3]$
v	velocity	$[\frac{m}{s}]$
V_0	dead volume	$[m^3]$
v_0	reference velocity of Stribeck effect	$[\frac{m}{s}]$
V_{0_G}	gas volume at p_{0_G}	$[m^3]$
V_A	volume of attenuator	$[m^3]$
V_c	cavity of a vibration compensator	$[m^3]$
V_D	volume of decoupling accumulator	$[m^3]$
V_H	cavity of a Helmholtz resonator	$[m^3]$
V_{oil}	amount of oil	$[m^3]$
v_{OP}	velocity at operating point	$[\frac{m}{s}]$
v_p	flow velocity inside a pipe	$[\frac{m}{s}]$
V_S	volume of supply accumulator	$[m^3]$
V_T	volume of tank accumulator	$[m^3]$
V_Y	node volume	$[m^3]$

x	position	$[m]$
x_d	desired position	$[m]$
x_{OP}	position at operating point	$[m]$
Z_0	pipe impedance	$[\frac{kg}{m^4 s}]$
$Z(s)$	frequency dependent impedance	$[\frac{kg}{m^4 s}]$

Superscripts

$\leftarrow$	back flow direction
$\rightarrow$	forward flow direction
$\star$	canonical form
$\top$	transposed
TM	Trade Mark

Subscripts

CS	supply sided check valve
CT	tank sided check valve
fc	flow control mode
pc	pressure control mode
VS	supply sided switching valve
VT	tank sided switching valve

Index

accumulator, 41
    bladder, 61
    membrane, 44, 61
    piston, 44, 74
advanced modelling, 78
air vessel, 3

ballistic mode, 26
block design, 49
boost current, 56
both-way, 12

canonical form, 122
cavitation, 5, 12, 29, 30, 37
compressibility, 27
contraction coefficient, 82
control
    experiments, 149
    position, 152
control unit, 134
controller
    compensation, 109
    design, 116
    flatness based, 113, 152
    P-, 107, 146, 152
converter
    boost, 162
    boost buck, 162
    buck, 11
    buck boost, 14
    Ćuk, 14
    split-pi, 14
    step down, 11, 13
    step up, 13
critical length, 32
cross flow, 56
cross-section, 160
    circular, 27
    ratio, 105, 157
cut-off frequency, 143
cutting, 40

cylinder
    differential, 35, 63, 102
    plunger mode, 12, 102, 149, 156

design
    compact, 70
    controller, 102
    procedure, 48
diaphragm, 44
differentiator, 139, 143
diode, 2
directed identity, 81, 87
Discrete-Fourier-Transformation, 88
displacement drives, 2
dissipation, 1
dual working principle, 7
duty cycle, 11

efficient configuration, 156
eigen
    modes, 6
    resonance, 6
electric
    buck converter, 15
    drive technology, 2
    resonance converter, 7
energetic performance, 144
energy
    kinetic, 3, 4, 12, 20, 58
    potential, 3
equilibrium, 104
etching, 40
experiments
    advanced, 144
    basic, 55

Fast-Fourier-Transformation, 28, 86
fatigue endurance, 38
FFT, 86
field effect transistor, 2, 11
flatness, 113
flow control mode, 16, 164

force capacity, 157
free-wheeling
  ratio, 17
  valve, 4
frequency
  domain, 85
  gap, 103
  natural, 46, 154
  shaping, 109
  switching, 34, 36
friction, 105

gain cross over frequency, 111
gas spring, 83
Gevrey-function, 140

Hagen-Poiseuille, 41
Helmholtz resonator, 31, 43, 52
Hurwitz-Polynomial, 122
hydraulic
  boost buck converter, 13, 162
  boost converter, 13, 162
  buck converter, 11
  D/A-converter, 8
  ram, 2, 13
  resonance converter, 7
  wave converter, 5
hydraulics
  digital, 8
  fast switching, 10
HydroLib, 28

IFFT, 86
inductance, 2, 40, 160
  coil, 71
  geometry, 64
  parasitic, 29
  spindle, 150
  threaded, 70
inertia, 5
input-output linearisation, 113
Inverse-Fast-Fourier-Transformation, 28, 86

Jacobian, 91

$\lambda/2$-resonance, 99
$\lambda/4$-compensator, 53
$\lambda/4$-resonance, 40
laminar, 27, 48
linearisation, 109
linearised observer dynamics, 119
Lipschitz, 80
load
  capacitance, 160
  dead, 102, 149
  sensing, 2
  specifications, 36
low power, 72

magnetic force, 57
malfunction, 9
manufacturing costs, 2
mass balance, 82
metering, 106
  edge, 82
method of characteristics, 28, 105
mobile hydraulics, 2
MOC, 28, 105
momentum balance, 103

node
  Kirchhoff, 57
  point, 19
  volume, 33, 77, 96, 100
noise, 34

observability canonical form, 120
observer
  complete, 121
  design, 118
  load, 127
  reduced, 134
oil stiction, 25
orifice
  equation, 79
  metering, 1
  root-function, 80
oscillator
  spring mass, 7

parasitic
  capacity, 32
  effects, 29
  inductance, 29
partial system, 103
periodic, 28, 79
pipe, 27, 60
polynomial function, 80
polytropic, 42, 83
power electronics, 38

pre-
  filter, 139, 141
  pressure, 144
  pressurised, 12, 156
  processing, 139
pressure
  attenuation, 42
  control mode, 18, 165
  node, 6
  symmetry, 106
process force, 127
proportional
  control, 1
  drive, 58
PT-2, 106
pulsation
  damper, 47
  engine, 2
pulse-width-mode, 11
PWM
  control, 24
  controlled, 104
  mode, 12, 14

quantisation, 8
quasi-static, 145

recuperation, 3, 20, 23, 24, 51
reflect, 31
reliability, 10
reservoir, 12
residual vector, 89
resistance
  control, 1, 58
  Hagen-Poiseuille, 41
resonance effect, 27
Reynold's number, 41
robustness, 9

side-branch, 6, 53
single pulse mode, 5
soft hydraulic system, 102
spill-over, 3, 13
spring-plate, 40
steady state, 79
stick-slip, 105
supply line, 33, 43
switching
  frequency, 34, 36
  interval, 88
  period, 105
synchronise, 56

tank
  line, 33
  preloaded, 14
  pressure, 31
thyristor, 2
time
  constants, 103
  domain, 79
  varying, 119
Time-Frequency-Domain-Iteration, 79, 85
trade-off, 70, 100
trajectory
  error, 116
  planning, 139
  pre-filter, 141
  pre-processing, 140
transfer function, 109
transition ratio, 18, 42
transmission line, 27
turbulence criterion, 41

valve
  ball, 150
  cartridge, 60
  check, 60, 81
    plate type, 39, 73
  comb, 38, 55
  digital, 8, 37
  flow control, 61
  multi poppet, 39
  on/off, 8, 37
  overlap, 25, 87, 105, 146
  poppet, 25, 37
  pressure relief, 50
  proportional, 82
  servo, 149
  spool, 25, 37, 82
  timing, 56
vibration compensator, 53

water hammer, 29, 31, 32
wave propagation, 5, 27, 105
winding, 64
working point, 93